



HAL
open science

Scintillation pathways in lead halide perovskite nanocrystals in liquid and solid media

Matilde Baravaglio

► **To cite this version:**

Matilde Baravaglio. Scintillation pathways in lead halide perovskite nanocrystals in liquid and solid media. Physics [physics]. Université Claude Bernard - Lyon I, 2023. English. NNT : 2023LYO10239 . tel-04801052

HAL Id: tel-04801052

<https://theses.hal.science/tel-04801052v1>

Submitted on 25 Nov 2024

HAL is a multi-disciplinary open access archive for the deposit and dissemination of scientific research documents, whether they are published or not. The documents may come from teaching and research institutions in France or abroad, or from public or private research centers.

L'archive ouverte pluridisciplinaire **HAL**, est destinée au dépôt et à la diffusion de documents scientifiques de niveau recherche, publiés ou non, émanant des établissements d'enseignement et de recherche français ou étrangers, des laboratoires publics ou privés.

**THESE de DOCTORAT DE
L'UNIVERSITE CLAUDE BERNARD LYON 1**

Ecole Doctorale N° ED52

Physique et Astrophysique de Lyon (PHAST)

Discipline : Physique

Soutenue publiquement le 24/11/2023, par :

Matilde Baravaglio

**Voies de scintillation dans les
nanocristaux de pérovskites halogénées
en milieux liquides et solides**

Devant le jury composé de :

Peter REISS Directeur de Recherche, CEA, CNRS	Rapporteur
Anna VEDDA Professeure, Université Milano-Bicocca,	Rapporteuse
Emmanuel BENICHOU Professeur, Université Claude Bernard Lyon 1, ILM	Président
Aurélie BESSIERE Chargée de recherche CNRS, Université Montpellier	Examinatrice
Anne Laure BULIN Chargée de recherche INSERM, Université Grenoble-Alpes	Examinatrice
Christophe DUJARDIN Professeur, Université Claude Bernard Lyon 1	Directeur de thèse
Benoit MAHLER Chargé de recherche CNRS, Université Claude Bernard Lyon 1	Co-Directeur de thèse
Cuong DANG Professeur associé, Nanyang Technological University	Invité

Table of Contents

Table of Contents	iii
List of Abbreviations	v
Introduction	1
Aim of this work	2
Thesis outline	4
1 Fundamental background	7
1.1 Colloidal semiconducting nanomaterials	7
1.2 Perovskite nanocrystals	12
1.2.1 Morphology and surface chemistry	18
1.2.1.1 Ligand binding and surface reactions	20
1.3 Ionizing radiations and scintillating phenomena	24
1.3.1 Traditional bulk scintillators	29
1.3.2 Nanostructured scintillators: perovskite nanocrystals	32
1.3.3 Liquid scintillators	37
2 Lead halide perovskite nanocrystals synthesis and characterization	43
2.1 Optical and structural characterization	43
2.1.1 X ray diffraction	44
2.1.2 Optical absorption	45
2.1.3 Photoluminescence	47
2.1.4 Photoluminescence excitation	48
2.1.5 Photoluminescence quantum yield	50
2.1.6 X-rays radioluminescence	51
2.1.7 Luminescence decay rate	54
2.1.8 Transmission electron microscopy	56
2.2 Colloidal perovskite nanocrystals synthesis	59
2.2.1 Nucleation and growth	59
2.2.1.1 Classical nucleation theory: Gibbs-Thomson model	60
2.2.1.2 Lamer mechanism	63
2.2.1.3 Ostwald ripening mechanism	64
2.2.1.4 Coalescence and oriented attachment	64
2.2.1.5 Intraparticle ripening	64
2.2.2 Hot injection synthesis	64
2.2.3 Ligand-assisted reprecipitation synthesis	66
2.3 Nanocubes and nanoplatelets selective synthesis	68

2.3.1	Precursors synthesis	68
2.3.2	OA/OAm-capped nanocrystals synthesis	69
2.3.3	Soy lecithin-capped nanocrystals synthesis	75
2.4	CsPbBr ₃ /CdS and CsPbBr ₃ /ZnS heterostructures	76
2.5	One-pot synthesis of multiple nanoplatelets populations	77
2.6	2D perovskite nanostructures	77
2.7	Embedding lead halide perovskite nanocrystals in polymeric matrices	78
3	Energy deposition in perovskite nanocrystals liquid scintillators	83
3.1	Energy deposition possible pathways	85
3.2	Sample quality optimization	86
3.2.1	Colloidal stability	87
3.2.2	Size selection	89
3.2.3	Photoluminescence quantum yield-improving surface treatments	92
3.3	Triple to Double Coincidence Ratio	99
3.4	Core/shell strategy for water stability	109
3.4.1	CsPbBr ₃ /ZnS "raspberry" heterostructure	110
4	Energy transfers in perovskite nanostructures	119
4.1	Perovskite coupling in scintillating heterostructures	120
4.2	Perovskite nanostructures assemblies	121
4.2.1	Nanoplatelets and nanocubes assemblies	121
4.2.2	Nanoplatelets stacks	128
4.3	Cs-doped halide perovskite 2D nanostructures	132
	Conclusions and perspectives	143
	Acknowledgements	149
	References	151

List of Abbreviations

2-AA	2-aminoanthracene
AIBN	Azobisisobutyronitrile
BGO	Bismuth germanium oxide
BMA	Butyl methacrylate
BzA	Benzoic acid
C₆Am	Hexylamine
CB	Conduction band
CynAc	Cynnamic acid
DDTC	Diethyldithiocarbamate
DIPN	2,6-diisopropylnaphthalene
DOS	Density of states
HAB	Hexylammonium benzoate
HAB/SoyL	Hexylammonium benzoate to soy lecithin ratio
HAC	Hexylammonium cynnammate
FFT	Fast Fourier transform
FRET	Forster resonance energy transfer
FWHM	Full width at half-maximum
LHPNC	Lead halide perovskite nanocrystal
LARP	Ligand-assisted reprecipitation
LED	Light-emitting diode
LSC	Liquid scintillation cocktail
NC(s)	Nanocrystal(s)
NP(s)	Nanoparticle(s)
NPL(s)	Nanoplatelet(s)
NRET	Non-radiative energy transfer
ODE	1-octadecene
OA	Oleic acid
OAm	Oleylamine
PEABr	Phenethylammonium bromide

PhCOBr	Benzoyl bromide
PL	Photoluminescence
PLE	Photoluminescence excitation
PMAO	Poly maleic anhydride-alt-octadecene
PMT(s)	Photomultiplier(s)
PPO	2,5-diphenyloxazole
PS	Polystyrene
QD	Quantum dot
QW	Quantum well
QY	Quantum yield
RL	Radioluminescence
SBMA	Sulfobetaine methacrylate
SoyL	Soy lecithin
TCSPC	Time-correlated single photon counting
TDCR	Triple to double coincidences ratio
TEM	Transmission electron microscopy
TFE	2,2,2-trifluoroethanol
TOF-PET	Time of flight - Positron emission tomography
TOP	Trioctylphospine
VB	Valence band
XRD	X-ray (powder) diffraction

Hai bisogno di te
hai bisogno di questo tempo
in cui non si cucina
e non si prega
si sta.
Soli e improvvisati
abbandonati e senza senso
si sta, frastornati
e vuoti. Si sta.
E l'indomabile fiducia
accucciata fuori dalla porta
come un cane folle
di devozione
dorme sonni
che contengono alba.

Hai bisogno di te

Chandra Livia Candiani

Introduction

Lead halide perovskite nanocrystals (LHPNCs) are semiconductors of ionic nature which emerged during the last two decades as one of the most promising materials in physics, chemistry and device engineering.[1] These structures were the first ones in the colloidal nanocrystals (NCs) family to exhibit bright photoluminescence (PL) over the entire visible spectral range without electronic surface passivation,[2] and they stand out in the nanomaterials field due to their very bright photoluminescence, with tuneable quantum-sized effects on excitonic emission, as well as their electronic properties' exceptional tolerance to the material's defects and surfaces.[1, 3–5]

Their outstanding optical and electronic properties of these nanostructures led to an exponential increase in the related published articles during the last two decades, with a vast variety of applications from photovoltaics to photocatalysis and optoelectronics, including light-emitting diodes (LEDs), colour conversion systems and quantum photonic technologies.[1, 6–9]

These colloidal metal-halide perovskites can now be synthesized in solution through rather easy and inexpensive syntheses, which allow to obtain shape-controlled nanocrystals showing narrow luminescence, short radiative lifetimes (ns to sub-ns), tuneable emission wavelengths and photoluminescence quantum yields up to more than 90% .[10, 11]

All of these exciting features, combined with the presence of heavy metals in the chemical composition, led perovskite materials to become a trending material also in the scintillation field, where they make good candidates for realizing ionizing radiations detectors.[12] This field is of great interest, since high energy radiation detection has a crucial role in high-energy physics experiments, oil drilling explorations, diagnostic imaging, nuclear and radiation prevention, and homeland security.[13–16]

Perovskite-based ionizing radiation detectors have been developed during the last two decades in different forms:[17] a first branch involves perovskite 3D bulk structures, which share with the traditional bulk scintillators the benefits of a high density and large-scale production methods, but also the drawbacks of a moderate radioluminescence

light yield, long time decays and high production costs.[18] On the other hand, their corresponding lead halide perovskite nanocrystals lack in their overall density but show higher, faster and tuneable luminescence, and thus a second research branch focuses on perovskite nanostructures, primarily in the form of colloidal nanocrystals embedded in plastic or resin matrices.[12, 19–26] The latter preserve the advantages of the bright and fast emission feature of the quantum-sized nanoparticles, and give them a good protection against humidity and oxygen; nevertheless, they inevitably lead to a low density composite, the matrices being mostly organic compounds. Nevertheless, in the case of applications requiring ultra fast emission, such as TOF-PET, heterostructures featuring lead halide perovskite nanocrystals hosted in a matrix can be the best option, giving the excellent emission rates of such nanostructures.[27–29]

Aim of this work

The here presented manuscript describes the strategies explored during this PhD project in order to describe and improve the performances of lead halide perovskite nanocrystals as scintillators, either in a liquid or solid form.

In order to understand the project behind the illustrated approaches it is important to be aware of the parameters that make these nanostructures promising scintillators, as their rather easily obtainable high luminescence and short emission decay time, as well as their inexpensive and easy fabrication.

On the other hand, it is crucial to focus on the features that need to be improved: a key parameter for a good scintillator is the overall material's density, since it impacts the stopping power towards the ionizing radiation, and thus the probability of interaction and, consequently, of radioluminescence. This is particularly important in the case of colloidal nanostructures, since they need to be dispersed in a matrix for protection against the environmental moisture. A matrix, which is typically organic, highly dilutes the overall material's density: even nanostructures containing components with high effective atomic number Z_{eff} , like the lead halide perovskite nanocrystals treated in this work, can thus result in low density composites.

Another parameter that needs to be optimized is the light yield. As a matter of facts, these nanomaterials have an intrinsically short Stokes shift, which implies a high overlap between the optical absorption and photoluminescence spectra. This results in a high probability of re-absorption of the light just emitted by the nanocrystals in the system, and thus decreases and slows down the overall light emission. Moreover, this probability of re-absorption increases with the concentration, since the emitted photons can either

end up trapped in the system, not being able to reach the detectors, or go through several emission-absorption-emission steps before escaping the system: this makes it hard to load a composite with a high amount of nanoparticles, even though it would benefit the stopping power, since it would negatively impact the light emission yield. Thus, without being able to rely on the increase of the quantity of matter, an optical light yield is crucial, since the more the incident radiations are converted in a narrow energy range of emitted photons, the more the latter are likely to reach the detectors: therefore, optimizing the light yield has a crucial role in the detection efficiency.

Consequently, this project focuses on strategies aiming to overcome the conflicting parameters impacted by lead halide perovskite nanocrystals short Stokes shift: increasing the nanocrystals concentration would be beneficial for the overall system's stopping power towards ionizing radiations, but on the other hand the light self-absorption limits the concentration increase. Thus, this thesis manuscript describes some studies developed to enhance the scintillating performances of such nanostructures, in either liquid or solid media, overcoming their limited possible loading in their host.

As a first approach, halide perovskite nanocrystals have recently arose high interest in the liquid scintillation field, again owing to their bright and tuneable light emissions, their fast decay time and high effective atomic number: nevertheless, their performances have been evaluated mainly as a dye, collecting the light emitted from other constituent of the liquid mixture and then emitting by fluorescence.[30–32] One example is found in literature of a study on CsPbBr₃ acting as both the ionizing energy collector and radioluminescence emitter, once successfully coupled with PPO,[33] which is traditionally used itself as a dye in organic liquid scintillators. Otherwise, the energy deposition mechanisms in such lead halide perovskite nanocrystals and the factors limiting their performances has yet to be explored. Liquid scintillation results then as an interesting topic and opportunity to study the interaction between perovskite nanocrystals and their surrounding media: in particular, great attention is focused in this work on the energy deposition mechanism and on the eventual interaction between the dispersed nanocrystals and the surrounding solvent. as a matter of fact, if the mechanism does involve energy transfers from the solvent to the colloids, similarly to what happens in traditional organic liquid scintillators, this would overcome the overall density issue, as the first energy collector would be the solvent.

A similarly conceived approach to artificially engineer lead halide perovskite nanocrystals' Stokes shift is coupling them with a surrounding partner material, like a bulk crystal or similar perovskite nanostructures with slightly different bandgaps. The latter's role would be to collect the incoming ionizing radiation, modulate it and transfer it to the chosen, lowest bandgap, final emitter: an optimal transfer would artificially enlarge the

overall system's Stokes shift, thus entailing a high light emission from the final perovskite NCs without having to increase their concentration, thus without increasing the risk of light re-absorption.

Thesis outline

The here presented manuscript describes the strategies explored during this PhD project in order to describe and explore the performances of lead halide perovskite nanocrystals as scintillators, and it is organized in 5 chapters as follows.

Chapter 1 will provide an introduction to the main topics discussed in this thesis: a fundamental background will be given on traditional colloidal semiconducting nanomaterials and their characteristic features, followed by an overview on perovskite nanocrystals. The latter section will explain into detail all the reasons that made lead halide perovskite nanocrystals so popular in various physics and chemistry fields, with a further focus on these structures' morphology and surface chemistry, and especially the surface interaction with the typical stabilizing organic ligands. Afterwards, some background will be given on ionizing radiations, followed by their traditional detectors in the form of bulk scintillators and liquid scintillators, with insights on each one's common application fields, advantages and disadvantages. The introduction chapter will be concluded by an explanation of why lead halide perovskite nanocrystals gained interest in the scintillation field and by an overview on the features needing further optimization.

Chapter 2 is conceived as a pedagogical instructions set for the lead halide perovskite nanocrystals synthesis and characterization: the basic principles of the optical and structural characterization techniques used in this work will be given, such as optical absorption and emission spectroscopy, photoluminescence excitation spectroscopy and photoluminescence quantum yield, X-ray radioluminescence, optical and X-ray luminescence decay rate, X-ray diffraction and transmission electron microscopy. Afterwards, some theoretical insights will be detailed about colloidal perovskite nanocrystals formation mechanism, in terms of nucleation and growth; this will be followed by an illustration of the hot injection and ligand-assisted reprecipitation methods, which are the most commonly used synthetic approaches. The final part of the chapter deals with the description of typical synthesis performed throughout this work, in particular dealing with the selective syntheses of either nanocubes or nanoplatelets populations, and finally with the option of embedding the colloidal nanostructures in a polymeric matrix.

Chapter 3 contains the work on lead halide perovskite nanocrystals as the primary emitter in liquid scintillators, and on the possible parameters to consider in order to

limit the light self-absorption, induced by the small Stokes shift, in such systems. The possible considered energy deposition mechanisms are illustrated, followed by an explanation of which parameters need to be optimized in order to be able to get information on the actual mechanism involved in the radioluminescence. This is followed by the optimisation of such parameters, namely the nanocrystals' colloidal stability, optimal size and photoluminescence quantum yield. Once the samples optimized, they were tested via the Triple-to-Double Coincidence Ratio technique, and the obtained information is presented and explained. The final section of the chapter involves the attempts to transfer such lead halide perovskite nanocrystals into polar solvents such as water, by growing a protective shell around the nanoparticles, with the aim of expanding the application fields of these liquid scintillators.

Chapter 4 continues the work on the Stokes shift artificial engineering of lead halide perovskite nanostructures, started in the previous chapter, but transposed to solid systems: the hypothesized energy transfers are illustrated, followed by the practical approaches that were explored. Different populations of lead halide perovskite nanoplatelets and nanocubes were mixed together in order to observe if efficient energy transfers from the first to the second species can occur; then, nanoplatelets of different thickness were produced via a one-pot synthesis and then stacked together on glass supports, and energy transfers from the thinnest to the thickest ones were investigated. Afterwards, the same approach was applied to the induction of sub-nanostructures formation inside 2D perovskite crystals and thin films, again in order to induce internal energy transfers and thus reduce the re-absorption phenomenon.

Conclusions and perspectives chapter finally concludes the work and discusses future outlooks.

Chapter 1

Fundamental background

1.1 Colloidal semiconducting nanomaterials

Colloidal semiconducting nanomaterials, such as the famous chalcogenides CdS (cadmium sulfide), CdSe (cadmium selenide), ZnS (zinc sulfide), and perovskite nanocrystals, are structures showing optical and electronic features of particular interest, owing to the combination of their direct bandgap nature and their nanometric size range. This particular information is key, since it results in their optical and electronic properties being significantly different from their bulk counterparts, thus explaining the interest that aroused around these materials.[34, 35]

Indeed, in bulk semiconducting materials electrons and holes have a continuous energy spectrum, but, when decreasing the material's size to the nanoscale, the energy levels become discrete and the wavefunctions of electrons and holes change. This change happens because their size is smaller than or comparable to the exciton Bohr radius of the material, which represents the average distance between an electron promoted to a higher energy state, after the absorption of a photon, and a positively charged hole, representing the now-empty original energy state. The illustration in Figure 1.1 shows how this phenomenon affects the density of states DOS in structures affected by confinement in one, two or three dimensions: for the aim of this work, the focus will be centered around 3D confined materials, also called quantum dots QDs, and 1D confined materials, also called quantum wells.[36]

In summary, when electrons are confined, their energy is quantized, just like the energy levels in an atom, and their wavefunctions change. In semiconducting nanostructures, such as quantum dots, the confinement of electrons and holes increases the system's energy: a first consequence is the absorption and photoluminescence features blue-shifting, with the corresponding wavelengths decreasing with the nanomaterial's size.[34, 37]

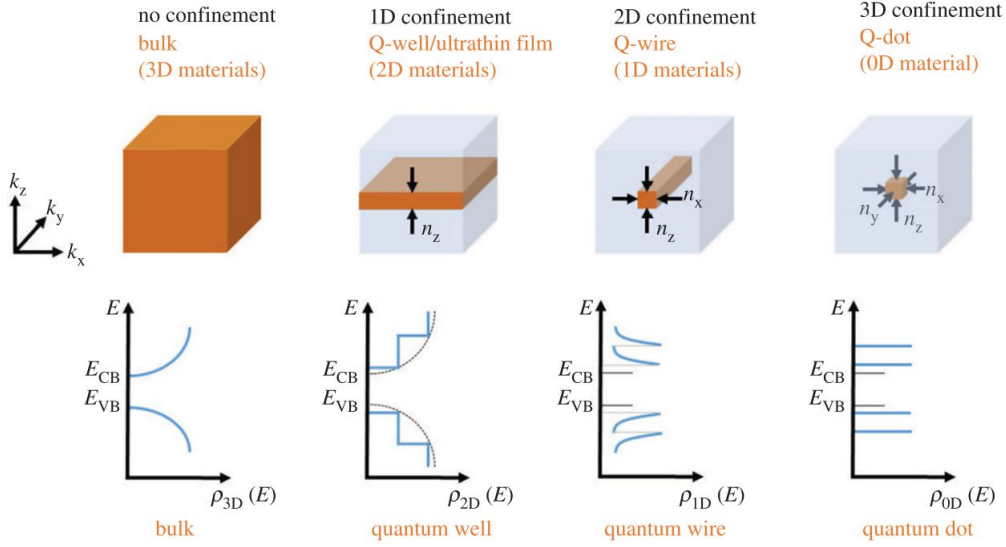


FIGURE 1.1: Schematic illustration of broken symmetry and functional form of the density of states in 1D, 2D and 3D confined materials. Reproduced from the work of Edvinsson et al.[36]

It is important to understand how the nanoparticles' size impacts their optical features, therefore more details are here presented on one of the most influencing parameters, thus the exciton Bohr radius. This factor is derived from the Bohr model, which was originally developed to describe the hydrogen atom: this model suggests that the electron and hole revolve around their common center of mass in circular orbits, similar to an electron in a hydrogen atom. The exciton results in an electrically neutral, composite quasi-particle, wherein the electron, promoted to a higher energy state after the absorption of a photon, and the hole in its original energy state, are attracted to each other by the Coulomb force.

The exciton Bohr radius represents the average distance between the electron and hole within the exciton. For 3D semiconductors, it is calculated by using the exciton's reduced mass, calculated from the ones of the electron and hole $\mu = (m_e m_h)/(m_e + m_h)$ and the static relative permittivity ϵ_r of the material as follows:[38]

$$r_n = \left(\frac{m_0 \epsilon_r a_H}{\mu} \right) n^2 \quad (1.1)$$

where m_0 is the free electron mass, n is a quantum number representing an energy level and a_H is the Bohr radius of the hydrogen atom. The exciton Bohr radius is an important parameter in the study of excitonic properties, such as energy levels, binding energy, and interaction strength, for various materials, including semiconductors and organic molecules.[34, 39] It provides insights into the spatial extent and stability of

excitons, which are crucial for understanding their behavior and applications, like in optoelectronic devices and for studying light-matter interactions in materials.

In particular, the light absorption and photoluminescence features of nanocrystals, as well as the effect of dopants, all depend strongly on the nanocrystals' radius. In fact, if r is the size of the confined dimension of the nanostructure, and r_B is its exciton Bohr radius, the ratio $\beta = r/r_B$ can be used to evaluate the confinement regime describing the system. When $\beta \gg 1$, thus the size of the NC is bigger than the exciton Bohr radius, the system experiences a weak confinement regime: in this case, the exciton's binding energy of is larger than the quantization energy of both the electrons and holes, and the optical spectra of these nanocrystals are determined by the quantum confinement of the exciton center of mass.[34] In this case, the exciton ground state energy is given by

$$\hbar\omega = E_g - E_b + \frac{\hbar^2\pi^2}{2Mr^2} \quad (1.2)$$

where E_b is the exciton's binding energy, E_g is the semiconductor's energy gap and $M=m_e+m_h$ is the exciton translation mass.[40]

However, the Coulomb force strongly affects the nanocrystal optical spectra as well, as the electron and hole are both confined in the same volume: the Coulomb energy of their interaction is on the order of $e^2/\kappa r$, where κ is the dielectric constant of the semiconductor. Since, as per the equation above, the quantization energy increases with decreasing size as $1/r^2$, whereas the Coulomb energy only grows as $1/r$, in large nanocrystals the Coulomb interaction is more important than the quantization energies of the electrons and holes.[34]

On the other hand, when $\beta \rightarrow 0$ the system is in a strong confinement regime, for which the optical spectra can be considered as spectra of transitions between electron and hole quantum-size levels. In this case, the electron-hole Coulomb interaction becomes only a small correction. The selection rules governing the interband transitions between quantum-size levels of parabolic conduction and valence bands are very simple: transitions are allowed only between levels with the same quantum numbers.[34] As a result, absorption spectra are given by the following equation:[41]

$$\hbar\omega_\nu = E_g - E_\nu^h(r) + E_\nu^e(r) - 1.8\frac{e^2}{\kappa r} \quad (1.3)$$

Therefore, the nanocrystals absorption and luminescence spectra are determined by quantum-size effects on the specie's electronic structure. In particular, the different responses to quantum confinement are precisely the main difference between traditional

Compound	r_B (nm)	Ref.
CdS	5.8	[42]
CdSe	5.3	[43]
CdTe	7.3	[44]
ZnSe	5.7	[45]
MAPbBr ₃	4.0	[46, 47]
MAPbI ₃	4.4	[46, 48]
CsPbCl ₃	5	[10]
CsPbBr ₃	7	[10, 49, 50]
CsPbI ₃	12	[10]

TABLE 1.1: Exciton Bohr radii for some examples of semiconductors.

quantum dots and perovskite nanocrystals, in terms of their optical features. Table 1.1 shows some examples of exciton Bohr radii for famous semiconductors, such as CdS, CdSe, CdTe and ZnSe, compared to the ones of some perovskite structures. The latter have indeed a much smaller Bohr radius, making the corresponding perovskite nanocrystals, whose size is typically in the order of 10-15 nm, experience weak confinement. This is the reason behind the fact that, in order to change perovskite 3D nanocubes' optical absorption and emission, a size selection alone doesn't allow to roam that much in the visible range, for which it is much more effective to change the chemical composition. On the other hand, in the case of perovskite 2D nanoplatelets, the quantum well's thickness is smaller than the exciton Bohr radius, and thus nanoplatelets' optical features are much more impacted by the quantum-size effects on the specie's electronic structure. This will be further shown in the following section, dedicated to perovskite nanostructures. On the other hand, traditional chalcogenide QDs undergo strong confinement, allowing to obtain very different optical features in all the visible range by only modifying the NCs sizes, as depicted in the example in Figure 1.2.[35]



FIGURE 1.2: Fluorescence of CdSe/CdS core/shell nanoparticles with a diameter of 1.7 nm (blue) up to 6 nm (red), giving evidence of the scaling of the semiconductor band gap with particle size. Reproduced from the work of Roduner et al.[35]

The cited examples, i.e. CdS, CdSe, and ZnS quantum dots have been particularly studied in the last forty years due to their unique properties.[51–55] CdSe nanocrystals, for instance, exhibit a large range of photoluminescence emissions in the visible spectrum, with a high quantum yield, easily obtainable just by controlling the NCs size; ZnS nanocrystals are known for their excellent stability and resistance to oxidation, making them ideal for applications that require long-term stability; CdS nanocrystals have shown to exhibit a strong piezoelectric effect, making them suitable for mechanical energy harvesting applications. These properties made these materials very popular during the recent development of optoelectronic devices, either alone or most commonly combined in core/shell structures allowing to benefit from their different advantages.[56–60]

Certainly, these quantized energy levels and adjustable energy gaps sparked significant interest in the field of nanomaterial science during the last century, due to the resulting unique properties and potential applications: for instance, the size-dependent energy band gaps, that can be tuned to obtain the emission of specific wavelengths of light, make nanostructures great candidates for optoelectronic devices such as light-emitting diodes (LEDs) and solar cells.[1, 6–9, 61] Furthermore, colloidal semiconducting nanomaterials have very high surface area-to-volume ratios, which enables them to interact with molecules and ions in their surroundings, making them excellent sensors for detecting gases, chemicals, and biological molecules.[62–67] Commercially, one of their most widely known uses is in forming the basis QLED television screens where dots of different sizes are excited by blue light and then emit pure red and green light to give the three-colour output of the pixels in a TV screen. Moreover, they also have uses in biotechnology, catalysis, sensors, solar cells and more. In particular, quantum dots have just been the topic of the 2023 Chemistry Nobel Prize, as the committee highlighted the use of quantum dots in medical devices that are used to map biological tissue: because the dots' fluorescence is brighter and longer-lived than that of other fluorescent tags, such as molecular fluorophores, they can help to guide surgeons when removing tumours, for example.[68] In 2021, global sales of quantum dots were worth around \$4 billion, a figure that is predicted to double by 2026.[69]

To conclude, colloidal semiconducting nanomaterials have garnered significant interest due to their unique properties induced by quantum confinement, which make them suitable for a wide range of applications including optoelectronics, biosensing and energy harvesting.

1.2 Perovskite nanocrystals

Halide perovskite nanocrystals stand out in the nanomaterials field as direct bandgap semiconductors of ionic nature which were the first in the colloidal NCs family to exhibit bright photoluminescence over the entire visible spectral range without electronic surface passivation,[2] showing very bright and fast photoluminescence, allowed by their direct bandgap (Figure 1.3), the quantum-sized effects on their excitonic PL emission, as well as a high tolerance of the electronic properties to the material's defects and surfaces.[1, 3–5]

Perovskite nanocrystals are named after their crystal structure, which matches the mineral perovskite, i.e. the calcium titanate CaTiO_3 , which was first discovered in the Ural mountains of Russia and named after Russian mineralogist L. A. Perovski (1792–1856). These nanomaterials thus appear in the ABX_3 structure, A and B being cations of largely different size, and X being an anion: typically the B^{2+} cation is in a 6-fold coordination with X^- anions, thus forming $[\text{BX}_6]^{4-}$ octahedra which are ideally arranged in a cubic structure, and where the bulky A^+ cation is in a 12-fold cuboctahedral coordination. An illustration is presented in Figure 1.4.

The nature of the A cations that can fit into this cavity is limited by the resulting structural stability, which can be evaluated by some tolerance factors, namely the octahedral factor μ , the Goldschmidt tolerance factor t , and the modified Goldschmidt tolerance factor τ .

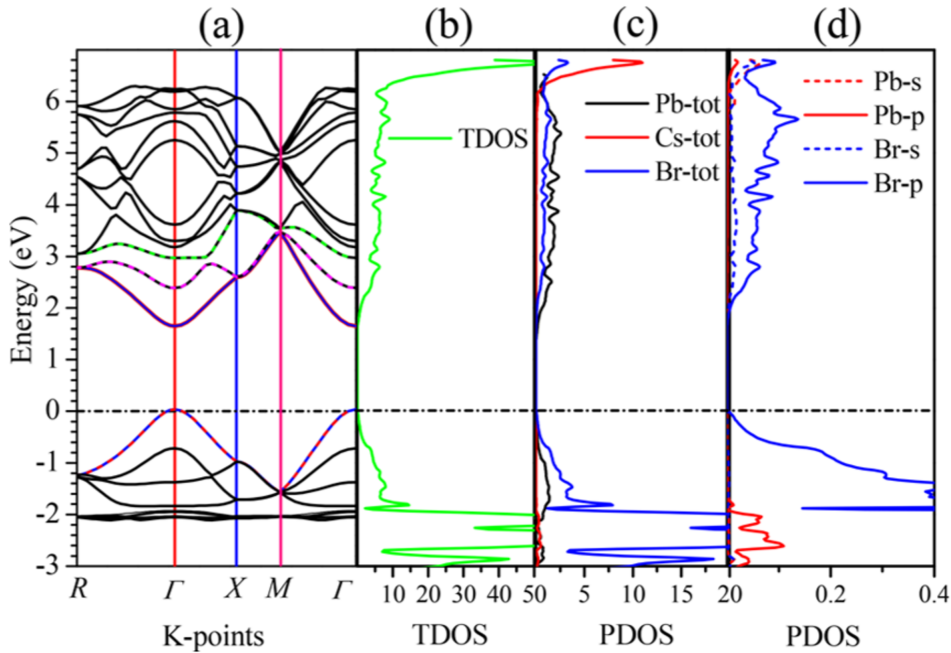


FIGURE 1.3: Band structure (a), TDOS (b), and PDOS of orthorhombic CsPbBr_3 obtained using the nmBJ-GGA+SOC potential (c, d). Reproduced from the work of Ghaithan et al.[70]

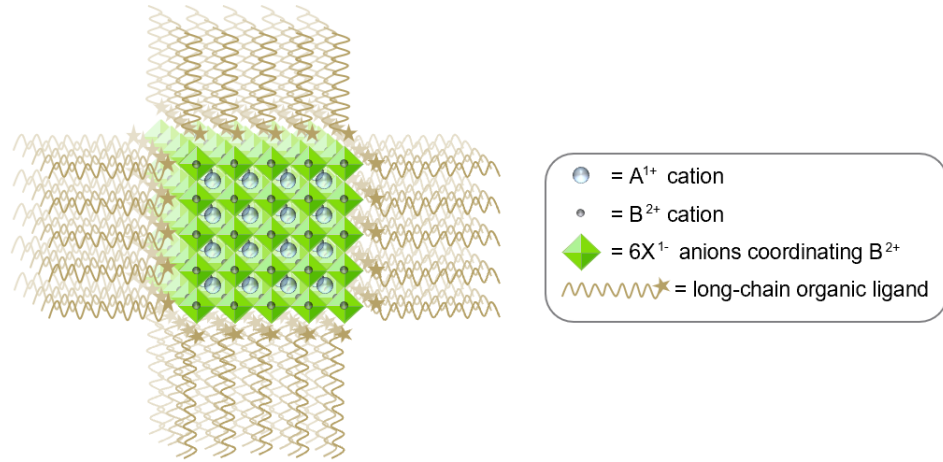


FIGURE 1.4: Illustration of a general ABX_3 perovskite colloidal cubic nanocrystal surrounded on the surface by its stabilizing organic ligands. The species dimensions are not in scale.

The simplest stability prediction factor is the octahedral factor, which is determined as the ratio of the ionic radii of the B cation r_B over the halide r_X :[\[71\]](#)

$$\mu = \frac{r_B}{r_X} \quad (1.4)$$

According to this this parameter, if μ ranges between 0.41 and 0.89, the $[BX_6]^{4-}$ octahedra, and by extension the perovskite structure, are considered stable.

Next, the Goldschmidt tolerance factor t can predict the stability of the perovskite structure based only on the chemical formula, ABX_3 , and the ionic radii, r_i , of each ion (A,B,X), and it is expressed as follows:[\[72\]](#)

$$t = \frac{r_A + r_X}{\sqrt{2}(r_B + r_X)} \quad (1.5)$$

This method has been used for the past 90 years to predict whether a material could be stable in a perovskite structure ($t \geq 0.71$), and whether in an orthorhombic or rhombohedral structure ($0.71 \leq t \leq 0.9$) or in a cubic structure, where the A and B cations have the ideal size ($0.9 \leq t \leq 1$). If $t \geq 1$, the A cation is too big or the B one is too small, and again the material will not be stable in a perovskite structure.

However, since recent studies have reported how this t factor lacks in accuracy, in particular showing different reliability for different halide compositions,[\[73\]](#) a new tolerance

factor, claimed to exhibit an overall accuracy of 92% and nearly uniform performance across oxides and halides, was proposed as it follows:[74]

$$\tau = \frac{r_X}{r_B} - n_a \left(n_a - \frac{r_A/r_B}{\ln(r_A/r_B)} \right) \quad (1.6)$$

In this formula, where n_a is the oxidation state of the cation A, r_i is the ionic radius of ion i, $r_A > r_B$ by definition, and $t < 4.18$ indicates perovskite structure.

According to these factors, a vast range of compositions results in stable ABX_3 perovskite structures, either fully inorganic or hybrid organic-inorganic: in the first case, A is a large monovalent cation, typically Cs^+ or Rb^+ , B is a bivalent cation, like Pb^{2+} , Sn^{2+} , Ge^{2+} and X is an anion, typically oxide O^{2-} or an halide like Cl^- , Br^- or I^- . Otherwise, in the case of hybrid organic-inorganic perovskite, the A component is represented by a small organic cations as methylammonium $CH_3NH_3^+$ (abbreviated MA^+) or formamidinium $CH(NH_2)_2^+$ (abbreviated FA^+). Halide perovskites structure usually deviate from the ideal cubic phase and present several polyforms depending on the temperature and composition, with their composition-dependent phase transitions described in recent literature.[75, 76]

This vast range of composition possibilities allows the development of diverse engineered materials for different applications, as just by tuning the chemical composition and the nanocrystals size it is possible to obtain tunable and narrow photoluminescence spectra in all the visible range and high color purity, with high photoluminescence quantum yields and fast photoluminescence decay times. Typically, by switching from chloride, to bromide, to iodide-based composition, it is possible to tune the photoluminescence maximum from blue to red color, with all the intermediate gradients obtained from mixed compositions, as illustrated in Figure 1.5.[1, 10]

These nanomaterials have quickly become a real trending topic, showing around 25000 papers containing the word “perovskite” in their title just in the past five years. The high interest towards them is justified by their great potential for a broad range of applications, from photovoltaics to optoelectronics and photocatalysis. Last years researches have investigated various aspects of both these materials photophysics, for stimulated emission and lasing,[10, 78–81] light-emitting devices,[82–87] and single-dot spectroscopy,[88–93]) as well as their chemistry, for surface reactions,[94–98] post-synthetic anion exchanges,[99–102] X-ray lithography,[103] shape-engineering,[104–107] self-assemblies,[108–111] and up-scaling and further variations of the synthesis.[112, 113] One of these nanocrystals most celebrated features is their bright PL, which does not require electronic passivation with epitaxial layers of wider-gap semiconductor[114–116];

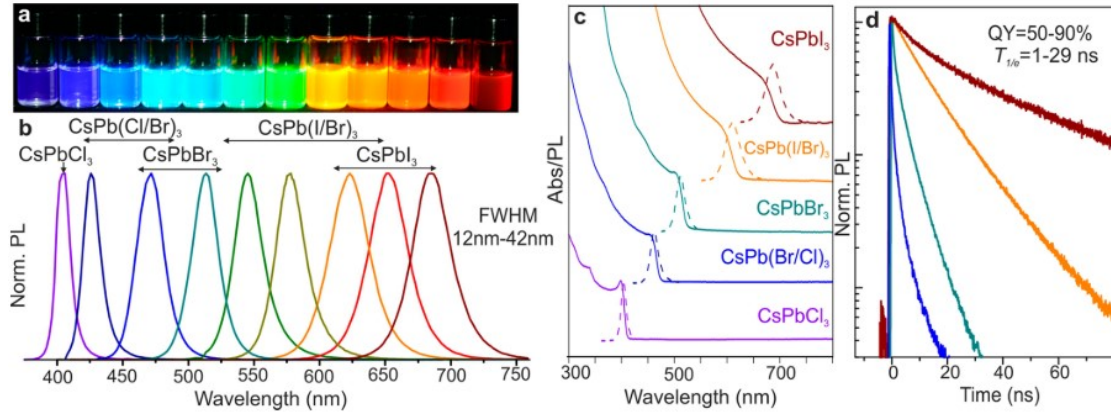


FIGURE 1.5: Colloidal perovskite CsPbX_3 NCs ($X = \text{Cl}, \text{Br}, \text{I}$) exhibit size- and composition-tunable bandgap energies covering the entire visible spectral region with narrow and bright emission: (a) colloidal solutions in toluene under UV lamp ($\lambda_{\text{exc}} = 365 \text{ nm}$); (b) representative PL spectra ($\lambda_{\text{exc}} = 400 \text{ nm}$ for all but 350 nm for CsPbCl_3 samples); (c) typical optical absorption and PL spectra; (d) time-resolved PL decays for all samples shown in (c) except CsPbCl_3 . Reproduced from the work of Protesescu et al.[10, 77]

moreover, other phenomenal characteristics include outstanding photovoltaic performances characterized by power conversion efficiencies exceeding 26%,^[117–120] very low density of carriers ($10^9 - 10^{11} \text{ cm}^{-3}$)^[121, 122] and traps ($10^9 - 10^{10} \text{ cm}^{-3}$),^[122] as well as high carrier mobilities ($25 - 100 \text{ cm}^2\text{V}^{-1}\text{s}^{-1}$).^[121, 123]

The optoelectronic features are not the only property for which these materials have been chosen for this work, since the presence of heavy B^{2+} cations in the chemical structure, in particular lead, give these nanomaterials a high Z_{eff} number, as well as the choice of caesium as the A^+ cation. Finally, in terms of the anion, the choice fell on bromide because of the superior brightness of Br^- -based perovskite nanocrystals compared to the chloride alternatives, and because of the better stability compared to the iodide counterparts.^[10] The interest of these particular CsPbBr_3 nanostructure thus relies on their suitability for efficient interactions with ionizing radiations, as better investigated later in this chapter. In fact, these nanocrystals show bright radioluminescence, with fast effective scintillation decay time τ_{eff} in the order of 10 ns.^[18, 21, 22, 24, 25, 124–126] This fast time response can be crucial for applications relying on time coincidence detection, as it is the case for time of flight-positron emission tomography (TOF-PET) scans for cancer detection, for example. This features are the reason why these materials were judged as promising candidates for the optimization of a new generation of fast, bright and easy-to-make scintillators.

All of these outstanding electronic and optical characteristics are quite surprising in light of the high structural disorder present in such materials, observable in the high density of vacancies (up to 1% of Schottky defects),^[127] unusual ionic rotations,^[128–130] and

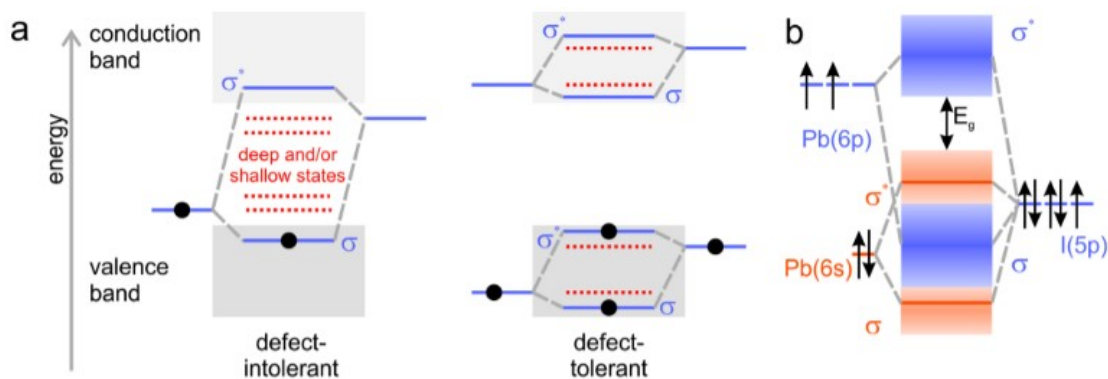


FIGURE 1.6: (a) Energy scheme of two limiting cases of the band structure in semiconductors: conventional defect-intolerant (left) and ideal defect-tolerant (right). Bonding and antibonding orbitals are identified as σ and σ^* , respectively.[130] (b) Simplified depiction of the bonding in MAPbI₃. [3] Reproduced from the work of Dirin et al.[136]

high ionic mobilities.[131–133] Normally, structural defects in semiconductors lead to a high density of corresponding defect energy states within the bandgap, resulting in trapping states: the rare feature where intrinsic defects do not lead to this detrimental consequence is the so-called defect-tolerance. The latter is one of the features which really makes these perovskite nanostructures stand out, as contrary to other traditional semiconducting nanocrystals, they are able to retain the electronic structure regardless of a high concentration of defects in the material.[3, 11, 123, 134, 135]

The defect-tolerance of the electronic structure of methylammonium lead iodide MAPbI₃ has been rationalized by Brandt et al.,[3] and it is illustrated in Fig. 1.6. Their work propose that the valence band’s maximum is formed by antibonding orbitals, arising from hybridization between the Pb(6s) and I(5p) orbitals. On the other side, the conduction band undergoes strong spin-orbit effect that result in its broadening: this results in the shifting of the bottom of the conduction band to below the Pb(6p) atomic orbital, which increases the likelihood that halide vacancies will form intraconduction band states. Consequently, compositional vacancies or interstitial atoms more likely result in resonances inside the bands, and not in detrimental intragap states.[130, 136]

In addition to that, it is not insignificant that these versatile lead halide perovskite nanocrystals are also obtained from easy and quite inexpensive synthetic processes, typically solution-based methods such as hot injection or ligand-assisted reprecipitation (LARP): with these methods, the particle size and emission wavelength can be tuned just by choosing the right precursors and reaction conditions. A description of these synthetic processes is given later in Chapter 2.

A final remark concerns a phenomenon that can have a detrimental impact on the optoelectronic properties of these perovskite nanostructures when they are highly concentrated, thus the significant potential self-absorption of the emitted light. Nevertheless,

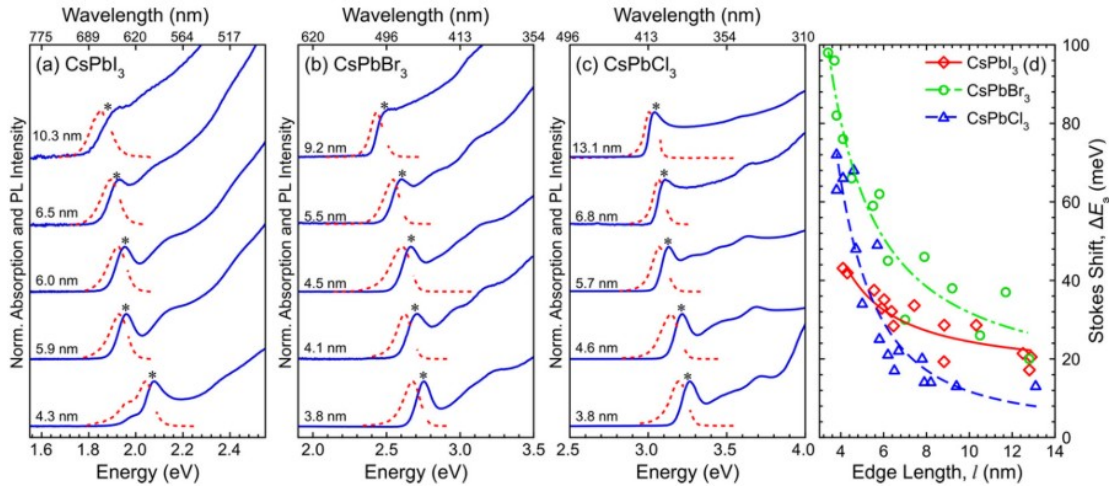


FIGURE 1.7: Ensemble absorption (solid blue lines) and PL (dashed red lines) spectra for a representative size series of (a) CsPbI₃, (b) CsPbBr₃ and (c) CsPbCl₃ NCs in toluene. PL spectra were acquired by exciting dilute NC ensembles at their respective band edges. Asterisks above each PL spectrum in (a-c) represent approximate PL excitation energies. TEM-derived l -values provided adjacent to corresponding spectra. Gaps in PL spectra indicate where Xenon arc lamp excitation has been cropped out. Spectra offset for clarity. (d) Associated Stokes shift versus l for CsPbI₃ (solid red line/diamonds), CsPbBr₃ (dashed-dotted green line/circles) and CsPbCl₃ (dashed blue line/triangles). Reproduced from the work of Brennan et al.[139]

high concentrations would be beneficial for the scintillation performances of the material, as they would increase its stopping power. This issue is due to their small Stokes shift, describing the phenomenon for which a fluorescent material's emitted light is shifted to longer wavelengths than the original absorbed light: this red-shift is due to the amount of energy lost during the process, due to non-radiative relaxation pathways like heat dissipation. When the Stokes shift is small, as in the case of lead halide perovskite nanocrystals, there is a high probability of light re-absorption, since the emission spectrum overlaps the absorption one: due to this overlap, the emitted light has a high chance of being re-absorbed by the surrounding nanocrystals and not being to escape from the medium and reach the PMT, causing a decrease in the photoluminescence quantum yield.[137, 138]

Brennan's studies on lead halide perovskite nanocrystals' Stokes shift concluded that these species' absorbing and emitting states are intrinsically different, and show size- and halide composition-dependent energies, as summarized in Figure 1.7.[139] The short Stokes shift results from intrinsic features due to band edge exciton fine structure, whereas reabsorption and polaron formation were excluded.[139–141] This interpretation was recently confirmed by temperature-dependent absorption and photoluminescence spectroscopy on CsPbBr₃ three-layers nanoplatelets, where a temperature-dependent Stokes shift was observed and attributed to the exciton fine structure.[142]

Nevertheless, this information still leaves room for some solutions. First, nanocrystals can be coupled with a fluorophore acting as a wavelength shifter, thus absorbing the light emitted by the NCs and emitting at a longer wavelength, not overlapping with the nanocrystals absorption spectrum anymore;^[25] otherwise, non-radiative energy transfers can be similarly used to red-shift the final light emission.^[143–149]

1.2.1 Morphology and surface chemistry

Perovskite QDs are generally cubic-shaped nanocrystals reflecting the intrinsic near-cubic symmetry of the crystal lattice: in fact, they are typically observed in three 3D polymorphs, namely cubic, tetragonal and orthorhombic, with the cubic phase existing at high temperature.^[150] In the case of colloidal CsPbBr₃ nanoparticles, they have been confirmed via synchrotron X-ray diffraction and total scattering techniques to have the orthorhombic (Pnma) structure,^[151] illustrated in Figure 1.8.

Nevertheless, the 3D cubic morphology is not the only possible one: depending on the precursors ratio and on the ligand type, it is possible to obtain either cubes, rods, platelets or wires,^[104–106, 161–164] the two latter illustrated in Figure 1.9.

The morphology of the nanostructure has a crucial impact on the resulting optical properties and applications: first, as already discussed, the more the structure's size is reduced, the more the excitons are affected by quantum confinement. The dimensionality has a key role in this, since a nanocube, a nanoplatelet (NPL) or a wire respectively undergo 3D, 2D or 1D confinement, resulting in different functional forms of the corresponding density of states, as previously illustrated in Figure 1.1. As discussed in

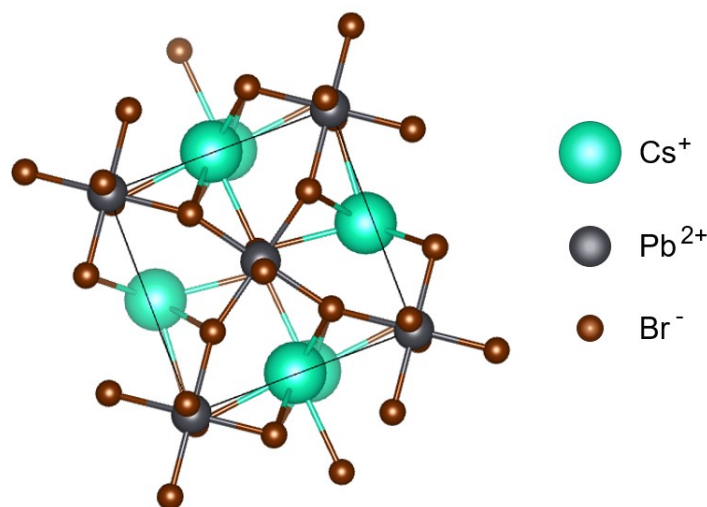


FIGURE 1.8: Illustration of the CsPbBr₃ Pnma orthorhombic structure. Reference XRD patterns were searched on Crystallography Open Database COD^[152–159] and imaged with VESTA software^[160].

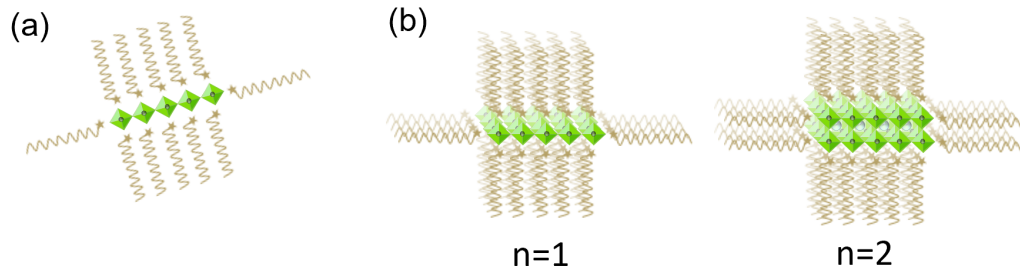


FIGURE 1.9: Illustration of ABX_3 perovskite nanowire (a) and nanoplatelets of increasing thickness (b), with their stabilizing organic ligands on the surface. Nanoplatelets' thicknesses are expressed in terms of the number of $[PbBr_6]^{4-}$ octahedra stacked planes n , and the illustration legend corresponds to that of Figure 1.4.

the previous section, whereas perovskite 3D nanocubes are not majorly affected by the quantum size effects on their excitons, in the case of nanoplatelets the thickness can be smaller than the material's Bohr radius: as shown in Figure 1.10, tuning the NPLs thickness allows their photoluminescence to roam in the visible range.[165] In addition to this effect, both the ligand bond strength and the nanoplatelets thickness play an important role in determining their optical properties,[166] as the stacking of $[PbBr_6]^{4-}$ octahedra planes leads to the formation of minibands, further shifting the bandgap energies; moreover, when the thickness $n \leq 2$, a new large exciton binding is found at an

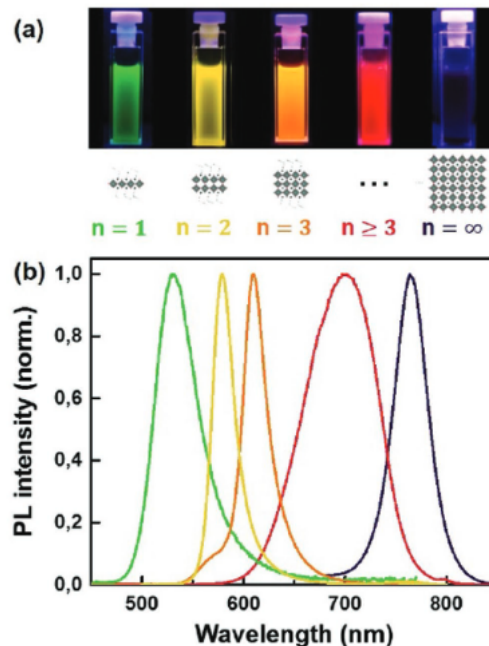


FIGURE 1.10: PL emission of MAPI NPLs of individual thickness. a) Images of cuvettes containing MAPI NPL suspensions illuminated with UV-light. From left to right, the thickness increases from a single monolayer ($n=1$) stepwise initially to a bulk-like value ($n=\infty$). b) PL-spectra of the aforementioned dispersions showing the blueshift with decreasing NPL thickness. Reproduced from the work of Hintermayr et al.[165]

energy up to several hundreds of meV, that partially counteracts the blue-shift induced by quantum confinement.[161]

Interestingly, the morphologies can be engineered in order to tune the resulting optical features. A first example is the exploitation of specific nanostructures aggregation, that in the case of 3D nanocubes can give rise to collective emission phenomena, showing shifted optical features.[109, 111] Then, in case of 2D nanoplatelets, literature provides examples of non radiative energy transfers occurring between stacks of nanoplatelets of different thickness, which has the effect of modifying the system's Stokes shift.[146, 147, 167] Nanowires, on their side, are promising candidates for optoelectronic devices,[105, 162] as lasing cavities.[79]

1.2.1.1 Ligand binding and surface reactions

The fact that lead halide perovskite nanocrystals do not need surface electronic passivation in order to maintain their optical features has already been discussed; however, since this work mainly discusses of colloidal systems, surface ligands are a crucial component of the studied samples. as a matter of fact, their role in these cases is to make the nanocrystals colloiddally stable by means of steric repulsion, i.e. to stabilize the dispersion and prevent the NCs aggregation and precipitation.

Many studies have been published in recent years unraveling the synthetic and post-synthetic chemistry of lead halide perovskite nanocrystals:[166, 171–174] the basis of these studies is the understanding of the nature of the bond between the nanoparticles and their surface stabilizing ligands.

A relevant and commonly-used approximation is the covalent bond classification (CBC), which considers every nanocrystal-ligand interaction as a covalent two-center-two-electron bond.[168] Based on the number of electrons donated by the ligand (in their neutral

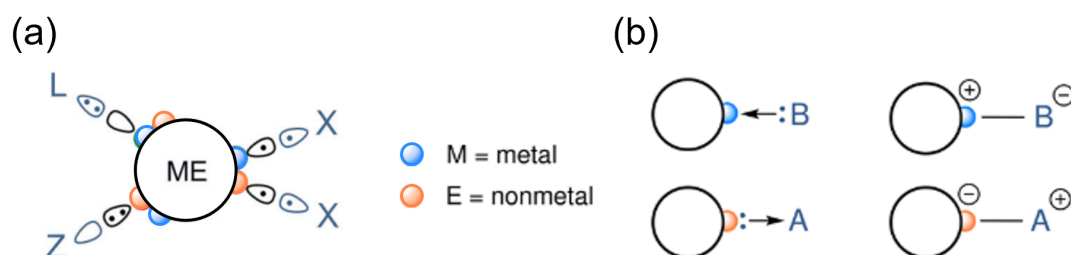


FIGURE 1.11: Illustration of the coordination of different types of ligands to metal-chalcogenide nanocrystals in Green's CBC classification[168] (a) and in the ionic model[169] (b). Figure (a) and (b) are reproduced respectively from the works of De Roo [170] and [171].

state) to the nanocrystal-ligand bond, the binding modes are classified as L, X, or Z type, respectively when 2, 1, or 0 electrons are donated by the ligand, as illustrated in Figure 1.11(a).[170]

Nevertheless, considering every bond a covalent interaction is not an accurate approximation in case of ionic interactions or hydrogen bonds: a second model that can be used to better describe these latter situations is the ionic model. This one classifies ligands as Lewis acids or Lewis bases, either neutral, respectively A or B, or charged, respectively A^+ or B^- in Figure 1.11(b).[169] It is good to underline that the CBC model classifies the binding modes, whereas the ionic one classifies the ligands.

Once this conceptual frameworks described, it is possible to move on to the nanocrystals binding motifs, i.e. the particular combinations of nanocrystal stoichiometry and ligand type.[170] Since these colloidal perovskite nanocrystals ionic nature imposes their synthesis and storage in nonpolar solvents, the condition of total charge neutrality applies. Written in the ionic model, five different types of binding motifs can be listed:[169, 171]

- $NC[(M^{n+})(B^-)_n]$: a cation rich core with anionic ligands
- $NC[(E^{n-})(A^+)_n]$: an anion rich core with cationic ligands
- $NC[A]$: a stoichiometric core with neutral Lewis acid ligands
- $NC[h]$: a stoichiometric core with neutral Lewis base ligands
- $NC[(A^+)(B^-)]$: a stoichiometric core with a stoichiometric mixture of cationic and anionic ligands

The binding motif rationalises the affinities of the NCs surface components with different ligands. In $CsPbBr_3$ nanocrystals the typical species found on the surface are $Cs^{\delta+}$ and $Br^{\delta-}$ anions, as it was confirmed by solid-state NMR spectroscopy,[175] with the charge densities depending on the species nature and on eventual vacancies. Good options of stabilizing ligands are then organic long-chain ammonium species, thus electron acceptors, and organic long-chain carboxylates, thus electron donors: typical examples are oleylammonium or quaternary alkylammonium cations, or oleate anions. As mentioned, the nature of the bonds depends on the species that are exposed on the surface, which depends of course on the nanocrystals chemical composition, and on their dimensions, the latter's dependency as illustrated in Figure 1.12(a).[176]

Lead halide perovskite nanocrystals developed in literature are traditionally stabilized by long and bulky amphiphilic ligands, e.g. oleylammonium and oleate,[95, 177] where

the alkylammonium cations occupy Cs surface positions and oleate anions bind to Pb sites.[175, 176]

Moreover, zwitterionic species are becoming increasingly popular as colloiddally stabilizing ligand:[98] this class of molecules has an equal number of both positive and negative charges in their structure, being then neutral as a whole. Having both positively and negatively charged functions, they are able to interact strongly with the surfaces of colloidal nanocrystals, which also present both partial positive and negative charges. Additionally, when zwitterions are also amphiphilic, with the two charged functions placed near one end and a long apolar chain on the other end, they can provide a good bulky and apolar barrier: this feature has already been described as effective in providing colloidal stability by preventing by steric hindrance the nanocrystals aggregation and growth.[176, 178] Examples of these species are sulfobetaines,[98, 179, 180] aminoacids,[181–183] polymers[184, 185] and natural compounds like soy lecithin, with which colloidal nanocrystals concentration as high as 400 mg/ml were obtained.[186]

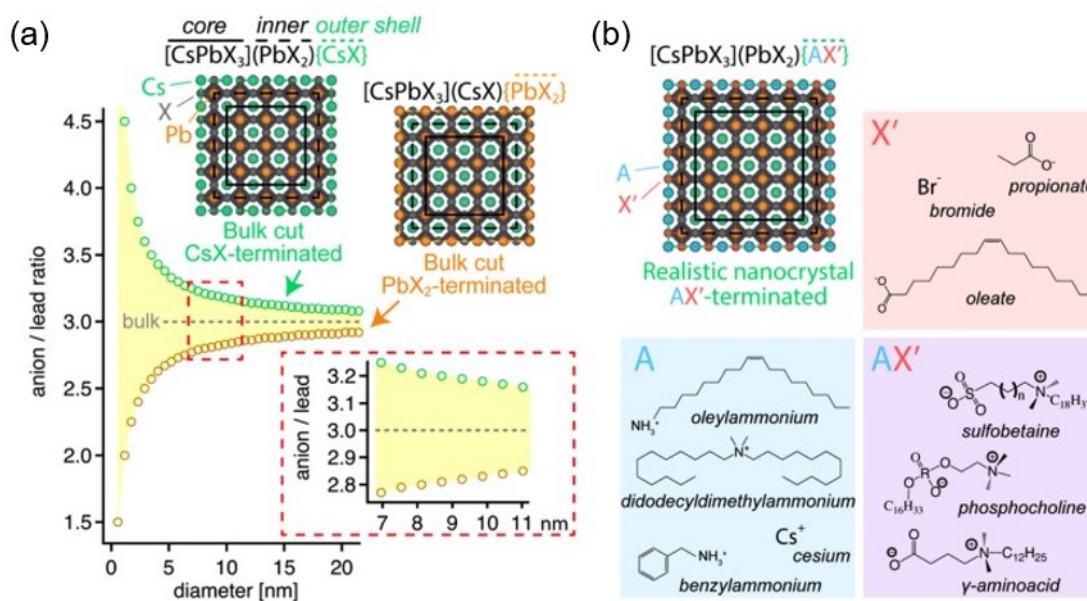


FIGURE 1.12: (a) Size-dependent halide/lead ratio (X/Pb) of cubic CsPbX_3 NCs, where Cs, Pb, and X atoms are depicted by green, orange, and gray spheres, respectively. Unlike in the bulk, in a NC the halide/lead ratio deviates from three, with the upper bound (green circles) and lower bound (orange circles) given by CsX and PbX_2 termination, respectively. The inset shows commonly found experimental sizes, for which the halide/lead ratio should vary only between about 2.8 and 3.2, indicated by the yellow shaded area. (b) To aid the discussion of aging, the NC is arbitrarily divided into core, inner, and outer shell. For a realistic NC requiring colloidal stability, the outermost layer is commonly replaced either by ligand pairs $\{\text{AX}'\}$, where A = cationic ligand (e.g., oleylammonium) and X' = anionic ligand (e.g., bromide, oleate), respectively, or more recently also with zwitterionic ligands $\{\text{AX}'\}$, e.g., sulfobetaines. In either case, the anion/lead ratio (now $[\text{X} + \text{X}']/\text{Pb}$) still falls within the yellow shaded area depicted in (a), and green circles correspond to full capping by the $\{\text{AX}'\}$ ligand shell. Reproduced from the work of Bodnarchuck et al.[176]

It is finally important to remark the amount of surface reactions possible for these CsPbBr₃ nanocrystals (Figure 1.13[187]):[171] first, the nature of the bonds with the ligands makes an adsorption/desorption equilibrium and continuous.[188–190] Second, simple ligand exchanges are possible, where a ligand is replaced by another of the same nature, like a Lewis bases and another Lewis bases, etc;[190, 191] also, Lewis acids can be displaced from the surface by Lewis bases and vice versa.[192, 193] Then, bound Lewis bases can be protonated and form salts of which the anion and the cation can both interact with the nanocrystal to balance the charge.[194] Moreover, mixed binding motifs can get formed depending on the surrounding chemical environment, for example the exchange of a halide for a carboxylate is facilitated by the presence of amine on the surface.[195]

Finally, the bound ligand can be converted in another chemical species that is no longer able to bind the nanocrystal surface, and thus leave it: examples include amidification, esterification, alkylation, etc.[196, 197] Ultimately, depending on the chemical environment, the whole CsPbBr₃ nanocrystals structure can be damaged, partially or fully converting to, for instance, CsX, CsPb₂X₅, PbX₂, or Cs₄PbX₆ phases,[198–206] or even fully disintegrate upon action of various polar agents or complexing agents.[176]

The described nanocrystals chemical dynamism has been extensively exploited during recent years[174] to finely tune the nanoparticles optical properties,[207–209] morphology,[105, 162, 210, 211] size[212, 213] and surface stability.

Nevertheless, this reactivity can be a drawback: the weakly-bond ligands and their adsorption/desorption equilibria make perovskite nanocrystals known to be chemically unstable.[176] In particular, they can fully disintegrate upon action of various polar

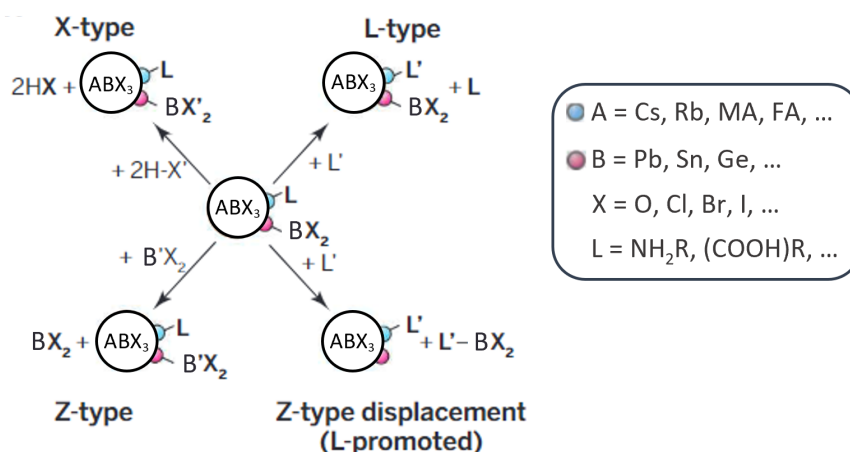


FIGURE 1.13: Examples of several ligand exchange reactions are shown. Adapted from the work of Owen et al.[187]

agents, namely water, or complexing agents. Strategies for mitigating the instability issues include addition of new ligands or inorganic salts to the synthesis,[98, 204, 214–217] post-synthetic treatments,[218–226] and their embedding into a solid matrix.[97, 184, 227–236]

In conclusion, the versatility of lead halide perovskite nanocrystals surface chemistry can be a great tool allowing to play both with the NCs dispersions size, colloidal and chemical stability, optical features and morphology, depending on the ligands' binding motifs and chemical structure, in terms of chain length and ramification. Therefore, this gives a vast variety of possibility for both the NCs synthesis optimal protocol choice and the development of post-synthetic treatments.

1.3 Ionizing radiations and scintillating phenomena

Ionizing radiation is a term including any type of radiation having enough energy to remove tightly bound core electrons from atoms. These radiations are composed of highly energetic particles or electromagnetic waves, and they can penetrate and interact with matter on an atomic level.

There are several sources of ionizing radiations, starting with natural sources such as cosmic rays coming from space and radioactive elements naturally present on Earth. Natural radiation comes from over 60 radioactive materials found in soil, water, and air: for example, Radon gas, which originates from rocks and soil, is a primary natural radiation source that is inhaled and ingested by individuals. Moreover, people receive natural radiation exposure from cosmic rays, particularly at high altitudes.

Additionally, there are human-made sources, including nuclear power plants, X-ray tubes, synchrotron accelerators, high-energy physics experiments involving high particle collisions, as well as industrial processes that produce radioactive materials. The majority of artificial radiation exposure comes from medical uses: diagnostic radiology examinations, nuclear medicine procedures, and radiotherapy treatments are the most common medical applications.

There are several types of ionizing radiations, each of them resulting from different emission phenomena and showing different features and interaction abilities: energetically unstable elements which disintegrate and emit ionizing radiation are called radionuclides.

Each radionuclide is identified by the type and energy of radiation it emits, as well as its half-life. The latter is the time required for the activity of a radionuclide to decrease by decay to half of its initial value, and this can range from fractions of a second to millions

of years, depending on the material and on the type of process. One disintegration per second is also used as a unity of measurement of the activity of a radionuclide, expressed in becquerels (Bq), which stands for the activity of a quantity of radioactive material in which one nucleus decays per second.

These ionizing radiations can have different natures, as they can manifest in the form of particles (alpha, beta) or electromagnetic waves (gamma or X-rays).

First, alpha particles consist in Helium nuclei, thus composed of two protons and two neutrons, relatively large and heavy: they are positively charged and show low penetrating power, as they can already be stopped by a sheet of paper.

Beta particles are high-speed electrons or positrons emitted during the decay of certain radioactive materials: their size is smaller compared to alpha particles, and they have greater penetrating power than the latter, for instance they can be stopped by a few millimeters of aluminium foil.

Further, gamma rays are electromagnetic waves of high frequency ($3 \cdot 10^{19}$ Hz) and energy (in the order of 100 keV): typically emitted by excited nuclei, they have no charge or mass, making them ultra-highly penetrating and capable of passing through thick layers of material. They require dense materials, such as lead or concrete, to effectively attenuate them.

Descending to less energetic waves, X-rays are also electromagnetic radiations, typically emitted by excited atoms, showing strong penetrability and a vast range of energies that classify them as either "soft", with energies below 10 keV, or "hard", with energies ranging from 10 to 200 keV.[237] With the discovery of X-rays by Wilhelm Rontgen in 1896,[238] and the invention of the photomultiplier tube, the research on X rays applications has made great progress: they are now widely used in various important fields such as medical imaging, nuclear medicine, nuclear prevention, high energy physics, homeland security and industrial non-destructive testing[27, 125, 239].

The working principle of X-ray imaging is to map the attenuation of X-ray radiation after it passes through different kinds of target. In the case of living matter, thus mainly for healthcare applications, X-rays can be used to obtain high-resolution radiographies of internal organs; on the other hand, objects of various composition can be tested for nuclear and homeland security and for industrial applications, with a daily-life example being the scanning of packages and suitcases operated by the transportation facilities.

From the healthcare point of view, many diagnostic imaging techniques, as well as therapies against cancer rely on these radiations, but on the other hand, exposure to these kinds of radiations can have severe biological effects, as the ionization process

can disrupt atoms and molecules in living cells. The consequent side-effects can range from mild, such as skin reddening, hair loss, burns, to severe, such as mutations or the development of cancerous cells.[240, 241] Also, lower radiation doses delivered over long periods (low dose rate) pose substantially less risk, because the body has a higher chance of repairing the damage; however, there is still a risk of long-term effects like cancer or cataracts that may appear years or decades later, and children and adolescents are more susceptible to radiation than adults.[242, 243] Therefore, for healthcare applications it is crucial to exploit the possible benefits of these radiations but at the same time to diminish the exposition time and intensity for the patient, meaning that the detection needs to be as efficient as possible. These needs match well with the proper safety measures and radiation protection protocols that must be set up in environments where ionizing radiation is present.

As X-rays exhibit the benefits of deep tissue penetration and a minimal background fluorescence in biological samples, the use of X-ray luminescence as an optical tool has been growing in its potential for addressing challenges in imaging, biosensing, and therapeutics. Recently, the introduction of nanocrystal scintillators has expanded the range of applications for X-ray luminescence, enabling high-resolution X-ray imaging, fluorescence-free detection of biomarkers, and noninvasive phototherapy in deep tissues. Additionally, X-ray luminescence shows promising results in overcoming the limitations of treating deep-seated lesions and achieving a combined approach of radiotherapy and phototherapy.[244]

On the nuclear security side, the fields that need optimal performances in ionizing radiation detection are numerous and varied in scope: the direct search, detection and identification of nuclear materials, the contamination zone mapping, the materials control and accounting, the weapons control and treaty verification, the countering of the threat of nuclear materials smuggling and so on. These applications have different requirements, depending of the detection type, and also a wide range of production demands.[125]

There are two main categories of modern X-ray detection techniques: direct conversion to electrical signals, and indirect conversion through scintillating materials. In the first case, the X ray is converted to an electrical signal by a semiconductor, whereas for indirect conversion the interaction between the X ray with a scintillating material produces a high amount of low energy, visible photons, that can be easily detected by low-cost sensing arrays like photomultiplier tube (PMT), avalanche photodiode (APD), amorphous-Si photodiode matrix, and charge-coupled devices.[14, 245]

As a matter of fact, there is currently hardly any direct converting material being possibly competitive for commercial use in X-ray medical imaging, with selenium (Se) detectors being the exception for mammography.[246] Even the most competitive direct

converters with high resolution, CdTe and CdZnTe (CZT), still suffer from low response rate and temporal effects such as long afterglow caused by electron trapping.[18, 246–248]

Moreover, large-size semiconducting wafers with low noise current and high mobility-lifetime-product are difficult to manufacture, making it challenging to achieve the desired price-to-performance ratio for commercial applications.[247] Therefore, emerging indirect conversion scintillating materials have attracted more research interests for ionizing radiations detection.[249]

Accordingly, as previously introduced, in order to detect and analyze ionizing radiations without their high energy damaging the instrument, the detection methods that have been conceived often involve scintillators, which act as indirect detectors: consistently with Figure 1.14, these materials convert the ionizing radiation into a large number of visible photons, which are in turn collected by a classic photomultiplier tube and then converted into an electrical signal, which is then amplified and recorded. The data collected via this type of setup provide information about the energy and intensity of the original ionizing radiation.

This detection principle would be impossible to understand without giving insights about the scintillation phenomenon, thus how one ionizing radiation in the order of MeV or GeV is down-converted to a large amount of low energy, visible photons of a few eV.

In most inorganic scintillators, the production of light is due to the excitation of electrons in the material's components (in general, luminescent centers acting as activators), which are promoted from their ground state to a highly excited energy level and then return to their ground state by releasing energy in the form of photons. Based on current consensus, three main stages are involved in the whole scintillation process, from the initial interaction between the high energy radiation and the scintillating matter to the final visible-light emission, and the schematic scintillation mechanism is presented in Figure 1.15.[250, 251]

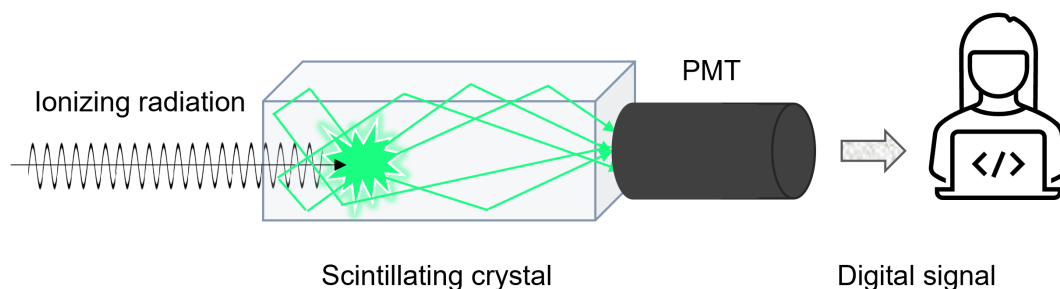


FIGURE 1.14: Schematic illustration of the functioning principle of a scintillation detector.

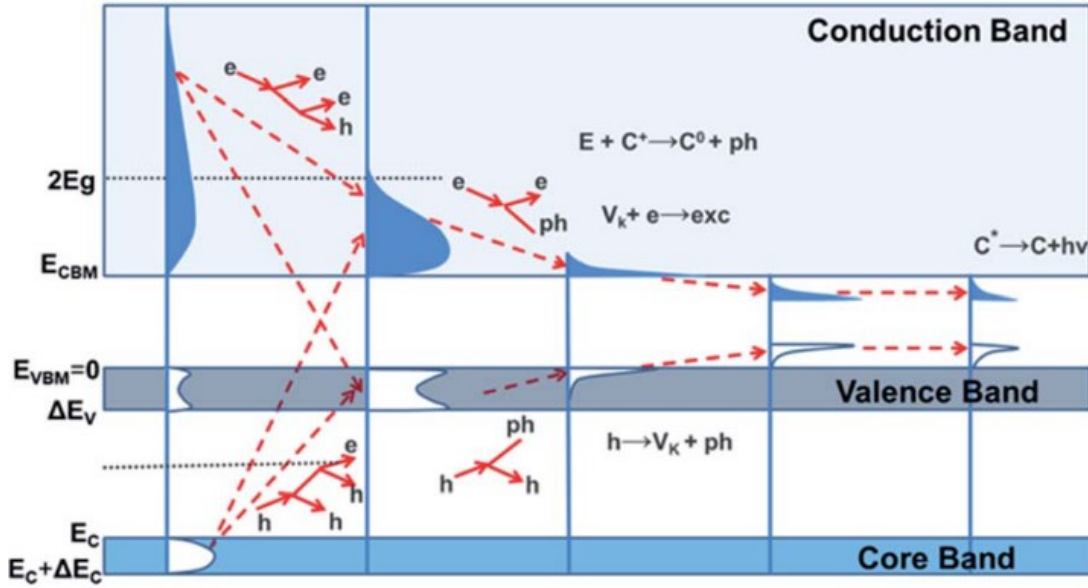


FIGURE 1.15: Schematic scintillation mechanism in inorganic bulk scintillation crystals, following the relaxation of the "hot" electron in its highly excited state. E_C refers to the top energy of core band, and ΔE_C represents the corresponding bandwidth; E_{VBM} refers to the top energy of the valence band VB ($E_{VBM} = 0$), and ΔE_V represents its bandwidth; E_{CBM} refers to the bottom of the conduction band CB, and E_g represents the bandgap; V_k stands for self-trapped holes, and C^+ represents ionic centers. Reproduced from the work of Vasil'ev et al.[250, 251]

In the first stage, the ionizing photon interacts with the scintillating material by producing a photoelectric effect: the radiation possesses an energy high enough to interact with the core electrons, leading to the latter's excitation to highly excited energy states. This excitation leads thus to the formation of what are called a deep hole (h^+), representing the former energy state of the now excited electron, and the latter, which is in turn called hot electron (e^-), respectively situated in the inner core band and in the conduction band CB. At this point, the hot electron rapidly undergoes a process called multiplication, where it interacts with the surrounding matter by inelastic e–e scattering, thus transferring its energy along its pathway and bringing other electrons in excited states; a parallel multiplicative process involves the deep hole as well, through Auger effect. As a consequence, h^+ between core and valence band and (e^-) in CB are rapidly formed by secondary electron excitation.

Once the multiplication step is over, i.e. when their energy is lower than the forbidden band, the relaxation continues through the creation of phonons from the thermalization of the electrons' excitation: this results in the generation of low kinetic energy e^- and h^+ energetically located in the conduction band's minimum and in the valence band's maximum, respectively. These relaxed electron-hole pairs, coupled as excitons, then

migrate towards native defects, external dopants or impurities present in the material's lattice, which can also eventually lead to trapped states.

The last stage involves the electron-hole recombinations of these excitons, that can follow radiative or non-radiative pathways: in the first case, scintillation occurs as the visible photons emission from the luminescent center.

The interaction between excitons may cause a reduction in the emitted photons quantity, and this issue is considered as a decisive factor on material density-effect, non-exponential decay, as well as nonproportional energy response.[251]

1.3.1 Traditional bulk scintillators

Once given the insights on the scintillation process and on how scintillation detectors work, it should be easier to understand what are the most important parameters that are used to evaluate the scintillators performances and their optimal applications.

First, the overall density and effective atomic number Z_{eff} are part of the key parameters for a good scintillation-based X and gamma ray detector, since they directly impact the stopping power of the material towards the ionizing radiation. as a matter of fact, the stopping power determines how efficiently a material will absorb the ionizing radiation: a high stopping power means that a large fraction of the incident radiation can be deposited in the material through the photoelectric interaction. Therefore, scintillators with high density and high Z_{eff} are preferable.

A second important point is the light yield, which corresponds to the ratio between the number of photons emitted per unit of deposited energy in the material. This parameter is expressed in photons/MeV and is given by the relation 1.7:[21]

$$LY = \frac{10^6 SQ}{\beta E_g} \quad (1.7)$$

In this formula, E_g is the bandgap, S represents the efficiency of electron-hole transport to the emissive center, Q is the luminescence quantum efficiency of the emissive center and β is a constant representing the losses, its value being generally considered as 2-3. A high light yield increases the signal to noise ratio, which is beneficial to the data collection and the image resolution, depending on the targeted application.

Moving forward, a parameter which is crucial for applications where the time resolution is a key factor is the decay time, which defines the time of emission of a photon after

the interaction with the radiation. As an example, a short decay time is very important for applications relying on time-of-flight (TOF) techniques, as well as the counting techniques using a coincidence time window.

Then, the radioluminescence spectrum's position and shape have to match well with the optimal efficiency of the used photodetector, in order to maximize the detection efficiency.

Moreover, a scintillator's energy resolution is its ability to discriminate different radiation energies, and thus it is very important for qualitative spectral measurements in some applications such as gamma ray spectroscopy.

Finally, it would be ideal to work with inexpensive materials of easy fabrication, stable towards chemical and radiation damage, not showing re-absorption and that is possible to produce on a large scale.

A perfect scintillator which excels in each of these properties has yet to be found, therefore the selection of the scintillator has to be made depending on the specific requirements of each application purpose.

Several scintillators are commonly used and commercially available in various applications, traditionally in the form of bulk single crystals. Nevertheless, the limitations imposed by the production process involved have led to the development and optimization of new materials, such as transparent ceramics, especially for applications that require very large volume or areas, and composite materials in attempt to couple the specific functions of the different phases.[125]

The first inorganic scintillating crystal NaI:Tl⁺ (sodium iodide doped with thallium) was discovered in in the late 1940s[252] and still remains a popular choice for many applications requiring a cheap, large and efficient scintillator.

Over time, a range of scintillators have been documented for various applications, like CsI:Tl⁺ (thallium-doped cesium iodide),[253] which is widely used as it is not hygroscopic and exhibits high light output, but has the drawback of not well matching spectrally with PMTs and having an exceptionally long decay time.

Besides, Bi₄Ge₃O₁₂ (bismuth germanate), or BGO,[254] shows great stopping power, making it an extremely effective ionizing radiations absorber, widely utilized in high-energy physics applications and positron emission tomography (PET), even though on the other hand its light output is much lower than the ones of NaI:Tl and CsI:Tl.

Moreover, it is possible to tune some optoelectronic features by doping the crystals structures with dopants, typically heavy transition metals. as a matter of fact, their

1. Fundamental background

Scintillator	ρ (g/cm ³)	Z_{eff}	Light Yield (photons/MeV)	Energy Resolution (%, at 662 keV)	λ (nm)	τ (ns)
NaI : Ti ⁺	3.7	50.8	43,000	6.7	415	230
CsI : Ti ⁺	4.5	54.0	66,000	6.6	560	1,000
CsI : Na ⁺	4.5	54.0	43,000	7.4	425	-
CsF	4.6	53.2	1900	19	390	2-4
BaF ₂	4.9	52.7	1430	10	175	0.8
CaWO ₄	6.1	75.6	15,800	6.3	425	6,800
PbWO ₄	8.3	75.6	140	-	475	10
CdWO ₄	7.9	64.2	19,700	6.5	495	104
Bi ₄ Ge ₃ O ₁₂	7.1	75.2	8,200	27	505	300
CdS : Te ²⁺	4.8	48.0	17,000	14	640	270-3000
ZnS : Ag ⁺	4.1	27.4	73,000	-	450	105
LaBr ₃ : Ce ³⁺	5.1	46.9	67,000	2.8	358	15
LaBr ₃ : Pr ³⁺	5.1	46.9	75,000	3.2	450-900	11,000
YAl ₂ O ₃ : Ce ³⁺	5.4	25.6	17,000	5.7	370	26
Lu ₂ SiO ₅ : Ce ³⁺	7.4	50.2	30,000	10	420	40
Lu ₂ SiO ₅ : Pr ³⁺	7.4	50.2	2,200	-	247	26
Lu _{2.25} Y _{0.75} Al ₅ O ₁₂ : Pr ³⁺	6.2	44.1	33,000	4.4	-	-
Anthracene	1.25	5.24	16,000	-	447	30
Stilbene	1.16	5.14	8,000	-	410	4.5
Naphthalene	0.96	5.18	2,000	-	348	80
2,5-Diphenyloxazole	1.06	5.52	8,800	-	405	7
p-Terphenyl	-	-	9,200	-	440	5

TABLE 1.2: Overview of some traditional inorganic and organic scintillators for X-ray and γ -ray detections. The abbreviations in the heading denote the density (ρ), the effective atomic number (Z_{eff}), the emission wavelength (λ) and the main scintillation decay time (τ). Reproduced from the work of Maddalena et al.[21]

introduction can enhance the luminescence efficiency, by choosing a dopant specie with a lower energy level than the bandgap of the host material: this results in the introduction of a new energy transition that enhances the probability of electron-hole recombination, and thus facilitates the radiative recombination process. Moreover, dopants can change the material's emission wavelength, which makes it possible to tailor the material for a specific application, and also improve the stability of the light-emitting structure, by trapping any highly reactive species that may cause a degradation of the material. Popular examples are Ce³⁺ and Pr³⁺ dopings, which can make the decay time faster (typically tens of ns) and increase the quantum efficiency. It is the case for the commercial lutetium orthosilicate LSO doped with cerium, Lu₂SiO₅:Ce, as well as lutetium–yttrium oxyorthosilicate LYSO Lu_{2(1-x)}Y_{2x}SiO₅:Ce.[255–260] These materials exhibit a high stopping power for gamma rays and thus are the scintillator materials most widely used today in PET detectors, due to their fast decay time (about 40ns against the 300ns of BGO) and excellent energy resolution, both convenient physical

properties for the detection of 511 keV annihilation photons.[245, 259, 261–263]

A summarizing table listing radioluminescence features of these traditionally used bulk single crystals is shown in Table 1.2.[21, 264]

All these widely used oxide bulk single crystals are typically produced via the well known Czochralski[265, 266] and Bridgman-Stockbarger[267, 268] methods,[269] that are the most chosen ones for large scale production, as the techniques can be fully automated, the growth of the crystal is controlled in real time, and the production yield is high. On the other hand, the manufacturing requirements as the high temperature above 1700°C, as well as the difficulties in finely tuning the materials' structure in terms of defects and dopants, result in these bulk crystals sharing typical drawbacks, like long decay times, afterglow phenomena caused by electron trapping in structural defects, and high hygroscopicity.[18]

Therefore, in general, commercial scintillators for the majority of large-scale applications rely on bulk solid-state single crystals; nevertheless, as mentioned while listing the scintillators ideal features, there is no perfect universal material, and single crystals share the drawbacks of moderate radioluminescence light yields, long decay times and high production costs.

1.3.2 Nanostructured scintillators: perovskite nanocrystals

In recent years, the increasing demand for radiation detection materials for many applications has led to extensive research on scintillators. In this context, the emerging knowledge about semiconducting nanocrystals made them receive increasing attention, due to their outstanding optical properties:[125] unlike the traditional bulk scintillators, nanocrystals show a narrow and bright emission, with the wavelength maximum that can be tuned all along the visible range. This is a very interesting solution to make the light output match the maximum light detection efficiency of the photomultiplier tube, and thus improve the overall detection efficiency. Furthermore, the solution-processability and practical scalability of nanostructured systems can also reduce the manufacturing cost and difficulty, compared to the traditional bulk single crystals, making nanostructures a promising material for radiation detection.

In the past two decades, the response of a large number of nanocrystals under high-energy electrons, alpha particles, X-rays and gamma rays has been widely studied. One of the first example is the characterization of the scintillating properties of CdSe/ZnS core/shell nanocrystals when interacting with alpha particles and gamma-rays radiations: these nanocrystals showed a scintillation efficiency two times better than that of

1. Fundamental background

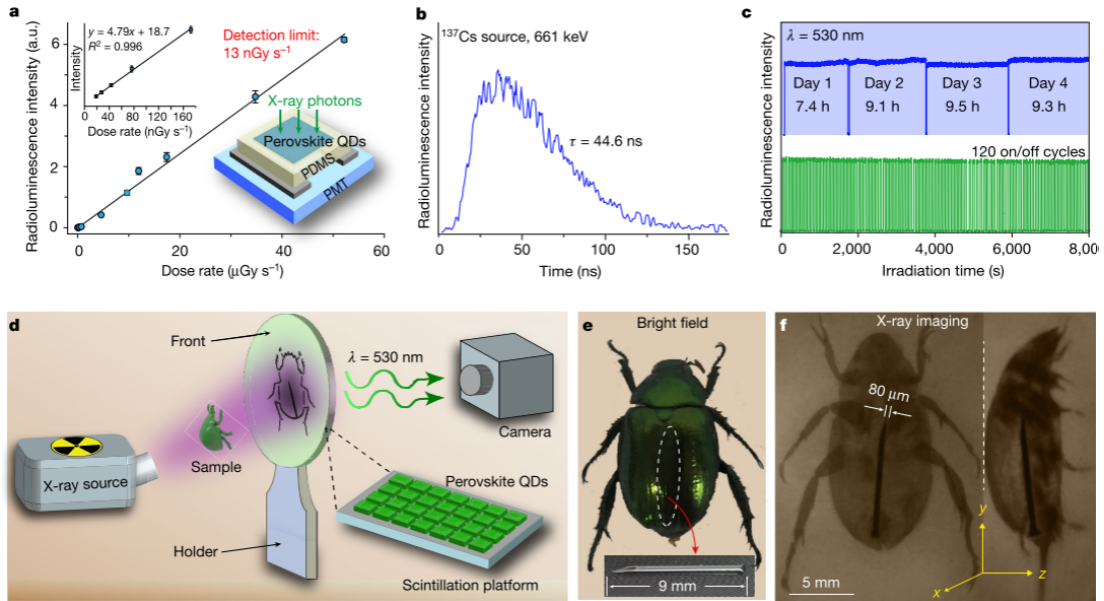


FIGURE 1.16: Radioluminescence measurements for a CsPbBr_3 -based scintillator as a function of dose rate. The left inset shows radioluminescence profiles measured at low dose rates (a); measured radioluminescence decay of the CsPbBr_3 -based scintillator under excitation with a ^{137}Cs source (photon energy, 661 keV) (b); photostability of the CsPbBr_3 -based scintillator against continuous X-ray irradiation ($\lambda_{\text{exc}} = 530$ nm, 50 kV; top) and repeated cycles of X-ray excitation at 30 kV with a time interval of 30 s ($\lambda_{\text{exc}} = 530$ nm; bottom) (c); schematic of the experimental setup used for real-time X-ray diagnostic imaging of biological samples, where a beetle is placed between the X-ray source and a scintillation platform covered with perovskite QDs (d); bright-field (e) and the X-ray (f) images of the sample, recorded with a digital camera. Reproduced from the work of Chen et al.;[12]

the conventional NaI:Tl bulk scintillator.[270, 271] This evidence paved the way for the following researches on nanostructured scintillators.

In recent years, following the wave of the novel knowledge about the optoelectronic features of lead halide perovskite nanocrystals, the latter has emerged also as a promising scintillation material. In particular, Chen et al. first reported all-inorganic lead halide perovskite nanocrystals as a new class of scintillators,[12] describing the X-ray photodetector reproduced in Figure 1.16 (a) and (d), consisting of a CsPbBr_3 nanocrystals thin film (about $120 \mu\text{m}$ thickness), a polydimethylsiloxane (PDMS) layer and a photomultiplier tube.

These nanostructures scintillating features reflect the optical ones, with bright radioluminescence spectra whose maxima are easily tuneable across the visible spectrum, just by tailoring the anionic component of the chemical structure or the nanocrystals dimensions. Moreover, unlike the traditional CsI:Tl scintillator, which has the issue of afterglow luminescence (scintillation decay time of 1,000 ns), these perovskite nanocrystals stand out for their ultrafast radioluminescence, which is typically in the order of 10 ns,[274, 275] allowing to obtain coincidence time resolutions of 100 ps or below at 511

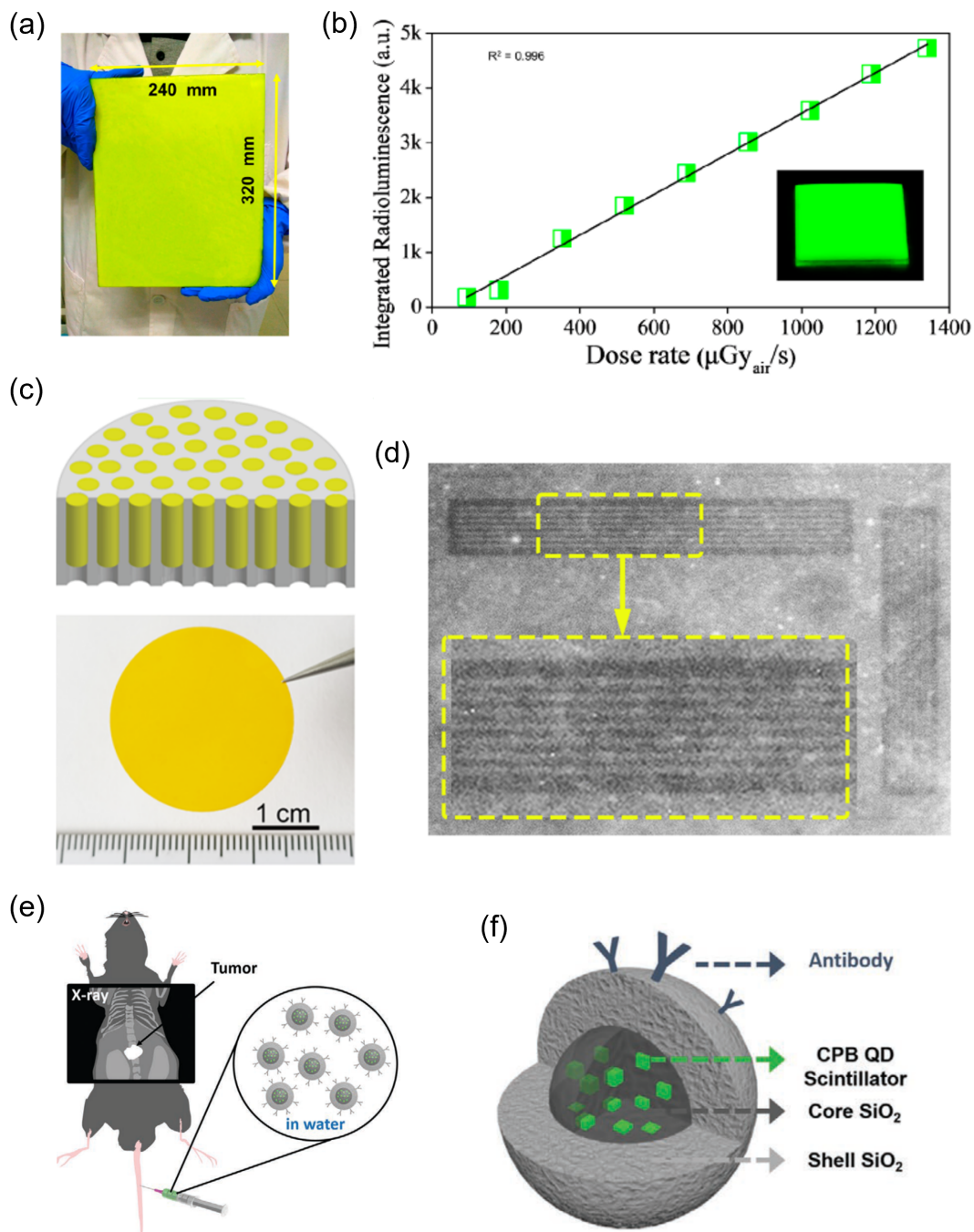


FIGURE 1.17: Large-area film of $\text{CsPbBr}_3@ \text{Cs}_4\text{PbBr}_6$ made by low-cost blade-coating technique (a), and the corresponding linear relationship between the film's integrated PL intensity and the X-ray dose (b). Reproduced from the work of Cao et al.[248] Schematic illustration of the single-crystalline perovskite nanowire arrays of CsPbBr_3 NWs in anodized aluminum oxide membranes (c), and the obtained X-ray image of a JIMA test pattern with a line spacing of $2 \mu\text{m}$ (d).Reproduced from the work of Zhang et al.[272] Schematic illustration of both the in-vivo utilization principle (e) and structure of the and $\text{CsPbBr}_3\text{-SiO}_2@ \text{SiO}_2$ -antibody core/shell nanoparticle (f). Reproduced from the work of Ryu et al.[273]

keV excitation:[276] this is a feature of high interest for the fast-timing applications, as the ones based on time coincidence and real-time imaging. As previously discussed, such fast luminescence decay is not common in traditional bulk crystals, whereas values of this order of magnitude can be accessed by organic scintillators. Nevertheless, the latter major drawback is their low Z_{eff} , limiting their efficiency of interaction with the ionizing radiations: this is not a problem instead for lead halide perovskite nanocrystals instead, which benefit from the high stopping power given by the presence of lead. Finally, their scintillation properties also benefit from the already discussed defect tolerance and high quantum yield.[277, 278] In fact, since the light yield of a scintillator is inversely proportional to the bandgap, perovskite materials, which often have a smaller bandgap than other scintillators, are expected to potentially reach extremely high-light yields, up to 250,000 photons/MeV.[21] In particular, CsPbBr₃ nanocrystals have been demonstrate to have a light yield of 33,000 photons/MeV[277] (54% of light yield of CsI:Tl[21]), which is much higher than that of bulk CsPbBr₃ single crystals, which show less than 1000 photons/MeV.[279] It is also important to underline that this possibly very bright luminescence can produce a high signal-to-noise ratio, and it is consequently promising for detection applications: for diagnostic exams, inferior detection limits mean being able to decrease the amount of radiation received by the patients, thus limiting the damage to their tissues. Finally, these systems can be processed from solution, not requiring high temperature or vacuum deposition technologies, thus making them easier and cheaper to process than bulk single crystals, and suitable for the mass scale production.

Recent literature presents countless examples of perovskite nanocrystals studied for scintillation, with advances involving different approaches aiming to face different issues. Typically, the need of surface stabilization and of obtaining a solid sample has led most research groups to embed the nanocrystals in polymeric matrices,[25], glass,[280] or bulk crystals.[248, 281] This need is a typical point needing optimization, since diluting the nanocrystals in a matrix has the drawback of decreasing the overall density of the system, thus lowering the detection efficiency and consequently the final light output. An example of remarkable matrix with high density density was presented by Cao et al.,[248] who developed films of CsPbBr₃ hosted inside Cs₄PbBr₆ matrix. With this approach, the group obtained stable and sensitive scintillating films, like the remarkable large-area one (360 mm × 240 mm) in Figure 1.17 (a), showing a sensitive response to X-ray irradiation, with the superior linearity between the integrated PL intensity of the CsPbBr₃@Cs₄PbBr₆ film and the X-ray dose, as depicted in Figure 1.17 (b).

Another interesting strategy developed in order to exploit the performances of lead halide perovskite nanocrystals as scintillators involves the engineering of their support, as it is the case for the work of Zhang et al. reproduced in Figure 1.17 (c).[272] In order to obtain a scintillator suitable for high-resolution imaging, which is typically limited

by the scintillator thickness, without stumbling upon debilitating self-absorption effects, their group used an anodized aluminum oxide membrane template, inducing the growth of arrays of 15- μm long single-crystalline CsPbBr_3 nanowires. This approach led to composites displaying high radiation resistance, giving X-ray images able to distinguish line pairs with a spacing of 2 μm Figure 1.17 (d): the combination of high spatial resolution, radiation stability, and easy fabrication makes these functionalized scintillators a promising candidate for high-resolution X-ray imaging applications.

Additionally, a remarkable result involving chemical stability in polar media is presented in the work of Ryu et al.,[273] who developed CsPbBr_3 - SiO_2 @ SiO_2 -antibody core/shell nanoparticles: these systems were found to be so chemically stable towards polar environment and biocompatible that they could be used for in-vivo imaging of cancer in a mouse, without leading to toxicity damages (Figure 1.17 (e) and (f)).

Despite the rapid development of the research on this topic in recent years, still the energy deposition and relaxation mechanisms in semiconductor nanocrystals are not fully rationalized. Similarly to bulk scintillators, the incidence of a high-energy radiation produces a highly excited hot electron and then a cascade of energetic electrons; on the other hand, Bulin et al. showed that, during this energy relaxation cascade, the spatial energy distribution between the nano-scintillators and the surrounding media leads to a significant loss in the light emission efficiency.[282] Also, the same study highlighted that a significant fraction of energy is deposited within the nanoparticles even if the initial interaction takes place in the surrounding media. Finally, the absence of transport process in direct gap nanocrystals semiconductor makes the hot electrons and holes directly thermalize towards the conduction and valence band edges. Due to quantum confinement, nanocrystals show discrete energy levels, which makes the understanding of the following steps not straightforward.

To date, the comparison between the temporally and spectrally resolved radiative recombination, produced by photoexcitation with 20 keV electrons ionizing radiation, has made it possible to identify and quantify the types of excitation states produced in NCs under high energy excitation.[283] This analysis directly reveals a dominant population of charged and multiexcitonic states, consistent with large contributions from carrier multiplication, multiple types of scattering and ionization processes during relaxation. Also, Auger effect appears to be a key factor restricting the study of excited states under ionizing radiation. The investigation of cathodoluminescence can provide guidance for the exploration of X-rays-induced exciton recombination.[284]

In conclusion, this research field still includes many aspects that are waiting for optimization, including structural optimization of the nanocrystals, their chemical and radiation stability enhancement, and their scalability.

1.3.3 Liquid scintillators

Scintillators are also used in the liquid state, as the so called liquid scintillation cocktails (LSC): traditionally, these are organic solutions that emit light when exposed to ionizing radiation such as alpha, beta, gamma and X rays.

These LSC are a way less active research topic in the scintillation field, as their performances have been optimized for a long time: techniques utilizing liquid scintillation counters are used to determine the activity of alpha-, beta- and gamma-emitters,[285] and they show excellent damage resistance, fast decay time, low cost and exceptional scalability.[286–291] In particular, these liquid scintillators offer the advantages of easy preparation of the sample, which is simply dissolved or dispersed directly in the LSC; moreover, the configuration of the setups typically involves an effective spherical-like 4π detection geometry, and there is also no physical barrier between the radionuclide and the scintillating agent. These factors give to LSC a very high sensitivity, which forms the basis of recognised international standards for detecting ^3H in drinking water,[292] with a minimal detectable activity of the order $1\cdot 10^{-4}$ Bq g $^{-1}$ and a detection efficiency of 60% achievable by most off the shelf counters.[293]

In virtue of these properties, they find large application for daily life analytical tests, as radioactivity level measurements for environmental, medical and security purposes,[294–299] in the study of biochemical reactions mechanisms by radioisotopic labelling,[300, 301] and in metrology;[288, 302, 303] also, they are used in huge international experiments for β -emissions and neutrino detection, such as XENON1T, KamLAND, Daya Bay, and RENO.[291, 304–306] For example, the Nobel-winning discovery of oscillation of atmospheric neutrinos was obtained by the SuperKamiokande group by using a huge water-based liquid scintillator detector, depicted in Figure 1.18.[307]

Nevertheless, their organic composition give them a low overall density: it has already been discussed, though, that the latter is a key parameter for some scintillation applications, since it impacts the stopping power of the material towards the ionizing radiation, and thus the probability of interaction. Therefore, an expansion of the commercial utilization of these kinds of systems is hindered by their relatively low effective atomic number Z_{eff} and consequent moderate interaction efficiency.

A possible improvement of these systems' overall performances is to substitute the organic fluorescent dyes with inorganic semiconductors such as lead halide perovskite colloidal nanocrystals, owing to their high effective atomic number, and again to their bright, tuneable emissions and fast decay time.[31, 33, 309–311]

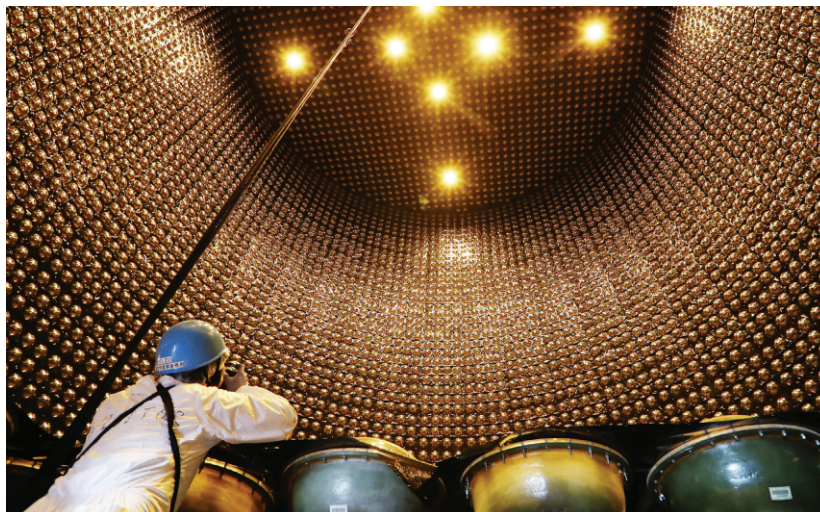


FIGURE 1.18: Picture of the huge SuperKamiokande neutrino detector built by the SuperKamiokande group. Reproduced from the dissemination article from Castelvechi.[308]

In order to give the background needed for the following chapters, a description of the liquid scintillating systems is here given. Traditionally used liquid scintillators are organic solutions, usually involving multiple components: first, the solvent, which was traditionally an aromatic compound such as toluene, xylene and pseudocumene, that nowadays have been substituted with safer, non-volatile options like diisopropylnaphthalenes (DIPN), linear alkyl benzene (LAB) or PXE (phenylxylylethane), as in Figure 1.19 (a). Then, the light-emitting compound of the mixture is an organic dye, typically a rigid conjugated aromatic structure: commonly used ones are 2,5-diphenyloxazole (PPO), 2-phenyl-5-biphenyl-1,3,4-oxadiazole (PBD), 2-(4-tert-butylphenyl)-5(4-biphenyl)-1,3,4-oxadiazole (butyl-PBD) and 2,5-bis-2-(tert-butylbenzoxazolyl)-thiophene (BBOT), as in Figure 1.19 (b).

Furthermore, the system contains a second dye, known as a wavelength shifter, which helps to maximize the overlap between the scintillator's emitted light and the maximum of light detection efficiency of the photodetectors, as well to ensure that the final emitted light does not overlap the other components' absorption spectra (Figure 1.19(c)). Finally some surfactant are needed ad stabilizing agents.[312] The sample whose radioactivity has to be measured is directly dispersed in this medium, and their interaction produces a signal as now discussed.

The cited multiple components are needed since liquid scintillators work on the basis of energy transfers, illustrated in Figure 1.20. When a radioactive samples is added, the emitted ionizing radiations interact with the surrounding molecules: the most abundant specie in the system is by definition the solvent, which has then the highest probability

1. Fundamental background

Solvent	Structure	Relative Pulse Height	Flash-Point (°C)
1,2,4-Trimethylbenzene (Pseudocumene)		112	50
1,4-Dimethylbenzene (P-Xylene)		110	30
Methylbenzene (Toluene)		100	5
Benzene		85	-11
1,4-Dioxane		65	12
Dodecylbenzene		91	150
1-Phenyl-1-(3,4-dimethylbenzene)ethane (FXE)		114	150
2,6-Di-isopropylnaphthalene (DIPN)		114	150

Name	Structure	λ (nm)	t (nsec)	Φ
PPO		375	1.4	0.83
PBD		375	1.0	0.69
Butyl-PBD		385	1.0	0.69
BBOT		446	1.6	0.61

Name	Structure	λ (nm)
POPOP		415
M ₃ -POPOP		427
Bis-MSB		425

FIGURE 1.19: Typical solvents in commercial liquid scintillation cocktails (a); properties of primary scintillators, in terms of their λ = fluorescence maximum, t = decay time, Φ = quantum yield (b); typical secondary scintillators with their fluorescence maximum λ (c). Reproduced from Perkin Elmer resources.[312]

of interaction with the incoming radiation. Therefore, the solvent molecules get excited to a high energy state.

At this point, the excited or ionized solvent molecules transfer this energy to nearby molecules, typically through non-radiative processes, leading to a chain reaction. In fact, this energy is transmitted to the dissolved molecules, typically the fluorescent dye, which is called the primary scintillator: in turn, the dye undergoes de-excitation processes, typically by relaxing back to its ground-level state through a radiative emission.

The system is usually engineered in such a way that a second fluorescent molecule, called the wavelength shifter, is present in the LSC with two roles, the first being to absorb the dye's photoluminescence and then re-emit light at a wavelength which better matches the maximum detection efficiency of the photodetectors; moreover, this wavelength shift

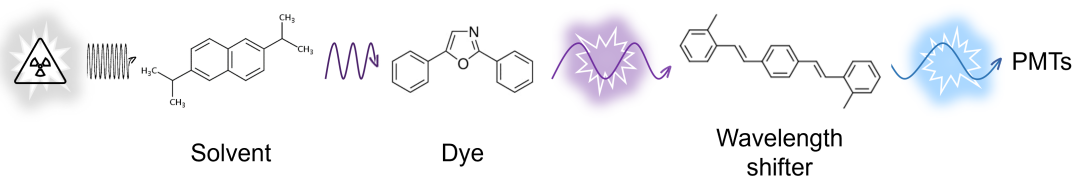


FIGURE 1.20: Schematic representation of the energy transfer processes involved in traditional organic liquid scintillation. As an example, here are shown DIPN (diisopropylnaphthalene) as the solvent, PPO (2,5-diphenyloxazole) as the dye and bis-MSB [p-bis-(o-methylstyryl)-benzene] as the wavelength shifter.

ensures that the final light emission does not get absorbed by any of the LSC components. This final light emission is finally detected by the PMT, which converts it into an electrical signal that can be analyzed and used to identify the type and energy of the original ionizing radiation.

In summary, liquid scintillators use chain energy transfers, from the radioactive sample dissolved in the solution to fluorescent dyes, in order to produce a visible radiation that can be detected and analyzed to identify the radiation type and energy.

The amount of steps involved in these processes and their overall rate, together with their already mentioned low density, leave room for possible improvement of these systems.

Conclusions

This chapter has given the background needed to understand the present work's context. First, traditional colloidal semiconducting nanomaterials have been presented, together with their outstanding opto-electronic features that put them at the center of last forty years of research in physics, chemistry and materials science, finally leading to quantum dots being the subject of the 2023 Nobel prize for chemistry. In particular, the dependency of their opto-electronic features on the NCs' dimension was explained in terms of the quantum-size effects on the specie's electronic structure.









Perovskite nanocrystals were then introduced as direct bandgap semiconductors which arose major interest in the community, as they were the first in the colloidal NCs family to exhibit bright photoluminescence over the entire visible spectral range without electronic surface passivation; also, they show very bright and fast photoluminescence, high tolerance of the electronic properties to the material's defects and surfaces, as well as an extremely versatile surface chemistry, which was described in detail. All of these features show these nanostructures' great potential for a broad range of applications, from photovoltaics to optoelectronics and photocatalysis.

A background on ionizing radiations and their detection, and thus on scintillators, was then illustrated. In particular, the parameters that define an ideal scintillator were listed: namely, typical selection criteria can be the material density, scintillation yield, time response, its radioluminescence spectrum's position and shape, its energy resolution and cost of production. An overview of the traditional bulk scintillators and the comparison with the nanostructured ones highlighted that, despite the bulk crystals being at the base of the majority of large-scale applications, nanocrystals can provide better

results in terms of scintillation light yield and fast time response: namely, CsPbBr₃ - based nanoscintillators have been shown as very promising candidates for fast-timing applications, due to their decay times in the order of 10 ns.

The present work will focus on the experimental exploration of lead halide perovskite nanocrystals performances as scintillating materials, either as liquid colloidal dispersions or as nanoparticles dispersed in solid matrices. In particular, CsPbBr₃ colloidal nanocrystals were the system of choice, owing to their superior radiation stability and radioluminescence intensity and time response compared to analogous perovskite NCs systems of different compositions. The main possible issue associated with these CsPbBr₃ nanostructures was highlighted, thus their short Stokes shift, which can lead to a high probability of self-absorption in the system: this work will focus on strategies developed to face this issue, both in solid and liquid systems, in order to further exploit the greatly promising radioluminescence features of these nanostructures.

Key points

-  **Colloidal semiconducting nanomaterials** are powerful tools for many applications in optoelectronics, owing to their excellent features in terms of tuneable photoluminescence, high quantum yield, versatility and cost.
-  **Perovskite nanocrystals** outstand in the colloidal semiconducting nanomaterials family, showing very bright and tuneable light emission, exceptional defects tolerance and being easy to synthesize and work with.
-  The **stabilizing ligands** have a crucial role in the nanocrystals surface chemistry and in the colloidal dispersions' stability towards precipitation, chemical damaging and surface quality.
-  **Scintillation** is a light emitting process from which one incident ionizing radiation (keV, MeV) is down-converted in the emission of multiple visible photons (eV).
-  Scintillator-based **detectors** are widely used in many fields: many types exist, either as **bulk materials**, or in the form of **nanoparticles dispersed in a matrix**, or as **liquid organic solutions**. An ideal, universal scintillator does not exist, thus the material has to be selected depending on the specific needs.
-  Colloidal **lead halide perovskite nanocrystals** are very promising materials for scintillation, since the bright and fast light emission allowed by their electronic structure is combined with the presence of lead, a **heavy element** which thus gives the material a high stopping power.
-  The main **challenges** involving lead halide perovskite nanocrystals are their composites' overall **low density** and their intrinsic **short Stokes shift**.
-  This work will focus on the study of **lead halide perovskite nanocrystals as scintillating materials**, either as liquid colloidal dispersions or embedded in solid matrices; a great focus will be directed on overcoming the above-mentioned challenges.

Chapter 2

Lead halide perovskite nanocrystals synthesis and characterization

The literature about lead halide perovskite nanocrystals has exploded in the last 20 years, and thus the reported variations of the possible nanocrystals synthesis approaches are countless: this work will focus on a few synthetic protocols and their modifications, depending on the outcome needed for the different applications.

This chapter illustrates the characterization techniques and synthetic protocols used in this work, with examples of the relative outcomes in terms of optical and structural characterization.[\[11, 313\]](#)

2.1 Optical and structural characterization

This section describes the optical and structural characterization techniques adopted throughout this work, namely optical absorption and emission spectroscopy, photoluminescence excitation spectroscopy and photoluminescence quantum yield, X-ray radioluminescence, optical and X-ray luminescence decay rate, X-ray diffraction and transmission electron microscopy; the section finally ends with a description of the instrumental setups employed.

2.1.1 X ray diffraction

X-ray diffraction (XRD) is a powerful technique used to investigate the structure and composition of crystalline materials at the atomic level, finding applications across various fields, such as materials science, chemistry, geology, pharmaceuticals, and more.

When a monochromatic beam of X-rays interacts with the electrons within a crystalline material, the X-rays get scattered in different directions, a phenomenon known as diffraction: this is due to the particular wavelengths of these X-rays, which have the same order of magnitude (1–100 angstroms) as the spacing between planes in the crystal. The scattered X-rays interfere constructively or destructively, forming a pattern of intensity known as a diffraction pattern, determined by Bragg's law:

$$n\lambda = 2d \sin \theta \quad (2.1)$$

where d is the spacing between the diffracting planes, θ is the radiation's incident angle, n is any integer, and λ is the wavelength of the beam.

The diffraction pattern can be captured using a detector, which records the intensity of X-rays at different angles. This intensity, as a function of the angle (2θ) is then analyzed to extract information about the structural arrangement within the crystal.

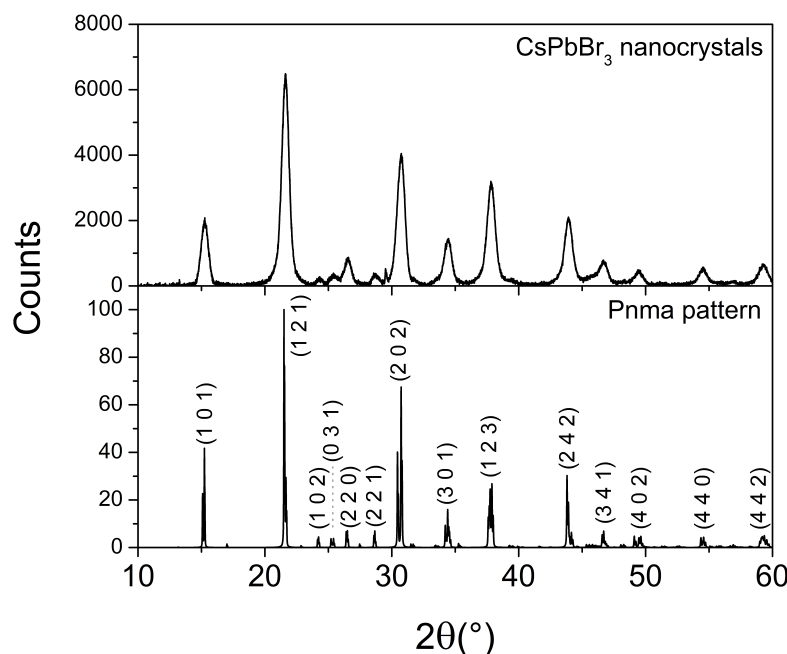


FIGURE 2.1: An example of CsPbBr₃ nanocrystals XRD diffraction pattern, with the matching Pnma orthorhombic CsPbBr₃ reference. Reference XRD patterns were searched on Crystallography Open Database COD.[152–159] and imaged with VESTA software[160].

X-ray diffraction provides several key types of information about the nature of the sample, such as the crystal structure, thus the relative positions of the atoms or molecules within the crystal lattice, the unit cell parameters, which define the size and shape of the crystal lattice; moreover, it can give information on the preferred alignment of crystal grains in a polycrystalline sample and on the preferred orientation of crystalline materials, it can identify the different phases present in a sample, thus distinguishing between different compounds or polymorphs within a sample.

Figure 2.1 shows a typical X ray diffractogram of CsPbBr₃ nanocrystals: their crystal system and their chemical composition can be easily identified by comparing the experimental data with references from literature.

In this work, X-ray diffraction was used to obtain information about the lead halide perovskite nanocrystals crystal structure, phase purity and eventual unwanted formed compounds.[314]

Instrumental setup

X-ray diffractograms were acquired on a MalvernPanalytical Aeris diffractometer equipped with a copper K α anode; samples were prepared by drying the colloidal dispersions on a low-background silicon substrate.

2.1.2 Optical absorption

Absorption spectroscopy is a versatile technique used in various fields such as chemistry, biology, physics and environmental science for qualitative and quantitative analyses. It provides valuable information about the composition, concentration, structure, and behavior of molecules present in the sample being analyzed.

This technique is used to analyze the nature of a sample by measuring the amount of light which gets transmitted through the sample, as a function of its wavelength: since different chemical functions or semiconductors' band gaps absorb specific wavelengths, depending on their electronic structure, it is possible to obtain both qualitative and quantitative information on the sample.

In the used setup, a light source emits a broad spectrum of light, usually in the form of visible or ultraviolet light: as the light passes through the sample, some specific wavelengths are absorbed by the different components of the sample. The transmitted light is then detected by a photodiode, which measures the intensity of this light. The obtained spectra can be plotted as the value of transmittance T, or absorbance A, as a

function of the wavelength or frequency of the initial incident light. The mathematical expression of transmittance, in Equation 2.2, sees I_t as the transmitted light intensity and I_0 as the incident light intensity, whereas the one for the absorbance, sees T as the transmittance, and I_t and I_0 as just defined.

$$T = \frac{I_t}{I_0} \quad (2.2)$$

$$A = -\log T = -\log \frac{I_t}{I_0} \quad (2.3)$$

From the absorption spectrum, it is then possible to get information on the sample's components, as each compound has a unique absorption spectrum, which can be compared to reference spectra; it is then possible to quantify those components' concentration, as the amount of light absorbed is directly proportional to the concentration of the absorbing species in a sample. This is described by the Beer-Lambert law (2.4), where A is the absorbance, η the molar attenuation coefficient or absorptivity of the light-absorbing species, l the optical path length and c the concentration of the light-absorbing species.

$$A = \eta l c \quad (2.4)$$

Therefore, absorbance spectroscopy can provide quantitative information about the concentration of a particular substance in a sample.

Figure 2.2 shows examples of typical spectra obtained for CsPbBr_3 nanocubes, which show a swift increase of the absorption at around 500-510 nm, varying in function of the nanocrystals size, and which corresponds to the first exciton transition; on the other hand, a spectrum for CsPbBr_3 nanoplatelets is shown, which presents absorption peaks

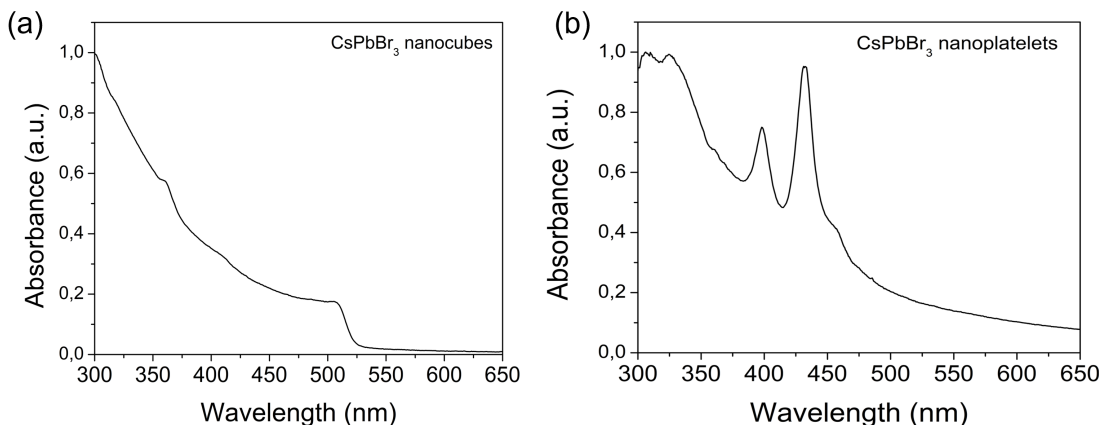


FIGURE 2.2: Examples of typical absorption spectra of CsPbBr_3 nanocubes (a) or $n=1,2,3$ nanoplatelets (b).

whose energy is related to the NPL thickness, in terms of their number of octahedra layers n . In fact, the thinner the nanoplatelet is, the more confined its excitons will be, increasing the system's energy: $n=1$ nanoplatelets show an absorption peak at 398 nm, $n=2$ at 429, $n=3$ at 438 nm, $n=4$ at 449 nm, $n=5$ at 459 nm.[106, 315] These two examples show how useful this technique is for a first and quick structural characterization of CsPbBr₃ nanocrystals.

Therefore, in this work, absorbance spectroscopy was used as the first characterisation tool for every colloidal nanocrystals sample, in order to obtain information about the structure, composition, concentration and transparency of the samples, as well as the reactions yields. Moreover, it was used to follow the reactions events during the preliminary tests, by tracking the changes in the absorbance of specific spectral areas over time.

2.1.3 Photoluminescence

Photoluminescence spectroscopy (PL) is a technique based on the ability of some materials of emitting light after being excited by photons, typically in the UV-Vis range.[316]

As previously described, when a material is exposed to a light beam, depending on this material's electronic structure it will absorb specific wavelengths: the incident photons' energy is absorbed by the electrons in the specie, promoting the energy of the system into an excited state. Once the system is in the excited state, it can relax back to its ground state through various processes, one of which is the fluorescence: in this case, the light is emitted with a delay statistic representing the PL decay time.

Photoluminescence spectroscopy involves exciting the material with a light source of a specific wavelength and measuring the consequent emitted radiation in terms of intensity and wavelength: the energy of the emitted light depends on the energy difference between the electronic excited and ground state, which differs from a specie to another, and thus this type of spectroscopy provides information about the nature of the sample, including its electronic and optical properties.

By analyzing the emission spectrum, several important parameters involving semiconducting materials can be determined: one of the key pieces of information, similarly to the absorption spectra, is their energy band gap, which provides insights into their electronic structure. Moreover, the intensity of the emission can also provide information about the presence of certain defects or impurities in the material.

Additionally, this technique can be used to study the exciton dynamics (the interaction between excited electrons and holes) and the recombination processes within the sample;

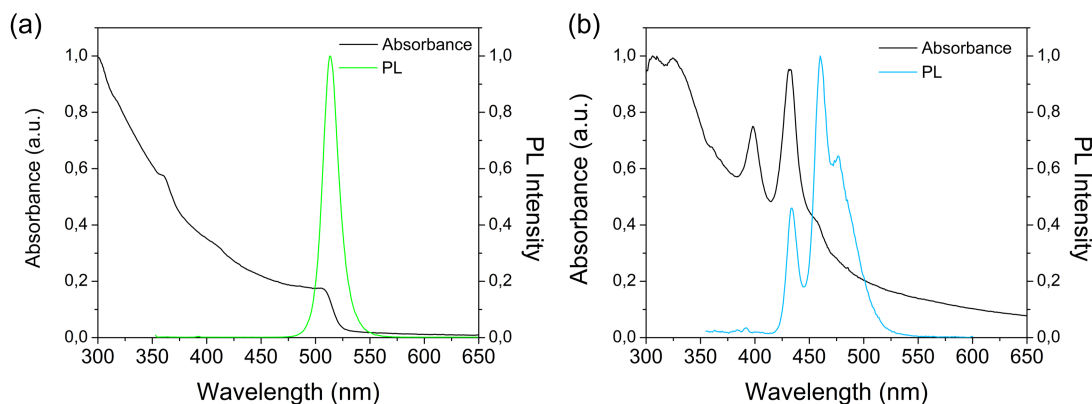


FIGURE 2.3: Same examples as the last Figure 2.2, with the addition of the typical photoluminescence spectra of CsPbBr₃ nanocubes (a) or n=1,2,3 nanoplalelets (b). Excitation wavelength $\lambda_{\text{exc}} = 350$ nm.

it is also sensitive to changes in temperature, pressure, and external factors, allowing for the investigation of their effects on the material.

Figure 2.3 shows the same two examples shown in the Absorption section in Figure 2.2, for CsPbBr₃ nanocubes and nanoplalelets, with the addition of their photoluminescence spectra. These spectra show that nanocubes generate a sharp and bright PL peak, whereas each population of nanoplalelets show a corresponding PL peak.

It has to be noticed that in both cases the Stokes shift, i.e. the distance between the absorption and photoluminescence maxima, is very short, which can be an issue since it cause self absorption phenomena: each photon that is emitted in the PL peak's range that overlaps with the absorption's one can be re-absorbed by the nanocrystals. This can cause a decrease in the photoluminescence yield, and an apparent slowdown of the emission process, in case of photons that go through multiple absorption - emission- re-absorption steps before reaching the detector. The intensity of the PL spectra is related to the luminescence yield, which is described later.

In this work, photoluminescence spectroscopy was used to study the fluorescence of the colloidal CsPbBr₃ nanocrystals and nanoplalelets, in terms of intensity, position and shape, in order to obtain information about the band gap, purity and surface quality of the samples, and to study the effects of experimental tests on the samples' optical properties.

2.1.4 Photoluminescence excitation

Photoluminescence excitation spectroscopy (PLE) is a technique used to study the energy levels and electronic transitions of a material.

Typically, once the emission wavelengths of the sample have been measured by PL spectroscopy, and thus the wavelength of interest are known, the technique works by fixing the detector at the desired wavelength, and scanning the excitation energies that lead to the target emission. This kind of spectra can then be directly compared to the absorption ones, leading to the identification of the species emitting at the targeted wavelengths.

This provides valuable information about the energy band structure, defect states, impurities, and other optoelectronic properties of the material. For instance, PLE is commonly used to investigate materials' bandgap and the energy levels of impurities or defects, and the types of electronic transitions occurring within the material.

Figure 2.4 shows the same two examples shown in the Photoluminescence section in Figure 2.3, for CsPbBr₃ nanocubes and nanoplatelets, with the addition of their photoluminescence excitation spectra. In the case of nanocubes, the PLE curve does indeed reproduce the absorption spectra depicted in Figure 2.2; meanwhile, in the case of nanoplatelets, the PLE curves respectively fixed at the different PL peaks give additional information, since they distinguish the source of each photoluminescence signal and also they better define the centers of the Gaussian distributions describing the absorption peaks of each nanoplatelets population.

In this work, PLE was used to study the electronic transitions leading to the light emissions, and more interestingly to study eventual inter-crystal energy transfers during Stokes shift engineering experiments.

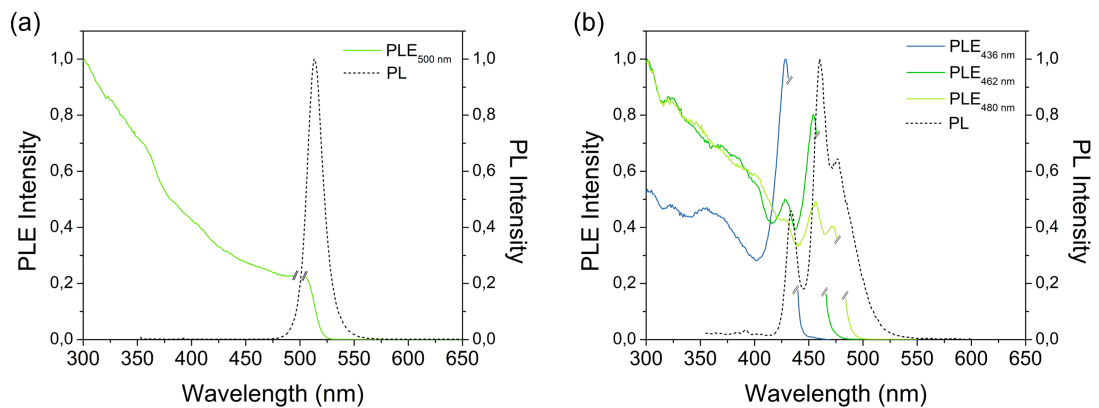


FIGURE 2.4: The examples shown in Figure 2.3 are reproduced here in dashed lines, with the addition of the typical photoluminescence excitation spectra (solid lines) of CsPbBr₃ nanocubes (a) or n=1,2,3 nanoplatelets (b). The PLE spectra are fixed at the λ_{em} indicated in the corresponding legends.

2.1.5 Photoluminescence quantum yield

The photoluminescence quantum yield (PLQY) measures the efficiency of light emission from a material under optical excitation, which is a crucial parameter in various fields, like material science, chemistry and optoelectronics: its study gives important information about the internal processes occurring during the light emission inside a material, the latter's quality in terms of the presence of defects, and overall the material's possible applications.

The measurement of PLQY works by exciting the material at an appropriate wavelength and measuring the amount of photons emitted via fluorescence: the ratio between the number of photons emitted by the sample and the amount of photons absorbed by it gives the internal PLQY, which will then be 0% for a non-fluorescent material and 100% for an ideal fluorophore that converts each absorbed photon into light emission.

There are multiple techniques available to measure PLQY, but one commonly used method, which is also the one used in this work, use an integrating sphere. The latter is a hollow, spherical chamber covered on the inside with a highly reflective and diffusive material, which ensures that the emitted light is scattered uniformly over all the emitted wavelengths.

For this experimental setup, illustrated in Figure 2.5, the sample is usually dispersed in an suitable solvent and transferred in a standardized quartz cuvette: then, it is placed at the center of the sphere. There, a light source is used to excite the sample at an appropriate wavelength based on the absorption features of the sample, and the emitted light is uniformly scattered by the integrating sphere and then collected by the detector. This measurement has to be performed both for the sample and a blank reference, in

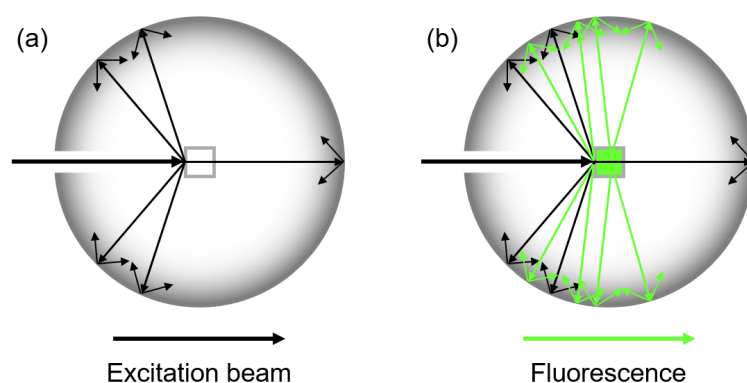


FIGURE 2.5: Schematic illustration of the two phases of photoluminescence quantum yield measurement, i.e. the measurement of the light diffusion by the support (in this case, a quartz cuvette containing the transparent solvent only) (a.) and the measurement of the sample's photoluminescence (b.).

this case a quartz cuvette containing the transparent solvent only, in order to take into account any excitation light diffusion and reflection caused by anything but the studied sample.

The PLQY values are then calculated by comparing the intensity of the emitted light from the sample and the blank reference as the ratio between emitted and absorbed photons.[317]

Overall, the photoluminescence quantum yield provides useful information, as it can allow to optimize and evaluate the performance of materials such as light emitting diodes (LEDs), solar cells, sensors, and fluorescence-based assays. Moreover, it is an useful tool in understanding the underlying processes involved in light emission, such as energy transfers and radiative or non-radiative decay pathways.

Instrumental setup

UV-Vis absorption spectra, photoluminescence (PL) spectra and quantum yields (PLQY) of the colloidal dispersions were obtained using an FS5 spectrofluorometer (Edinburgh Instruments). Absorption spectra were obtained in transmission mode. Typical photoluminescence spectra were recorded at an excitation wavelength of 350 nm, an integration time of 100 ms per data point, and a spectral resolution of 1 nm. Typical PLQY were obtained at an excitation wavelength of 365 nm, an integration time of 100 ms per data point, and a spectral resolution of 0.4 nm. Samples are prepared by dilution in a quartz cuvette.

2.1.6 X-rays radioluminescence

The radioluminescence (RL) spectroscopy is a technique based on the ability of some materials of emitting light after being irradiated with a ionizing radiation, similarly to the photoluminescence spectroscopy with UV-Vis radiations. In particular, X-ray luminescence spectroscopy refers to a technique used to study the properties and behavior of materials by analyzing their luminescent response to X-ray excitation: this involves the interaction between high-energy X-ray photons and a scintillating material which emits in response lower-energy photons, which can be then detected and analyzed.

The process begins by irradiating the sample with X-rays, the used setup operating at energies ranging from a few keV up to several tens of keV: when the radiation interacts with the material, the interaction with its atoms or molecules can result in various phenomena such as X-ray absorption, scattering, or luminescence, the latter being the center of interest of X-ray luminescence spectroscopy.

By analyzing this type of luminescence, it is possible to get information about the electronic structure, defects, impurities, and to test the efficiency of the scintillating process as compared to the PL process, since it involves additional transfer states as explained in Chapter 1. The intensity, energy, and wavelength distribution of the emitted light provide valuable insights into the composition, crystal structure, and overall characteristics of the sample.[251]

Overall, X-ray radioluminescence spectroscopy is a powerful tool for investigating the properties and behavior of different materials at the atomic and molecular level and their complex sequences of energy transfers.

In this work, X-ray RL is used to assess the scintillation properties of the lead halide perovskite nanocrystals samples, either in the liquid state, as colloidal dispersions, or in the solid state, as dried films deposited over Si supports, or embedded in matrices like polymers. An example of typical spectra obtained from CsPbBr₃ nanocrystals dried over Si is shown below (Figure 2.6): a comparison that is interesting to make is between the PL and RL spectra obtained in the same conditions, as it can show that the two different emissions can be produced by different emitting centers, as it is the case in this example. A possible explanation to this difference can reside in the higher penetrability of X-rays, that could favor collective emissions from the centers below the surface.

Moreover, it was interesting in some cases to image some samples under X-ray irradiation, as shown in the example below, where CsPbBr₃ samples were embedded in a zwitterionic block copolymer (Figure 2.7). In this case, the technique helped to acknowledge that it was possible to obtain a flat-surface and aggregation-free sample only at low

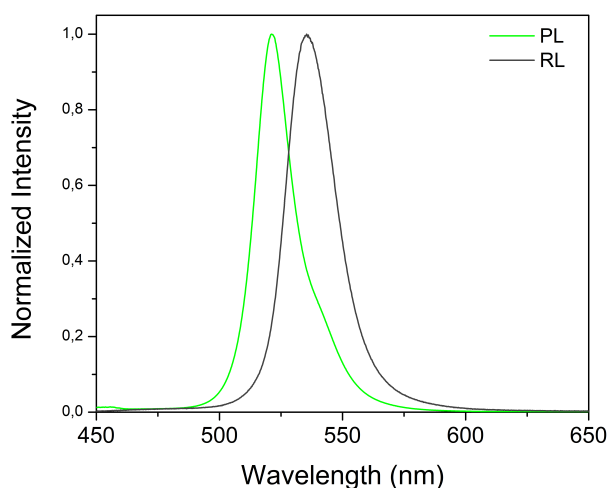


FIGURE 2.6: Comparison between the photoluminescence spectrum (green line) obtained at an excitation $\lambda_{\text{exc}} = 405$ nm and the radioluminescence spectrum (dark gray line) obtained with X rays produced at 20 kV and 30 mA.

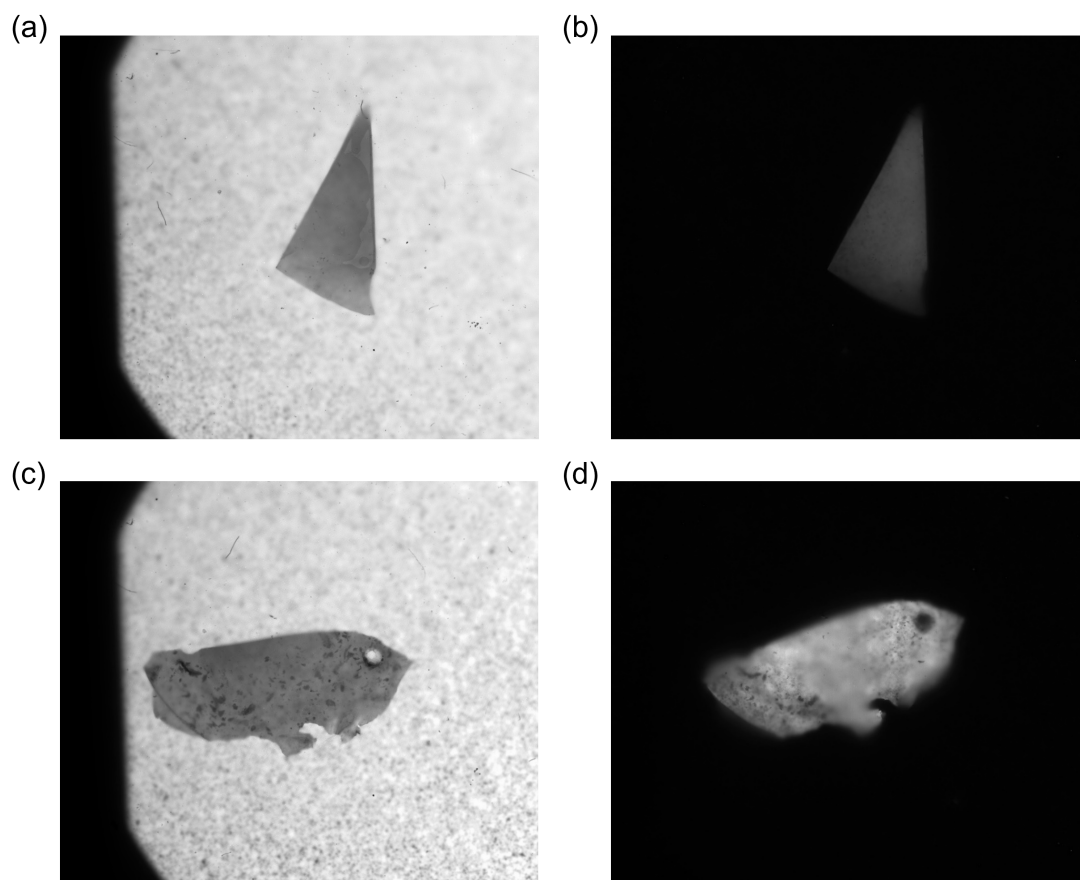


FIGURE 2.7: Images in radiography (left side) or radioluminescence (right side) mode of samples loaded in mass with 15% NCs, respectively (a) and (b), and 40% NCs, respectively (c) and (d).

NCs loading (Figure 2.7 (a), (b)), whereas for high loading the obtained samples clearly showed NCs aggregations (Figure 2.7 (c), (d)).

Instrumental setup

Radioluminescence's setup is illustrated in Figure 2.8: the RL spectroscopy setup consists of an X-rays tube emitting Bremsstrahlung X-rays from accelerated electrons (typically from 20 to 35 kV) bombarding a tungsten anode (Inel XRG 3000). The spectrum is measured using a SR500i-D2 mono-chromator (Andor) and an Andor Newton EM-CCD camera (DU970P-UVB) and is corrected for the spectral sensitivity of the system. Additionally, a LED emitting at $\lambda = 405$ nm can be used in order to obtain the PL spectrum in the very same conditions of the RL one, which greatly facilitates the comparison. Samples are prepared by drying them on a Si substrate.

On the other hand, for X-rays imaging the detection is obtained via a camera (Andor Zyla HF-FOP) and a removable scintillating screen. The latter is put in front of the

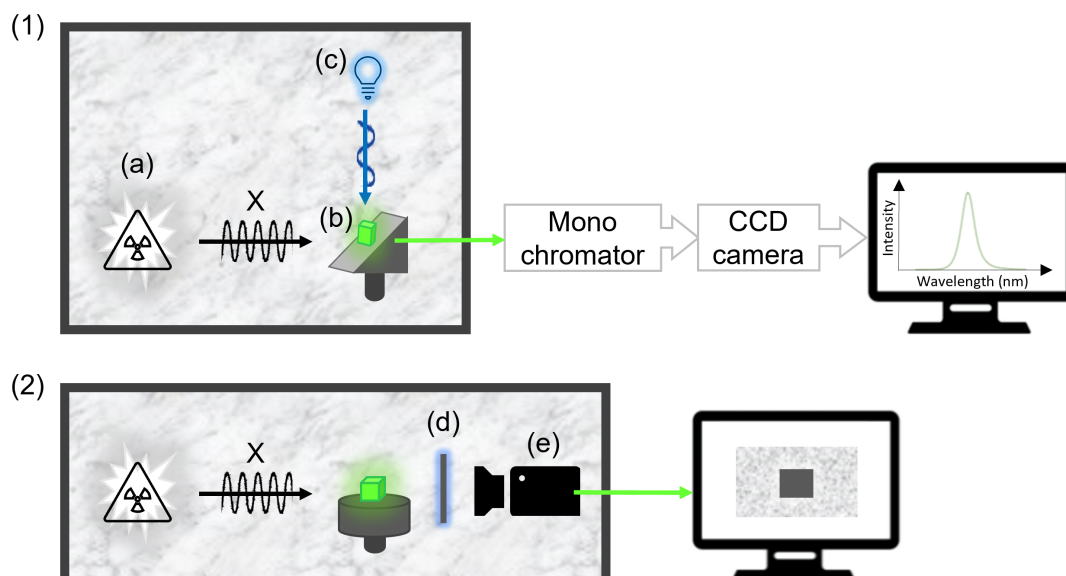


FIGURE 2.8: Scheme of the radioluminescence experimental setup. The key elements for the RL spectroscopy (1) are the X ray tube (a), the sample holder (b), a LED emitting at $\lambda = 405$ nm (c); in the imaging setup (2) a removable scintillating screen (d) and a camera (e) are present as well. Everything is covered by a protective shield.

camera when the desired output is a radiography of the samples, whereas it is removed to obtain a scintillation image. This whole setup is covered by a protective shield to prevent the radiation from leaking.

2.1.7 Luminescence decay rate

Light emission decay rate study is a technique used to investigate the dynamics of the light emitted by the population of the emitting state as it decreases after excitation, giving information useful for applications in materials science, energy research, biomedical imaging and environmental analysis. For the purposes of this work, the evaluation of the decay rate is used to verify the fast-emitting properties of the CsPbBr_3 samples and to estimate any quenching processes.

In the simple cases, the light emission is subject to exponential decay, which can be expressed by the following differential equation 2.5, where I is the light intensity, t is the time and η is a positive rate called the exponential decay constant:

$$\frac{dI(t)}{dt} = -\eta I \quad (2.5)$$

$$I(t) = I_0 e^{-\eta t} \quad (2.6)$$

where $I(t)$ is the light intensity at time t , and I_0 is the light intensity at time $t = 0$.

The exponential decay equation can be written in terms of the mean lifetime, where the exponential time constant τ , relates to the decay rate constant η as $\tau = 1/\eta$:

$$I(t) = I_0 e^{-t/\tau} \quad (2.7)$$

and that τ is the time at which the population of the assembly is reduced to $1/e$ times its initial value.

The light emission can decay via one or more different processes simultaneously: in general, these decay routes have different probabilities of occurring, and thus occur in parallel at different rates with different time constants. The total decay rate of the light emission intensity I is determined by analyzing the exponential decay curve of the emitted light intensity over time, which is given by the sum of all the decay routes:

$$-\frac{dI(t)}{dt} = \sum_{i=1}^n I \eta_i = \sum_{i=1}^n \eta_i I \quad (2.8)$$

$$I(t) = I_0 e^{-\sum_{i=1}^n \eta_i t} \quad (2.9)$$

In timing applications a useful figure of merit is the effective decay time τ_{eff} :[\[318\]](#) if R_i are the relative light yields (normalized to the area) of the decay time components τ_i , with $\sum R_i = 1$, then

$$\tau_{\text{eff}} = \left(\sum_{i=1}^n \frac{R_i}{\tau_i} \right)^{-1} \quad (2.10)$$

In material science, the decay rate study is used to investigate the luminescent properties of materials for various applications, such as optoelectronics, photocatalysis, and sensing. It helps in understanding the efficiency and mechanisms of light emission and quenching processes, optimizing material design, and improving device performance.

This technique is also widely used in photovoltaics, semiconductor physics, environmental monitoring, medical diagnostics and drug development, these lasts typically by means of fluorophore-labeled compounds.

In this work, both the optical luminescence and the radioluminescence decay rate were studied, thus the luminescence following either an optical or an X-ray excitation, in order to obtain information on the internal dynamics occurring during these two different processes.

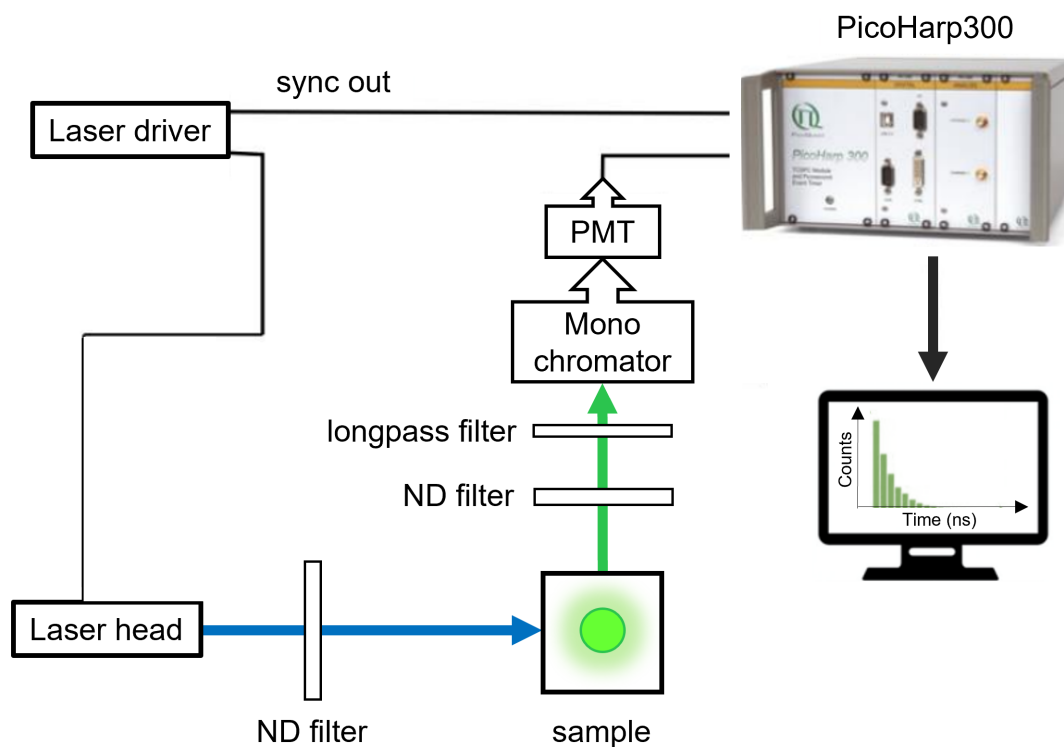


FIGURE 2.9: Scheme of the luminescence decay rate's setup.

Instrumental setup

Photoluminescence decay rate's setup is illustrated in Figure 2.9: it consists of a pulsed laser emitting at 405 nm, a monochromator, a photomultiplier tube (PMT), the PicoHarp300 time-correlated single photon counting (TCSPC) and several filters. The irradiation source can be exchanged with a second pulsed laser emitting X rays, in order to obtain the radioluminescence decay rate. Samples can be placed either solid, dried on a Si substrate, or eventually liquid, in a quartz cuvette.

2.1.8 Transmission electron microscopy

Transmission electron microscopy (TEM) is a powerful imaging technique able to visualize the internal structure and morphology of materials at very high magnifications. Unlike light microscopy, which uses photons, TEM uses a beam of electrons that is transmitted through an ultra-thin sample.

In such a microscope, electron beams are generated by an electron gun and focused onto the sample using a series of electromagnetic lenses. The sample needs to be very thin (typically around 100 nanometers) to allow electron transmission: as the electrons pass

through the sample, they interact with its atoms, resulting in several interactions such as scattering, diffraction, and absorption.

The interaction of electrons with the sample provides valuable information about its composition, crystal structure, and morphology. This information is collected and converted into an image using a detector, typically a digital camera. The resulting TEM images have a much higher resolution than optical microscopy, allowing the visualization of individual atoms or atomic lattice planes.

TEM finds numerous applications in various fields of science and technology, such as material science and nanotechnology research, where it allows to study crystals, defects, grain boundaries and interfaces. It is indeed used to investigate the structure, properties and dimensions of materials such as metals, ceramics, semiconductors, polymers, nanoparticles, nanowires, nanotubes, and other nanostructures.

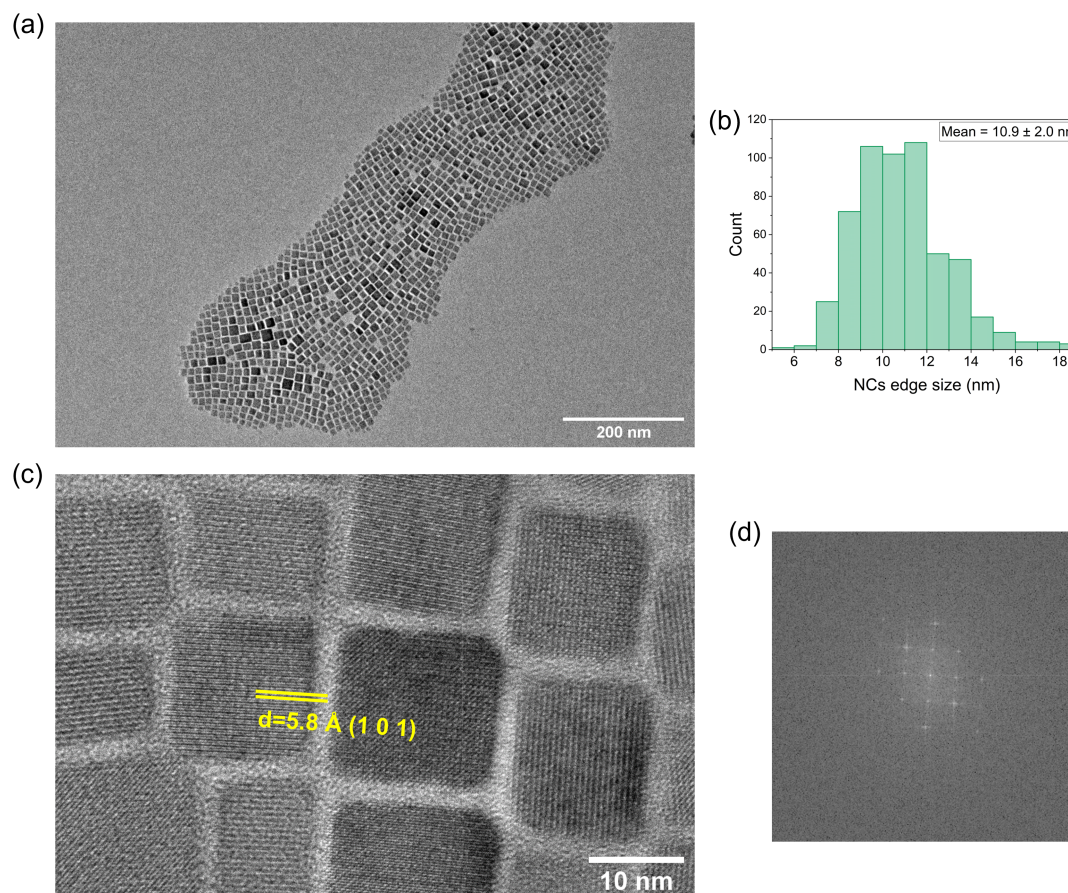


FIGURE 2.10: Example of a typical TEM characterization: an image of CsPbBr₃ nanocrystals at a quite low (25 000 X) magnification (a), the statistics of the average nanocrystals edge size which can be obtained by analyzing multiple images of different areas of the grid (b), an image at high (400 000 X) magnification showing the inter-planes distance identifying the crystalline planes (c), which is obtained by the image's FFT (d). All TEM images were treated with ImageJ imaging program.[319]

Moreover, TEM is also used to reveal the detailed structure of biological specimens: it can provide indeed important insights for studying viruses, understanding cellular organization and exploring the fine structure of tissues and organs.

Finally, TEM is employed to perform advanced material characterization such as electron diffraction, energy-dispersive X-ray spectroscopy (EDS) and electron energy-loss spectroscopy (EELS). These techniques provide information about the crystallographic structure, elemental composition, and electronic properties of materials.

Figure 2.10 shows an example of how TEM was used for the purposes of this thesis: when imaging a CsPbBr₃ nanocrystals sample, the NCs are easily recognizable as cubes of a more or less dispersed average size depending on the sample, with a good contrast on the that makes them clearly defined taking many images of different areas of the grid allows to calculate a statistics of the average NCs size and to have a general overview of the sample's quality in terms of possible organic impurities. Besides that, at high magnification it is possible to obtain high resolution images, allowing to see at the nanomaterials at the atomic scale and to identify the crystalline planes: calculating the Fourier transform of these high resolution images gives the values of the inter-planes distances, which is informative for the identification of both the crystalline phase and composition.

It is worth remarking that, since this technique involves exposing the samples to an electrons beam, the latter can react with lead halide perovskite nanocrystals: over time, this can result in morphological transformations[320] and in the reduction $\text{Pb}^{2+} \rightarrow \text{Pb}^0$, resulting in the nanocrystals disruption with the apparition of metallic lead clusters.[321, 322]

In this work, transmission electron microscopy was used to determine the morphology and the average dimensions the obtained CsPbBr₃ nanocrystals and nanoplatelets , and also to study the formation of heterostructures by visual observation and by measuring the inter-planes distances by the images Fourier Transforms.

Instrumental setup

TEM images were acquired on a JEOL JEM-2100 TEM equipped with a LaB₆ electron source, operating at 200 kV. Samples are prepared by drying them on a carbon grid.

2.2 Colloidal perovskite nanocrystals synthesis

As already stated, in the past 20 years the development of colloidal nanoparticles-based technologies has been pursued intensively, due to the enormous technological applications and fundamental interest that they brought to the scientific community.

This has led to the exploration of a large number of synthetic procedures, resulting in different outcomes in terms of nanocrystals dimension, chemical composition, optoelectronic features, scalability and most suitable application: this section aims to describe the theory and practice of the most used synthetic approaches.

Colloidal perovskite nanocrystals can be synthesized in several ways, mainly via the hot injection method and the ligand-assisted reprecipitation (LARP), or less commonly via the solvothermal method and the electrochemical deposition.

First, the hot injection method takes its name from the main reaction step, thus the injection of a solution of precursors into a hot solvent while stirring constantly. On the other hand, the ligand-assisted reprecipitation is operated at room temperature: the precursors are dissolved in a small amount of a suitable solvent, and then injected into a large amount of a bad solvent, causing the nanocrystals precipitation.

For the solvothermal method, the precursors are dissolved in a solvent and heated at high temperature and pressure; the mixture is then allowed to cool slowly to obtain perovskite nanocrystals.[205, 323–325] A similar process can take place under microwave stimulation: precursors are dissolved in a solvent and irradiated with microwaves until the formation of perovskite nanocrystals.[326–328] Finally, for the electrochemical deposition, an electric potential is applied to a solution of precursors, allowing to deposit perovskite nanocrystals onto a substrate.[329, 330]

The most popular approaches are the hot injection and the LARP ones, which were also the ones used along this work: therefore, this section aims to describe the mechanisms and setups involved in these two synthetic processes, initially by summarizing the theory behind them, and finally by portraying typical reaction setups.

2.2.1 Nucleation and growth

The mechanisms involved in the syntheses of uniform nanocrystals has been a focus of research ever since quantum dots appeared, and significant endeavors have been dedicated to their rationalization. This growth understanding and exploitation enables to synthesize nanocrystals with tuneable dimensions, compositions and resulting features,[331] with the best results, in terms of quality and uniformity, obtained through processes

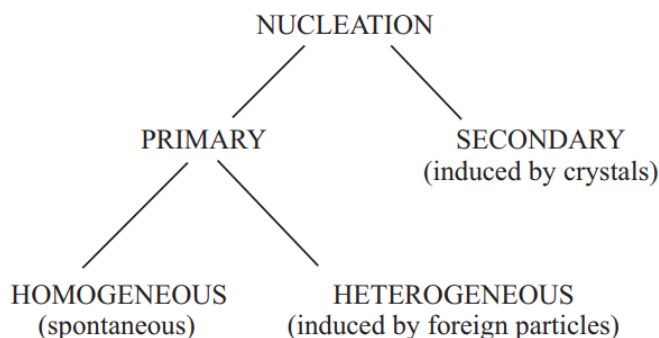


FIGURE 2.11: Simple scheme classifying the different terms used for crystal growth. Reproduced from the work of Mullin[335].

involving the precursors' thermal decomposition, like the hot injection or the heat-up methods.[332–334]

The understanding of the mechanisms involved in these nanocrystals synthesis has to go through the two main phases of it, thus the nanocrystals nucleation and subsequent growth: for the growth of crystals in solution, it typically occurs in presence of species acting as seeds, allowing the crystallization reaction to happen at the interface between such seeds and the solution. These seeds are called nuclei and can be either introduced externally or generated in the solution.[335]

Thus, nucleation refers to these nuclei formation phenomenon, and it is possible to distinguish between primary and secondary nucleation. The first one refers to nucleation processes occurring without the presence of other crystalline matter, whereas secondary nucleation applies to the situations where nuclei are generated in proximity of crystal already present in a supersaturated system. In turn, primary nucleation includes two identifiable situations, since when nuclei form evenly within the initial phase it is called homogeneous nucleation, whereas heterogeneous nucleation occurs at structural irregularities, such as container surfaces, impurities, grain boundaries, and dislocations.[335, 336] This classification can be used to describe the nucleation in many chemical syntheses, and a simple scheme is displayed in Figure 2.11.

Detailed insights on the classical nucleation model and on the most popular nucleation/-growth mechanisms of nanocrystals are now discussed.

2.2.1.1 Classical nucleation theory: Gibbs-Thomson model

The process of forming homogeneous nuclei can be analyzed thermodynamically by considering the total free energy of a nanoparticle, which is the sum of its surface free energy and its corresponding bulk's free energy.[333, 335]

The thermodynamic theory of formation of the new phase is described by the classical Gibbs-Thomson theory. The Gibbs free energy of a nucleus is in general expressed as the sum of a bulk term ΔG_1 , proportional to the volume of the nucleus, and a surface term ΔG_2 , proportional to its surface area.[337] The volume term ΔG_1 is negative, which is the driving force for nucleus formation, whereas the surface term ΔG_2 has a positive contribution, due to the formation of a solid and liquid interface. For a spherical particle of radius r , the surface energy γ and the free energy of the bulk crystal ΔG_v give a total free energy ΔG :

$$\Delta G_T = \Delta G_1 + \Delta G_2 = \frac{4}{3}\pi r^3 \Delta G_v + 4\pi r^2 \gamma \quad (2.11)$$

ΔG_v has a dependence on the temperature T , Boltzmann's constant k_B , the supersaturation of the solution S , and its molar volume, v .

$$\Delta G_v = \frac{-k_B T \ln(S)}{v} \quad (2.12)$$

Since the surface's free energy is always positive and the crystal's free energy is always negative, it is possible to find a maximum free energy through which a nucleus will pass and form a stable nucleus: the critical size r_{crit} is reached when free energy ΔG gets to a maximum, thus when $d\Delta G/dr = 0$, which also defines the critical free energy ΔG_{crit} .

$$\Delta G_{crit} = \frac{4}{3}\pi \gamma r_{crit}^2 \quad (2.13)$$

$$\Delta G_{crit} = \frac{16\pi \gamma}{3\Delta G_v^2} \quad (2.14)$$

$$r_{crit} = \frac{-2\gamma}{\Delta G_v} = \frac{2\gamma v}{k_B T \ln(S)} \quad (2.15)$$

The so-defined critical radius r_{crit} corresponds to the minimum size at which a particle can endure in solution without re-dissolving: a nucleus with $r < r_{crit}$ will dissolve into the solution, whereas a nucleus with $r \geq r_{crit}$ can exist for further growth. The same is true for the particle's free energy, where a critical free energy is required to obtain particles stable in solution.[338] This situation is described by the curves in Figure 2.12.

A nucleation rate of N particles during a time t can be described using an Arrhenius type equation:

$$\frac{dN}{dt} = A \exp\left(-\frac{\Delta G_{crit}}{k_B T}\right) \quad (2.16)$$

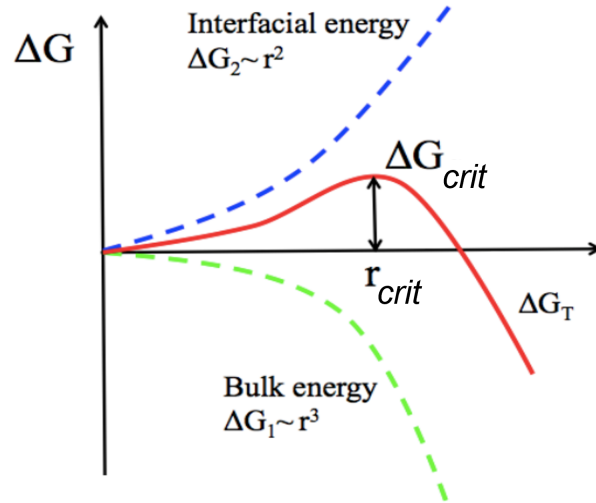


FIGURE 2.12: Free energy diagram for nucleation explaining the existence of a critical nucleus. Red curve is the total Gibbs free energy as a function of the nuclei radius. ΔG_{crit} is the homogeneous nucleation energy barrier, and r_{crit} is the critical radius. The bulk term ΔG_1 that scales with r^3 is plotted in green, whereas the interfacial energy ΔG_2 is the blue curve and is proportional to the surface area r^2 .

$$\frac{dN}{dt} = A \exp\left(\frac{16\pi\gamma^3 v^2}{3k_B^3 T^3 \ln^2(S)}\right) \quad (2.17)$$

From this, it is possible to experimentally vary parameters as supersaturation, temperature, and the surface free energy and thus study the systems kinetics: the largest effect on nucleation rate comes from supersaturation, where a change from $S=2$ to $S=4$ causes an increase in the nucleation rate about 10^{70} .^[333]

On the other hand, if the solution contains so-called active centers, such as impurities, walls, bubbles, drops, etc., a heterogeneous nucleation occurs. In this scenario, the energy barrier for nucleation is globally decreased. Unlike in homogeneous nucleation, the nuclei form on the surface of these impurities: as a result, they no longer come in a spherical shape, but rather form caps, forming a spherical contact angle θ with the surface (Figure 2.13).

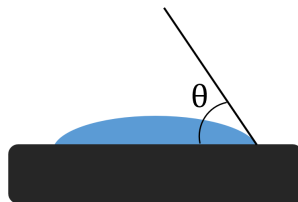


FIGURE 2.13: Representation of the contact angle θ in the case of heterogeneous nucleation.

If $\theta \leq \pi$, nuclei and active centers have a high affinity. The surface term is strongly decreased, and after applying this correction to the law of homogeneous primary nucleation, it results that the free energy needed for heterogeneous nucleation is directly proportional to a function of the contact angle θ .^[339]

2.2.1.2 Lamer mechanism

The LaMer mechanism was originally developed to describe the synthesis of sulfur hydrosols,^[340, 341] but it is nowadays widely cited as a classical theory for the formation of uniform colloidal particles.

According to this mechanism, the process of nucleation and growth can be divided into three steps, shown in Figure 2.14: first, a sudden increase in the concentration of free monomers in the solution, and secondly the monomer undergoes a "burst-nucleation," which significantly reduces the concentration of free monomers in the solution. This nucleation rate is described as "effectively infinite," and is not followed by almost any further nucleation, due to the low concentration of monomers. Finally, the third phase sees subsequent growth under the control of monomer diffusion through the solution.

It is worth noticing that if a reaction is not stopped after an adequate time, a fourth stage is established, where the nanoparticles increasingly grow due to Ostwald ripening (see the following section): larger nanoparticles, which are thermodynamically favoured, compete with smaller ones, and then keep on growing owing to the dissolution of smaller particles and thus refreshed availability of components.

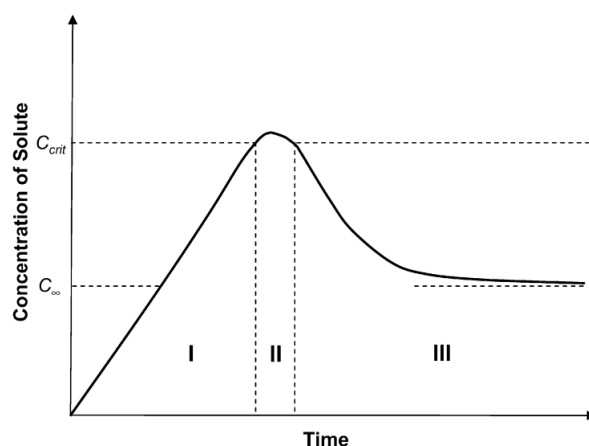


FIGURE 2.14: LaMer nucleation and growth diagram scheme. Reproduced from the work of Sugimoto^[342].

2.2.1.3 Ostwald ripening mechanism

Ostwald ripening[343] describes a growth mechanism induced by the change in solubility of nanoparticles depending on their size, as predicted by the Gibbs-Thomson relation. Due to the high solubility and surface energy of smaller particles in solution, they redissolve, allowing larger particles to keep on growing.

Specularly, digestive ripening is essentially the opposite of Ostwald ripening. In this case, smaller particles grow at the expense of larger ones. This formation process is once again controlled by the particle's surface energy in solution, causing larger particles to redissolve and smaller particles to grow.

2.2.1.4 Coalescence and oriented attachment

Coalescence and oriented attachment are similar processes, but differ in terms of the crystal lattice orientation at the grain boundary. In coalescence, there is no specific preference for attachment,[344] whereas in oriented attachment, there is a common crystallographic alignment that allows for continuous crystallographic planes.[345] It has been observed that particles will rotate and come into contact until their crystallographic orientations match, or until a twin match occurs, and there is no consensus if this attraction has Coulomb or van der Waals nature.[346]

2.2.1.5 Intraparticle ripening

Intraparticle ripening[347, 348] involves the diffusion of monomers along the surface of a nanomaterial, leading to a change in the particle's shape over time. This occurs under specific conditions, where the energy of monomers in the solution is lower than that of the nanoparticles' crystal facets. This means that the surface energy of the particle is nearly equal to that of the bulk solution, resulting in no net diffusion without an influx of monomers onto the particle's surface. The only instability in the system is the surface energy of the different facets of the particle itself. In this scenario, high energy facets dissolve, while low energy facets grow, resulting in apparent intraparticle diffusion.

2.2.2 Hot injection synthesis

The hot-injection method was introduced in the early stage of quantum dots studies by Murray and co-workers, for the synthesis of cadmium chalcogenide nanocrystals.[349] This synthetic process is based on the fast nucleation which is initiated by the swift

injection of a final precursor into a hot solution, that already contains all the other precursors.

Hot-injection enables the synthesis of monodispersed nanocrystals, with the only drawback of making it difficult to scale up the synthesis, due to the complexity of rapidly mixing all the precursors at the very same time when it comes to large quantities.

The hot-injection typical setup for the synthesis of lead halide perovskite nanocrystals is illustrated in Figure 2.15.

The precursors of the desired nanocrystals are first dissolved in a high-boiling-point solvent, such as octadecene. Then, this solution is heated up (usually around 120-150°C), creating a highly reactive environment where the precursors can interact with one another.

At this point, a solution containing a metal precursor and a reducing agent are injected into the hot reaction solution, triggering the nucleation and rapid growth of nanocrystals: in order to stop this otherwise uncontrolled growth, the mixture is rapidly cooled down with ice to stop the reaction and stabilize the products.

The resulting nanocrystals are then isolated from the reaction mixture using various methods, such as centrifugation or precipitation.

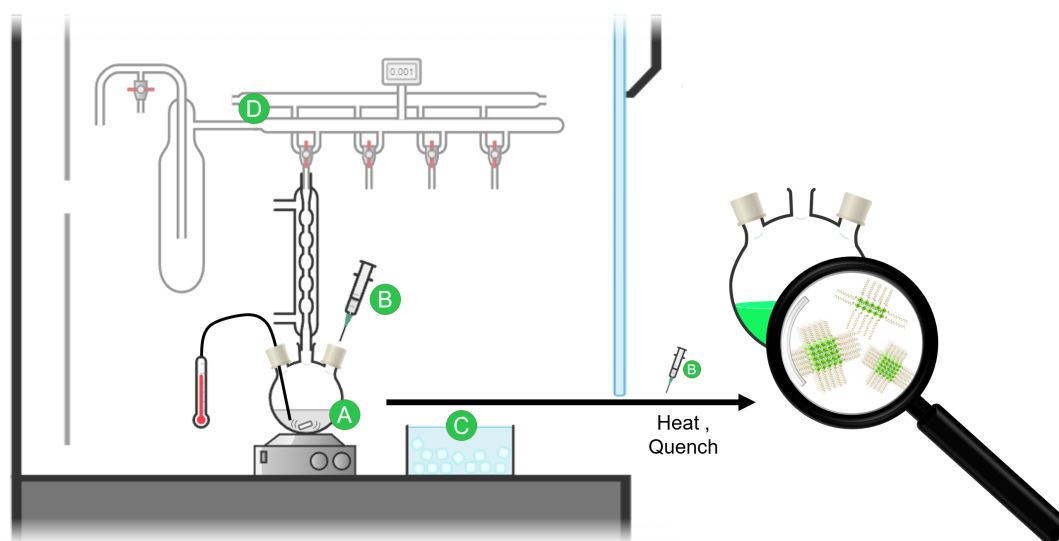


FIGURE 2.15: Illustration of the hot injection synthetic approach. The three-neck flask (A), containing CsPbBr_3 nanocrystals precursors and a magnetic stirrer, is stirred and heated up while the temperature is kept under control by a thermocouple. The reaction is initiated by the swift injection at high temperature of a final precursor (B) and then it is quickly thermally quenched by an iced water bath (C). The whole system is kept under controlled atmosphere by being connected to a Schlenk line (D).

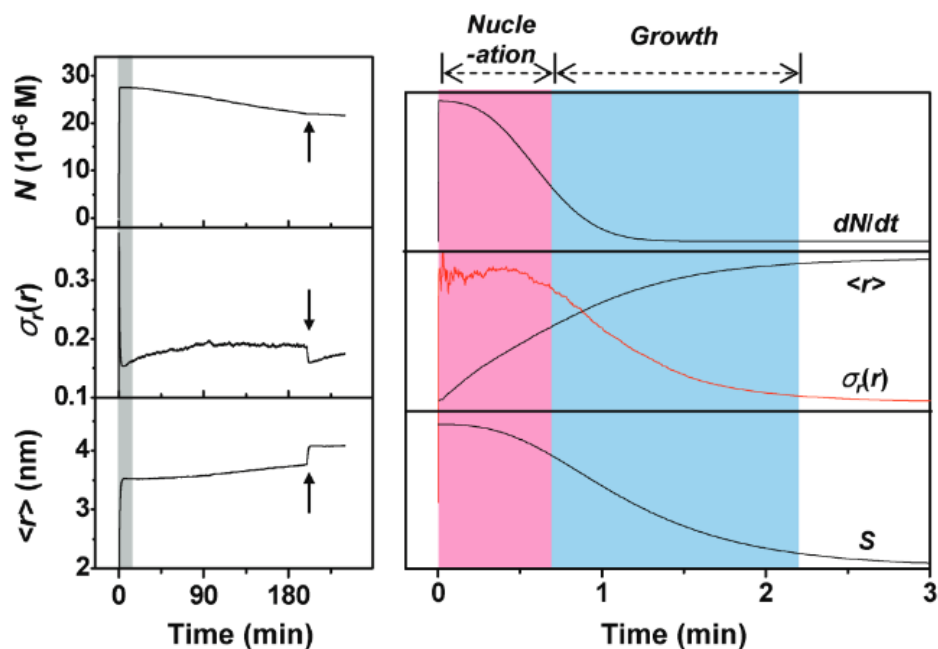


FIGURE 2.16: Computer simulation reproducing the hot-injection process. The vertical gray stripe indicates the first few minutes after the injection, which is magnified in the right panels. N , $\sigma_r(r)$, $\langle r \rangle$, dN/dt and S are the number concentration of the nanocrystals, the relative standard deviation of their radii, the mean radius, the nucleation rate, and the supersaturation level, respectively. Areas colored with red and blue correspond to the nucleation and the growth periods, respectively. Reproduced from the work of Klabunde[350].

Overall, the key to the hot-injection method is the high temperature and rapid mixing, which promote the formation of uniform and well-defined nanoparticles. Additionally, the choice of precursors and reaction conditions can be carefully controlled to yield nanoparticles with specific shapes, sizes, and properties.

With regards to the nucleation and growth mechanisms involved in this synthetic approach, it was assessed that, schematically, hot-injection can be considered as a special case of the LaMer model, omitting the first stage. As a matter of fact, as shown in Figure 2.16 the rapid injection of the precursors causes a high supersaturation level at the start of the nucleation period: this means that the system doesn't go through the phase of monomer accumulation typical of the LaMer mechanism.[333]

2.2.3 Ligand-assisted reprecipitation synthesis

Ligand-assisted reprecipitation (LARP) is a fast, reproducible and rather easy technique used to synthesize colloidal nanoparticles at room temperature.[351]

This method involves a two-step process, illustrated in Figure 2.17: it begins with the preparation of a precursor solution, containing the metal ions to be precipitated and the

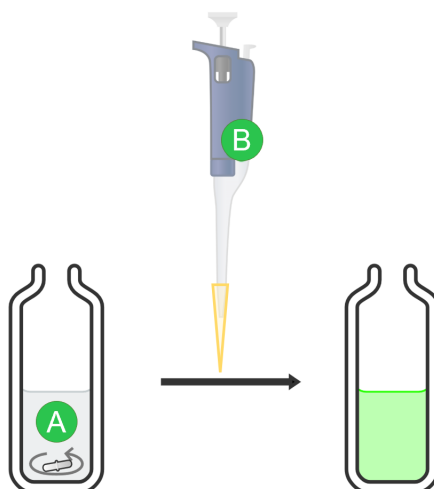


FIGURE 2.17: Illustration of the ligand-assisted reprecipitation synthetic approach: a large volume of a liquid chosen as a bad solvent for the nanocrystals (A) is stirred vigorously, when a small volume of a highly concentrated solution of nanocrystals precursors is injected into it (B), causing the nanoparticles precipitation.

chosen surface stabilizing ligands. Typically, this solution is highly concentrated in a small amount of a highly polar solvent, in which the polar precursors are well dissolved.

In the second step, a small amount of this precursors solution is quickly injected in a much larger volume of a poor solvent, typically another organic liquid with a polarity value unsuitable to keep the metal ions dissolved: this quick injection causes the precursors to oversaturate in the poor solvent, and consequently nucleate and precipitate as nanoparticles. As the process happens at room temperature, it is impossible to apply a swift thermal quenching by a cold shock, causing to these nanoparticles to grow increasingly larger by agglomeration or Ostwald ripening.

In contrast to the classic LaMer model, where the nucleation occurs in one solvent with one precursor, the LARP technique involves two separate solutions, multiple precursors and ligands, and the nucleation is triggered after the two solvents are rapidly mixed.

In the case of colloidal MAPbBr_3 nanocrystals synthesised via LARP method, it was observed by Huang et al.[352] that the initial precursors concentration plays a role in determining the resulting particles, as low precursors concentration is found to only be sufficient for the formation of small NCs of poor surface quality, whereas at high precursor concentration the system is more likely to produce larger particles due to a larger availability of precursors in the solution. It was also proposed that the increased ratio of Pb:ligand may also help to activate the particles surface by decreasing the surface density of the capping ligand, increasing the surface accessibility for the precursors and yielding a higher growth rate. Finally, when a too high concentration of precursors is used, the NCs solution is found to be colloiddally unstable and thus instantaneously form

a precipitate has a tendency to form: in that case, the nucleation and growth always happen until the excess concentration of the precursor falls to a low enough level. The resulting particles may be not entirely protected by ligands, which is detrimental as well to the NCs' colloidal stability.

Finally, a work from Udayabhaskararao et al.,[353] about colloidal CsPbX₃ nanocrystals synthesised via LARP method, proposes that the synthesis mechanism occurs through the seed-mediated nucleation model, where Pb⁰ nanoparticles formed during the first reaction steps would act as seeds.

2.3 Nanocubes and nanoplatelets selective synthesis

For this work's purposes, lead halide perovskite nanocrystals were mainly synthesized via different hot-injection approaches, chosen as facile methods able to produce well controlled populations of nanocrystals and in rather high amounts. In particular, the work was driven by the need of mastering the synthesis of selective populations of nanocrystals, either in 3D or 2D structures, in order to avoid to add yield-lowering separation and purification steps. Also, a great focus was concentrated on the production of highly colloiddally stable nanocrystals dispersions, through the careful choice of the stabilizing ligand.

The chemical synthesis reaction usually takes place in a three-neck round-bottom flask, as illustrated in Figure 2.15. The central neck is connected with a reflux condenser, in turn connected with the Schlenk line that is used either to make vacuum during the degassing phase, needed to obtain an oxygen, carbon dioxide and humidity free environment, either to keep the reaction mix under inert Argon atmosphere. On the other hand, the lateral necks are sealed with rubber septa and are used either to hold the temperature probe, either to inject precursors or withdraw amounts of the crude reaction mix. The flask is maintained under an inert atmosphere, heated by a heating mantle and kept under stirring by a magnetic rod.

2.3.1 Precursors synthesis

Cs-oleate was obtained by mixing cesium carbonate (6.4 mmol) and oleic acid (20.5 mmol) in ODE (21 mL) in a 50 mL three-neck flask, under vacuum at 75°C, until completion of gas evolution. The resulting product was stored under Ar.

Pb-oleate was obtained by mixing lead acetate (19 mmol) and oleic acid (38 mmol) in ODE (26 mL) in a 50 mL three-neck flask, under vacuum at 65°C, until completion of gas evolution. The resulting product was stored under Ar.

TOP-Br₂ was synthesized in a controlled atmosphere Argon glovebox in a 50 mL three-neck flask, by gently mixing trioctylphosphine (18 mmol) with bromine (16 mmol) added dropwise at room temperature: the exothermic reaction gives a white crude, which is cooled down at room temperature, and then dissolved in 26 mL of anhydrous toluene.

Bromide salts of hexylamine and 2-aminoanthracene were obtained by mixing in a 50 mL three-neck flask 1.25 mmol of the precursor amine and 0.280 mL of hydrogen bromide, in 20 mL of ethanol. The reaction mixture was left stirring under Argon atmosphere and in an icy water bath for 10h; once the reaction was completed, the resulting solution was dried under vacuum, rinsed six times with diethylether and finally dried under vacuum and at 80°C. The final product was stored in the glovebox for further use.

2.3.2 OA/OAm-capped nanocrystals synthesis

The synthesis of OA/OAm-capped CsPbBr₃ nanocrystals was realized by slight modifications of a hot-injection procedure described by Imran et al. at first reproduced as detailed below.[\[354\]](#)

This protocol relies on the strong reactivity of acyl halides towards nucleophilic compounds (i.e. amines, alcohols, carboxylic acids) which form carboxylic acid derivatives even at room temperature (respectively amides, esters, anhydrides) and simultaneously release hydrohalic acids, as illustrated by the reactions in Figure 2.18. Compared to other synthetic protocols used in literature, relying on salts as the CsPbBr₃ precursors, this approach has the advantage of promoting one type of quick reaction, between highly reactive species, which helps developing a reproducible synthesis protocol, avoiding the formation of byproducts (and the consequent yield loss) and also obtaining rather monodispersed populations of nanocrystals.

Thus, preparing a solution of Cs⁺ and Pb²⁺ cations, dissolved in the organic solvent by nucleophilic molecules like amines and carboxylic acids, and then injecting acyl halides at a desired temperature triggers the release of halide ions and, consequently, the nucleation and growth of metal halide nanocrystals.

Among the possible acyl halide molecules, the authors of the reference paper selected benzoyl halides since they are low cost and have a sufficiently high boiling point (around

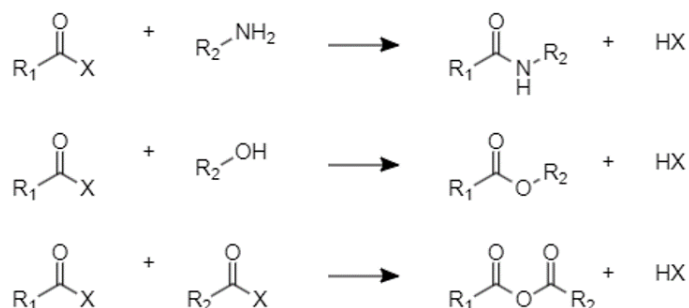


FIGURE 2.18: Reactivity of acyl halides towards nucleophilic compounds.

200 °C), which allows for the synthesis of lead halide perovskite nanocrystals at relatively high temperatures. Furthermore, considering the strong reactivity of acyl halides toward nucleophilic species, another important aspect of benzoyl halides is that they are more stable than aliphatic acyl halides as a result of their stabilization by the aromatic π -overlap between the carboxylate function and the phenyl one.[355] Indeed, the more stable the anion precursor is, the more controlled the release of the halide ions should be, which should allow to finely tune the size distribution of the synthesized nanocrystals.[356]

Cesium carbonate (Cs_2CO_3 , 48 mg, 0.295 mmol), lead acetate ($\text{Pb}(\text{OAc})_2 \cdot 3\text{H}_2\text{O}$, 228 mg, 0.6 mmol), oleic acid (OA, 0.9 ml, 2.83 mmol), oleylamine (OAm, 3 ml, 3 mmol) and octadecene (ODE, 15ml), were added to a 50 ml three-neck round-bottom flask. The resulting mixture was heated up to 130°C under vigorous stirring and vacuum conditions for 1 h, to remove moisture and oxygen and to produce oleate metal complexes. The flask was then filled with argon and the mixture was heated up to 170°C: benzoyl bromide (PhCOBr , 0.21 ml, 1.78 mmol) was injected, and the mixture was immediately cooled down with an ice bath, to prevent the nanocrystals growth. The CsPbBr_3 nanocrystals were then centrifuged at 8k RCF for 10 min: the precipitate was redispersed in 10 ml of toluene, whereas the supernatant, when needed, was centrifuged again after adding a small volume of ethanol (until the solution became turbid). This second precipitate was redispersed in 10 ml of toluene as well.

A typical early sample obtained with this procedure is hereby described. The centrifugation purification process results in the separation of different populations: bigger sized nanocubes are more impacted by the centrifugal force and precipitate, whereas the smaller-size population is too light to precipitate, and thus stays stable in the supernatant until destabilized by some a more polar liquid, ethanol in this case. The absorption spectra (Figure 2.19 (a)) reflect this situation, with the first exciton's transition of the nanocubes in the precipitate occurring at 510 nm, whereas the supernatant's one shifts to 503 nm due to confinement. The latter spectrum reveals the presence of a

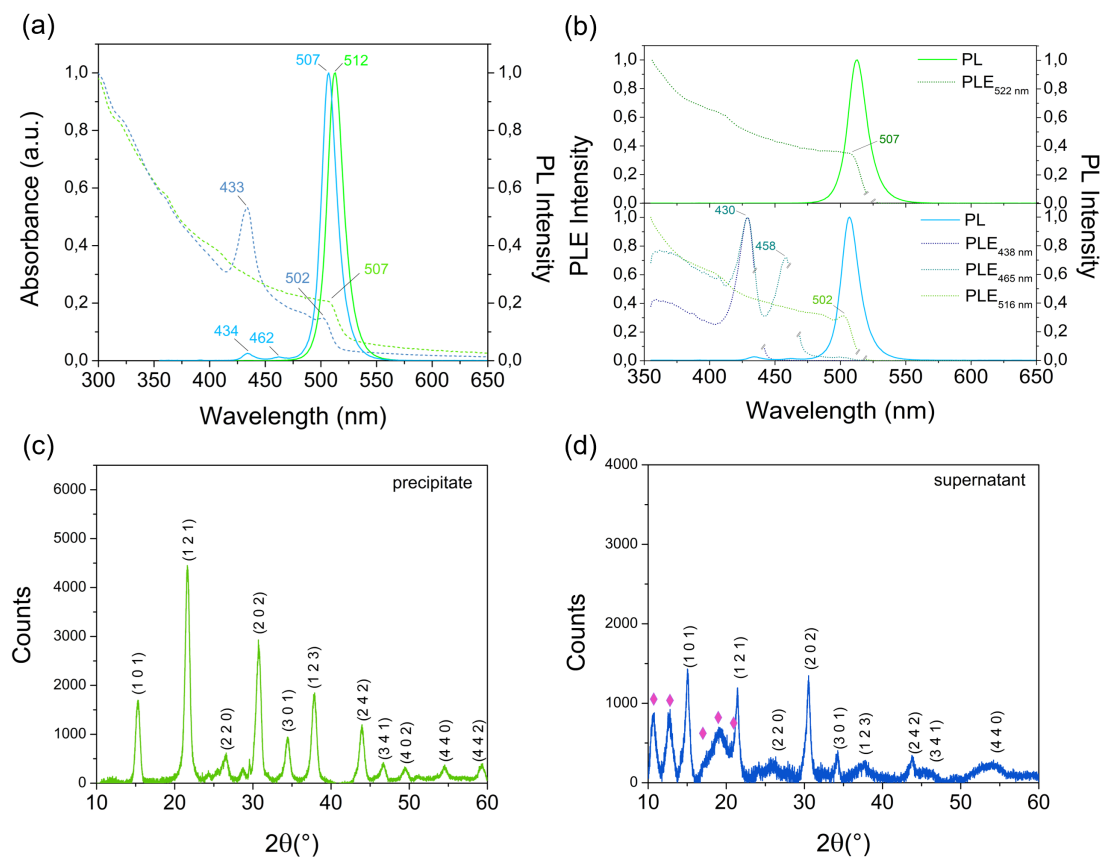


FIGURE 2.19: Typical features of early OA/OAm-capped CsPbBr₃ colloidal nanocrystals, once the sample washed via centrifugation: the absorption and photoluminescence ($\lambda_{\text{exc}} = 350$ nm) spectra, respectively in dashed and solid lines, of the precipitate and supernatant, respectively in green and blue (a), the PLE spectra (dotted lines) of the precipitate and the supernatant, respectively in the upper and lower side of (b), and the XRD patterns of the precipitate and supernatant, respectively (c) and (d). In the latter, pink diamonds indicate the peaks associated with the stacking periodicity of the nanoplatelets.

population of nanoplatelets identified by the absorption peak at 433 nm, typical of $n=2$ nanoplatelets.

The PLE spectra (Figure 2.19 (b)) registered at the emission wavelengths associated with the nanocubes and nanoplatelets present in the precipitate and supernatant, respectively upper and bottom section, show the sources of the different photoluminescence peaks. The population of bigger nanocubes, associated with the emission peak centered at 512 nm, shows a PLE spectrum that perfectly matches the absorption one; on the other hand, the PLE of the supernatant shows that the emission peak centered at 507 nm is exclusively associated with the population of smaller nanocubes, whereas the nanoplatelets trigger the low-intensity emission peaks at 434 nm and 462 nm. It is interesting to notice that the PLE spectrum related to the emission at 462 nm reveals the presence of $n=4$ nanoplatelets, whose typical absorption peak at around 460 nm is

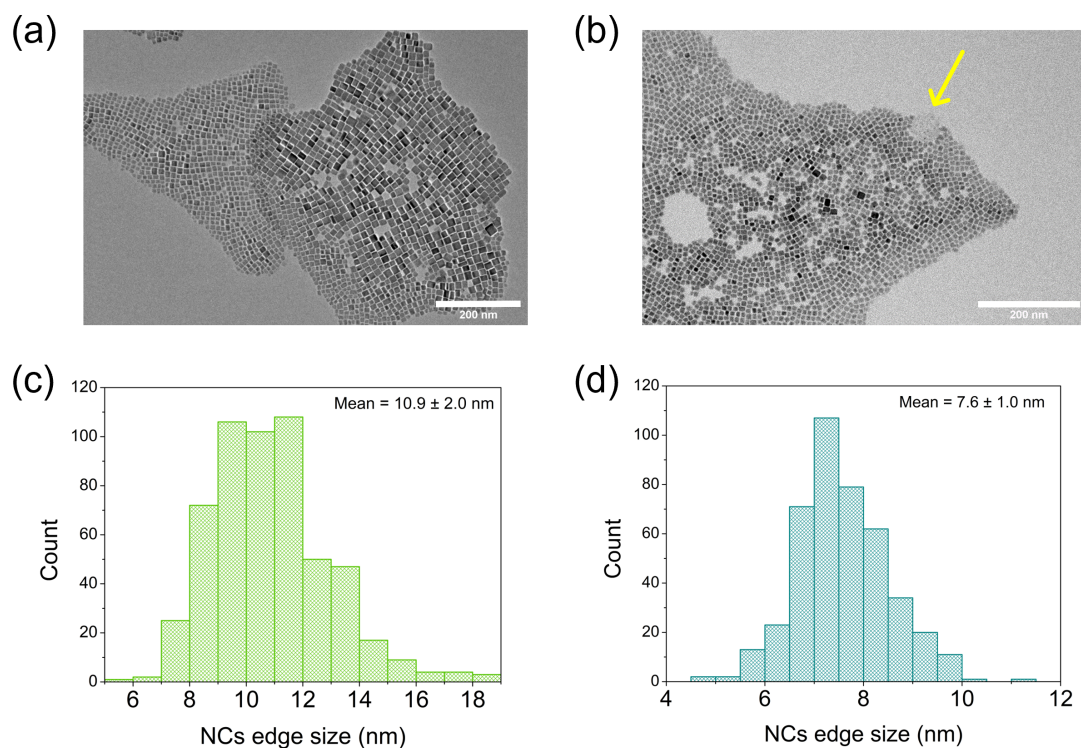


FIGURE 2.20: TEM images of the early OA/OAm-capped CsPbBr_3 colloidal nanocrystals in the precipitate (a) and in the supernatant (b); in the latter, the yellow arrow indicates a nanoplatolet. Scale bar equals 200 nm. Below, the corresponding nanocubes size histograms, respectively (c) and (d).

hidden in the absorption spectrum.

The XRD pattern of the precipitate (Figure 2.19 (c)) identifies the CsPbBr_3 nanostructures as orthorhombic, as well as the one for the supernatant population (Figure 2.19 (d)), which also presents some peaks at repeating intervals of 4.2° , indicated by the pink diamonds, associated with stacking periodicity of the nanoplatolets.

Finally, the TEM images show a polydispersed population of nanocubes for the precipitate (Figure 2.20 (a), (c)) and a monodispersed, smaller-sized one, additioned with the presence of nanoplatolets, in the supernatant (Figure 2.20 (b), (d)).

The systematic presence of both a population of nanocubes and nanoplatolets was solved by finding the good precursors ratios needed to obtain either one or the other, which are shown in Table 2.1, and the good PhCOBr injection temperatures, namely 150°C for cubes and 120°C for platelets.

Moreover, the ethanol initially used as a dispersion de-stabilizer, for precipitating light species via centrifugation, was quickly substituted with other slightly polar organic liquids, such as acetone or ethyl acetate, since ethanol was found to induce the nanoplatolets ripening. Figure 2.21 shows a 30 minutes time sequence of absorption spectra of a

Reactant	Specie	Cubes	Platelets
Cs_2CO_3	Cs^+	1	1
$\text{Pb}(\text{OAc})_2 \cdot 3\text{H}_2\text{O}$	Pb^{2+}	2	8
PhCOBr	Br^-	4	16
OA	OA	6	25
OAm	OAm	6	25

TABLE 2.1: Relative precursors molar ratios needed to selectively obtain either nanocubes or nanoplatelets from the above-described hot injection method.

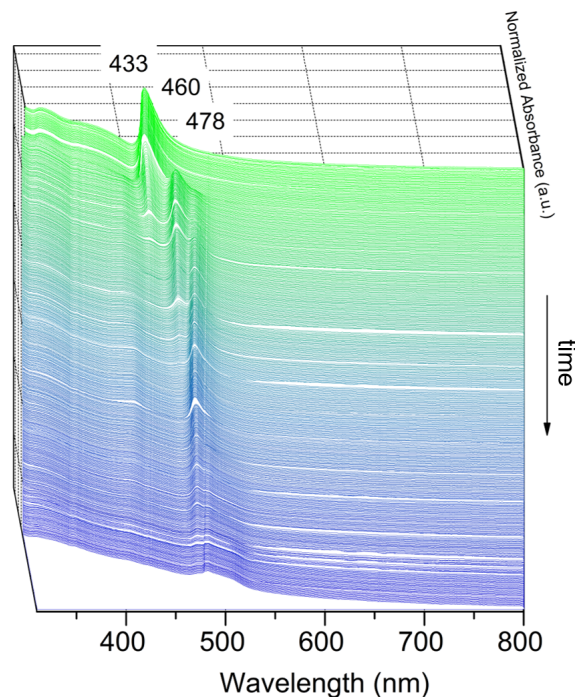


FIGURE 2.21: Absorption spectra following the ripening effect of ethanol on a nanoplatelets population over 30 min.

$n=2,3,4$ platelets sample after the injection of $100 \mu\text{l}$ of ethanol. The thinnest platelets undergo a ripening process, since the $n=2$ and $n=3$ absorption peak slowly disappear, to the benefit of a growing population of mixed $n \geq 3$ nanoplatelets.

An example of two samples consisting of either nanocubes or nanoplatelets obtained as just described is illustrated in Figure 2.22: in the first case, the only absorption feature is the nanocubes excitonic transition at 508 nm , that shifts to 491 nm in the supernatant as already seen, but without the appearance of any nanoplatelet population (Figure 2.22 (a)). The other sample's absorption spectra (Figure 2.22 (b)), on the other hand, show different populations of platelets with different thicknesses, mainly $n=2$ at 431 nm , but with traces of $n=3$ at 457 nm .

The TEM image for this selective nanocubes synthesis protocol (Figure 2.22 (c)) shows a monodispersed population of cubic nanocrystals, whereas the TEM image for the

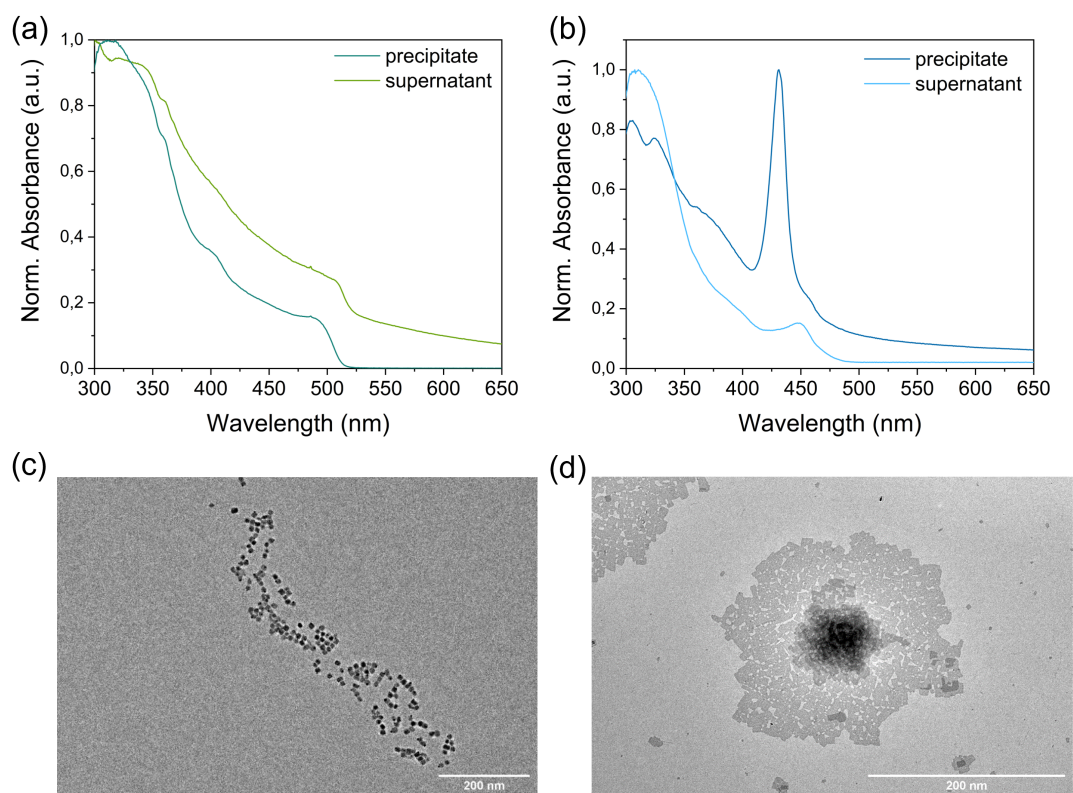


FIGURE 2.22: Characterization of selective nanocubes or nanoplatelets syntheses by absorption spectroscopy, respectively (a) and (b), and the corresponding TEM images of nanocubes (c) and nanoplatelets (d).

nanoplatelets one shows thin and large nanoplatelets, drying in a flat position instead of lateral stacking.

A very different result is obtained by performing the selective nanoplatelets synthesis at very mild condition, namely at a temperature of 30°C and during a relatively long time.

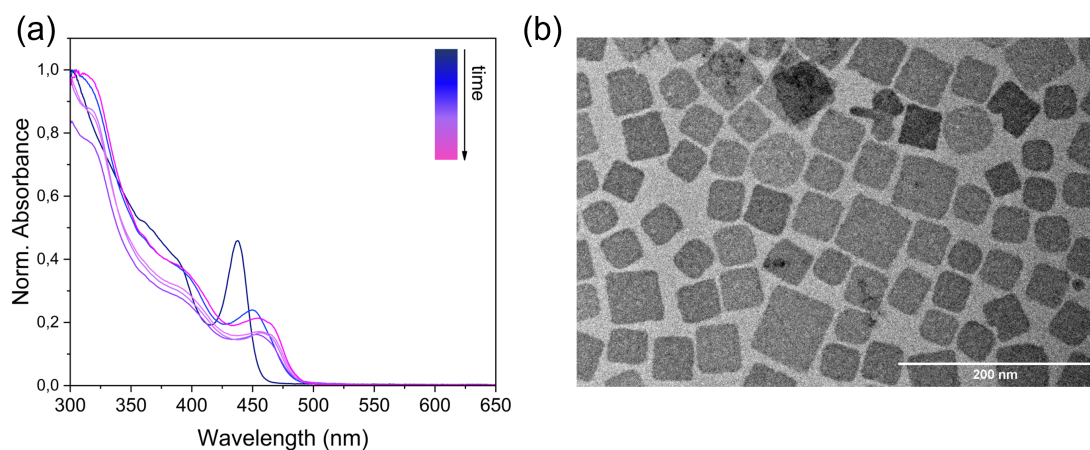


FIGURE 2.23: Characterization of nanoplatelets synthesized under mild conditions by absorption spectroscopy (a) and the corresponding TEM image (b).

The process was followed over time by taking the absorption spectra of small volumes withdrawn from the reaction medium, shown by Figure 2.23 (a). Throughout 30 mins of reaction, the nanoplatelets absorption peak slowly shifts from 437 nm ($n=2$ thickness) to 455 nm ($n=3$) and finally sets as a broad absorption band centered around 460 nm.

The final result is thus a sum of $n \geq 3$ populations, with large lateral dimensions, as shown by the corresponding TEM image (Figure 2.23 (b)).

2.3.3 Soy lecithin-capped nanocrystals synthesis

Another synthetic protocol used in this work aims to the production of soy lecithin-capped CsPbBr₃ nanocrystals, as this molecule has been reported to allow the colloidal stabilization of CsPbBr₃ nanocrystals at concentrations up to 400 mg/ml by Krieg et al.[186]

The soy-lecithin capped CsPbBr₃ nanocrystals were synthesized by scaling-up the procedure described by Krieg et al.: [186] in a 250 mL three-neck flask, Cs-oleate (8 mmol), Pb-oleate (12.5 mmol) and soy lecithin (2.5 mmol) were dissolved in 100 mL of ODE and degassed under vacuum at 50°C for 1h. The flask was then filled with Argon and the temperature raised to 120°C, and 25 mmol of TOP-Br₂ were injected swiftly; the flask was immediately quenched with icy water.

The purification process involves three consecutive centrifugations at 9k RCF for 2 minutes, adding acetone (twice the crude's volume) during the first two and redispersing the precipitate in decreasing amounts of anhydrous toluene.

The colloidal dispersions concentrations were evaluated by using the intrinsic absorption coefficient of CsPbBr₃ nanocrystals described by De Roo et al.[357]

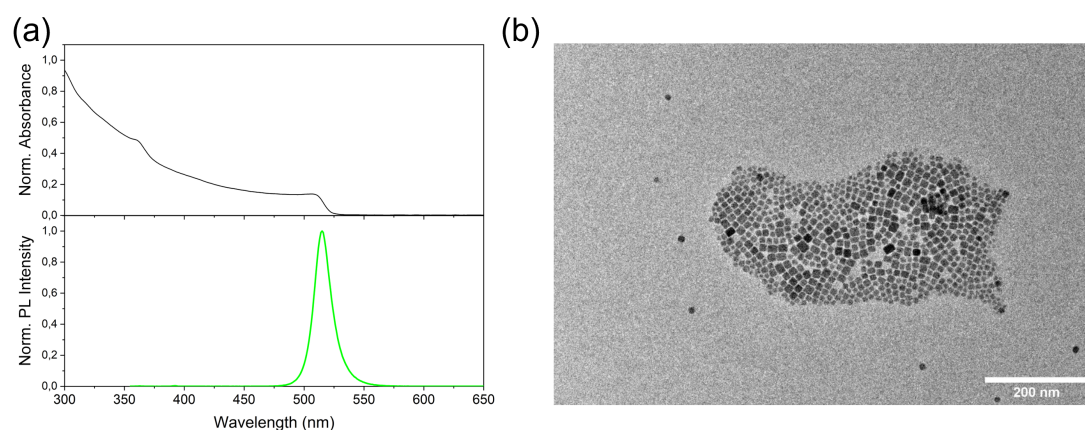


FIGURE 2.24: Typical soy lecithin-capped CsPbBr₃ nanocrystals' absorption and photoluminescence ($\lambda_{\text{exc}} = 365$ nm) spectra (a) and TEM image (b).

A typical sample obtained via this protocol is characterized by the features shown in Figure 2.24: the absorption spectrum (Figure 2.24 (a)) shows the first exciton transition at 509 nm, and the corresponding PL spectrum shows a sharp and bright peak centered at 515 nm. The TEM analysis reports a quite polydispersed range of CsPbBr₃ nanocubes, with an average edge size of 12±3 nm.

2.4 CsPbBr₃/CdS and CsPbBr₃/ZnS heterostructures

Cd-oleate 0.38 M was prepared by dissolving, in a 50 ml three-neck flask, 383 mg of CdO and 3.9 ml OA in 3.9 ml ODE. The mixture was heated at 280°C under Ar flow for 1h, during which the mixture changes color from red to colorless. Finally, the solution was degassed at 110°C for 30 minutes.

Cd-myristate 0.125 M was prepared by dissolving 9.3 g of sodium myristate in 750 ml methanol. The mixture was stirred under Ar atmosphere for 1h, after which a solution of 3.7 g of cadmium nitrate dissolved in 120 ml methanol were added. The white precipitate was filtered through a Buchner funnel and washed with methanol 3 times, and finally dried under vacuum overnight.

S/OAm 1 M was prepared by mixing 96 mg of S in 3 ml OAm during 30 minutes at 85°C.

OAmBr. In a 25 mL three neck round bottom flask, 10 ml OAm and 1 ml HBr are loaded and heated to 80°C under vacuum for 1h under inert Ar atmosphere. The temperature was then raised to 120°C and the mixture was heated for 2h: once the process finished, the mixture, still hot, was transferred in an Ar flushed vial, subsequently sealed with a septum. Once the mixture cooled down, it resulted in a wax-like white-yellow product.

CsPbBr₃/CdS. In a three-neck flask, 69 mg of PbBr₂ were dissolved in 5 ml ODE and then dried under vacuum at 120°C for 1h; the atmosphere was then changed to Ar and 0.5 ml of OAm and 0.5 ml of OA were injected. After complete solubilization, the temperature was raised to 150°C and 0.125 ml of a 0.4 M Cs-oleate solution in ODE were swiftly injected. At this point, 1 ml of Cd-oleate 0.38 M in ODE and 0.4 ml of S 1 M on OAm were mixed in 3.6 ml ODE and then injected dropwise minutes in the CsPbBr₃ dispersion. The latter injection time and the temperature during the injection were varied to study their influence; other tested variants substitutes Cd-oleate with Cd-myristate, used in the same molar quantities, and others change the precursors ratios. After the injection completed, the mixture was allowed to react for another 20 minutes, and finally stopped by cooling it down with icy water. The sample was then collected

by rinsing the flask with 5 ml toluene, and then purified by centrifugation at 10 kRCF for 2 minutes and discarding the supernatant.

CsPbBr₃/ZnS were prepared by synthesising CsPbBr₃ nanocubes 2.45 M in ODE as described in Chapter 2; once the colloidal dispersion formed, 7 μ l of OAmBr were injected, and 5 mg of solid Zn(DDTC)₂ were added. The mixture was sonicated for 5 minutes and then heated at 80°C under vacuum for 30 min, and finally heated at 120°C for another 30 min. The resulting mixture was purified twice by adding a toluene:acetone 1:1 mixture and centrifuging it at 8 kRCF for 10 minutes. Other tested variants change the reaction temperature, time and precursors ratios.

2.5 One-pot synthesis of multiple nanoplatelets populations

In a 50 mL three-neck flask, Cs₂CO₃ (9 mg, 0.05 mmol), Pb(OAc)₂ · 3H₂O (150 mg, 0.4 mmol) and OA (0.4 ml, 1.3 mmol) were dispersed in 15 ml of ODE and then degassed under vacuum for 1h at 120°C. Once the metal oleates-producing reactions were complete, OAm (0.4 ml, 1.2 mmol) was added to the mixture, as its addition at the beginning with the other precursors was found to lead to byproducts formation. Temperature was then set at T=150°C and PhCOBr (0.1 ml, 0.8 mmol) was swiftly injected in the flask, followed by the quick reaction quenching operated by immersing the flask in an icy water bath.

The reaction crude was then retrieved from the flask with the addition of 5 ml toluene, and purified via two cycles of centrifugation at 10 kRCF for 10 minutes.

2.6 2D perovskite nanostructures

Li-(PEA)₂PbBr₄ crystals and film preparation. The syntheses of 2D perovskite nanostructures as either crystals or films, here detailed, were performed by Dr. F. Maddalena (CINTRA UMI CNRS/NTU/THALES). The following protocols were reproduced from Ref.[358] . Dimethyl sulfoxide (DMSO, anhydrous), phenethylammonium bromide ((PEA)Br, 98%), lead bromide (PbBr₂, 98%), and lithium bromide (LiBr, \geq 99%) were purchased from Sigma-Aldrich. Undoped precursor solution was prepared by dissolving equal molar amount of (PEA)Br and PbBr₂ in DMSO under stirring at 100 °C for 2h under N₂. Crystals were obtained by evaporating DMSO from 3M precursor solution in ambient environment slowly; it could take a few weeks. The crystal

precipitate was then washed with diethyl ether and dried under vacuum for future characterizations. For Li-(PEA)₂PbBr₄ crystals, the procedure was the same as that of the undoped one except for the addition of LiBr to the precursor solution. The amount of LiBr depends on the molar ratio between Li and Pb. Here, it should be noted that the ratio is from the precursor instead of the final product. For the film preparation, precursor solution (1:1, 2M concentration for high viscosity) was spin-coated on a UV-ozone treated cover glass substrate with 500 rpm for 60 s (acceleration: 100 rpm per s). In the last 30 s, a heat gun was applied right on top of the film to blow-dry the film with hot air flow. The film was baked at 100 °C on a hot plate for another 20 min.

2.7 Embedding lead halide perovskite nanocrystals in polymeric matrices

Lead halide perovskite nanocrystals were embedded in a polymeric matrix in order to obtain a solid sample suitable for X-ray imaging and to stabilize more efficiently the NCs from oxygen and humidity. For the aims of this work, the choice fell on the zwitterionic polymers described in literature.[184, 185] The CsPbBr₃ were synthesized using sulfobetaine-18 as a matching surface ligand.

CsPbBr₃ nanocrystals synthesis. Cesium-oleate (0.8 mmol), lead-oleate (1 mmol) and sulfobetaine-18 (0.5 mmol) were combined in 50 ml ODE in a 100 ml three-neck flask equipped with a stir bar. The mixture was dried at 120°C under vacuum for 30 min and then placed under nitrogen atmosphere: the temperature was then increased to 180°C and 0.35 mmol of TOP-Br₂ were swiftly injected. The flask was immediately cooled down with an iced water bath.

The reaction crude was then centrifuged at 10k RCF for 20 min, and the precipitate was purified by repeating three times the redispersion in anhydrous toluene, the addition of twice its volume of ethyl acetate and then the centrifugation at 10k RCF for 2 minutes.

Zwitterionic block copolymer. Butyl methacrylate BMA (20 mmol), sulfobetaine methacrylate SBMA (0.62 mmol) and azobisisobutyronitrile AIBN (0.16 mmol) were combined as a solution in 2,2,2-trifluoroethanol TFE (20 ml) in an inert Argon atmosphere glovebox. The container was sealed, removed from the glovebox and then heated at 78 °C for 8h. The resulting solution was cooled to room temperature, precipitated into methanol, and then purified by re-dissolving the precipitate into chloroform and then re-precipitate it into methanol. The colorless precipitate was dried in a rotavapor: once dry, it resulted in 1.71 g of product.

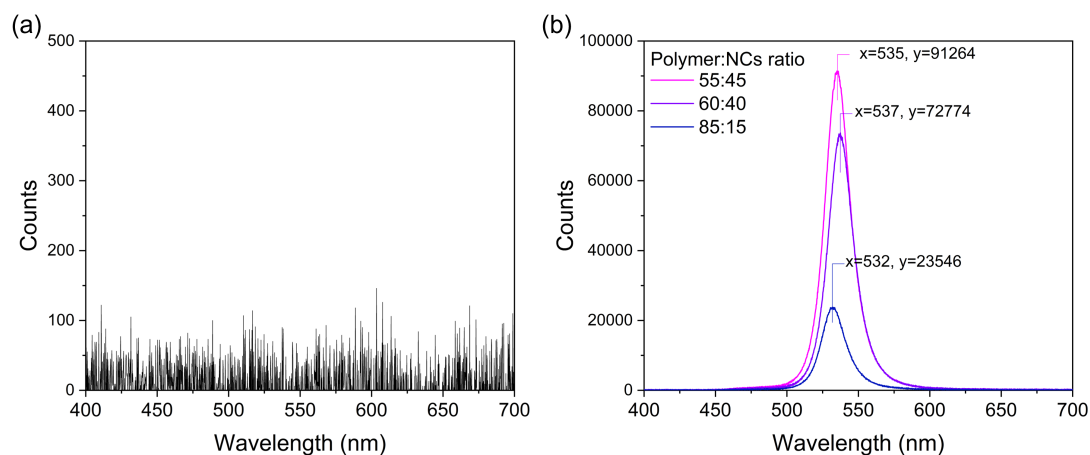


FIGURE 2.25: Radioluminescence spectra of the pure polymer (a) and of the latter loaded with increasing mass percentages of the sulfobetaine-capped CsPbBr₃ (b).

CsPbBr₃ nanocrystals embedded in the zwitterionic block copolymer. An amount of the colloidal sulfobetaine-capped CsPbBr₃ was mixed with a volume of the zwitterionic block copolymer dissolved in chloroform at varying mass ratios and then dried in a teflon mold.

These samples of lead halide perovskite nanocrystals embedded in a zwitterionic block copolymer were characterized for radioluminescence: Figure 2.25 (a) shows that the copolymer alone does not scintillate, which is good news as it means that it will not false the features of the CsPbBr₃ nanocrystals. On the other hand, the radioluminescence spectra of the NCs-loaded polymeric samples show relative intensities which are consistent with the amount of CsPbBr₃ nanocrystals loaded in the three samples.

Conclusions







This chapter detailed the aspects closely related to the experimental work, thus illustrating the characterization techniques first, and then detailing the main lead halide perovskite nanocrystals synthesis approaches and the mechanisms explaining the involved nucleation and growth processes.

For this work's purposes, lead halide perovskite nanocrystals were mainly synthesized via different hot-injection approaches, chosen as facile methods able to produce well controlled populations of nanocrystals and in rather high amounts. In particular, the work was driven by the need of mastering the synthesis of selective populations of nanocrystals, either in 3D or 2D structures, in order to avoid to add yield-lowering separation and purification steps. With this purpose, the classic synthesis of OA/OAm-capped

CsPbBr₃ nanocrystals was optimized until finding the optimal molar ratios between the precursors needed to selectively obtain either 3D nanocubes or 2D nanoplatelets.

Also, a great focus was concentrated on the production of highly colloidally stable nanocrystals dispersions, through the careful choice of the stabilizing ligand. For this purpose, soy lecithin was chosen as the most performing stabilizing agent, on the basis of its strong binding to the nanocrystals surfaces thanks to its zwitterionic nature, and of its high steric hindrance.

Key points

-  Lead halide perovskite nanocrystals are characterized via optical spectroscopy, typically **UV/Vis absorption**, **photoluminescence** and its **quantum yield** as well as its **decay time**. Moreover, the scintillation features are evaluated through **radioluminescence** and its **decay time** features. Other structural characterizations involve the **XRD diffraction**, and **TEM imaging**.
-  These nanostructures **nucleation** is described by the classical **Gibbs-Thomson model**, and their **growth** by different models, such as **Lamer mechanism** and **Ostwald ripening**.
-  The most used synthetic protocols for CsPbBr₃ nanocrystals are the **hot injection** and **ligand-assisted reprecipitation** methods.
-  In this work, the used hot-injection protocols were chosen on the basis of the reaction mechanism: namely, **highly reactive compounds** were chosen as the reaction trigger, in order to obtain a reproducible protocol, giving pure products and rather monodisperse nanocrystals size distributions.
-  **Selective syntheses** of either nanocubes or nanoplatelets were obtained by optimizing the molar ratios between the precursors.
-  Optimal colloidal stability was achieved by choosing a hindered, zwitterionic molecule, thus **soy lecithin**, as the **surface stabilizing ligand** when highly concentrated nanocrystals colloidal dispersions were needed.

Chapter 3

Energy deposition in perovskite nanocrystals liquid scintillators

As introduced in Chapter 1, liquid scintillation-based technology is a less explored technique compared to the more traditional solid state approaches, even though techniques utilizing liquid scintillation counters can be used to determine the activity of alpha-, beta- and gamma-emitters;[\[285\]](#) moreover, the great sensitivity of such systems make them a favorite choice in the detection of very low gamma-emitters such as tritium ^3H .[\[293, 294, 359\]](#) Additionally, these liquid mixtures show excellent damage resistance, fast decay time, low cost and exceptional scalability.[\[286–289, 291\]](#) These advantages make them find large application for daily life analytical tests, as radioactivity level measurements for environmental, medical and security purposes,[\[294–299\]](#) and in the study of biochemical reactions mechanisms by radioisotopic labelling;[\[300, 301\]](#) also, they are used in huge international experiments for β -emissions and neutrino detection, such as XENON1T, KamLAND, Daya Bay, and RENO.[\[291, 304–306\]](#)

However, the organic composition of these systems, and consequently their low effective atomic number Z_{eff} , give them a very low density: as already stated, though, the latter is an important parameter for a scintillating material, since it is correlated with the material's stopping power, thus its effectiveness in interacting with the ionizing radiation and consequently its scintillation yield. All things considered, organic liquid scintillating cocktails (LSC) make a great compromise for the above-mentioned analytical applications, where their high sensitivity, scalability and fast time response overcome the moderate stopping power drawback.

The current and well established technique is based on the interplay between the different components of an organic liquid scintillation cocktail, in which each organic substance plays a role in the scintillation mechanism: as described in Chapter 1, the analyte is

directly dissolved in the mixture, and the outcoming radiation is collected by the most abundant component, by definition the solvent. The latter then transfers its excitation energy, through non-radiative interaction, to a dye, which in turn emits light: this emission is absorbed by another dye, called a wavelength shifter, which re-emits the energy in the form of a longer wavelength radiation, allowing the overall outcoming light to optimally match the detection efficiency of the instrument's detector. Additionally, some stabilizers are needed to keep the components stable in solution; however, the need of all these organic components entails the exposure of the system to light losses risks, and can result in an overall process slowdown. In conclusion, it appears clear how, by reducing the amount of components needed, simplifying these systems would benefit their efficiency.

In this context, halide perovskite nanocrystals recently started to arise interest in the liquid scintillation field, again owing to their bright and tuneable light emissions, their fast decay time and high effective atomic number: nevertheless, despite the great amount of studies around nanoscintillators for other applications like medical imaging, their utilisation as substitutes for organic molecules is a yet unexplored research field. In fact, in this context they had been mainly tested as wavelength shifters,[30–33, 360] thus the last light emitter in the energy transfers chain, still leaving the role of the primary light emitter to organic dyes. A recent exception is represented by the work presented by Lian et al,[361] who obtained colloidal perovskite-mediated aqueous-based liquid scintillators with a light yield as high as 8037 and 3058 photons/MeV at °C and 30°C, respectively, which outperformed typical aqueous-based liquid scintillators composed of 10% PPO/linear alkylbenzene in water (only 585 photons/MeV).[362] Nevertheless, these systems lack of a more fundamental comprehension of the deposition mechanisms in such colloidal dispersions, which would though be highly beneficial for the understanding of each component's role and, consequently, the optimization of the system.

Therefore, the way that colloidal CsPbBr₃ NCs behave as radioluminescence emitters in a liquid organic medium still needed to be studied: in particular, the excitation mechanism of the nanoparticles was not straightforward to predict, since both a direct excitation from the radioactive source and an energy transfer from the solvent could be plausible. In the first case, light would be emitted only when the ionizing radiation coming from the radioactive source impacts a nanocrystal, implying that the light emission intensity would be highly dependent on the NCs concentration in the colloidal dispersion; otherwise, if the mechanism involves an energy transfer from the excited solvent as it happens in organic mixtures, the overall efficiency would be less impacted by the NCs concentration, since the first energy collector would be the solvent, thus the major component of the solution.

Another interest of this study comes from the fact that an efficient light-emission process and a high lead halide perovskite nanocrystals loading ratio would offer an alternative in the liquid scintillation field, with a much increased stopping power compared to the traditionally used LSC: this would be highly beneficial, as it would offer systems with higher scintillation yields, and also involving fewer components, thus fewer energy transfers steps needed for the overall light production process, which can result in longer time responses.

Finally, an additional part of the following study covers some attempts to make lead halide perovskite nanocrystals chemically stable in water, in order to offer a well performing liquid scintillator compatible with water-based samples, without the need of adding any surfactants. In fact, as it will better described in the dedicated section, many analytical applications of LSC involve water-based samples, and the only way to disperse them in traditional organic liquid scintillators is by the addition of high amounts of surfactants. Nevertheless, this can lead to detection and reproducibility issues, which thus explain the interest of developing water-based stable CsPbBr₃ liquid scintillators.

Summarizing, this work aims to explore the potential of CsPbBr₃ as liquid scintillators, by studying the excitation mechanism of such nanoparticles in an organic solvent medium and the possibilities of making them stable in water.

3.1 Energy deposition possible pathways

The first aspect that needs to be addressed involves the light emitting process occurring in the liquid medium when the light emitting specie is a CsPbBr₃ perovskite nanocrystal. As a matter of fact, two options are likely to describe the system: either an energy transfer chain, or a direct excitation of the dispersed nanocrystals by the radioactive source (Figure 3.1).

The first case would reproduce the processes involved in traditional organic liquid scintillators, as discussed in Chapter 1: the ionizing radiation emitted by the source interacts with the solvent, i.e. the most abundant component of the dispersion, and then the resulting excited solvent molecule would go back to its ground state by transferring its excess energy to an acceptor, in this case the dispersed nanocrystals; the latter would then emit light as a result of their own de-excitation process.

Compared to an organic dye in traditional organic scintillating cocktails, one of the main differences is that perovskite nanocrystals have good scintillation features themselves, as a result of their high Z_{eff} and of their electronic structure. Consequently, even a direct interaction between the ionizing radiation and a nanocrystal, not mediated by

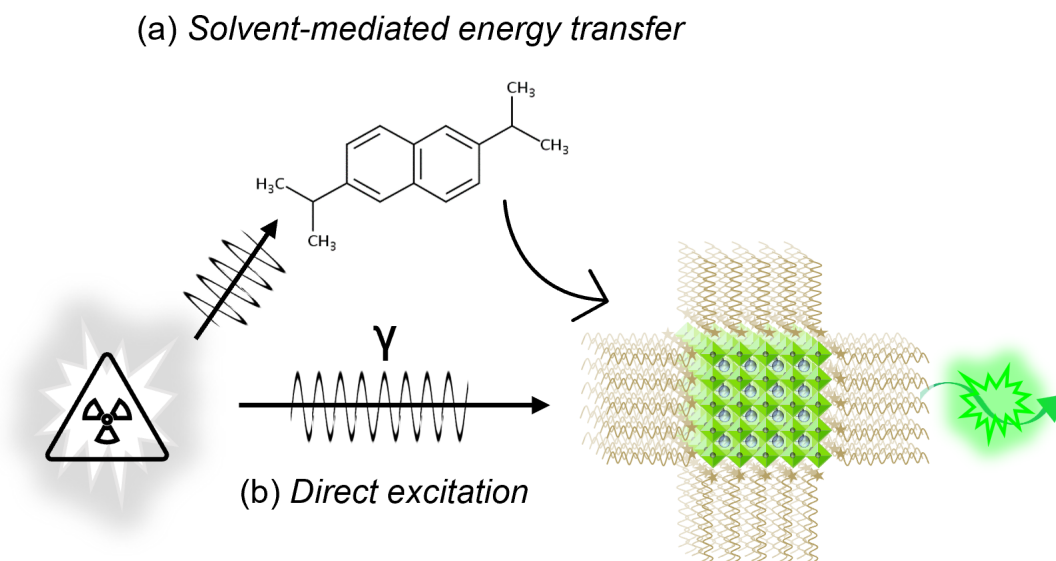


FIGURE 3.1: Scheme of the two main possible excitation pathways for a perovskite nanocrystal dispersed in an organic solvent: a solvent-mediated energy transfer, reproducing the scheme describing organic liquid scintillating cocktails (a), and direct excitation of the dispersed nanocrystals by the radioactive source (b).

the solvent, can result in the emission of photons; moreover, the interaction between the organic solvent and the ligand-capped inorganic nanocrystals, in terms of geometry and steric hindrance, and consequently the probability of energy transfers from one to another, is not straightforward to predict. Therefore, scintillation coming from the direct excitation of the lead halide perovskite nanocrystals is also a possibility.

The following study will be then focused on the understanding of the scintillation mechanism in these systems, after a preliminary optimization of such CsPbBr_3 nanocrystals in terms of colloidal stability and surface quality.

3.2 Sample quality optimization

The evaluation of the performances of colloidal CsPbBr_3 nanocrystals as liquid scintillators was preceded by an optimization of the NCs optical features. Therefore, the attention was first focused on the colloidal stability at high concentration, needed in order to increase the amount of active matter in the dispersion and thus the probability of radioluminescence emission; then, the surface quality was optimized, which is important since the presence of surface defects impacts both the photoluminescence quantum yield PLQY and the luminescence decay time.

At the same time, it is important to recall that these nanostructures suffer from a short Stokes shift, as described in Chapter 1, meaning that their emission spectra highly

overlap with the absorption ones, and thus a high loading comes with a severe increase of self-absorption of the emitted light, entailing both a reduction and a possible slowdown of the light emission. Since the amount of steps involved in traditional liquid scintillation is considered as a drawback, this work is focused on the improvement of lead halide perovskite nanocrystals performances alone, without having to add any stabilizer nor wavelength shifter.

This means that, without a wavelength shifter in the lead halide perovskite nanocrystals colloidal dispersions, a compromise concentration value has to be found in order to increase the quantity of active matter as much as possible while preserving a maximum of the light emission; moreover, some chemical approaches can be used in order to improve the surface quality, which not only enhances the photoluminescence quantum yields, but also improves the light emission time response.

Finally, two factors which have to be taken into account in order to get good signal detection are the light production and collection: for the former, the samples must exhibit high PLQYs, high intrinsic scintillation yields and, depending on the NCs excitation mechanism, an efficient solvent-to-nanoparticles energy transfer, where the nanocrystals stabilizing ligands would play a crucial role.

The optimization of the above-mentioned parameters will be discussed in the following sections.

3.2.1 Colloidal stability

Colloidal stability is a crucial parameter when it comes to the study of colloidal dispersions as liquid scintillators, especially in terms of the understanding of the light emission process: a stable colloid would allow the evaluation of the radioluminescence features as a function of the concentration, which would give access to interesting information. In particular, the issue of the short Stokes shift of these nanomaterials, which has been discussed in Chapter 1, is a central problem when it comes to high concentrations: in this case the emitted photons are more likely going to stay trapped, re-absorbed by the sample, than to escape it and reach the detectors. Thus, the possibility of working with increasingly concentrated stable samples would allow to study this self-absorption phenomenon and to optimize the system, in order to minimize it.

Moreover, whether the light emission is caused by a direct excitation of the nanocrystals or by energy transfers from the medium would change the system's response as a function of the nanocrystals concentration. In fact, in the first case the relationship is expected to be linear, whereas in the case of energy transfers it would not, since



FIGURE 3.2: Picture showing the deposition of a precipitate in a typical micromolar oleylammonium-capped CsPbBr₃ colloidal dispersion.

the light collector would be the solvent: therefore, the energy transfer probability may have a complex dependence on the separation distance between the primary interaction and the nanoparticle. Thus, having increasingly concentrated stable samples would also be a key to study the light emission mechanism of colloidal lead halide perovskite nanocrystals dispersed in a solvent.

Additionally, this need for colloidal stability also meets a technical requirement, as the Triple to Double Coincidence Ratio measurements, that were used to evaluate the systems' scintillation performances, can last for a day or more. It is thus clearly crucial to work with samples maintaining their stability for the entire duration of the performed experiments.

In this respect, the classic oleylammonium-capped perovskite nanocrystals fail to satisfy the colloidal stability needs, since typically the obtained dispersions are unstable even at low concentration, as shown in Figure 3.2.

The improvement of colloidal stability is achievable by choosing the optimal synthetic protocol, since both the stabilizing ligand choice and the size of the nanocrystals have a crucial impact on the highest concentrations that can be achieved.

Soy lecithin, a zwitterionic capping ligand whose structure is shown in Figure 3.3(a), has been shown to allow the synthesis of colloidally stable dispersions even at concentrations as high as 400 mg/mL (Figure 3.3 (b)).^[186] As discussed in Chapter 1, a zwitterion, i.e. a chemical specie presenting multiple localized charges on its structure, but which is globally neutral, can be a good stabilizing ligand to lead halide perovskite nanocrystals as the positively and negatively charged ends can interact with different components of the nanocrystals surface, acting like a bidentate ligand, whose bond is more entropically stable than a monodentate one.

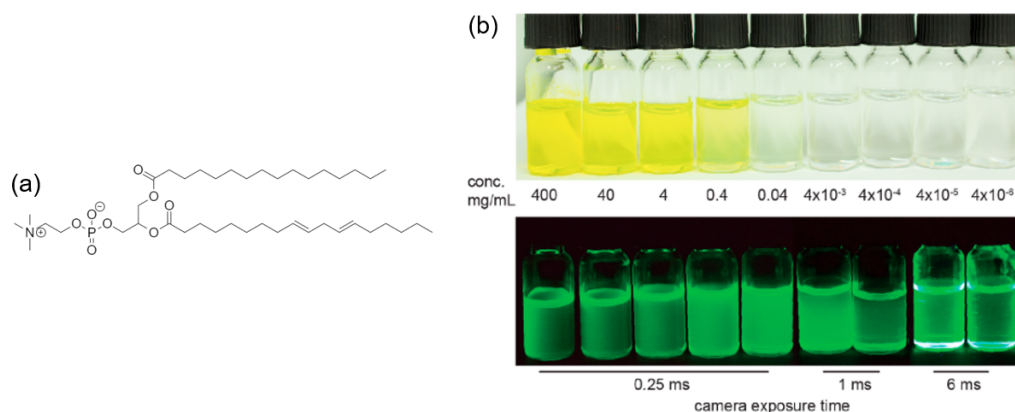


FIGURE 3.3: Soy lecithin's molecular structure (a) and vials containing lecithin-covered CsPbBr₃ nanocrystals of about 8 nm at various concentrations (indicated on the figure) under day light and UV light, respectively, from the work of Krieg et al.[186] (b).

These considerations led to the choice of working with soy lecithin-capped CsPbBr₃ nanocrystals : such colloidal stability will allow to evaluate the nanocrystals performances at different concentrations in order to evaluate their efficiency, the self-absorption influence and to study the light emission mechanism.

3.2.2 Size selection

A parameter that was worth exploring is these nanocrystals average size, since it can impact their optical features: as discussed in Chapter 1, lead halide perovskite nanocrystals are described as in a weak confinement regime, thus meaning that the quantum-size effect of their excitonic features has less impact than the Coulomb interaction between the electron and hole. Therefore, even though decreasing these structures dimensions only induces slight changes in their electronic structure, it is important to assess every parameter that may have an impact, thus also the average size of the nanocrystals and the dispersion of their size distributions.

In order to evaluate the nanocrystals dimensions effect without risking to introduce other variable factors, as it could happen by independently synthesize several individual nanocrystals samples of different average dimensions, just one polydispersed sample was synthesized, and different size selection were extracted from it.

The different fractions were isolated via selective precipitation by centrifugation, as illustrated in Figure 3.4 (a). First, 10 mL of the pristine sample, added with 10 mL of anhydrous acetone (as a dispersion de-stabilizer), were centrifuged at 10k RCF for 10 min: the supernatant, containing the smallest fraction of nanocrystals that managed to remain stably dispersed in the liquid medium, was then added with 15 more mL of anhydrous acetone and centrifuged again at 10k RCF overnight, in order to precipitate

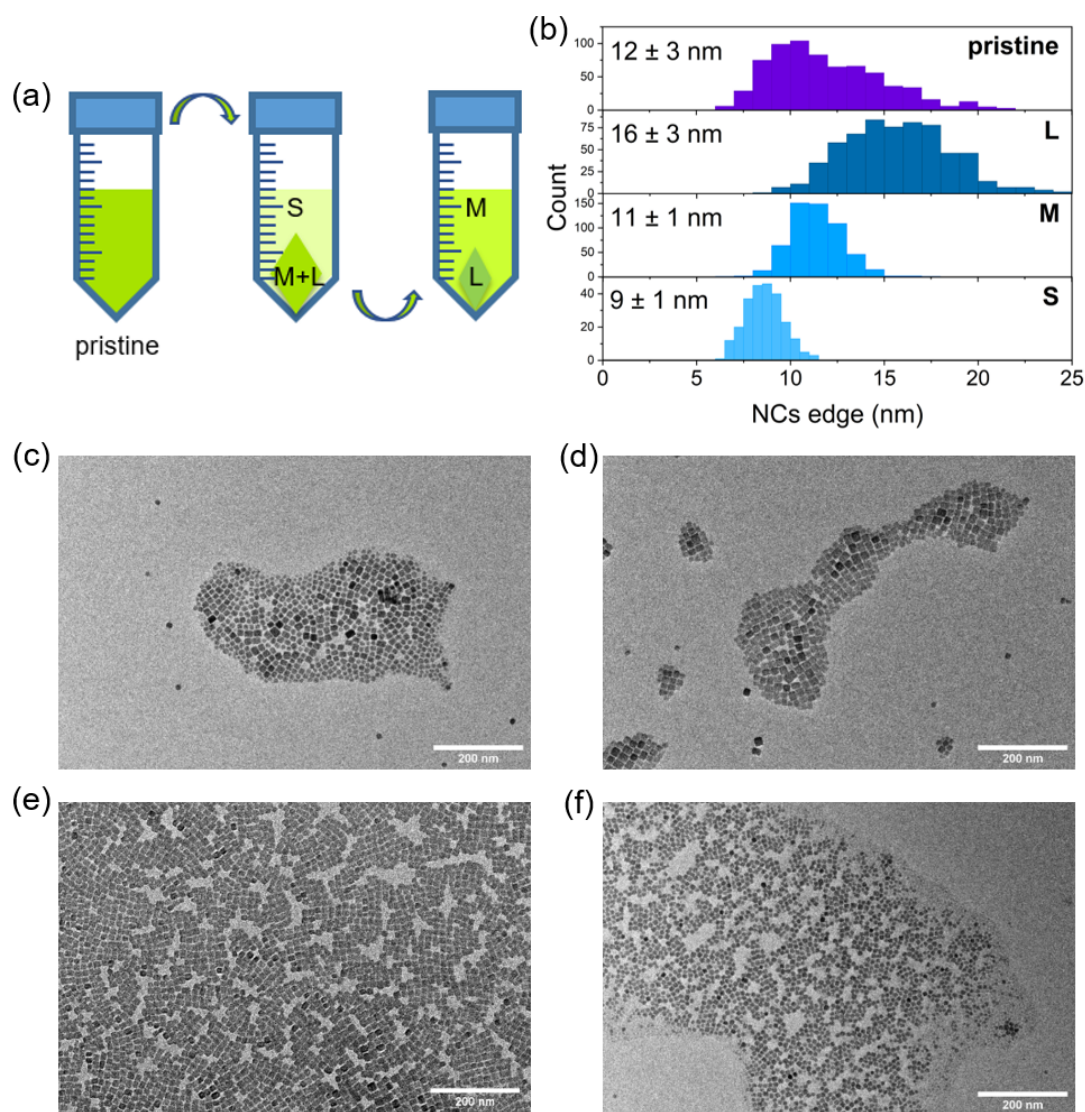


FIGURE 3.4: Illustration of the selective precipitation by subsequent centrifugations (a) and histogram of the obtained selected sizes (b); TEM images of the pristine sample (c) and of the selected fractions, the largest (d), the medium (e) and the smallest (f). Scale bar equals 200 nm.

this smallest NCs fraction. The precipitate from the very first centrifugation, containing bigger NCs, was then redispersed in 10 mL of toluene and centrifuged at 10k RCF for 30 minutes: the resulting supernatant contained the medium-sized nanocrystals, whereas the precipitate contained the biggest ones.

Figure 3.4 shows the comparison observed with the TEM between the pristine sample, polydisperse, and the size fractions obtained by selective precipitation: while the pristine sample's nanocrystals have an average edge of 12 ± 3 nm, the largest, medium and smallest obtained fractions' ones measure 16 ± 3 , 11 ± 1 and 9 ± 1 nm respectively.

With regards to their optical properties in solution (Figure 3.5 (a)), these fractions'

absorbance and fluorescence features slightly change according to the size decrease, with a -3 nm blue shift from L to S sample for both the first exciton's absorption peak and the fluorescence emission's maximum, consistently with the quantum confinement effect. The same shift is observed in the photoluminescence of the nanocrystals dried on a Si wafer, with the addition of a second emission band around 535 nm that is observed in both the pristine sample and in the M-size selection; similarly, the radioluminescence spectra are centered around 535 nm for these two samples, whereas the S-size is blue-shifted around 525 nm and the L-size shows both the emission bands. As these lower energy bands are observed only in the dried samples (Figure 3.5 (b)), and not in solution (Figure 3.5 (a), bottom), it is possible that they result from nanocrystals collective emissions, due to their self-assemblies;[110] this effect could be enhanced under X-ray excitation, due to the latter higher penetrability, leading to the higher intensity of the lower energy emission bands for radioluminescence compared to photoluminescence (Figure 3.5 (b)).

The XRD patterns, in Figure 3.6 (a), evidence the size decrease as well, with a +47% enlargement of the peaks for the small-size sample compared to the large-size one, which matches the same 47% difference in the nanocrystals dimensions obtained from the TEM images. Finally, the scintillation decay times at this stage do not show remarkable changes following the size selection (Figure 3.6 (b)).

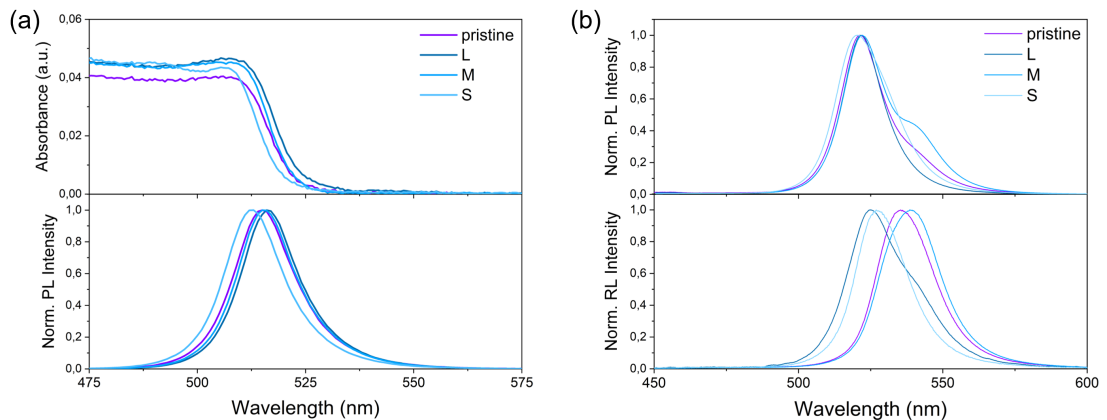


FIGURE 3.5: Characterization of the pristine sample and the size fractions extracted from it: the optical absorption at the first exciton and the photoluminescence spectra of the samples dispersed in DIPN at an excitation wavelength of 365 nm (a) and the photoluminescence ($\lambda_{\text{exc}} = 405$ nm) and radioluminescence (excitation at 20 kV, 30 mA) spectra (b) of ~ 80 nm thick samples dried on silicon wafers.

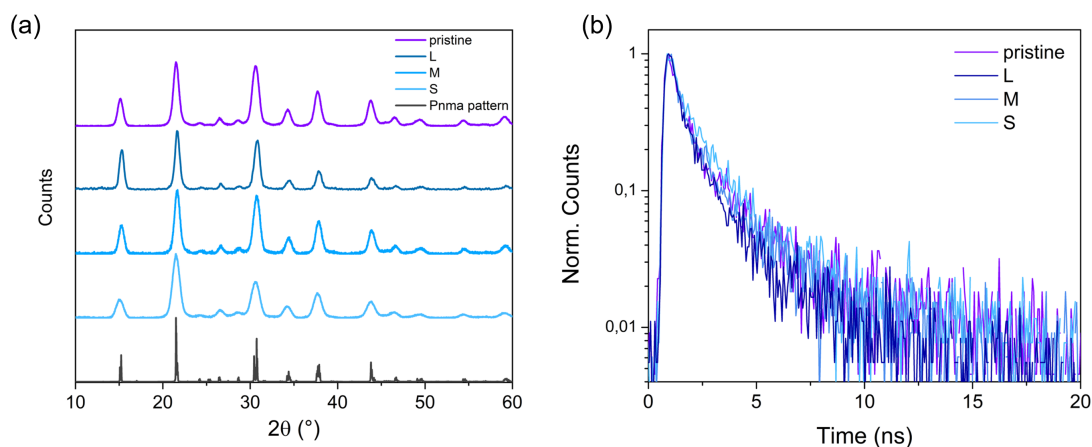


FIGURE 3.6: The XRD patterns of the pristine sample and the size fractions compared to the orthorhombic reference pattern (a), and the radioluminescence decay time under X rays (20 kV) (b) of ~ 80 nm thick samples dried on silicon wafers.

3.2.3 Photoluminescence quantum yield-improving surface treatments

As previously stated, the great advantage of using soy lecithin as the stabilizing ligand, a long and quite bulky zwitterionic molecule that strongly binds to the NCs surfaces, is that it allows to obtain colloiddally stable dispersions, crucial factor for increasing the nanoparticles loading in the liquid mixture. On the other hand, such a big and bulky molecule can inhibit the eventual energy transfers from the excited organic solvent to the NCs during the liquid scintillation process. Moreover, the obtained colloidal dispersions show photoluminescence quantum yields which do not exceed 50%, which is an important issue in terms of light emission efficiency.

This light emission efficiency can be mainly caused by surface defects, such as vacancies, adatoms or clusters (Figure 3.7), which can be repaired by surface treatments.[174, 363] Typically, different functional groups can be used depending on the surface defect nature:

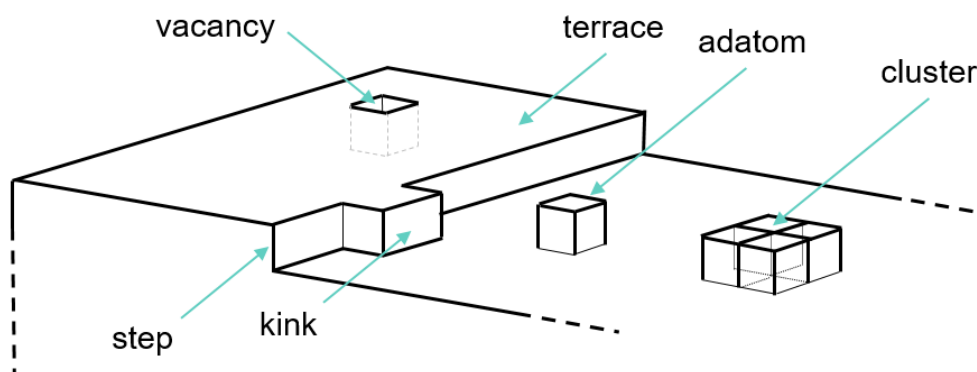


FIGURE 3.7: Illustration of the main possible defects that can be found on the surface of a nanomaterial.

for example, in literature ammonium bromides are shown to interact with both lead and bromide vacancies,[208, 223, 277, 364], and carboxylic acids are shown to have affinity for lead adatoms and nanoclusters.[365]

Consequently, different kinds of organic molecules were tested in this work for surface treatment experiments, with the aim of repairing the surface defects that impact the soy lecithin-capped CsPbBr₃ nanocrystals PLQY. A second possible benefit of these surface treatments depend on both the energy deposition mechanism describing the scintillation process and on the way the added chemicals interact with the nanocrystals surface: as a matter of fact, if the light emission mechanism reproduces the traditional organic LSC energy transfers, and if the added chemical stays bound to the nanocrystals surface, then it is possible that this new ligand improves the energy transfer from the solvent. This is conceivable for two main reasons, one being the shorter and less bulky structure of the used chemical with respect to soy lecithin, which may allow the solvent to come closer to the nanocrystal, with the distance being a crucial factor for non-radiative energy transfers.[366–368] The second reason applies to surface treatments involving conjugated species, since with their presence on the nanocrystals surfaces, their delocalized electrons could take part in such energy transfer from the outer solvent molecule to the inner CsPbBr₃ nanoparticle.

These surface treatments were typically performed by mixing under ambient conditions the original soy-lecithin capped nanocrystals dispersions with adjusted amounts of the chemical, exploring increasing chemical-to-lecithin ratios. The mixtures were then stored at ambient conditions.

Figure 3.8 shows the list of tested molecules, and includes different kinds of organic systems containing various functional groups. It begins with ammonium bromides, that

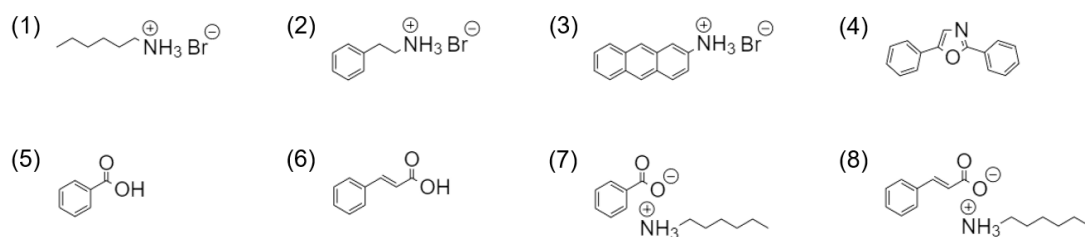


FIGURE 3.8: List of the chemicals tested as a surface treatment: hexylammonium bromide (1), phenethylammonium bromide (2), 2-aminoanthracene bromide (3), 2,5-diphenyloxazole (4), benzoic acid (5), cinnamic acid (6), hexylammonium benzoate (7) and hexylammonium cinnamate (8).

can interact with lead and bromide vacancies,[208, 223, 277, 364] here functionalizing either an alkyl chain, a non conjugated alkyl-phenyl group or a conjugated aromatic system: first, hexylammonium bromide (C_6AmBr) and phenethylammonium bromide (PEABr), respectively Figure 3.8 (1) and (2), were chosen as examples of non-conjugated ammonium bromide salts, with the latter also containing a phenyl group, and 2-aminoanthracene bromide (2-AABr), in Figure 3.8 (3), was chosen as a conjugated aromatic homologous. Moving forward, the other selected molecules are conjugated systems: as already mentioned, this feature, involving electronic wavefunctions which are delocalized over the whole structure, was thought to possibly be more efficient for coupling the $CsPbBr_3$ nanocrystals with the organic solvent in case of non-radiative energy transfers. Therefore, among the other tested species, 2,5-diphenyloxazole (PPO) (Figure 3.8 (4)) was tested since it is a commonly used dye in traditional liquid scintillators, that also emits in the $CsPbBr_3$ absorption range;[369] afterwards, carboxylic acids, as benzoic acid (BzA) and cinnamic acid (CynA), respectively Figure 3.8 (5) and (6), were tested as surface treatments since they have been reported to have affinity for lead adatoms and nanoclusters.[365] Finally, in order to study a double approach, these two last carboxylic acids were mixed with hexylamine in order to obtain hexylammonium benzoate (HAB) and cinnamate (HAC), respectively Figure 3.8 (7) and (8), aiming to test if the two charges would both cooperate in binding to the nanocrystals surface.

Starting from the optical features, Figure 3.9 shows the influence of the different kinds of tested chemical functions on the photoluminescence quantum yield PLQY. The results were split in two graphs in order highlight different features: firstly, Figure 3.9 (a) includes treatments that didn't bring any remarkable or stable improvement of the PLQY, like 2-aminoanthracene bromide, cinnamic acid and PPO. The curve obtained from the use of hexylammonium bromide would have been considered as a good result, but unfortunately the such-treated colloidal nanocrystals undergo a severe chemical degradation, resulting in their complete dissolution and loss of optical features within some minute. This degradation is attributed to the complexing action of the terminal ammonium group towards $[PbBr_6]^{4-}$ units. The graph also contains the curve corresponding to hexylammonium cinnamate, which actually provides a good PLQY improvement as a function of its addition to the mixture, however the choice fell on pursuing the next phase of experiments with its homologous hexylammonium benzoate, its effect looking more promising, as shown below.

Figure 3.9 (b) shows the PLQY modification as a function of the addition of increasing amounts of phenethylammonium bromide, benzoic acid and hexylammonium benzoate. Phenylethylammonium bromide brings interesting results, as the PLQY increase until a value of $64 \pm 18\%$, at a reactant-to-soy lecithin ratio at which the other treatments are either ineffective or destructive to the $CsPbBr_3$ nanocrystals chemical stability. The

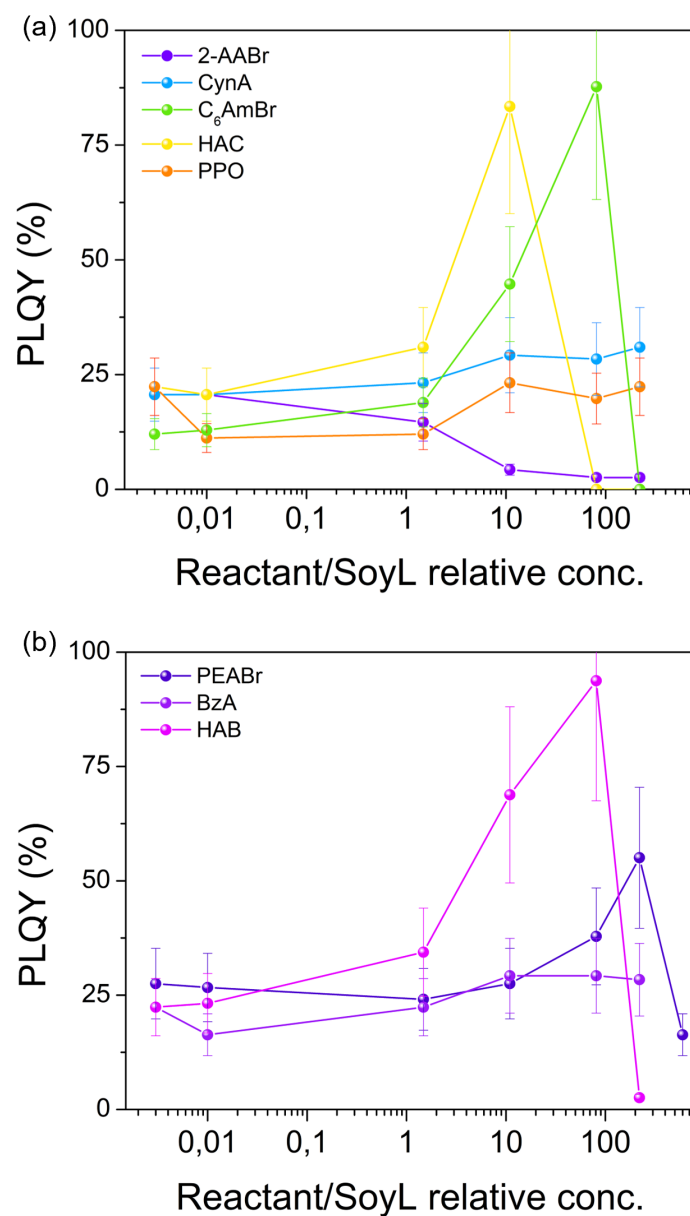


FIGURE 3.9: Comprehensive results of the surface chemical treatments on soy lecithin-capped CsPbBr₃ nanocrystals in terms of PLQY ($\lambda_{\text{exc}} = 365 \text{ nm}$) as a function of the reactant-to-soy lecithin molar ratio: the effect of 2-aminoanthracene bromide (2-AABr), cinnamic acid (CynA), hexylammonium bromide (C₆AmBr), hexylammonium cinnamate (HAC) and 2,5-diphenyloxazole (PPO) (a); below, phenylethylammonium bromide (PEABr), benzoic acid (BzA) and hexylammonium benzoate (HAB) (b).

treatment with hexylammonium benzoate, then, shows a very good PLQY increment, reaching $94 \pm 26\%$ at a reactant-to-soy lecithin molar ratio of 80, whereas its corresponding simple carboxylic acid has almost no effect. This observation strengthens the idea that coupling ammonium and carboxylate function is beneficial, since in this case the PLQY reaches good values without completely dissolving the CsPbBr₃ nanocrystals, as it was instead the case for hexylammonium bromide: an ammonium salt was then considered more efficient in this case for repairing the NCs surface defects, by stabilizing

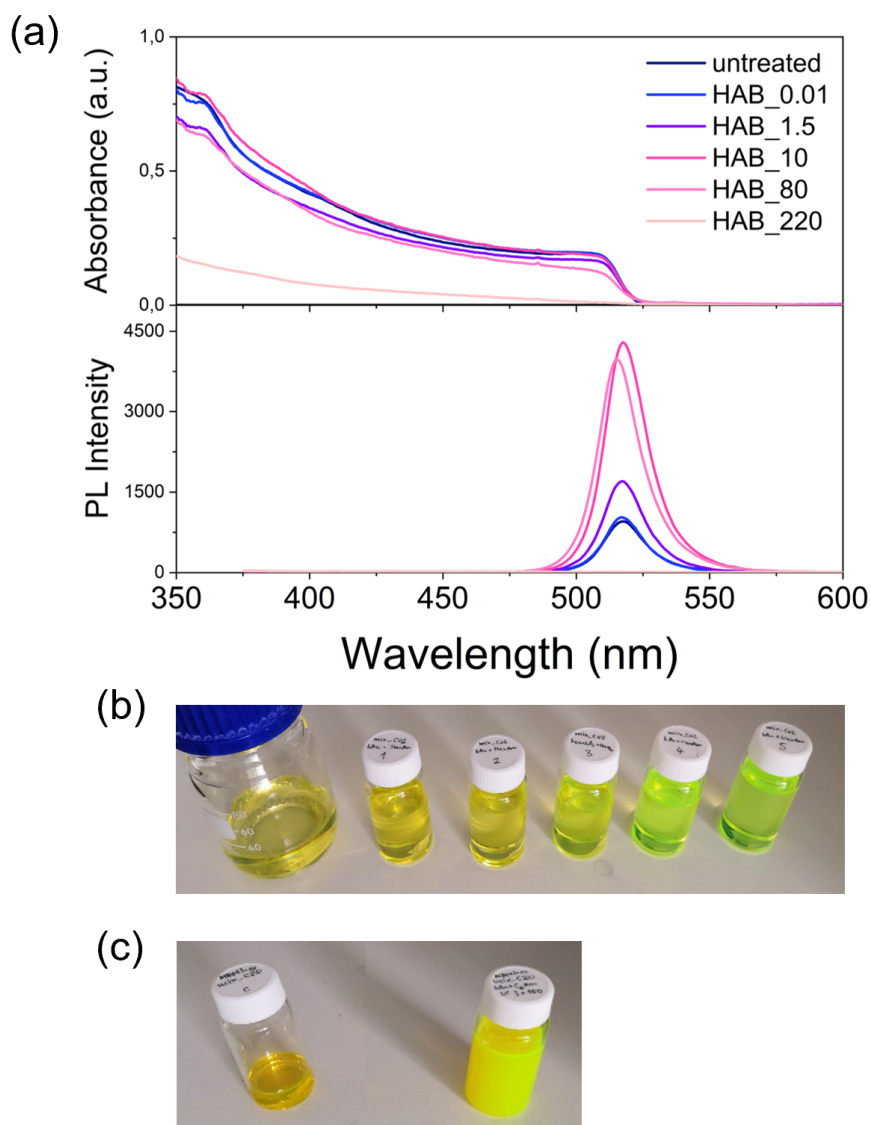


FIGURE 3.10: The absorption and photoluminescence spectra obtained by treating soy lecithin-capped CsPbBr₃ nanocrystals with increasing amounts of hexylammonium benzoate (a), and the pictures of the untreated and increasingly treated colloidal samples under natural sunlight at a concentration of 0.056 mg/ml (b) and 5.6 mg/ml (c).

bromide and lead vacancies. Therefore, the test that was considered the most successful and thus promising for the following experimental studies is the hexylammonium benzoate one.

Looking at the optical features of the samples treated with hexylammonium benzoate, it becomes again apparent that an excessive amount of the reactant can cause chemical degradation of the CsPbBr₃ samples: Figure 3.10 (a) shows that the absorption and photoluminescence spectra of the treated samples reach the best preservation of the absorption's shape and intensity and the maximum PL intensity for the sample treated with a hexylammonium benzoate-to-soy lecithin (HAB/SoyL) molar ratio of 10. Even

though the PLQY results commented above pointed to the HAB/SoyL molar ratio of 80 as the most highest-achieving sample, it has to be noticed that this comes with a partial dissolution of the nanocrystals, as shown by the shape deformation of the corresponding absorption spectrum. The ratio of HAB/SoyL of 10 was then considered as the most promising treatment in terms of PLQY (about 70%) and chemical stability.

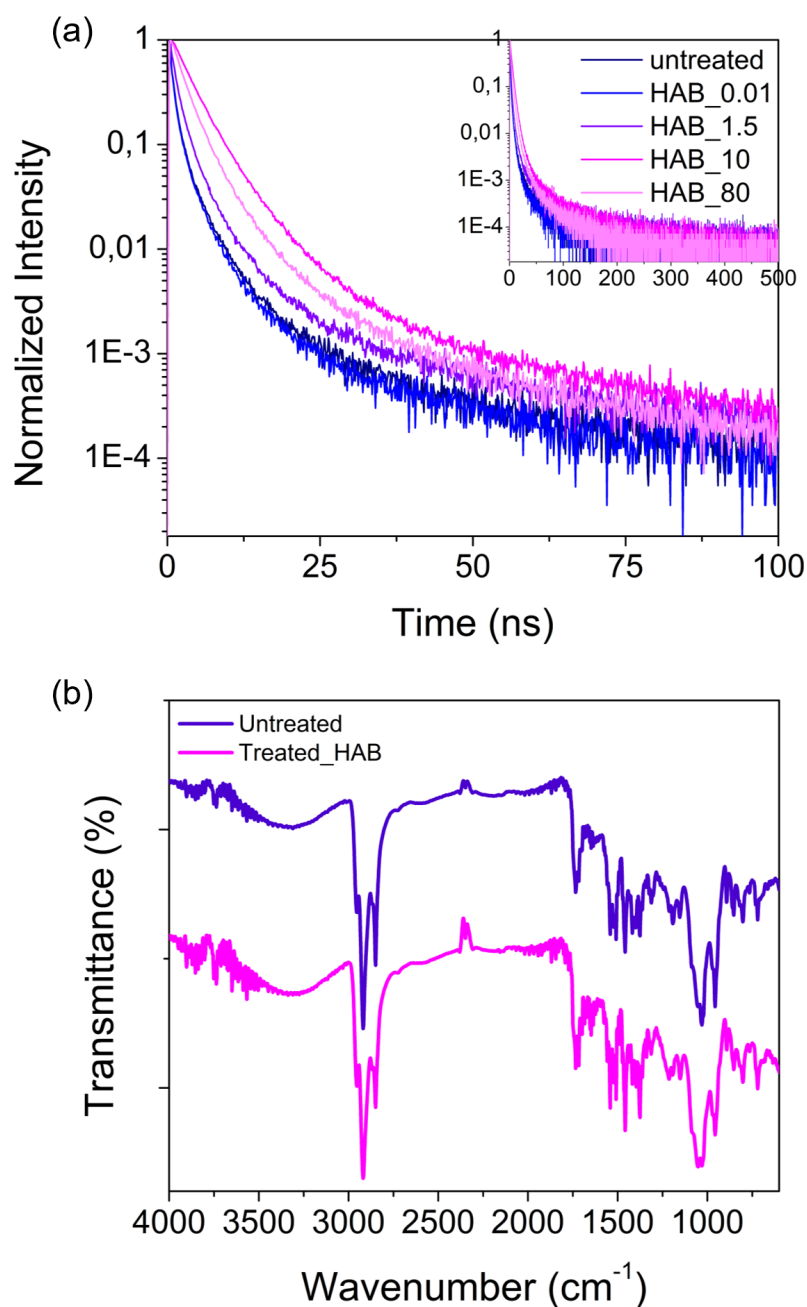


FIGURE 3.11: The fluorescence decay time of the colloidal dispersions ($\lambda_{\text{exc}} = 440$ nm) obtained after treating soy lecithin-capped CsPbBr₃ nanocrystals with increasing amounts of hexylammonium benzoate (a); the FTIR spectra of the dried untreated and HAB-treated samples (b).

Figure 3.10 also shows pictures of increasingly HAB-treated colloidal samples under natural sunlight at a concentration of 0.056 mg/ml (b), and below the samples 100 times more concentrated either untreated (left) or treated at a HAB/SoyL ratio of 10 (right) (c). The change of color, that shifts from pale yellow to bright green, is a nice visual observation of the increased PLQY.

The choice of the HAB/SoyL ratio of 10 as the best sample is in accordance with the photoluminescence decay time features (Figure 3.11 (a)). In fact, the decay improves progressively for increasing amounts of hexylammonium benzoate, finally reaching an improved monoexponential decay for the sample treated with a HAB/SoyL of 10; instead, for the sample with a HAB/SoyL of 80, the curve shape regresses back to the previous trend. This could be attributed again to the partial dissolution of the nanocrystals of this sample, earlier detected in its absorption spectrum, which experience surface deterioration due to the excessive amounts of ligands.

Finally, in order to understand if hexylammonium benzoate does bind to the nanocrystals surfaces, or it only reacts with them, a FTIR measurement was conducted: the comparison between the untreated and treated sample is shown in Figure 3.11 (b). The untreated sample features the characteristic peaks associated to alkyl groups, thus the C-H stretchings between 2971 and 2863 cm^{-1} , as well as their scissoring and rocking modes below 1500 cm^{-1} ,^[370] and the stretching vibration of the C=O bond at 1736 cm^{-1} , typically associated to saturated aliphatic esters:^[371] this is consistent with the presence of soy lecithin on the nanocrystals surface. On the other hand, the spectrum obtained from the sample treated with hexylammonium benzoate does not show any remarkable differences, as it features the same peaks found for the untreated sample, but no addition of a C=O stretching vibration at lower wavenumber, as it would be expected for a α,β -unsaturated C=O bond as the one in hexylammonium benzoate's structure,^[371] nor the signals at 3032 cm^{-1} , 1506 cm^{-1} or 738 cm^{-1} that are typical of an aromatic ring.^[372] The final conclusion was then that hexylammonium benzoate only acts as a surface repairing agent, but does not bind to the nanocrystals surfaces as a ligand.

In conclusion, the chemical treatment with hexylammonium benzoate has been proved successful in repairing the defects on the involved nanocrystals surfaces, having a key beneficial impact on the photoluminescence quantum yield of these soy lecithin-capped CsPbBr₃ nanostructures. This PLQY optimization has as a consequence the reduction of the overall light detection issues due to self absorption, as the emitted photons, even in case of re-absorption along their path, are much more likely to be emitted again and eventually reach the detector. The scintillation performances of these fully optimized samples were then ready to be tested.

3.3 Triple to Double Coincidence Ratio

The evaluation of the colloidal CsPbBr₃ nanocrystals scintillating behavior in solution, in real utilization conditions, was done via the Triple to Double Coincidence Ratio (TDCR) method: this technique, based on a coincidence method, can give information about the light emission, the self-absorption phenomena and the scintillation quantum yield,[373, 374] a parameter which is not straightforward to evaluate in the case of nanostructures, due to the complex energy deposition scheme under ionizing radiation excitation.[282]

This setup uses ²⁴¹Am as a 59.5409 keV γ emitting excitation source in order to study the interaction between this radiation and the sample. The linear interaction probability μ (in cm⁻¹) of a γ photon with a material with effective atomic number Z_{eff} is given by the following formula:[375]

$$\mu = \frac{n_e \sigma_e}{Z_{\text{eff}}} \quad (3.1)$$

where n_e is the electron density (cm⁻³) and σ_e is the interaction cross section of the material (cm²).

The interaction cross section σ_e combines all the 3 types of interaction of the ionizing radiation with matter, thus the photoelectric effect, the Compton effect, and the creation of pairs. Being the first two phenomena the ones involved in TDCR, a brief description is here presented and illustrated in Figure 3.12[376].

The photoelectric effect corresponds to the situation where the γ photon is absorbed, leading to the ejection of an electron (photoelectron) from a core level (K, L, M,...) of the scintillator. The ejected photoelectron has a kinetic energy $E_c = E_g - E_l$, where E_l is the binding energy of the level it was ejected from. This kinetic energy, following successive interactions, will contribute to the emission of light, as well as the atom left in the excited state, which will eventually radiatively de-excite. Therefore, through the photoelectric effect all of the emitted light corresponds to the total energy deposition of the initial incident γ photon: since the latter has well-known energy, in principle this gives rise to the same number of scintillation photons each time.

Furthermore, especially in the presence of heavy elements, it may happen that the subsequent X-ray fluorescence escapes from the crystal, mainly from K levels: an "escape peak" is thus observed, and its amplitude depends on the dimensions of the crystal. Far from the absorption thresholds K, L, M,..., the photoelectric effect's cross section σ_{pe} is

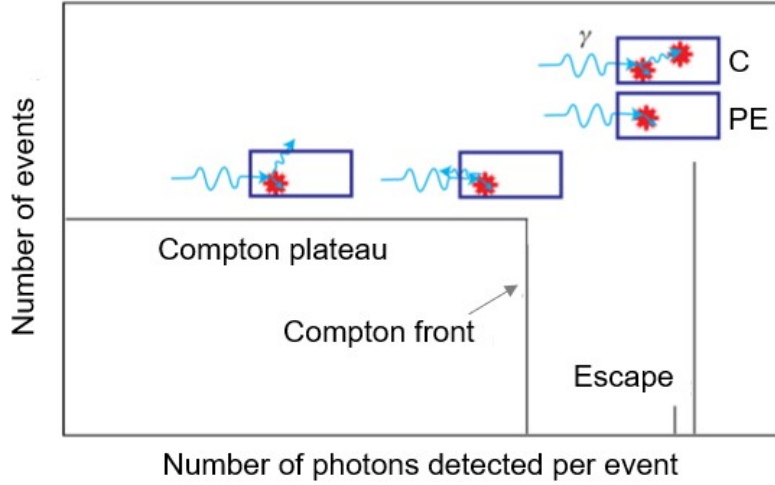


FIGURE 3.12: The framed drawings represent the Compton events, the photoelectric effect (PE) and the case where an event Compton gives rise to a reabsorbed γ photon. In this case, the energy filed is similar to the PE case. The escape corresponds to the case where part of the energy escapes from the crystal by X-ray fluorescence. part in red symbolizes the emission of light linked to the energy deposit of the electron diffused or resulting from the ionization. Reproduced from the work of Dujardin[376].

proportional to $Z_{\text{eff}}^5/E_\gamma$: [375] therefore, the scintillator's effective atomic number is an important criterion when the photoelectric effect is used for detection.

Next, the Compton effect corresponds to the inelastic scattering of the incident γ photon on an electron in the material. By noting θ the angle between the direction of the incident photon and that of the scattered photon, of energy E'_γ , the kinetic energy E_c acquired by the electron and that of the diffused γ photon is given by:

$$E_c = E_\gamma - E'_\gamma \quad (3.2)$$

with $E'_\gamma = E_\gamma / (1 + (E_\gamma(1 - \cos\theta)/m_0C^2))$ and m_0 as the mass of the electron at rest.

The scattered γ photon can either be reabsorbed or escape. If it's reabsorbed by the scintillator, then the total energy deposited is equal to that of the incident photon, just as in the case of the photoelectric effect: in this case, it contributes to the photoelectric peak and cannot be distinguished from a photoelectric event. Otherwise, if the scattered γ photon escapes, then the deposited energy corresponds to that of the scattered electron. Depending on the scattering angle θ , the energy of the scattered electron and therefore deposited in the crystal varies from 0 to $E_\gamma / (1 + (2E_\gamma/m_0C^2))$. This last value corresponds to the Compton front. The whole of this continuum is names the Compton plateau (Figure 3.12). The cross section of the Compton effect σ_C is proportional to $Z_{\text{eff}} / E_\gamma$. [375]

With that in mind, the TDCR experiments performed on colloidal CsPbBr₃ nanocrystals aim at studying their scintillating features under 59.5409 γ excitation. The phenomenon which is more likely to happen in such a liquid system is the Compton effect: this is why the detection of the scattered γ photons can give important information on the deposited energy.

The experimental setup involves three photomultipliers (PMTs) positioned all around the sample, together with a CdTe spectrometer and a gamma spectrometer, and a sealed ²⁴¹Am source placed under the sample (illustration in Figure 3.13).[\[373, 374, 377\]](#) The γ rays emitted by the source interact with the sample mainly by Compton effect: this produces a scattered γ photon and a photoelectron. The latter then follows a path, whose length depends on its energy and on the medium, and ends up being absorbed by an energy acceptor: in liquid scintillation processes, as already discussed, the most probable interaction results in the excitation of the solvent, which then transfers its energy to a dissolved dye, which then emits light.

Every scintillating event is likely to produce many photons, which then travel through the liquid sample in different directions: if nothing stops their trajectory, each of them can reach a PMT, and in particular multiple photons emitted by the same event can ideally reach different PMTs at the same time, the latter respecting the statistics of the scintillation decay. The TDCR technique is based exactly on this idea: if two photons reach two PMTs at the same time within a short coincidence time window, leading to what is called a double coincidence (D), these D signals are interpreted as a count of the emissive events out of the natural thermal noise of the PMTs. The number of times that these coincidence are not just double, but triple, thus when three photons reach the three PMTs A, B and C within the same coincidence time window, this is interpreted as an indication of the intensity of the corresponding emissive events. Essentially, the number of triple coincidences allows to evaluate the average number of detected photons per scintillating event, regardless of the PMTs efficiency.

The measurement, then, consists in the evaluation of the photon detection coincidences in the three PMTs. In this configuration, the signals collected by a single PMT only, thus leading to no coincidences with the other ones, are considered as either noise, either an indication of self-absorption phenomena: as a matter of fact, if the sample can re-absorb the photons, these latter will struggle to travel safely up to the PMT, since they will be more probably be re-absorbed along the way.

Double coincidences, then, are considered as reliable detected events, thus the “D” factor is considered as a measure of the number of emissive events occurred during the scintillation process.

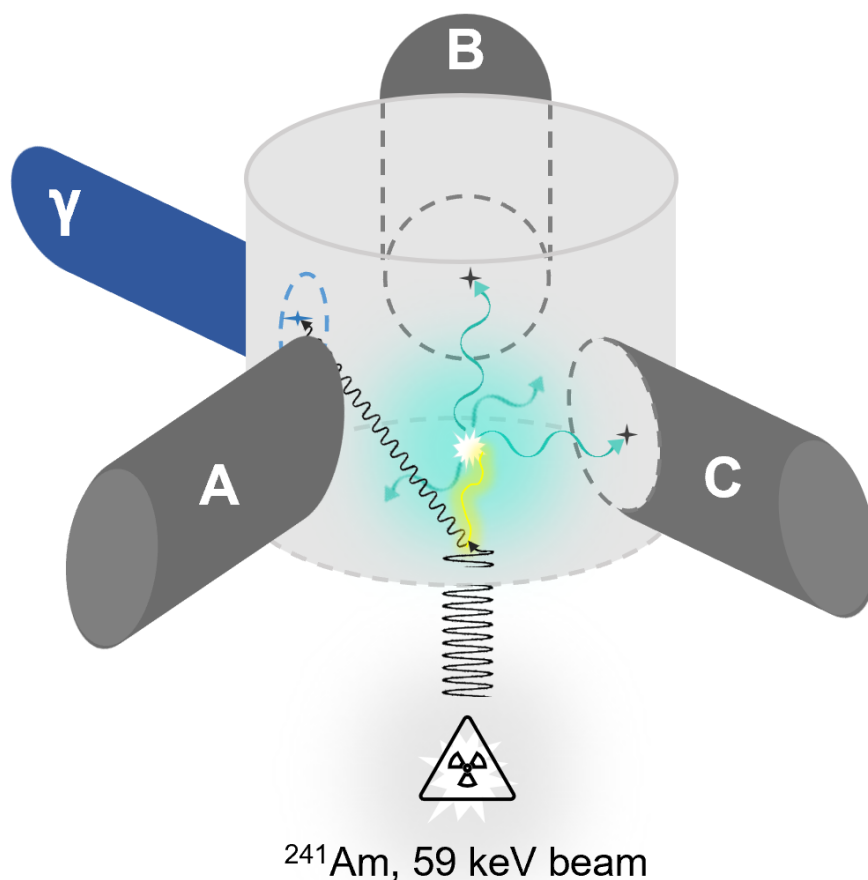


FIGURE 3.13: Setup and working principle scheme of the TDCR setup developed at LNE-LNHB:[373] the external radioactive source irradiating the sample, leading to a Compton effect that produces on one hand a scattered γ photon, that can be detected by the γ detector, on the other hand a photoelectron that can result in scintillation, emitting photons which can impact the three photomultipliers A, B and C.

If a too high self-absorption probability impacts the system, it is not probable to observe coincidences, but on the contrary the analysis will be dominated by single detections from the individual PMTs, whereas D, thus the count of the reliable emissive events, will tend to zero.

Finally, the triple coincidences T are evaluated as a measure of the intensity of those emissive events: resulting from these considerations and from the setup's geometry, the T/D factor, thus the triple to double coincidences ratio, is mathematically related to the scintillation yield via the following formula, where n represents the average number of photons detected per emissive event:[374]

$$n = -3\log\left(1 - \frac{T}{D}\right) \quad (3.3)$$

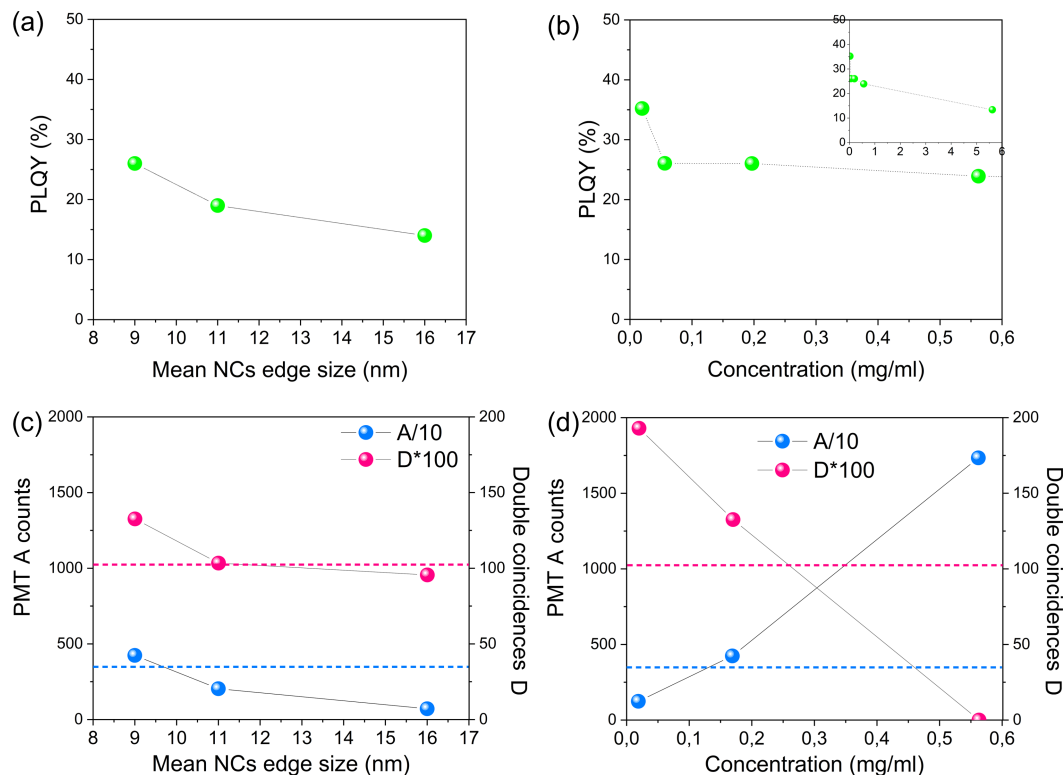


FIGURE 3.14: Preliminary tests on untreated soy lecithin-capped CsPbBr₃ colloidal dispersions: at the top, the PLQY as a function of the mean nanocrystals size and of their concentration, respectively (a) and (b). Below, their corresponding TDCR results, respectively (c) and (d), in terms of single detections from one PMT and of the number of emissive events D. Note that the single detections A and the double coincidences D had to be respectively divided by 10 and multiplied by 100, in order to compare these values with the ones for the liquid scintillator reference Ultima Gold (UG), represented by the dashed horizontal lines.

A first set of TDCR measurement was conducted on untreated CsPbBr₃ nanocrystals samples of increasing average size, and their PLQY and TDCR results are compared in Figure 3.14 (a) and (c), respectively. The trend favors smaller nanocrystals, even though in general the obtained values are rather poor, in comparison with the performances of the liquid scintillator reference Ultima Gold: the single detections A, which can portray the noise, are 10 times higher than the reference, whereas the number of emissive events D is 100 times lower.

A second set of TDCR measurements was then conducted on untreated CsPbBr₃ dispersions of increasing concentrations, and their PLQY and TDCR results are depicted in Figure 3.14 (b) and (d), respectively. The measurements show that increasing the concentration massively degrades the scintillation performances, as the number of double coincidences D drops: this was interpreted as evidence that at high concentration the system experience stronger self-absorption, preventing the emitted photons to reach

the detectors before being re-absorbed by the medium. In this case again, the obtained values are far poorer than the Ultima Gold reference.

The concentration value that was chosen to pursue the study was then 0.056 mg/mL, which corresponds to an optical density at the first exciton of 0.2, which was the only sample at this preliminary stage to show a reasonable amount of emitted photons, and also the one with the highest photoluminescence quantum yield, consistent with a less impacting self-absorption.

A great step forward in the improvement of these systems performances was then allowed by the chemical surface treatments discussed in the previous section.

The above described surface-treated samples were thus tested for the Triple to Double Coincidence Ratio measurement, in order to observe the effects of the chemical treatment on the scintillation processes. The first plot shows that, for treated and untreated dispersions at the same concentration (light blue, blue and yellow data), there is a clear correlation between the average n , defined in equation 3.3, and the optical quantum yield: n shows a behaviour which is consistent with the PLQY enhancement, and thus

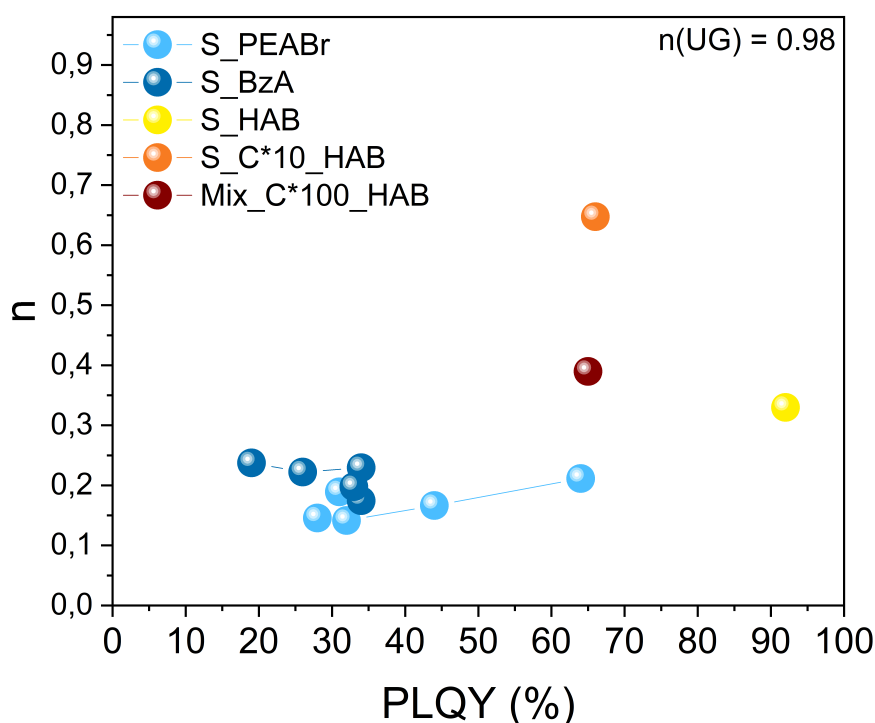


FIGURE 3.15: TDCR results in terms of the number of photons detected per emissive event n as a function of the PLQY for samples treated with phenylethylammonium bromide (PEABr), benzoic acid (BzA) and hexylammonium benzoate (HAB). The upper limit of the vertical axis represents n for the reference liquid scintillator Ultima Gold (UG).

with the improved NCs surfaces quality. The best result is again obtained with the hexylammonium benzoate treated mixtures, which double the pristine sample's scintillation yield-related parameter n even in the case of a colloidal dispersion 100 times more concentrated than the previous. Since the light emission corresponds to the last stage of the scintillation mechanism, the significance of the optical quantum yield on the scintillation quantum yield is convincingly demonstrated.

That said, this linear-like behavior, coupled with the FTIR result discussed above that showed that HAB specie does not bind to the CsPbBr₃ surface, put forward the hypothesis that the light emission processes come from direct excitation of the nanocrystals from the radioactive source, more than from some solvent-mediated energy transfers.

Additionally, the double effect of a concentration increase is shown in the $n=f(\text{PLQY})$ plot in Figure 3.15: when increasing the concentration by a factor of 10, n increases by more than a factor 2, whereas a 100-fold higher concentration causes the average n to decrease back to a value comparable to the diluted sample. This result unequivocally indicates that, even for high-quality surface nanocrystals, the possible CsPbBr₃ NCs loading increase is limited: a too high concentration brings back the self-absorption issue

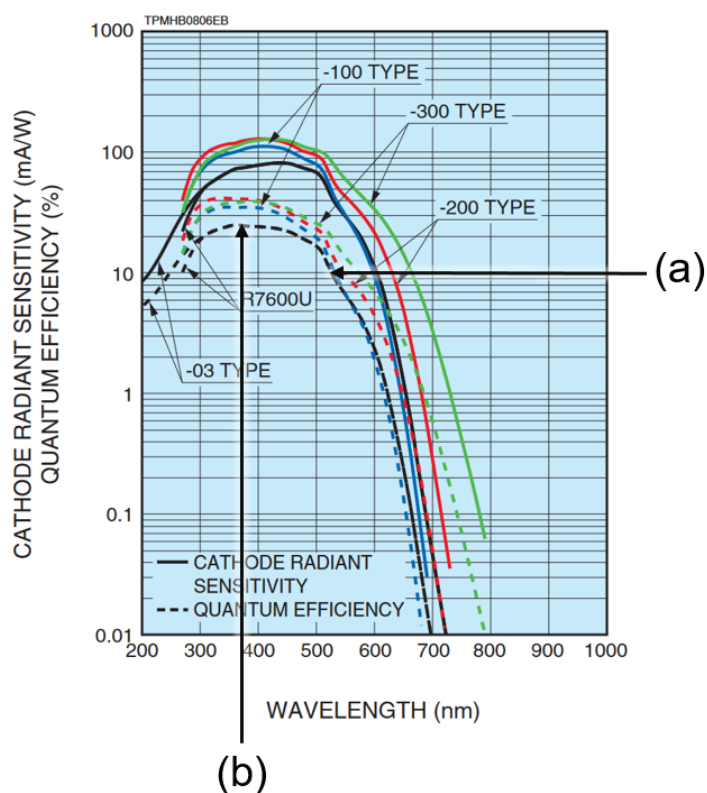


FIGURE 3.16: The setup PMTs' sensitivity as a function of the detected wavelengths, where (a) points to the CsPbBr₃ emission and (b) to "Ultima Gold" standard's one.

due to the already mentioned strong overlap between the emission and the absorption spectrum, frequently observed in such direct band gap semiconductors.

It is also worth noticing that in the case of the moderately concentrated HAB-treated sample, the obtained n value is comparable with the liquid scintillator standard Ultima Gold, when considering that the PMTs of the setup are twice less sensitive to CsPbBr_3 emission wavelength than for UG's one (Figure 3.16). This is highly remarkable, since the tested lead halide perovskite nanocrystals colloidal dispersion are about two orders of magnitude less concentrated than UG.

On the other hand, the mentioned improvement in the impact of self-absorption between untreated and treated samples is well depicted in Figure 3.17. as a matter of fact, in the case of the untreated colloidal dispersions, all the concentrations values that it was possible to test give around the same amount of detected emissive events D ; on the other hand, this value increases by around 10- and 100-fold in the case of the samples treated with hexylammonium benzoate.

Figure 3.17 also shows that the treated samples show a linear increase of the scintillating events as the concentration increases. Again, this linear-like behavior encourages the

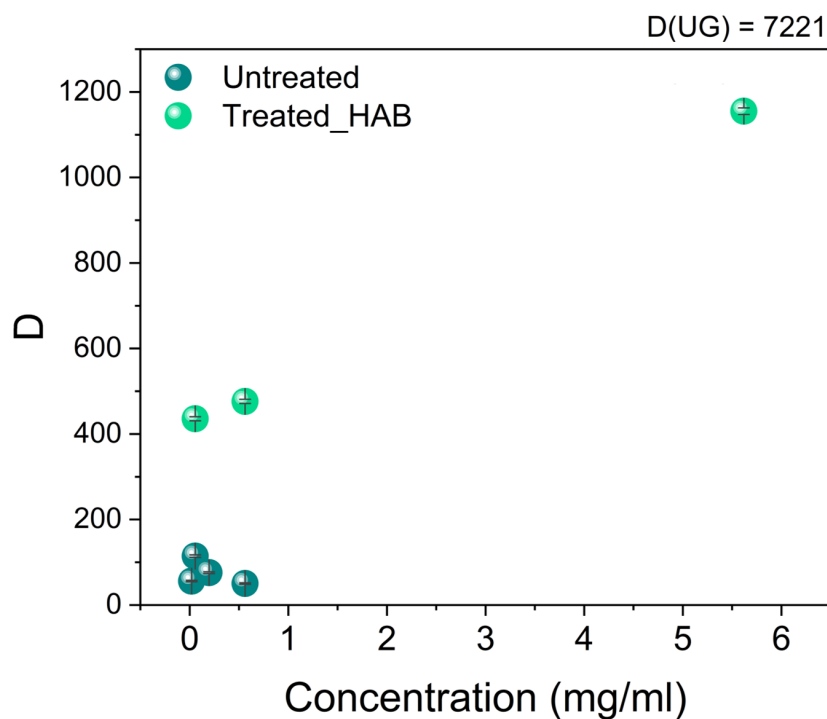


FIGURE 3.17: Number of detected emissive events D as a function of the concentration of untreated soy-lecithin CsPbBr_3 nanocrystals and of samples treated with hexylammonium bromide. $D(\text{UG})$ indicates the number of emissive events detected for the reference liquid scintillator Ultima Gold (UG).

hypothesis that the light emission mostly come from direct excitation of the nanocrystals from the radioactive source, more than from some solvent-mediated energy transfers. In fact, in the latter case the observed D increase wouldn't be expected as linear as a function of the nanocrystals concentration, as the primary radiation acceptor would be the solvent: therefore, the energy transfer probability would more likely show a complex dependence on the separation distance between the primary interaction and the nanoparticles.

The increase of the average n portrayed above requires careful analysis: as previously described, such an increase may be due to an increase of the intrinsic scintillation yield, or to a variation in the mean deposited energy, which is clearly observed in Figure 3.19. Figure 3.18 plots the number of photoelectrons n_{pe} as a function of the photoelectron energy. The spectrum is restricted to the range below 10 keV due to potential perturbations arising from double Compton events at higher energies. Both the HAB-treated diluted and 100 time more concentrated samples exhibit almost the same scintillation yield about 0.25 photoelectrons per deposition of 10 keV: this highlights that within these concentrations range, increasing the concentration does not impact the intrinsic scintillation yield, implying that the increase observed in Figure 3.15 can be attributed to a change of the mean deposited energy.

Finally, the energy deposition mechanism in such colloidal CsPbBr_3 systems is determined, by comparing the number of emissive events D detected by the three photomultipliers in coincidence with the detections of the gamma-spectrometer. In fact, considering the ratio between the number of emissive events D and the number of high energy photons detected by the gamma-spectrometer, this D/γ ratio is considered as the detection

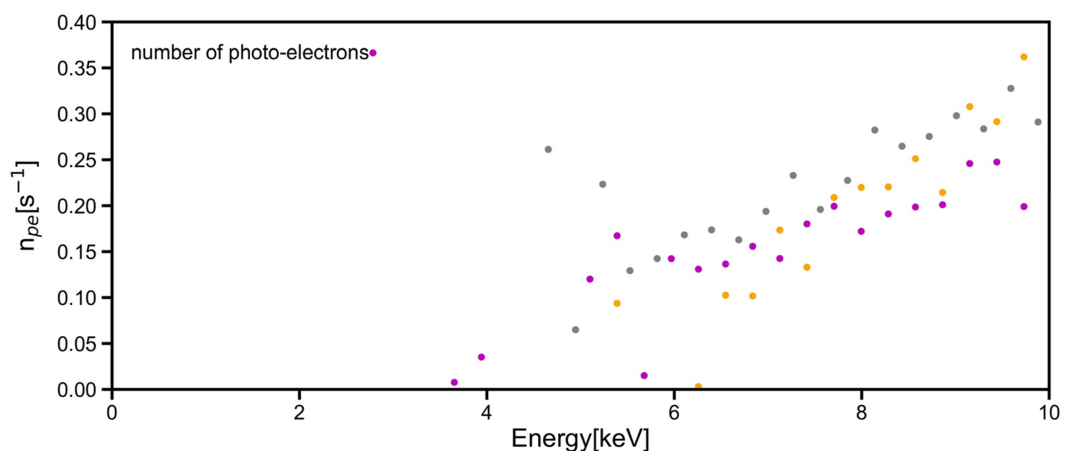


FIGURE 3.18: Number of photoelectrons n_{pe} per photoelectron energy, in the case of the untreated sample (dark green), the corresponding concentration sample treated with hexylammonium benzoate (purple) and the HAB-treated one at a 100 times higher concentration (yellow).

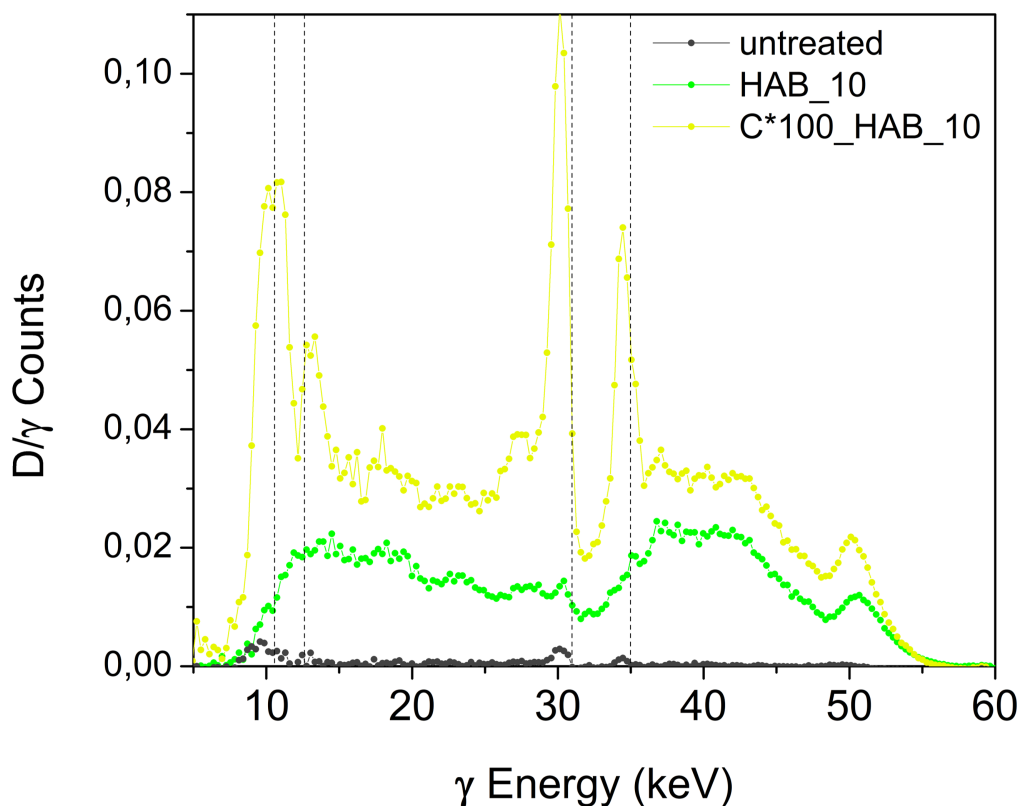


FIGURE 3.19: The detection efficiency per energy of the detected γ photons, for the untreated and treated with HAB samples (respectively dark grey and green), and for the HAB-treated sample with a 100-fold higher concentration. Vertical dashed lines mark the average X-fluorescence emission thresholds for Pb ($L_{\alpha} = 10.55$ keV, $L_{\alpha} = 12.61$ keV) and Cs ($K_{\alpha} = 30.97$ keV, $K_{\beta} = 34.98$ keV).

efficiency of the whole scintillation event. This detection efficiency thus depend not only by the intrinsic scintillation yield, but also on the number of effective emissive events.

Figure 3.19 plots this D/γ parameter with respect to the energy of the high energy photons detected by the gamma-spectrometer: in the case of the untreated colloidal dispersions, the very low amount of detected emissive events D makes only a few features to stand out of the noise, which correspond to the average X-fluorescence emissions from caesium and lead. On the other hand, when considering the treated sample at the same concentration, the curve has a structure, showing features describing γ -photons scattered by Compton and double Compton effect.

Differently, when increasing the concentration by 100-fold, the same curve shape describing the scattered γ -photons is observed, but the detection efficiency dramatically increases for the energies corresponding to the X-fluorescence emitted by caesium and lead: the D/γ ratio indeed increases by around 10-fold for these X-fluorescence peaks, whereas for the scattered photons the detection efficiency increases of about a factor 2. This indicates that the dominant primary energy deposition mechanism for a high

concentration on nanocrystals is the direct interaction between the source's 59 keV γ -photon and the CsPbBr₃ nanoparticles. Moreover, the detection efficiency increase for the Compton photons looks more pronounced for lower-energy detected γ -photons, thus when a higher-energy primary electron is formed. This could reflect the situation where this primary interaction occurs in the solvent, but very close to a CsPbBr₃ nanoparticle, meaning that the primary electron and its resulting electron shower can directly interact with the nearby nanocrystal.

In conclusion, after several steps of sample quality improvement involving size selection via selective precipitation and multiple chemical treatments aimed at repairing the surface defects, some stable and bright colloidal CsPbBr₃ dispersions, even at high concentration, were obtained and tested as liquid scintillators. This study on lead halide perovskite nanocrystals as liquid scintillators was concluded, then, with the presentation of a direct energy deposition.

3.4 Core/shell strategy for water stability

It has already been mentioned that traditional liquid scintillators are a mixture of different organic components, dissolved in an apolar, aromatic solvent. Nevertheless, a vast range of liquid scintillation applications covers aqueous samples, namely the identification and quantification of radioactive agents in human blood, urine and tissues, or in the environment, in water bodies and flora.

Now, the miscibility of water with the above-mentioned typical organic apolar solvents is very poor, thus LSC have to be added with a vast range of surfactants, used to bring the aqueous phase into close contact with the organic one.[285] Once the surfactants are present, the addition of water forms a microemulsion, thus a dispersion of small droplets, with an approximate radius of 10 nm, stabilized by the detergents.[378] Many detergents have been investigated in literature, involving non-ionic, anionic, cationic and amphoteric surfactants,[378] and within each group, it is possible to choose the favored chemical for the specific application. The close contact allowed by the optimal dispersion of the droplets in the organic solvent can produce an efficient energy transfer, meaning that radioisotopes can be successfully identified and quantified even in aqueous solutions.

Nevertheless, this amount of components needed in a traditional LSC not only entails the exposure of the system to light losses risks and to a decrease of the light emission rate, but also it can make it complicated to get reliable results for aqueous samples. as a matter of fact, surfactants can stabilize only a small concentration of aqueous samples.

For example, Triton X-100 is often used as an agent for the formation of stable emulsions for liquid scintillation counting, and in its case the maximum amount of water that can be mixed with the LSC is around 40%, with counting efficiencies around 10% for ^3H and 50% for ^{14}C .[\[294\]](#) The limited maximum miscibility can be a great issue, since the analytes already come diluted in water, and also the system can result in a highly diffusive biphasic emulsion, or in the formation of foam: this can reduce the overall mixture transparency, leading to problems in the light detection and to experimental reproducibility issues.[\[379\]](#) This need for surfactants adds further complication in the LSC system, and can decrease its overall efficiency. Nevertheless, as already mentioned, water-based samples are a significant part of the utilization of liquid scintillators, thus possible amelioration of these systems deserve to be explored.

As seen in the previous sections, lead halide perovskite nanocrystals can make good light emitters in liquid scintillation cocktails, even without the need of energy transfer from the solvent, thus it is worth it to attempt to transfer these CsPbBr_3 nanocrystals into polar solvents. Chapter 1 already discussed that water is a great enemy of these structures, as their ionic bonds are easily dissolved by such a polar specie. Consequently, the only plausible strategy to protect the nanocrystals is to grow a protective shield all around their surface, obtaining a core/shell structure.[\[380\]](#) Consequently, such shell material needs to be stable in polar environment, thus to be held by covalent-like bonds, and also to be either transparent to CsPbBr_3 nanocrystals emission, or to show fluorescence after absorbing their emission; moreover, it would also be ideal for it to match the crystal structure of the nanoparticles, in order to promote the shield material to evenly grow on their surfaces.

The current section involves the attempts to grow a protective shield around the nanoparticles, aiming to facilitate the application of these liquid scintillators with aqueous samples, without needing to add surfactants to the mixture.

3.4.1 $\text{CsPbBr}_3/\text{ZnS}$ "raspberry" heterostructure

Techniques aiming to increase the stability of nanocrystals towards the environment, namely moisture, involve their covering with a shield material: the choice can fall on either polymers,[\[195, 234–236, 381–384\]](#), salts,[\[385\]](#) oxides like ZnO [\[386\]](#) or SiO_2 [\[273, 387–389\]](#) or another semiconductor, like ZnS ,[\[390–392\]](#) PbS ,[\[393\]](#) or CdS .[\[394, 395\]](#)

In the matter of this work, the attempts were focused on CsPbBr_3 /semiconductors core/shell heterostructures, judging that not only the covalent-bond shield would be an effective protection against water, but it would also be interesting to observe the interaction between the two semiconducting materials during the light emission process.

as a matter of fact, an eventual energy transfer between the to adjacent materials could improve the Stokes shift of the overall system.

The following set of experiments involves the attempts to grow a shell of either CdS or ZnS around CsPbBr₃ nanocrystals, ideally in a one-pot synthesis: two hot injection processes are involved, the first aiming to form CsPbBr₃ nanoparticles, the second forcing the growth of CdS on their surface, via heterogeneous nucleation. In particular, tests involving CdS shells were conducted as variations based on the work of Tang et al.[394],

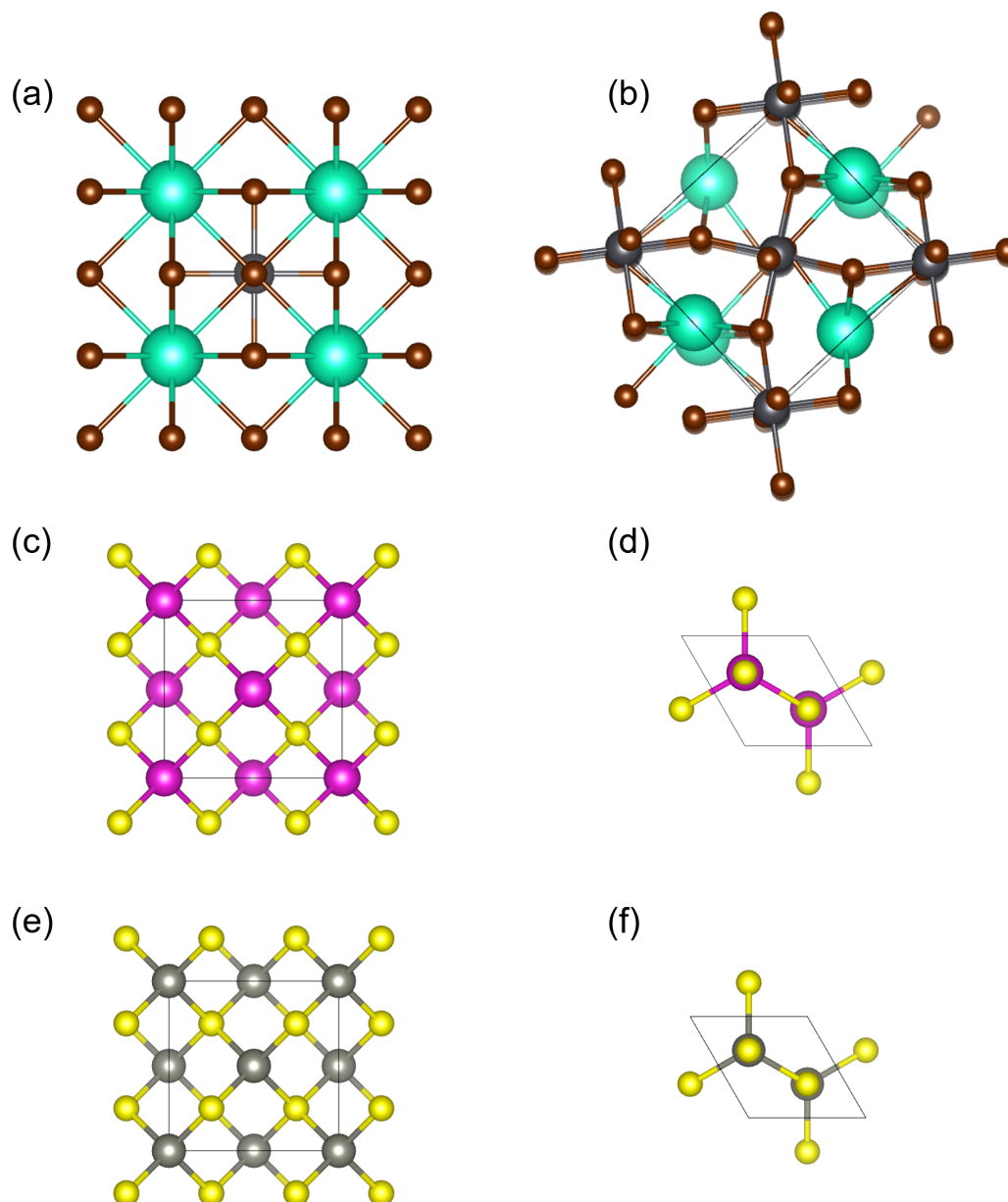


FIGURE 3.20: Crystal structure representations of CsPbBr₃ either in the cubic Pm-3m or orthorhombic Pnma structure, respectively (a) and (b), and both CdS and ZnS in their zinc blende F-43m structures, respectively (c) and (d), or wurtzite P36mc structures, respectively (d) and (f).

whereas the experiments on ZnS shells were prepared as variations of the work of Ravi et al.[391] For the synthetic protocols, please refer to section 2.4.

Ideally, the perfect structure match would happen between two similar crystal structures, with similar symmetries and cell dimensions. Regarding the respective crystal structures, ideally all the three CsPbBr₃, CdS and ZnS can have cubic crystal structures (Figure 3.20 (a), (c), (e)), but it has already been discussed that CsPbBr₃ colloidal nanocrystals are rather arranged in an orthorhombic structure (Figure 3.20 (b)); moreover, both CdS and ZnS can also have an hexagonal wurtzite structure (Figure 3.20 (d), (f)). Additionally, the presence in CsPbBr₃ of the large Cs⁺ cation makes the cell much bigger than the ones of CdS and ZnS.

Consequently, by attempting to grow a CdS or ZnS shell around CsPbBr₃ nanocrystals, it would be difficult to obtain an even, homogeneous epitaxial growth (Figure 3.21 (a)), but it would be more logical to expect a raspberry-like structure, illustrated in Figure 3.21 (b). This kind of heterostructure reflects the situation where the shell material experiences multiple heterogeneous nucleation, triggered by the presence of the CsPbBr₃ surfaces, which then grow expanding; eventually, all these expanding particles would make contact and end up covering the initial CsPbBr₃ nanocrystal.

The first set of syntheses was conducted on CdS shells, taking into account the work of Tang et al.[394] The parameters that were considered as the most relevant in order to promote the growth of CdS on CsPbBr₃ were the precursors relative ratios, the reaction temperature and the duration of the CdS precursors injection: consequently, these parameters were varied in different combinations in order to find the optimal nucleation/growth conditions. Nevertheless, these attempts did not lead to the formation of

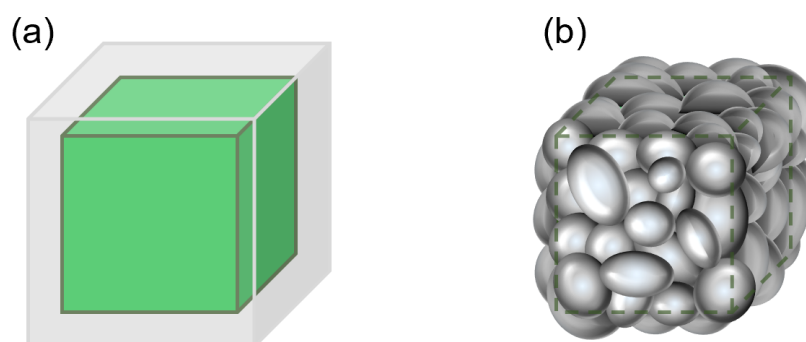


FIGURE 3.21: Illustration of an ideal core/shell cubic heterostructure, where the shell has grown evenly on the core structure (a), and of a raspberry-like one (b).

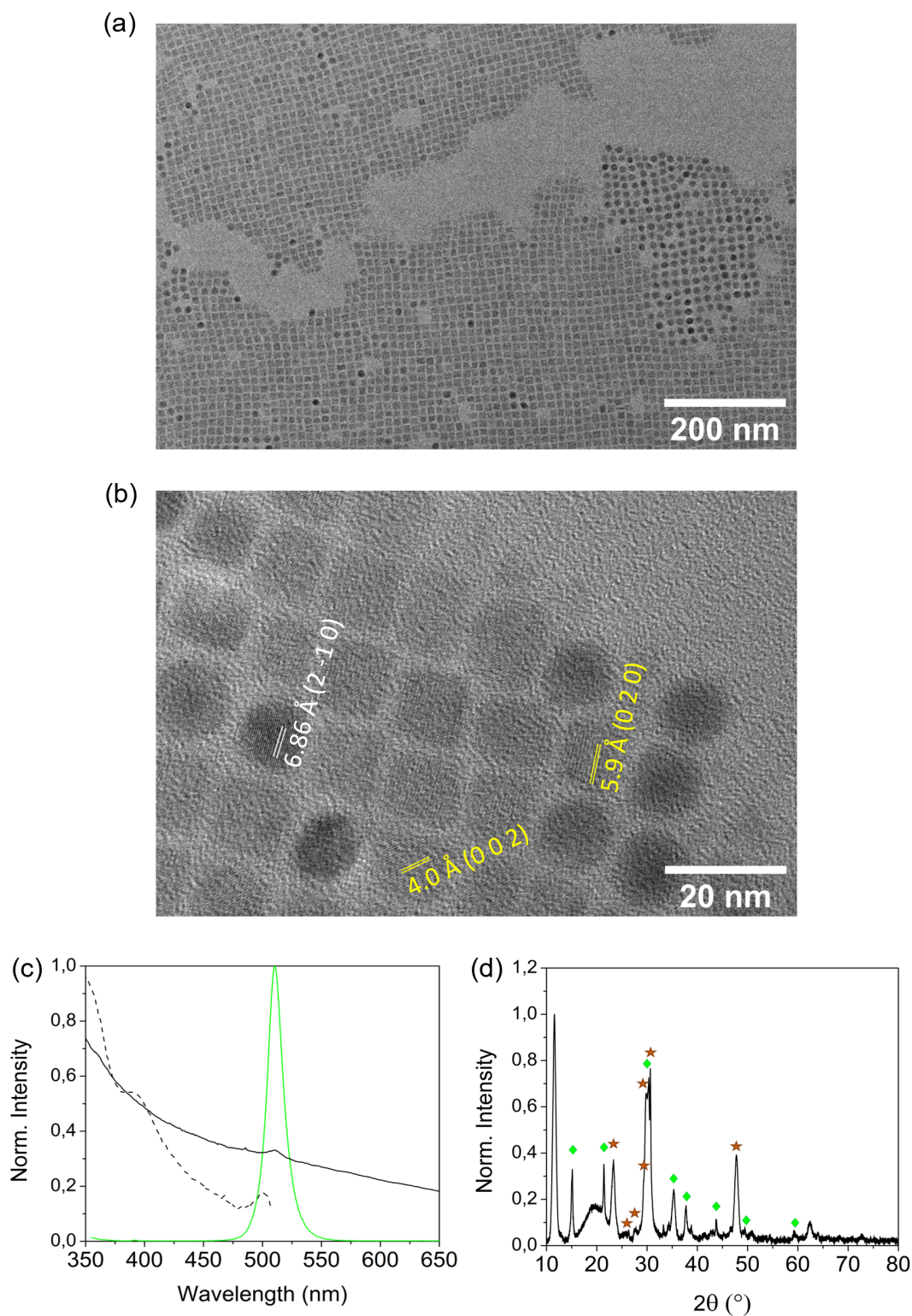


FIGURE 3.22: Optical and structural features of an attempted $\text{CsPbBr}_3/\text{CdS}$ heterostructure. TEM images at low magnification (a) and high magnification (b), where the inter-planar distances are indicated in yellow for orthorhombic CsPbBr_3 and in white for trigonal Cs_4PbBr_6 ; absorption spectrum (black, solid line), PL spectrum ($\lambda_{\text{exc}} = 350 \text{ nm}$) (green, solid line) and the corresponding PLE spectrum at $\lambda_{\text{em}} = 512 \text{ nm}$ (dashed line) (c); XRD pattern of the obtained $\text{CsPbBr}_3/\text{Cs}_4\text{PbBr}_6$ mixture (d). In the latter, green diamonds mark the orthorhombic CsPbBr_3 pattern, whereas the brown stars mark the trigonal Cs_4PbBr_6 one.

the desired shell, as the main result of these reaction was actually the partial degradation of the initial CsPbBr_3 nanocrystals and the formation of a Cs_4PbBr_6 phase, caused by the prolonged exposure to high temperature (typically 150°C or 180°C). An example of a typical result is here presented: in this case, the chosen Cd:Pb ratio is 2, the CdS precursors are Cd-myristate and sulfur dissolved in oleylamine,[396] and the latter precursors dropwise injection was conducted at 150°C during 40 minutes.

The TEM images (Figure 3.22 (a) and (b)) show two main populations, one being cubic-shaped nanocrystals, and the other being round/hexagonal shaped ones. The FFT operated on the high magnification images reveal the presence, along with the CsPbBr_3 structure, of the Cs_4PbBr_6 phase, which shape is consistent with literature.[397]

This finding is consistent with the optical properties of such system, shown in Figure 3.22 (a), featuring an absorption spectrum typical of a highly diffusive sample, in which only a peak at 515 nm is recognizable; the PL peak can be attributed to both CsPbBr_3 nanocrystals or Cs_4PbBr_6 nanocrystals of around 15 nm edge. The structural confirmation is given by the XRD pattern, in Figure 3.22 (b), revealing the presence of Cs_4PbBr_6 along with CsPbBr_3 and no sign of CdS. This can be explained by the reaction temperatures, that were probably too high to maintain CsPbBr_3 nanocrystals stable, but too low to allow the CdS nanocrystals formation.

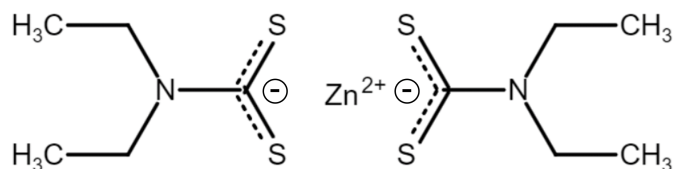


FIGURE 3.23: Comprehensive resonance structure of zinc diethyldithiocarbamate.

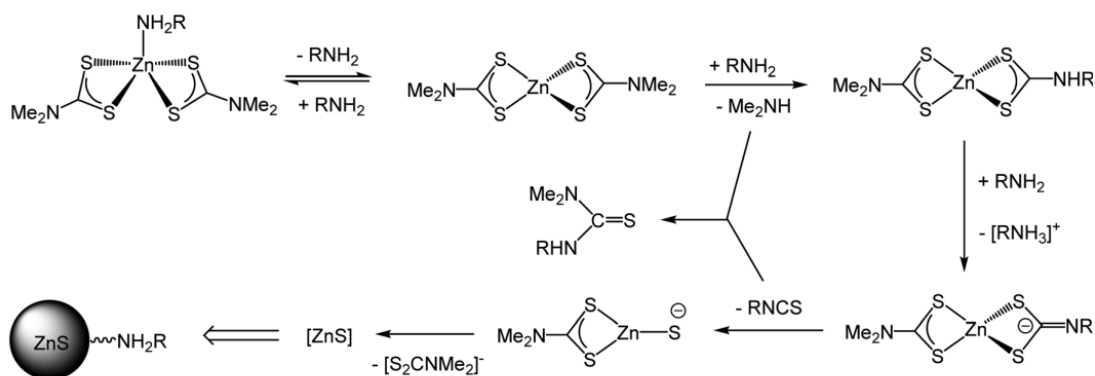


FIGURE 3.24: Mechanism proposed by Islam et al. for the formation of ZnS from the thermal decomposition of precursors like zinc diethyldithiocarbamate in the presence of primary amines. Reproduced from their work.[398]

The next set of syntheses involves the attempt of growing ZnS nanostructures around previously synthesised CsPbBr₃, using as the first inspiration the work of Ravi et al.[391]. The used ZnS precursor is Zn(DDTC)₂, shown in Figure 3.23, which carries two sets of resonant and negatively charged S-C-S bonds, coordinating one Zn²⁺ cation. In presence of primary amines like the oleylamine that is used in these protocols, this specie can decompose as depicted in Figure 3.24, producing one ZnS pair and eventually ZnS nanocrystals. In this case, Zn(DDTC)₂ was added in its solid form to previously synthesised CsPbBr₃ colloidal nanocrystals, and then processed: thus, for this synthesis optimization, the parameters that were varied were the precursors ratio, the temperature and the reaction time.

Eventually, an additional source of zinc was added, in order to prevent potential competitive reactions and byproducts to capture the zinc, which still is in a 1:4 ratio compared to sulfur in Zn(DDTC)₂, and to ensure that excess of sulfide does not sulfidize the perovskite into PbS: varying amounts of zinc stearate, a commercial product, were added, until the final result shown in Figure 3.25 was obtained. Experimentally, this synthesis was conducted based on the protocol described in Chapter 2, using a Zn(DDTC)₂:Cs ratio of 25, with the addition of an amount of Zn-stearate equal to 2.25 times the amount of Zn(DDTC)₂, and the reaction temperature held at 290°C during 1h.

The optical features in Figure 3.25 (a) show a -15 nm shift of the PL peak, together with its +88% FWHM enlargement. From the high temperature used to perform the synthesis, it is expected to observe the formation of Cs₄PbBr₆, which is yet probably not the cause of the PL peak enlargement, as it was not the case for the previously discussed CsPbBr₃/Cs₄PbBr₆ mixture in Figure 3.22 (c), but it is still identifiable from the XRD patterns highlighted in Figure 3.25 (b). From the latter, the successful formation of ZnS is confirmed as well, notably in its wurtzite structure. The morphology of these nanocrystals is observed through TEM (Figure 3.25 (c) and (d)), that confirms the kind of heterostructure that was more likely expected, thus the previously illustrated raspberry-like one: the FFT operated on the high resolution TEM image identifies the (0 0 2) planes of ZnS nanocrystals, which are indeed aggregated around an empty spot. This is interpreted as an indication that, either during the reaction or during the purification steps, the CsPbBr₃ around which ZnS did grow underwent some dissolution issues, also meaning that the shielding provided by ZnS was not covering the whole nanocubes surface.

Nevertheless, this is a promising result, which will have to be further perfected in future experimental series, aiming to obtain ZnS shells completely covering the scintillating CsPbBr₃ nanocrystals, thus allowing them to be dispersed in water media without being

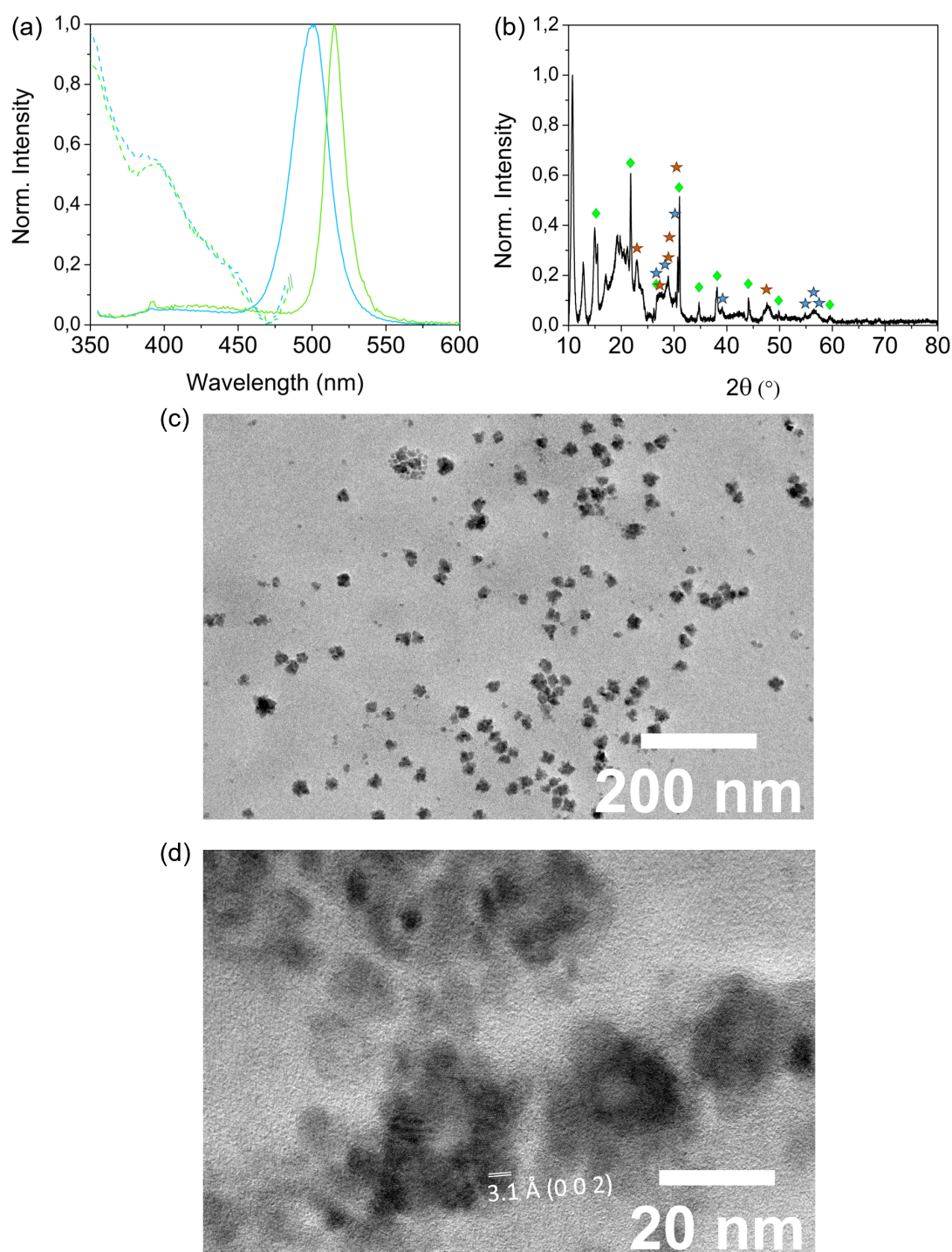


FIGURE 3.25: PL spectra ($\lambda_{exc} = 350$ nm) of the precursors mixture before heating (green, solid line) and of the product (light blue, solid line), with the respective PLE spectrum at $\lambda_{em} = 490$ nm (corresponding respective color, dashed line) (a); XRD pattern of the obtained CsPbBr₃/ZnS heterostructure (b). In the latter, green diamonds mark the orthorhombic CsPbBr₃ pattern, brown stars mark the trigonal Cs₄PbBr₆ structure, and blue stars mark the wurtzite ZnS one. TEM images of the obtained raspberry-like CsPbBr₃/ZnS heterostructures, at low magnification (c) and high magnification (d), where the inter-planar distance indicated in white designs the (0 0 2) planes in P63mc ZnS.

dissolved by the polar environment, and to be implemented in routine liquid scintillation analyses of water-based samples.

Conclusions

This chapter has presented the work on CsPbBr₃ colloidal nanocrystals dispersions as liquid scintillators, especially aiming at understanding the energy deposition mechanism in such colloidal nanostructures and their possible interaction with the surrounding organic solvent.








In order to study these systems, the CsPbBr₃ nanocrystals features were first optimized in terms of size distribution and optimal concentration, and finally in terms of their photoluminescence quantum yield, which gave the most relevant results. Namely, the NCs were treated with chemicals of different nature, in order to repair the surface defects and consequently their PLQY. In particular, the surface treatment with hexylammonium benzoate made it possible to obtain an average number of photons detected per emissive event which is comparable to the used reference Ultima Gold organic liquid scintillator.

A Compton-TDCR experiment was then used to finely characterize the energy deposition processes in these solvent/NCs binary mixture. The study demonstrated that, contrarily to traditional organic liquid scintillators, where the energy is mainly deposited in the solvent, perovskite nanocrystals themselves are the main energy acceptors. This is most likely due to the high density of the nanocrystals, due to the presence of heavy elements such as lead and caesium. Therefore, lead halide perovskite nanocrystals have a double role as liquid scintillators, being at the same time energy deposition centers and visible light emitters.

These results can be readily extended to the more general case of composites materials involving nanocrystals in a matrix, and improve our understanding of the use of such nanostructures for scintillation. They further pave the way to the development of new liquid scintillation cocktails, either introducing nanocrystal emitting centers, or nanocrystals as γ absorbers, or both.

Finally, some synthetic protocols were described, aiming at the formation of a protective shell of a covalent-bond material over the surface of CsPbBr₃ nanocrystals, with the goal of obtaining water-stable samples. Promising results were obtained via the formation of a raspberry-like CsPbBr₃@ZnS core/shell structure: further protocol optimizations are expected to lead to fully shielded scintillating nanocrystals, suitable for the considerable amount of applications of LSC needing water stability.

Key points

-  **Liquid scintillation** is a powerful technique that is primarily used in radioactivity level measurements for environmental, medical and security purposes, in the study of biochemical mechanisms, in international high energy physics experiments and in metrology.
-  **Traditional liquid scintillating cocktails** are **organic mixtures** composed of a solvent, a dye, a wavelength shifter and some stabilizers. The scintillation process in these systems involves **chain energy transfers** from the solvent to the dissolved active molecules.
-  CsPbBr₃ **lead halide perovskite nanocrystals** have been studied in this work as the **primary emitter of a liquid scintillator**, in order to evaluate their performances and to understand the energy deposition process.
-  Several steps of sample quality improvement were conducted, involving **size selection** via selective precipitation and multiple **chemical treatments** aiming to repair the **surface defects**: the most stable and bright colloidal CsPbBr₃ dispersions were obtained after treatment with **hexylammonium benzoate**.
-  CsPbBr₃ nanocrystals were tested via the **Triple to Double Coincidence Ratio** technique, which showed for the chemically treated samples results comparable with the "Ultima Gold" liquid scintillation standard. The results allowed to determine the **energy deposition mechanism**, which is dominated by the **direct excitation** of the colloidal nanocrystals by the radioactive source.
-  Many applications of routine liquid scintillation-based measurements involve analytes dissolved in **water media**. The ionic nature of CsPbBr₃ makes them chemically unstable towards water: experimental tests were then conducted in order to grow a **core/shell heterostructure** where either CdS or ZnS nanostructures would shield CsPbBr₃ from the polar environment.
-  A **successful CsPbBr₃/ZnS core/shell heterostructure** was obtained, showing a **raspberry-like morphology**: further experimental test are planned in order to optimize the CsPbBr₃ nanocrystals surface covering and thus their successful **stabilization in water**, allowing their further exploitation in liquid scintillation-based techniques.

Chapter 4

Energy transfers in perovskite nanostructures

As discussed in Chapter 1, the small Stokes shift of lead halide perovskite nanocrystals can be an issue when scintillation processes are involved, as typically the latter benefit from a high quantity of matter: the risk of self-absorption of the emitted light, caused by the overlap between the optical absorption and emission spectra, draws a limit in the possible amount of nanocrystals that it is possible to load in a sample. Moreover, the self-absorption phenomenon also delays part of the detected light, which is a critical aspect when fast timing is foreseen. In Chapter 3 it has been discussed how in a liquid scintillator system, if the role of the primary energy collector is played by the solvent, this nanocrystals limited concentration issue would be overcome, as the incident energy would be collected by the high amount of solvent and then transferred to the final light emitter, without the latter's low concentration limiting the amount of energy absorbed by the system.

The same approach can be applied to solid multi-component systems, by engineering the coupling between different structures, as bulk crystals, nanoplatelets of different thicknesses and nanocubes. The aim is here again to establish a transfer from a first component present in high percentage, acting as the energy collector and transferring this energy to a second component, which releases it as a radiative emission: this emission wavelength not being in the absorption range of the energy collector, the light would be much less likely to get re-absorbed by the system. Thus, the following chapter discusses different strategies explored in order to enhance the overall luminescence of multi-component systems without having to increase the CsPbBr₃ nanocrystals concentration until strongly self-absorbing levels.

4.1 Perovskite coupling in scintillating heterostructures

As introduced in Chapter 1, the main issue with nanocrystals embedded in a typical polymeric matrix is the resulting composite's poor density, which implies a poor stopping power against ionizing radiations. Nevertheless, the stopping power is an important factor for scintillators, as it impacts the probability of interaction with the incident radiation and thus the probability of light emission. Interesting alternatives to a polymeric matrix exist and are found in literature: as a first example, in the work of Cao et al.,[248] a heterostructure is developed where the matrix consist in a bulk Cs_4PbBr_6 host, where highly emissive CsPbBr_3 nanocrystals are embedded. This solution is claimed not only to enhance the attenuation of X-rays, but also to give high chemical stability to the CsPbBr_3 NCs.

Another approach is described among the community working on the possible solutions to satisfy the ideal performances needed for TOF-PET technologies: the currently used detectors consist in LSO:Ce single crystals, due to their high luminescence and availability, but showing a time response which is far from the nanosecond-one needed to optimize the time resolution of the detectors.[399–401] To bypass the current performance limitations, the concept of a heterostructured detectors has been proposed,[402, 403] and has become one of the trending approaches explored for TOF-PET detectors.[404]. This approach aims at splitting the scintillation mechanisms between two materials, one acting primarily as an absorber and one as an ultra-fast emitter. In fact, the excited photoelectrons produced by the interaction between the ionizing radiation and a material, when undergoing the relaxation processes, deposit amounts of energy all along their path: thus, if a dense component is at close distance to a fast emitter, an interaction with a γ ray occurring in the dense component can result in the radioluminescence from the fast emitter.

Therefore, a possible solution to the self-absorption issue of perovskite nanomaterials can be an efficient energy sharing from a dense surrounding matrix, which would result in the perovskite only having the role of emitting the light induced by the photoelectrons produced in the dense matrix. This would thus lead to a bright and ultrafast light emission, because of the combination between the high stopping power of the bulk matrix and the fast timing properties of the perovskite nanomaterial.

The design rules for these heterostructured detectors are outlined in the work of Krause et al.,[405] presenting a survey of heterostructure performances as a function of the detector design. The study reports the consequences of the detector's design on various parameters, among which the energy sharing between the two components is of particular

interest. Based on these considerations, Rogers et al. applied this approach on a fiber-type heterostructured scintillator,[29] consisting in two-dimensional perovskite crystals grown from solution inside functionalized BGO crystals. Their findings indicate that a portion of the radioluminescence emitted by such system does indeed come from energy sharing from BGO to the 2D perovskite, which can be a good lead for the optimization of fast-timing scintillation detectors.

Taking inspiration from the cited proofs of concept, different approaches were then developed and discussed in the further sections of this chapter, involving either energy transfers between CsPbBr₃ nanocrystals or exploiting structural doping within perovskite 2D crystals. This is considered as natural continuation of the work illustrated in the previous chapter, but simply translated to solid media: in fact, here again the aim is the understanding and exploiting of the relationship between the luminescent perovskite nanocrystals and their surroundings.

4.2 Perovskite nanostructures assemblies

Strategies applied in order to decrease the overlap between the absorption and emission spectra of species having small Stokes shifts typically involve dyes: however, perovskite nanomaterials have been proven to be able to overcome their small Stokes shift just by energy transfers engineering, without the need of adding different materials.[25, 167, 406, 407] Consequently, the here-presented approaches involve the attempts to establish energy transfers between perovskite nanostructures of different dimensionality, in order to decrease artificially the overlap between the overall system's absorption and emission spectra.[146, 147, 167]

4.2.1 Nanoplatelets and nanocubes assemblies

A first considered approach involves the coupling between perovskite nanoplatelets and nanocubes, exploiting their different spectral features, and in particular the nanocubes' higher PLQY. The typical absorption and photoluminescence features of nanocubes or nanoplatelets samples, respectively in Figure 4.1 (a) and (b), show that the nanoplatelets emission spectra, whichever thickness considered, fall in the nanocubes absorption range, whereas the nanocubes' PL emission wavelength is poorly absorbed by the nanoplatelets. This observation satisfies one of the criteria allowing Forster energy transfers (FRET) between species,[366, 367] thus the non-radiative energy transfer between two closely spaced molecules, where the donors's emission spectrum overlaps the acceptor's absorption one. Another key parameter involved in FRET processes is the distance between

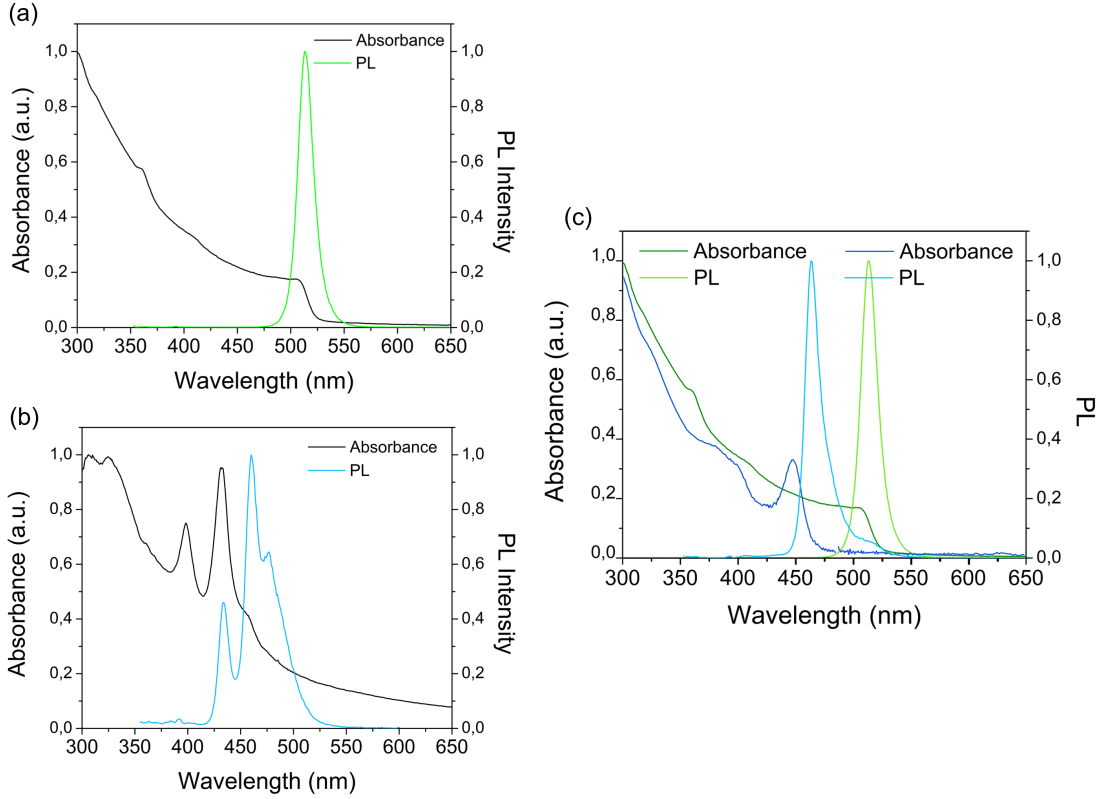


FIGURE 4.1: Absorption and photoluminescence ($\lambda_{\text{exc}} = 350$ nm) of typical CsPbBr₃ nanocubes (a) and n=1,2,3 nanoplatelets (b); overlap between such spectra for the chosen nanocubes (green lines) and nanoplatelets (blue lines) mixed for the coupling tests here discussed (c).

the donor and the acceptor R , as the FRET efficiency (E) has a dependency from R^{-6} as per the dipole-dipole coupling mechanism defined as follows:[368]

$$E = \frac{1}{1 + (r/R_0)^6} \quad (4.1)$$

where R_0 is the Förster distance of the donor-acceptor pair, i.e. the distance at which the energy transfer efficiency is 50%.

Therefore, the efficiency of this kind of energy transfer depends on several factors, namely the distance between the donor and acceptor, the process being the most efficient when the molecules are separated by distances between 1-10 nm, the geometry of their interaction, meaning the respective orientations of the two species, and the respective dielectric constants.[368]

Hernández-Martínez et al. presented a study on the theory of non-radiative energy transfers (NRET) between nanostructures of different dimensionality,[143] focusing on energy transfers from nanoplatelets (quantum wells, QW) to nanoparticles (NP) of CdTe. By imposing the condition that the donor size is smaller than the separation distance

between the donor-acceptor pair and assuming the spherical symmetry of the acceptor, their work obtains the information illustrated in Figure 4.2, focused on the distance d and the angle θ_0 defined in Figure 4.2 (a).

In particular, the NRET rate in Figure 4.2 (b) appears to be favored by both short distances d and small angles θ_0 , as the rate decreases very fast as d and θ_0 increase. Figure 4.2 (c) depicts the contour profile plot for the QW-to-NP transfer rate, with the top panel illustrating the energy transfer rate as a function of the distance, at a fixed angle θ_0 , and the right panel showing the transfer rate as a function of the angle at a fixed distance. The authors notice that the transfer rate in this QW-to-NP case follows the same distance dependency as the nanoparticle-to-nanoparticle and nanowire-to-nanoparticle transfer rate, thus being inversely proportional to d^6 .^[408] Consequently, they suggest the NRET rates are dictated by the acceptor's dimensionality, but not the donor's. Therefore, it appears that the transfer rate strongly depends on both the angle and the distance.

Consequently, it is clear that the here discussed approach, aimed to induce NRET between CsPbBr₃ nanoplatelets and nanocubes, will be highly impacted by the geometry of their interactions, which would be optimal between nanostructures of adapted lateral sizes, at short distances and small angles.

The configurations in which these species dry with respect to each other is difficult to anticipate, thus a set of exploration samples was prepared. The aim was to observe the light outputs from different nanoplatelets-to-nanocubes ratios and test if the nanoplatelets could be efficient energy donors towards the nanocubes. Samples of the two different morphologies were separately synthesised, in particular by choosing a monodisperse population of thick platelets ($n=4$) with optimal overlap of its PL emission with the chosen nanocubes absorption spectrum, as shown by the spectra in Figure 4.1 (c). Appropriate amounts of these samples were then mixed together with PMAO as an embedding matrix:^[235] these mixtures were then dried over Si wafers, obtaining the samples in Figure 4.3 (a), (b).

The obtained photo- and radioluminescence spectra are shown in Figure 4.3 (c) and (d). It is interesting to compare the two behaviours: first, considering the mixtures of nanocubes and nanocrystals, the intensities of the PL peaks associated with the nanocubes, at 525 nm, increase linearly with the increasing relative amount of nanoplatelets in the mixture, as depicted in Figure 4.3 (e). On the other hand, the RL peaks associated with the nanocubes show a less consistent increase, but they also suggest a performance improvement at increasing amount of nanoplatelets (Figure 4.3 (f)). Seeing both the PL and RL nanocubes-associated emissions increase as a function of the increasing amount of nanoplatelets gives a clear indication that energy transfers do occur within the dried

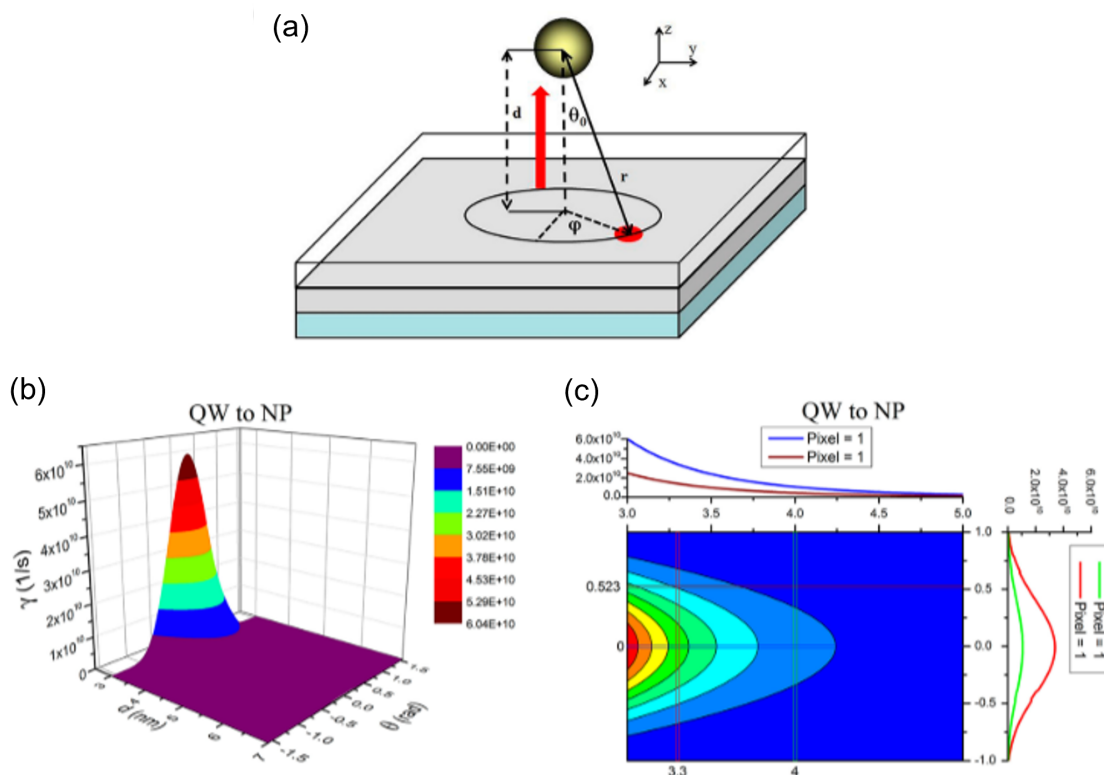


FIGURE 4.2: Schematic for the energy transfer from a quantum well to a nanoparticle (a), where red arrows show the energy transfer direction, red circles represent an exciton in the α -direction, d is the separation distance, θ_0 is the azimuthal angle between d and r , and ϕ is the radial angle. Average NRET rate for the CdTe QW-to-NP pair as a function of the distance and angle (b). Contour profile map for the average NRET rate for the CdTe QW-to-NP pair, with the top panel at a fixed angle (blue and wine curves representing the cases at $\theta_0 = 0$ and $\theta_0 = \pi/6$, respectively) and right panel at a fixed distance (red and green curves representing the cases at $d = 3.3$ nm and $d = 4.0$ nm, respectively) (c). Reproduced from the work of Hernández-Martínez et al.[143]

films, whether radiative or not. Moreover, the PL spectra show that the nanocubes alone produce a 525 nm emission comparable to the one of the nanoplatelets-to-nanocubes ratio of 2: this suggest that, in order to observe energy transfers in such mixtures, it is necessary to increase the nanoplatelets:nanocubes molar ratio beyond the 2:0 threshold.

On the other hand, the trend followed by the nanocubes-associated radioluminescence is not as easy to rationalise, probably due to the higher penetration power of X-rays and to the different relaxation mechanisms involved in scintillation compared to fluorescence, as described in Chapter 1.

Further information can be obtained from the emission time decays features: the PL time decay maps centered on the nanocubes' emission wavelength are presented in Figure 4.4. It is observed that the sample exclusively containing nanocubes shows faster emission, concentrated in the first 2 ns, whereas each of the mixed samples is more impacted by a second, slower component. As a matter of facts, no significant difference is detected

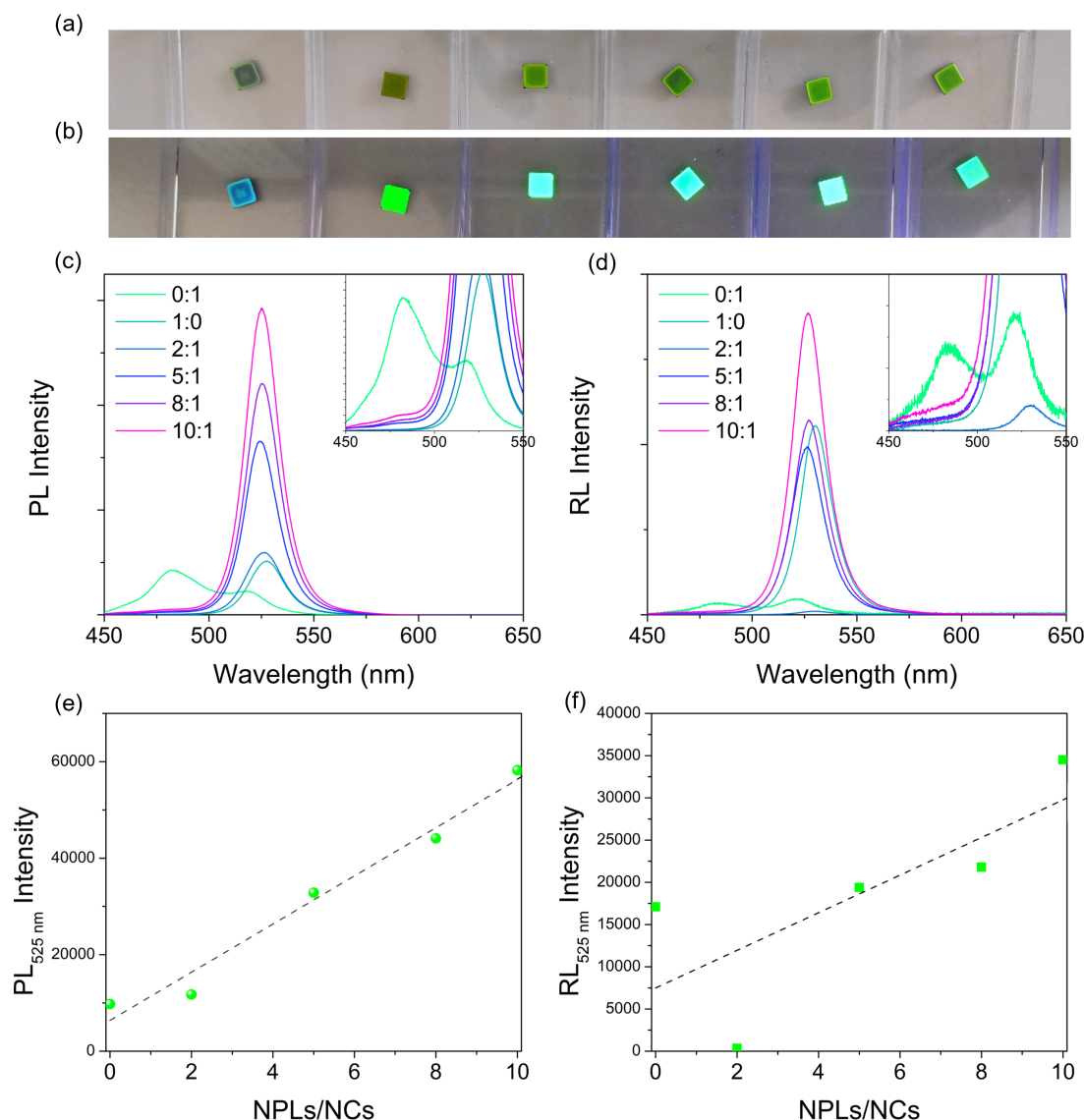


FIGURE 4.3: The tested samples involving the coupling between nanoplatelets and nanocubes are shown, either under natural light or under $\lambda_{\text{exc}} = 405$ nm excitation, respectively in (a) and (b): from left to right, the first sample contains nanoplatelets only, and the second nanocubes only, whereas by proceeding towards the right the samples involve nanoplatelets-to-nanocubes ratios of 2:1, 5:1, 8:1 and 10:1. The corresponding photo- and radioluminescence spectra are depicted, respectively under $\lambda_{\text{exc}} = 405$ nm (c) and 20 kV, 30 mA X-ray excitation (d). Below, the progression of the intensity of the emissions at $\lambda = 525$ nm are plotted as a function of the nanoplatelets/nanocubes ratio, respectively in (e) for the PL and (f) for the RL.

between the behaviours of the mixtures, which does not help giving more insights on the light PL emission processes occurring in the systems.

The most probable issue interfering with the reproducibility of these experiments relies in the way the different populations of nanocubes and nanoplatelets dry with respect one to another: as stated above, the most important factors impacting on the efficiency of the FRET phenomenon is the proximity between the energy donor and acceptor and the

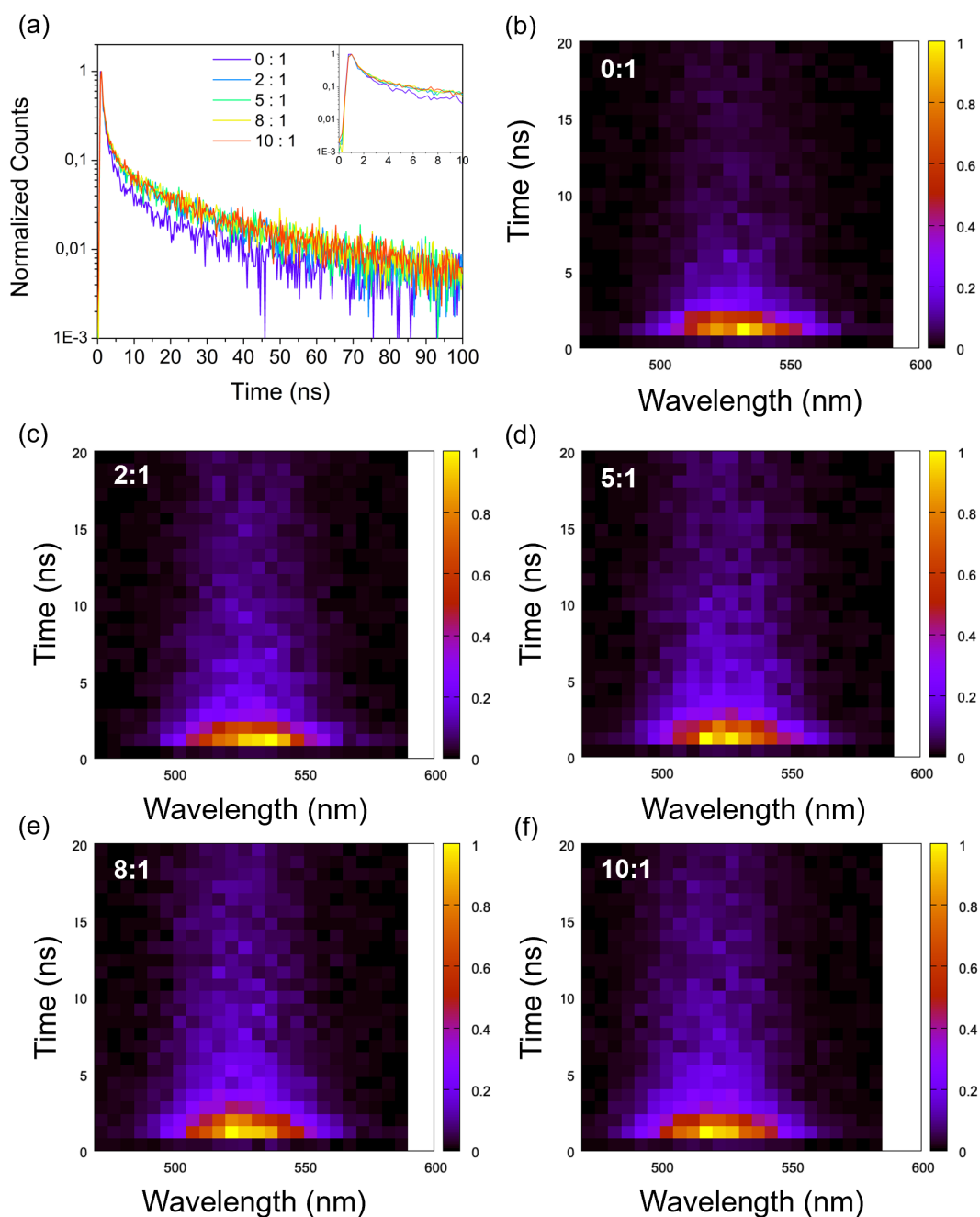


FIGURE 4.4: Photoluminescence time decay curves of the mixtures dried over Si wafers corresponding to nanoplatelets:nanocubes molar ratios of 0:1, 2:1, 5:1, 8:1 and 10:1, with a top-right inset zooming on the first 10 ns (a). The corresponding PL time decay maps of the first 20 ns of emission as a function of the emission wavelength are also shown, respectively in (b), (c), (d), (e), (f). These PL emission decays are obtained under $\lambda_{\text{exc}} = 405$ nm pulsed excitation (1 MHz).

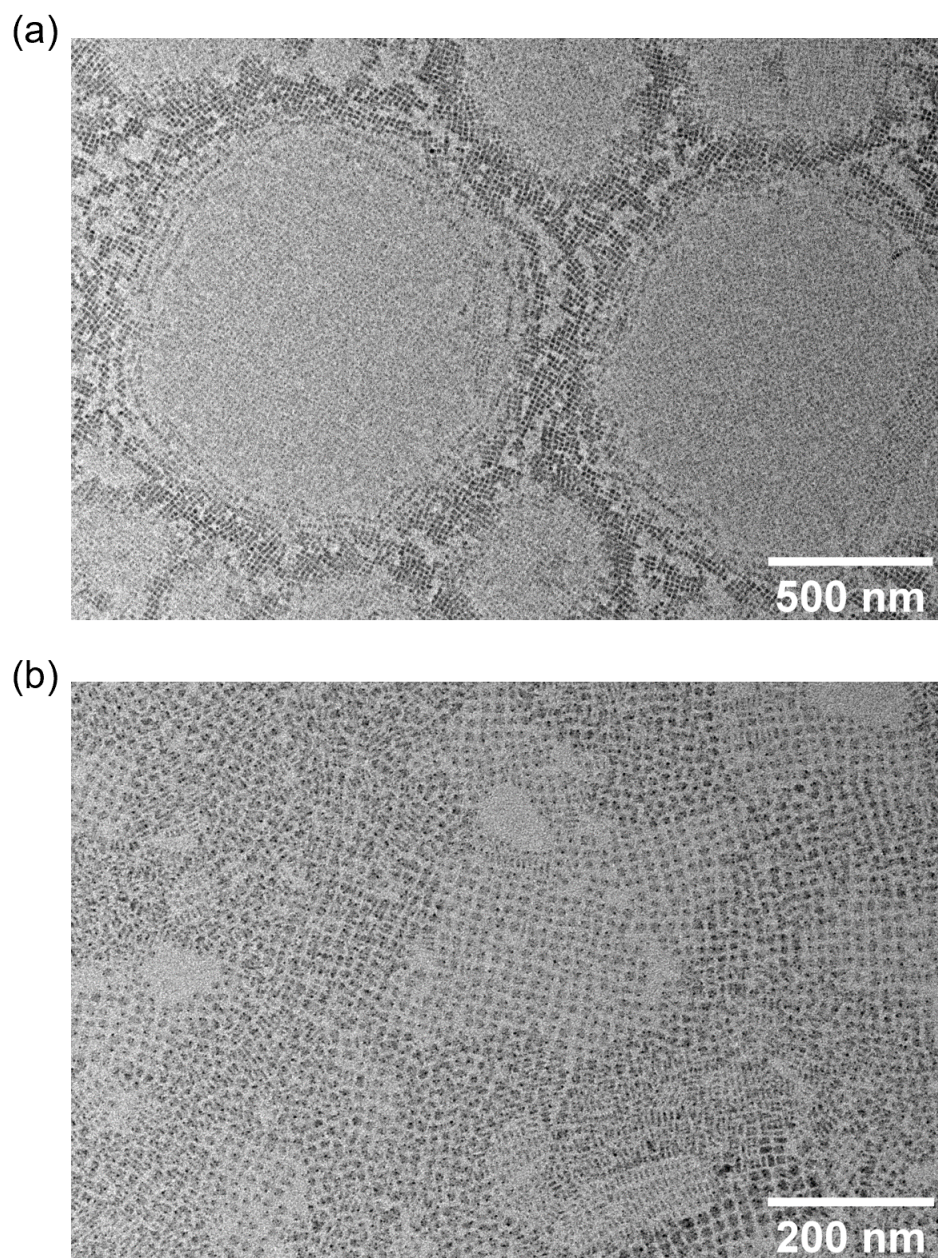


FIGURE 4.5: TEM images, at smaller (a) and higher magnification (b), showing the way nanoplatelets and nanocubes populations dry by segregating separately with respect to one another.

angle with which they interact. Consequently, in the ideal nanocubes and nanoplatelets mixture, the two different species should have to evenly dry leaning one on the other. Nevertheless, TEM observations as in Figure 4.5 show that, even though the lateral dimensions of the chosen platelets match the nanocubes' edge size, the two populations can be found in the same sample either separately segregated, as in Figure 4.5 (a), with the nanoplatelets crystallizing in stacks, or actually dry in proximity to each other, as in Figure 4.5 (b).

Since imposing to the nanoplatelets to uniformly dry laying on the nanocubes surfaces is not straightforward, these mixed systems can be difficult to control: nevertheless, energy transfers from the nanoplatelets to the nanocubes were indeed observed, and developing some strategies to force a more even contact between the two populations would be a good pathway to follow in order to artificially engineer the Stokes shift of such nanostructures.

4.2.2 Nanoplatelets stacks

Yet, this tendency of perovskite nanoplatelets to stack together can be used to this cause's benefit, to design a multi-component system with the same goal of the just discussed mixture, i.e. an artificial way to increase the overall system's Stokes shift by exploiting energy transfers among the components.[146, 147] As a matter of fact, by designing a mixture of nanoplatelets of increasing thicknesses, as illustrated in Figure 4.6, the corresponding thickness-dependent absorption peaks and PL emissions are expected to satisfy again one of the criteria needed for FRET transfers to occur, thus the donor's emission peak overlapping the acceptor's absorption spectrum.

Moreover, in this case, the drying dynamics of the nanoplatelets should allow the proximity between the donor and acceptors, making non-radiative energy transfers more likely to occur. These observations lead to the possibility that the thinnest nanoplatelets of the

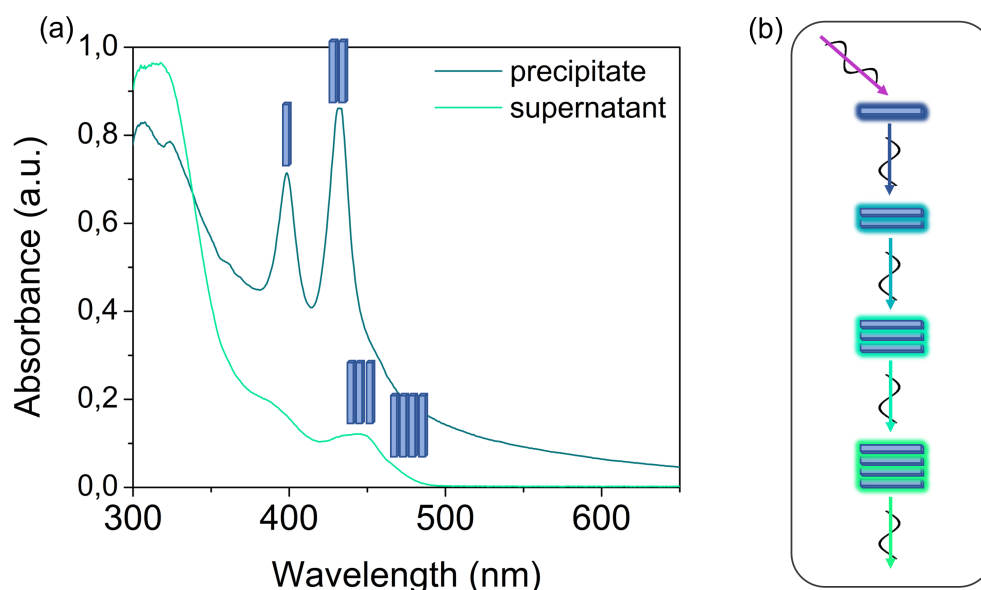


FIGURE 4.6: Nanoplatelets of thicknesses between 1 and 4 octahedra layers obtained from the developed one-pot synthesis, with the populations of $n=3,4$ highlighted by the isolation by centrifugation (a). In (b), an illustration of the idea behind these nanoplatelets stacks, aiming to produce energy transfers from the thinnest to the thickest populations.

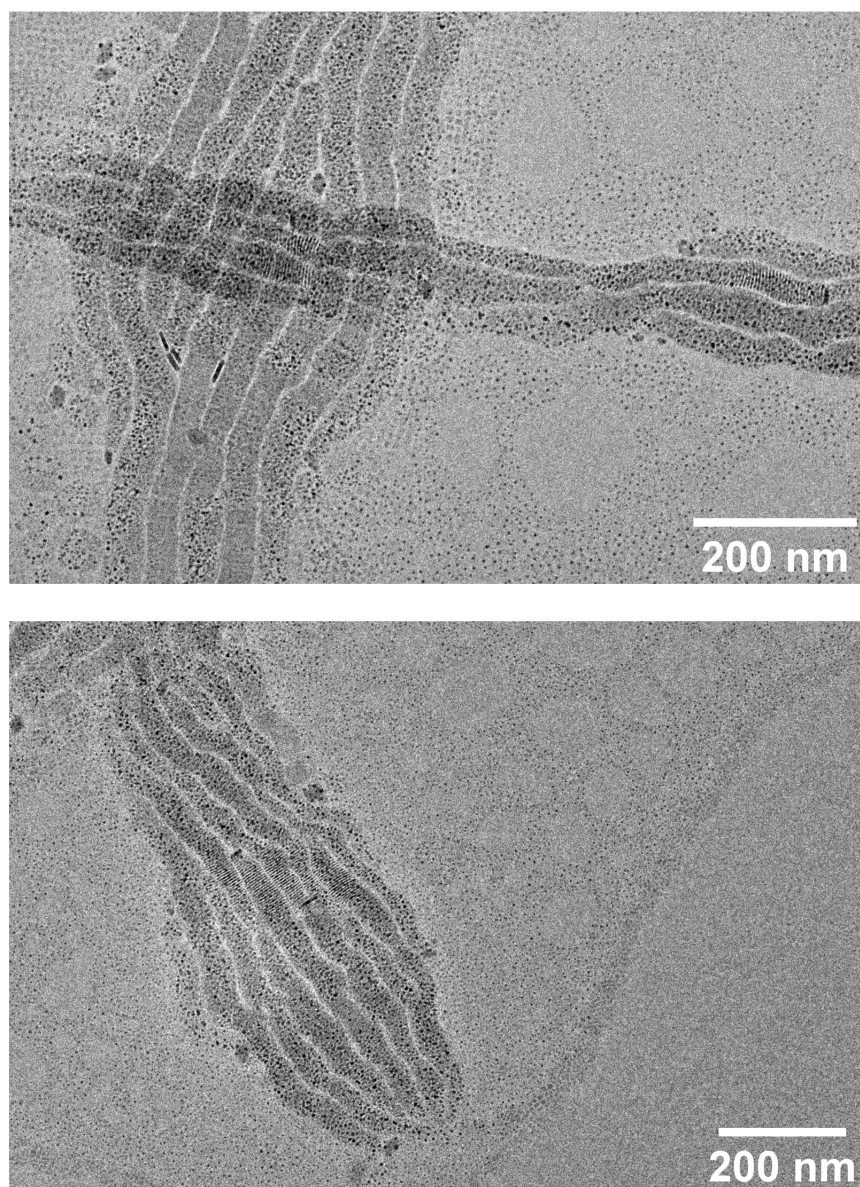


FIGURE 4.7: TEM images showing the tendency of these mixed-thicknesses perovskite nanoplatelets to stack together.

mixture would non-radiatively transfer their energy to the thickest ones, which would then play the role of the final light emitters. Once again, this chain of transfers would allow to promote an efficient emission from the thickest population, present in moderate amounts, by exciting the thinnest nanoplatelets, instead present in high amounts: this allow to avoid the high risk of self-absorption by playing on the artificial Stokes shift of the overall multi-component system. This approach is found in literature applied to a luminescent solar concentrator device:[167] since numerous attempts to reproduce the procedure described in the reference paper were unsuccessful, finally an original one-pot protocol was developed, producing a mixture of CsPbBr_3 nanoplatelets of different thickness. The synthetic protocol can be found in section 2.5. The affinity between these

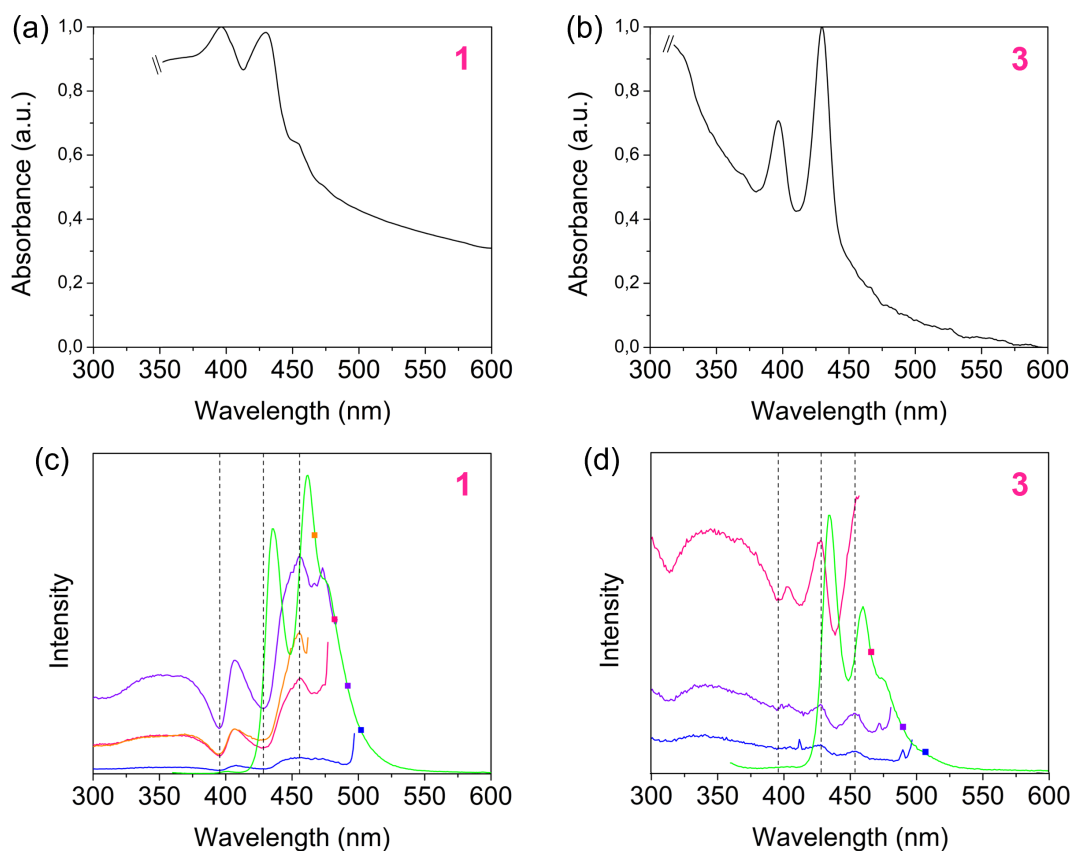


FIGURE 4.8: Absorption spectra of dried films of CsPbBr₃ nanoplatelets of different thicknesses dried on glass supports, respectively (a) and (b); the curves were cut in the low wavelength range because of instrumental artefacts due to the thickness of the films. Their corresponding PLE spectra are showed in (c) and (d). The emission wavelengths targeted by each PLE spectrum are indicated by the corresponding color square positioned over the PL spectra ($\lambda_{\text{exc}} = 350 \text{ nm}$), the latter in green.

NPLs populations during the drying process were observed through TEM microscopy, as depicted in Figure 4.7.

Thus, various amounts of the obtained mixtures were then dried over a glass support, at ambient temperature and atmosphere, in order to obtain depositions with varying quantities of matter. Figure 4.8 shows the typical results obtained for films labeled "1" and "3", the latter corresponding to the quantity of matter deposited on the glass support and thus to the films' thicknesses: namely, "1" corresponds to an approximate thickness of $0.1 \mu\text{m}$, whether "3" to less than a half of it.

The technique used in this case to evaluate the occurring of energy transfers was the evaluation of the PLE spectra, whose utilisation for similar issues has been previously developed by Baronnier et al.[409] This study is based on the principle that if the emission peak of the thickest nanoplatelets is linked to the excitation of the thinnest ones, this would be a sign of an energy transfer, even though the nature of the latter

(i.e. radiative or not) would not be determined. Here, for the film "1", on in Figure 4.8 (c), it is observed that the PLE spectra associated to the thickest nanoplatelets emission actually drop in correspondence of the thinner platelets' absorption peaks. This is interpreted as a signal that the thinnest NPLs do not transfer energy, but on the contrary they only absorb the light provided by the instrument during the spectrum acquisition, without participating to the targeted emission. On the other hand, in the case of very thin samples, the PLE spectra related to the thickest platelets' emission show positive peaks corresponding to the $n=2$ and $n=3$ ones, as shown in Figure 4.8 (d). This do imply a transfer, either radiative or not, which could be further confirmed by other techniques such as Transient Absorption spectroscopy. In fact, the observation of energy transfers through PLE spectroscopy has limitations in terms of the samples thickness, which appears to be too high in the case of the "1" films. Further measurements can thus be foreseen, in order to confirm the efficiency of such energy transfers also in thicker films.

Examples of radioluminescence spectra recorded from these multi-component NPLs mixtures are here shown: Figure 4.9 shows the comparison between RL and PL spectra of two different "1" samples, obtained by drying the same amounts of nanoplatelets mixtures from samples synthesized in the same way. Even though the systems should be equivalent, the observed behaviors are different: in the one on the left, the radioluminescence spectrum features peaks at higher wavelength than the ones present in the corresponding PL, whereas in the right one the peak positions of the RL spectrum match the photoluminescence ones. Therefore, despite reproducibility issues probably due to differences in the order of the nanoplatelets stacks from one sample to the other, probably due to the superposition of layers of NPLs one above the other, the energy coupling between the nanoplatelets of different thickness looks successful. In fact, the stacks formed by the NPLs during their crystallization favor the light emissions at high

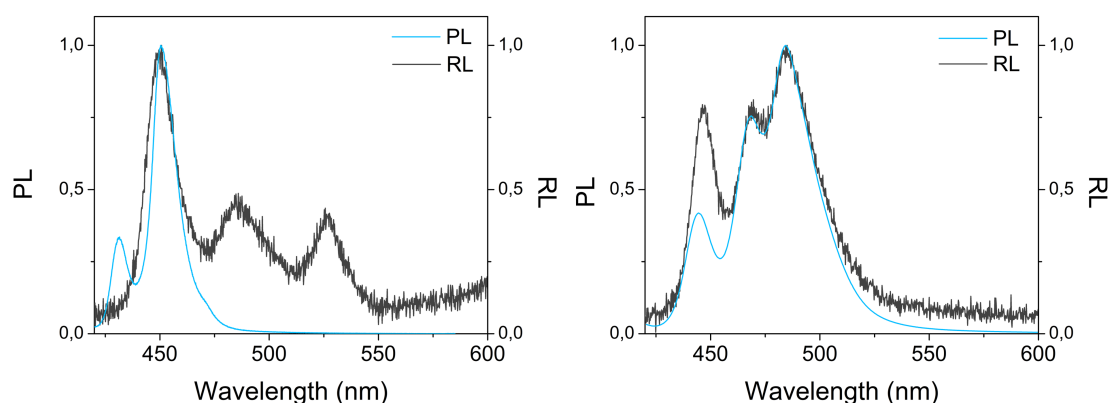


FIGURE 4.9: Comparison between the photo- and radioluminescence spectra of "thick" films from two identically-obtained mixtures of CsPbBr₃ nanoplatelets of $n \geq 1$.

wavelength, despite the lower amount of $n > 3$ nanoplatelets in the samples, under both photo- and X ray excitation.

In conclusion, this approach designed to improve the light emission efficiency from mixtures of CsPbBr_3 nanoplatelets of different thicknesses, by artificially engineering the overall system's Stokes shift, led to successful results. The energy transfers from the $n=2$ population of NPLs to the thicker ones were detected via the study of their PLE spectra: however, other techniques such as transient absorption spectroscopy would be a good implementation to this study, as the outcome would be less hindered by the excessive thickness of some of the tested films. This approach was found to be suitable for applications based on scintillation too, whereas further optimizations would be needed to better manipulate the order of the nanoplatelets stacks, and thus achieving better reproducibility of the photo- and radioluminescence features of identically-obtained thick films.

4.3 Cs-doped halide perovskite 2D nanostructures

Organic/inorganic hybrid perovskites can be grown from solution in the form of bulk crystals while keeping features typical of 2D dimensionality, such as their low fabrication costs, low intrinsic trap density, nanosecond fast response and potentially high light yield, as well as a vast range of possible exploration: as a matter of facts, just like their corresponding colloidal nanocrystals, they are stable in various chemical compositions,[410] and also tolerate doping.[411] These versatile layered structures are indeed potential candidates for high light yield scintillators, as they have small band gaps between 3 and 4 eV and large exciton-binding energy.[24, 358]

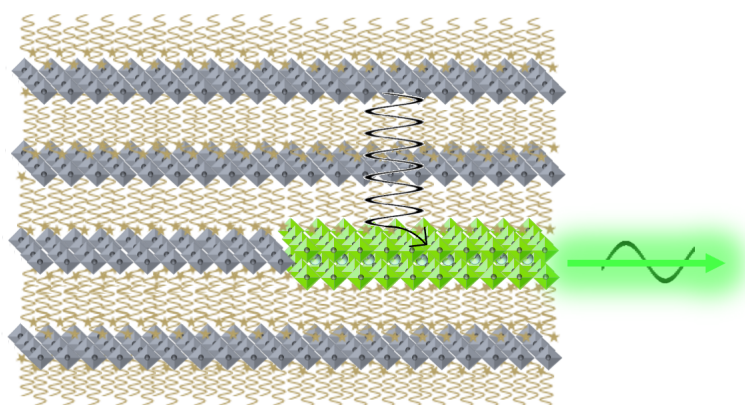


FIGURE 4.10: Illustration of the approach designed to induce non-radiative energy transfers inside perovskite 2D crystals.

Consequently, the same non-radiative energy transfer principle illustrated in the previous sections was applied to two-dimensional crystals: the goal in this case is to induce the formation of sub-nanostructures inside such 2D perovskite crystals and thin films. The approach was developed as part of a collaboration with the Nanyang Technological University of Singapore, in particular with Professors C. Dang and M. Birowosuto, and Doctor F. Maddalena, and it is illustrated in Figure 4.10: by inducing the formation of local areas where a CsPbBr_3 bilayer has crystallized between perovskite monolayers, it could be possible for FRET to occur, from the monolayers to the bilayers. Thus, by varying the protocol of synthesis from solution, namely by adding small amounts of a Cs^+ precursor to an otherwise Cs-free perovskite reaction mixture, the formation of local bilayers of CsPbBr_3 among the 2D perovskite monolayers was studied.

Following this approach, $\text{PEA}_2\text{PbBr}_4$ samples were compared as either thin films drop-cast on glass or Si support or as 2D crystals grown from solution as described by Xie et al.,[358] with the addition of Cs^+ in Cs:Pb various molar ratios. The synthetic protocols

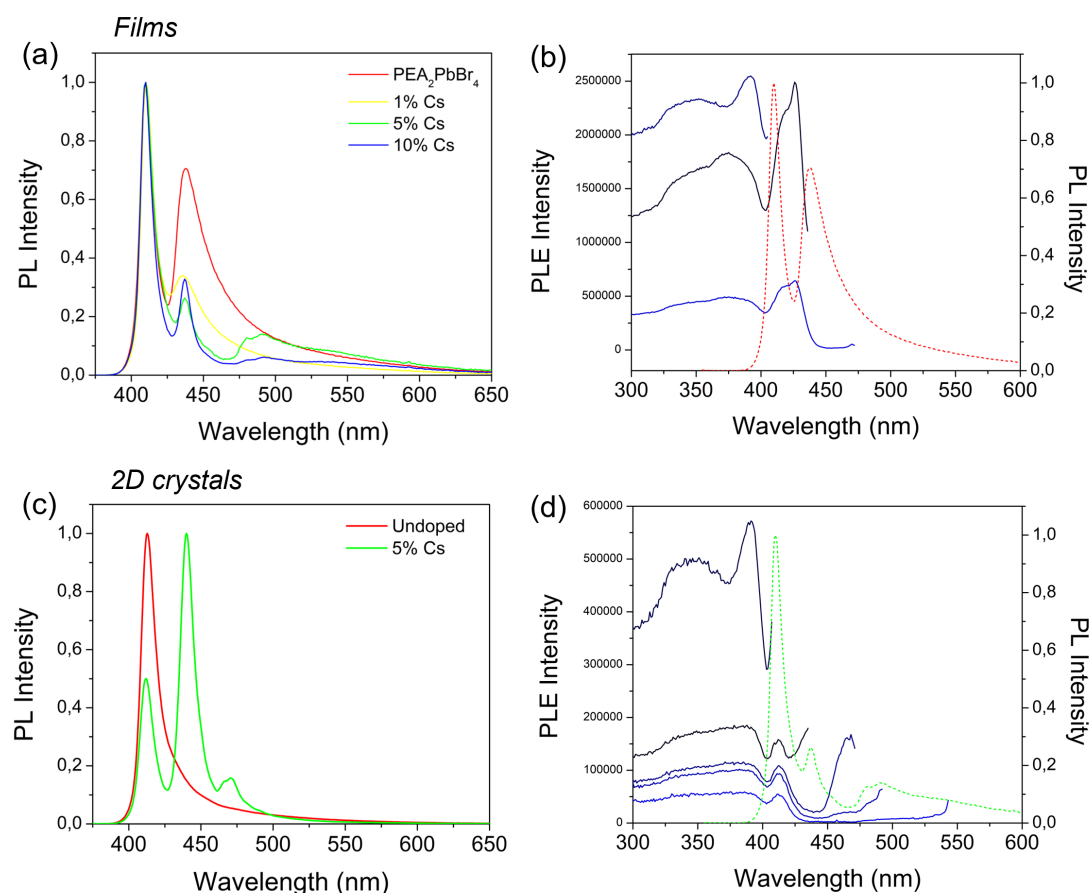


FIGURE 4.11: On the left, the photoluminescence spectra ($\lambda_{\text{exc}} = 355 \text{ nm}$) of undoped and Cs-doped $\text{PEA}_2\text{PbBr}_4$ perovskite thin films or 2D crystals, respectively (a) and (c). On the right, the PLE spectra associated with the main PL peaks of the thin films either undoped (b) or doped with 5% Cs (d).

can be found in section 2.6. Starting with $\text{PEA}_2\text{PbBr}_4$ thin films (Figure 4.11 (a)), it is observed that for all the measured samples the dominant peak is the one corresponding to the PL emission from the monolayers, at 410 nm; the untreated sample also presents a strong emission at 435 nm, which would be associated with bilayers, if cations were present and allow their formation. In this case, the current information does not allow the assignation of this peak for the undoped system. This 435 nm signal gets much weaker with the addition of Cs in the structure and it is the only additional feature observed for the 1% Cs sample. Instead, the 5% Cs thin film shows multiple emission bands at wavelength higher than 475 nm, which could be attributed to either layers thicker than $n=4$, or to the local presence of 3D perovskite nanocubes; similar emission bands are observed in the case of 10% Cs, but much weaker. The PLE spectra recorded on the 5% Cs thin films, in Figure 4.11 (d), do not show signs of energy transfers from the thinner layers to the thicker, as no peaks associated to the mono- or bilayers appear in the PLE spectra centered on the long wavelength emissions.

It is then interesting to observe the difference between the photoluminescence spectrum of the single crystal produced with the addition of 5% Cs, compared to the undoped one. As a matter of facts, three emission peaks appear, associated with mono- bi- and tri-layers, with the dominant signal being the one of the bi-layers; on the contrary, the monolayers signal gets reduced by 50%. Since these spectra are recorded at a λ_{exc} of 355 nm, this single crystal appears to have gained in its Stokes shift thanks to the 5% doping with caesium.

A very different behavior is observed in the case of BA_2PbBr_4 samples: starting with the thin films (Figure 4.12 (a)), the PL of the undoped sample features two peaks, the most intense one centered at 410 nm, typical of monolayers, and a second one at 437 nm, again suggesting the presence of bilayers, even though no large A^+ cation is present. The spectrum evolves when a Cs:Pb ratio of 1:100 is added, as the emission associated with the bilayers doubles of intensity. The outcome is very different after the addition of 5% Cs, as the most intense emission is still coming from monolayers, but many new peaks appear: the bilayers' emission is weaker than the pure BA_2PbBr_4 , whereas a quite intense emission centered at 465 nm rises, as well as a shoulder at 480 nm, a peak at 493 nm and another shoulder at 510 nm. All of these emission features are typical of increasing n -layers, until that 510 nm emission that looks more like the presence of 3D nanostructures: it is then surprising to see that the addition of 10% Cs, instead of following this tendency, shows instead the presence of mono, bi- and tri-layers only.

In order to observe if an energy transfer occurs between the different n -layers, the PLE spectra were analyzed in more detail: the curves associated with the monolayers of the 5% Cs sample, in Figure 4.12 (b), actually match the undoped BA_2PbBr_4 (Figure 4.12

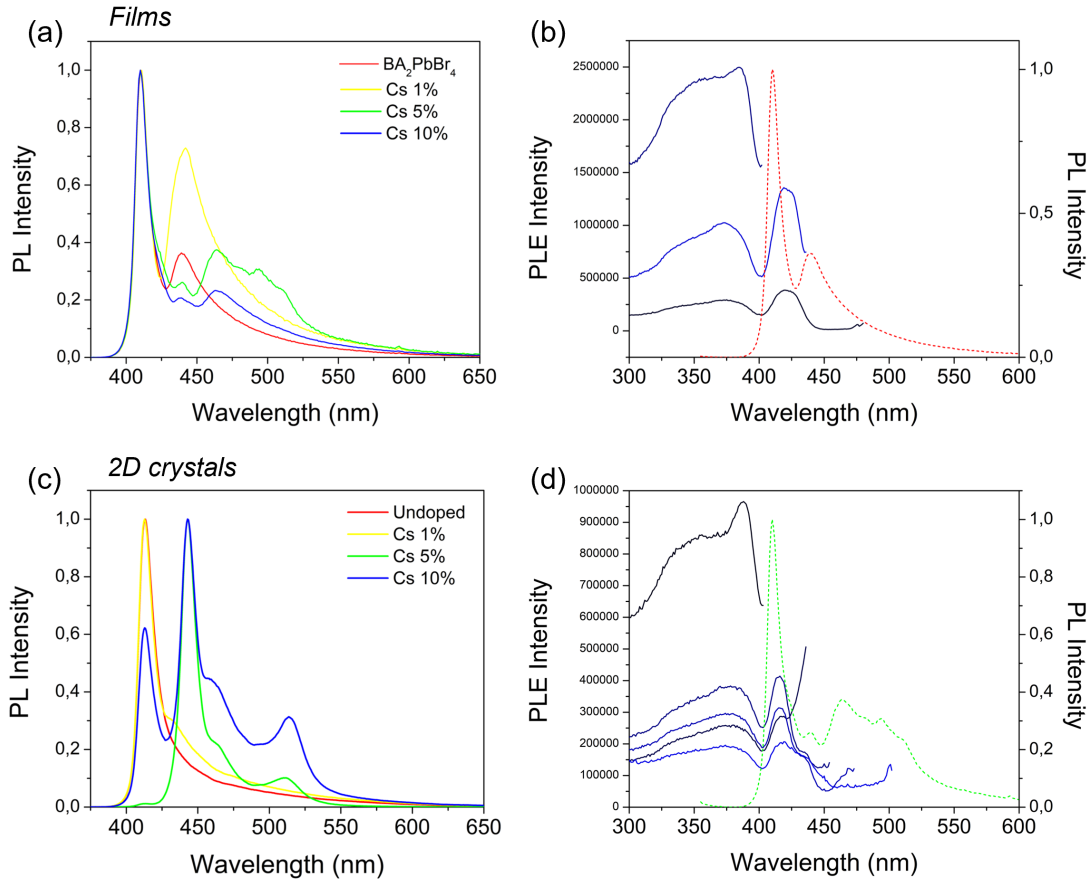


FIGURE 4.12: On the left, the photoluminescence spectra ($\lambda_{\text{exc}} = 355 \text{ nm}$) of undoped and Cs-doped BA_2PbBr_4 perovskite thin films or 2D crystals, respectively (a) and (c). On the right, the PLE spectra associated with the main PL peaks of the thin films either undoped (b) or doped with 5% Cs (d).

(c)), with the monolayer-associated wavelength causing an intensity drop in each of the PLE spectra, as the opposite of what would be expected in case of an energy transfer from the monolayers to the others. A clear signal is observed instead at around 435 nm, thus the bilayers, that appear to be involved in each of the lower energy emissions: it thus look like the addition of 5% Cs has in fact produced local layers of multiple thickness, with the bilayers being able to transfer energy to the thicker ones.

The different behavior depending on the amount of caesium present in the BA_2PbBr_4 thin films could be consistent with the PL spectra obtained from the Cs-doping of the corresponding single crystals. As shown in Figure 4.12 (b), while the undoped crystal only emits at 410 nm and the addition of 1% Cs only adds a shoulder around 435 nm, the further addition of Cs has a very different outcome: surprisingly, the crystal doped with 5% Cs has the monolayers' emission almost completely suppressed, with the PL spectrum being now dominated by the bilayers' emission at 435 nm, together with a shoulder appearing at 465 nm and another band at 512 nm looking like 3D perovskite nanostructures. This result is remarkable, as the spectrum is recorded under

an excitation wavelength of 355 nm, and in this case the Stokes shift looks much larger than any other sample in this work. Then, this tendency is again not followed by the 10% addition, which shows back the monolayers' peak, even though it is no longer the dominant one.

The features of the Cs-doped BA_2PbBr_4 were further explored by observing the behaviour of intermediate Cs:Pb ratios between a minimum of 0% Cs and a maximum of 10% Cs in thin films. Their absorption spectra, in Figure 4.13 (a), show the peaks associated with $n \geq 2$ increase at increasing amount of Cs^+ added in the precursors solution photoluminescence associated with the $n \geq 2$ layers is highlighted in Figure 4.13 (b), and the increase of the respective peaks' intensities is plotted as a function of the Cs^+ concentration in the structures (Figure 4.13 (c)). These plots show slightly different behaviors depending on the emitter: first, all the $n > 2$ populations experience a swift

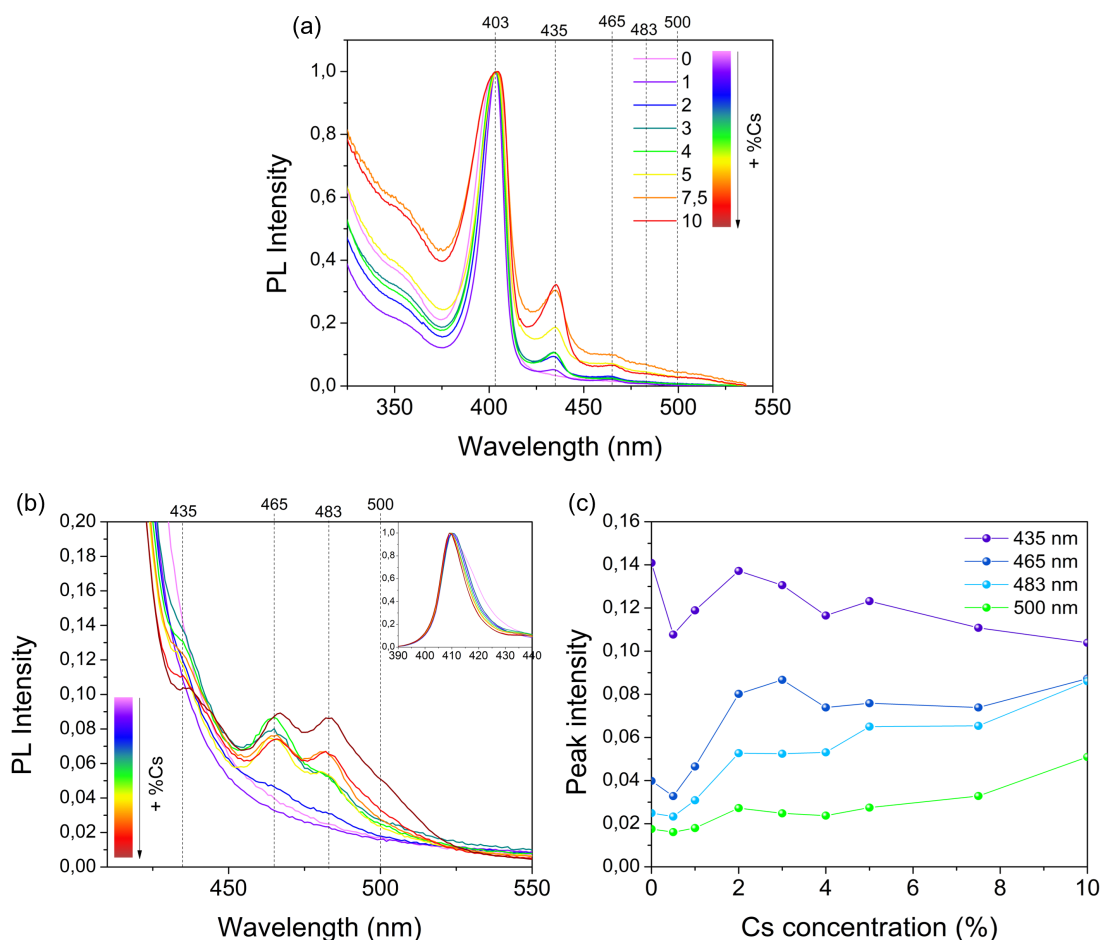


FIGURE 4.13: Absorption (a) and photoluminescence spectra of the Cs-doped BA_2PbBr_4 thin films, untreated or added with Cs:Pb ratios of 0.5, 1, 2, 3, 4, 5, 7.5 and 10%. The spectra in (b) are zoomed in the emission area of the $n \geq 2$ layers, whereas the inset at the upper right shows the entirety of the spectral range. The intensities of the PL peaks associated with the layers of different thickness are then plotted as a function of the Cs^+ concentration in the thin film (c).

increase in their photoluminescence when the Cs concentration is increased from 0% to 2%, with the exclusion of the intensities detected for the sample with 0.5% Cs. Nevertheless, as it can be observed in the upper-right inset in Figure 4.13 (b), the shape of the pure, Cs-free BA_2PbBr_4 thin film's PL emission is broader than the Cs-doped ones, suggesting that the sample contains itself some structural alterations compared to the expected exclusively monolayered structure. Therefore, the lower intensities of the 0.5 % Cs thin film has rather to be attributed to the larger tail of the $n=1$ PL peak of the Cs-free sample.

The PL peaks then keep on increasing for increasing Cs concentration, at a rather steady pace for the $n=4$ (483 nm) and 3D (500 nm) structures, whereas the $n=3$ (465 nm) emission shows an unmatched increase corresponding to the 0.5 % Cs thin film, as high as the final value obtained at 10 % Cs, the latter producing the highest PL intensity for each of the layered species.

It is of great interest that the only population showing the opposite behavior is the $n=2$ layered one, whose PL intensity steady decreases as the Cs concentration increases, particularly starting from the 2% Cs sample and on. This is of great interest, as the fact that this only population loses PL intensity, whereas the other ones' rise, can be an indicator that an energy transfer is occurring in the system, from the $n=2$ layers to the thicker ones.

The study of the photoluminescence time decay features can be an excellent tool to observe non radiative energy transfers, as typically the involved species' time responses are impacted. If a non-radiative energy transfer is occurring, the statistics of the involved donor and acceptor photoluminescence time responses change: in fact, on one hand the presence of the acceptor offers to the donor an additional de-excitation pathway, and in turn the PL decay time curve of the acceptor gets modified according to the donor's time response statistics. Consequently, typically the donor's PL decay time constant gets shorter, whereas the acceptor's one gets longer.[412]

The photoluminescence time decay curves in Figure 4.14 (a) and (b) show that the evolution of the light emission dynamics as a function of the addition of Cs is very different depending on the examined emission wavelength: namely, the 410 nm emission associated with perovskite monolayers shows a trend, where the curve gradients increase gradually approaching the intermediate Cs concentrations of 2% and 3% (dark and light green curves, respectively), and then decreases back again for higher Cs concentrations. Differently, the decay curves associated with the emission at 471 nm (Figure 4.14 (b)) show a steady decrease of the curves' gradient for increasing % Cs concentrations, which is consistent with the corresponding more intense emission at that wavelength.

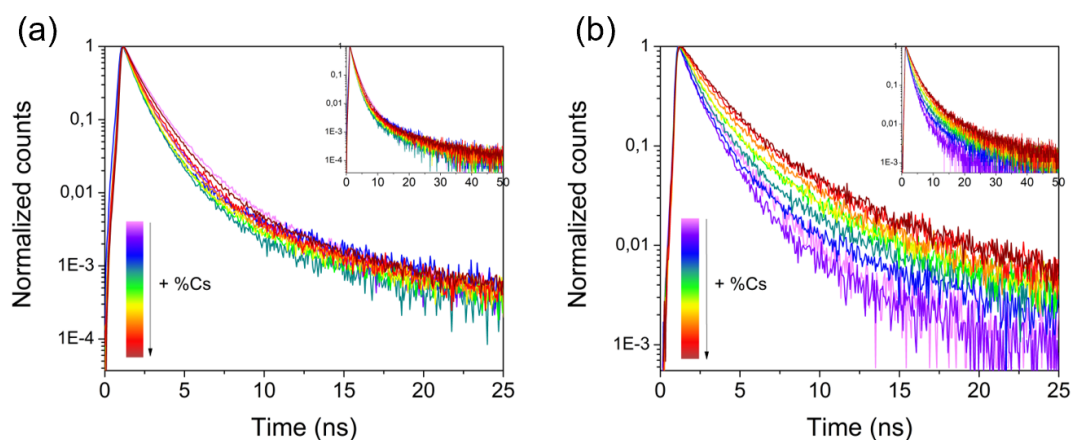


FIGURE 4.14: Photoluminescence time decay curves of the Cs-doped BA_2PbBr_4 thin films, added with progressively increasing Cs:Pb ratios, precisely 0, 0.5, 1, 2, 3, 4, 5, 7.5 and 10%. The time decay curves refer to the PL emission centered at 416 nm and 471 nm, respectively in (a) and (b).

The just described photoluminescence time responses were then analyzed via a four exponential decays fitting, and each of the parameter of interest is plotted in Figure 4.15 as a function of the increasing Cs concentration. While the time decay constants relative to the 410 nm emissions (Figure 4.15 (a)) keep a constant value, the time responses at 471 nm are quite different. As a matter of facts, the decay time constants swiftly increase when the Cs concentration reaches 2%, but then keep a constant value until the 7.5% Cs thin film. Then, all the decay time constants swiftly increase again for a Cs concentration of 10%, even though their impact on the overall performance is mitigated by the low corresponding relative light yields, as depicted in Figure 4.15 (d). Regarding these relative light yield plots, it is interesting to note that, while the τ_1 relative light yield keeps a constant value both for the emission centered at 410 nm and 471 nm, the τ_2 and τ_3 show perfectly symmetrical responses (besides for the 10% Cs concentration at 471 nm), and their behaviors are inverted, comparing the 410 nm and 471 nm cases.

All this information is summarized by the effective time decay constant τ_{eff} , a figure of merit defined in Chapter 2 that takes into account both the relative light yields associated with the multi-exponential fit and their individual decay time constants. Figure 4.15 (e) thus plots these τ_{eff} as a function of the Cs concentration. It results that, whereas the emissions at 410 nm show decreasing τ_{eff} for increasing Cs concentrations, on the contrary the ones at 471 nm increase, again with behaviors that are symmetric one with respect to the other. This is interpreted as an indication that transfers do occur in the layered system, as the phenomena leading to the 410 nm emission get substituted by the emission at longer wavelength.

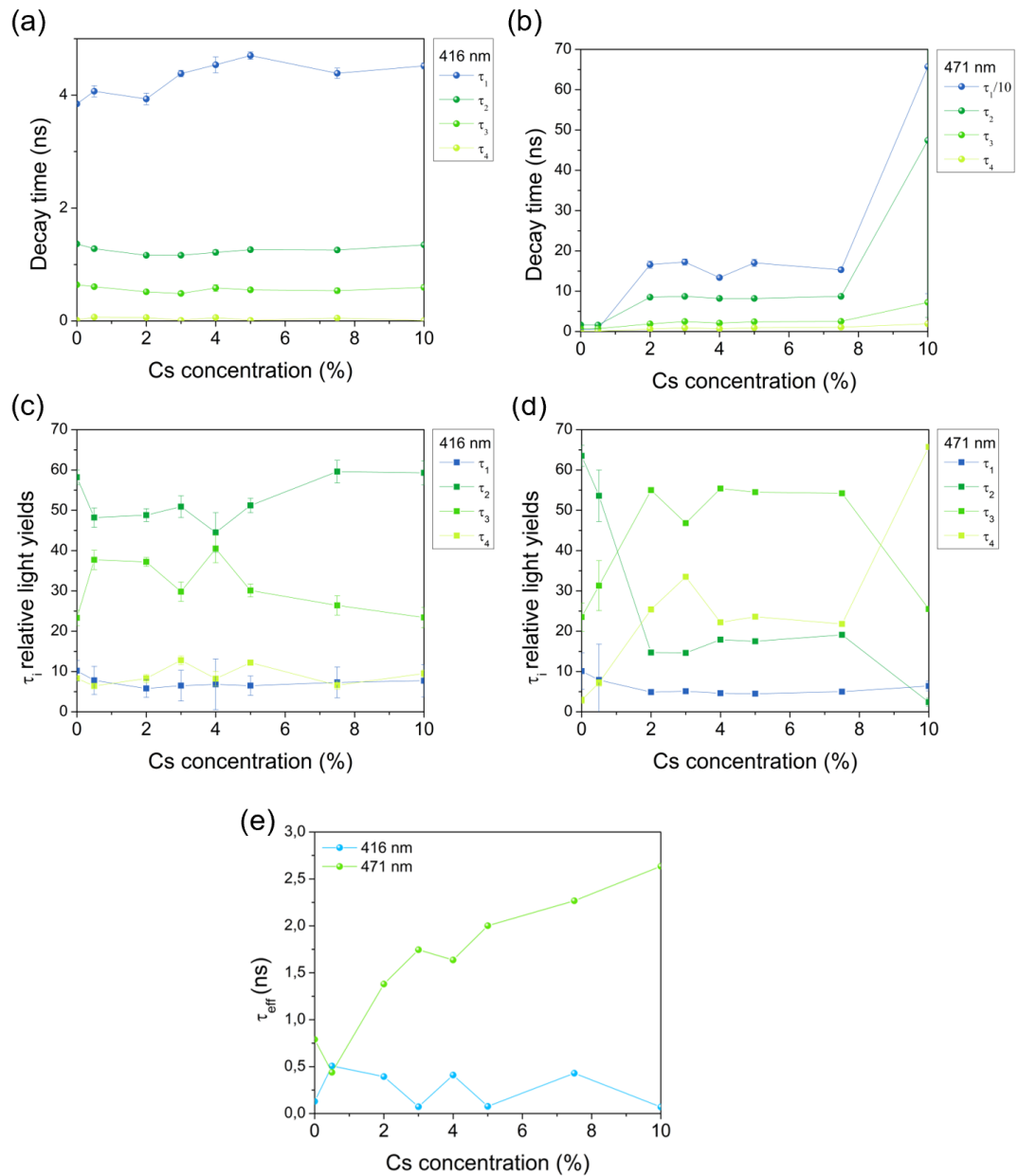


FIGURE 4.15: The decay time constants τ_i derived from a four exponential decays fit of the PL emission centered at 416 nm and 471 nm, as a function of the concentration in Cs in the thin films, respectively in (a) and (b). It has to be noted that the τ_1 response in (b) was divided by a factor of 10 for a better visualization. Below, the corresponding relative light yields (normalized to the area) of the decay time components τ_i , respectively (c) and (d). Finally, the τ_{eff} for the PL emission centered at 416 nm and 471 nm, again as a function of the concentration in Cs (e).

This set of experiments was thus successfully able to show energy transfers between layers with different thickness of perovskite Cs-doped BA_2PbBr_4 thin films, and to identify these energy transfers as non-radiative. This approach is thus suitable for improving the system's overall Stokes shift by decreasing the overlap between the absorption and emission centers. The next experimental step would then consist in optimizing the phenomenon, namely to be able to select and finely control the layers populations, and to further study these transfers inside the bulk 2D perovskite crystals. Moreover, it would be of great interest to test these multilayered systems in a heterostructured bulk material, as discussed with regard to the functionalized BGO filled with perovskite 2D crystals.

Conclusions

This chapter presented different approaches developed in order to artificially modify the Stokes shift of lead halide perovskite nanocrystals assemblies, by engineering energy transfers between the components.

First, a system consisting of mixtures of CsPbBr_3 nanoplatelets and nanocubes was studied, by comparing the nanocubes-associated photoluminescence of samples containing a fixed quantity of nanocubes and increasing amounts of nanoplatelets. Transfers from the latter to the nanocubes were indeed observed, both under photo- and X-ray excitation, even though some reproducibility issues would still benefit from further optimization. Therefore, this approach can be a good pathway to follow in order to artificially engineer the Stokes shift of such nanostructures.

A second approach involving nanoplatelets of different thickness was then presented, as these systems were expected to give rise to energy transfers for the same reasons of the above-mentioned nanoplatelets and nanocubes mixtures, but also in virtue of the NPLs tendency of crystallizing in stacks. This approach, designed to artificially engineer the overall system's Stokes shift, led to successful results: in fact, the energy transfers from the $n=2$ population of NPLs to the thicker ones were detected via the study of their PLE spectra. However, other techniques such as transient absorption spectroscopy would be a good implementation to this study, as the outcome would be less hindered by the excessive thickness of some of the tested films. This approach was found to be suitable for applications based on scintillation too, whereas further optimizations would be needed to better manipulate the order of the nanoplatelets stacks, and thus achieving better reproducibility of the photo- and radioluminescence features of identically-obtained thick films.

A final approach involving perovskite 2D structures was then presented, as part of a collaboration with the Nanyang Technological University of Singapore, in particular with Professors C. Dang and M. Birowosuto, and Doctor F. Maddalena. In this case, the aim is to induce the formation of sub-nanostructures inside such 2D perovskite crystals and thin films, again in order to exploit energy transfers to artificially increase the overall Stokes shift. This set of experiments was successfully able to show energy transfers between layers with different thickness of perovskite Cs-doped BA_2PbBr_4 thin films, and to identify these energy transfers as non-radiative. This approach is thus suitable for improving the system's overall Stokes shift, by decreasing the overlap between the absorption and emission centers. The next experimental step would then consist in optimizing the phenomenon, namely to be able to select and finely control the layers populations, and to further study these transfers inside the bulk 2D perovskite crystals. Moreover, it would be of great interest to test these multilayered systems in a heterostructured bulk material, as discussed with regard to the functionalized BGO filled with perovskite 2D crystals.

 **Key points**

- ❏ The work on the optimization of the CsPbBr₃ perovskite nanostructures light emission efficiency, by overcoming their short Stokes shift, was transposed to **solid coupled systems**, namely nanoplatelets and nanocubes mixtures, different nanoplatelets population assemblies, and Cs-doped 2D perovskite crystals.
- ❏ Experiments were conducted on assemblies of perovskite nanocrystals with different dimensionality, in order to study eventual **energy transfers**: transfers **from the nanoplatelets to the nanocubes** were indeed observed, both under photo- and X-ray excitation, even though some reproducibility issues would still benefit from further optimization.
- ❏ Further results were obtained while studying CsPbBr₃ **n nanoplatelets of different thickness**, which show the tendency to **stack together** in long chains, thus in a favorable conformation for energy transfers. The latter were indeed observed via PLE spectroscopy.
- ❏ Another tested strategy involved **organic/inorganic perovskite 2D crystals**, thus layered perovskite structures: by **doping with Cs⁺** such systems, the **formation of new local structures** within the layers was induced.
- ❏ Promising results were obtained from **Cs-doped BA₂PbBr₄ thin films**, where **energy transfers were observed** through optical spectroscopy and photoluminescence dynamics.

Conclusions and perspectives

The here presented work fits into the context of one of the most active research fields over the last 40 years, i.e. semiconducting nanocrystals: it was no surprise that quantum dots were the topic of this year's Nobel prize for chemistry, as these structures have exhibited outstanding optical and electronic features, with the greatest variety of possible applications in physics, chemistry and materials science.

In this context, lead halide perovskite nanocrystals, a particular kind of nanostructured semiconductor of ionic nature, stand out in the nanomaterials field due to their very bright and fast photoluminescence, their electronic properties' exceptional tolerance to the material's defects and surfaces, as well as their very promising performances as scintillators.

In the beginning, this manuscript has given the information needed to understand the present work's context, first in the form of a background about traditional colloidal semiconducting nanomaterials. In particular, the dependency of their opto-electronic features on the NCs' dimension was explained in terms of the quantum-size effects on the specie's electronic structure.

Perovskite nanocrystals were then introduced as direct bandgap semiconductors, which arose major interest in the community owing to their great potential for a broad range of applications, from photovoltaics to optoelectronics, photocatalysis and scintillation detectors. The scintillation features of these nanocrystals were precisely the main topic of this PhD project, as CsPbBr₃ nanostructures in particular have been proved to exhibit bright radioluminescence, with ultra-fast time response: these features can be highly beneficial in high energy radiation detection applications, which have a crucial role in high-energy physics experiments, diagnostic imaging, nuclear and radiation prevention, and homeland security.

The main characterization techniques were detailed, together with all the corresponding typical outcomes that can be expected when working with such nanostructures: this section is particularly aimed at giving pedagogical information to future beginners in the

field. Similarly, the experimental protocols that were optimized during this work were detailed, featuring the selective synthesis of either CsPbBr₃ nanocubes or nanoplatelets, as well as the one-pot synthesis of multiple thickness nanoplatelets populations, and the growth of a protective shell around CsPbBr₃ nanocubes.

It has been highlighted that the main possible issue associated with these CsPbBr₃ nanostructures is their small Stokes shift, which can lead to a high probability of luminescence self-absorption in the system: the interest was thus focused on strategies developed to face this issue. Therefore, the here presented manuscript has presented a variety of strategies aiming to improve the scintillation performances of lead halide perovskite nanocrystals, either in as liquid colloidal dispersions or as nanostructures coupled with solid matrices. In particular, the main goals of these approaches were on one hand the artificial engineering of the systems Stokes shift, and on the other hand the understanding of the involved processes, namely the energy deposition mechanisms, which is often overlooked in the many experimental works found in literature.

In terms of liquid systems, this manuscript has presented an extensive study on CsPbBr₃ colloidal nanocrystals dispersions in DIPN as liquid scintillators, especially aiming at understanding the energy deposition mechanism in such colloidal nanostructures and the latter possible interaction with the surrounding organic solvent. After the optimization of the nanocrystals colloidal dispersions in terms of size distribution and optimal concentration, chemical treatments aiming to repair the surface defects, and thus the system's PLQY, were conducted. In particular, the surface chemical treatment involving hexylammonium benzoate was found successful in producing highly photo- and radio-luminescent systems even at high concentration, thanks to the improved surface quality of the nanocrystals and thus the improved efficiency of light emission. Moreover, the liquid scintillation performances of these treated systems were showed to emit an average number of photons detected per emissive event which is comparable to the used reference Ultima Gold organic liquid scintillator.

These chemically treated nanocrystals colloidal dispersions were then evaluated via Compton-TDCR experiments, in order to finely characterize the energy deposition processes in these solvent/NCs binary mixture. The study demonstrated that, contrarily to traditional organic liquid scintillating cocktails, where the energy is mainly deposited in the solvent, in these colloidal dispersions perovskite nanocrystals themselves are the main energy acceptors. This is attributed to the high density of the nanocrystals, due to the presence of heavy elements such as lead and caesium. Therefore, lead halide perovskite nanocrystals have a double role as liquid scintillators, being at the same time energy deposition centers and visible light emitters.

This study of colloidal perovskite nanocrystals dispersions would highly benefit from further investigation, first of all with a completely different approach on the surface ligands. In fact, it would be very interesting to implement a new project focused on finding a good colloidal stabilizing ligand which also presents fluorescence features, in particular with emission in the absorption range of perovskite NCs. Indeed, in this case the surface ligands would be suitable to act as efficient energy donors in non-radiative energy transfers to the nanocrystals, with which they are by definition in close contact, which was described as a crucial parameter for FRET phenomena. An effective coupling in this system would thus provide a highly efficient light detection from the dispersed NCs, which would be less impacted by the latter self-absorption probability: in fact, the difference of this approach with the studies presented in literature involving fluorophores and NCs mixtures is that the latter typically involve radiative energy transfers, which can slow down the process and do not help avoiding the self-absorption in the system. Instead, non-radiative energy transfers from the surface ligands to the nanocrystals could allow to reproduce the energy transfers mechanism describing organic liquid scintillation cocktails, thus forcing the energy deposited in the solvent to be collected by the ligands and then transferred to the NCs, making it possible to keep the latter's concentration below values detrimental for the overall emission.

Moreover, the here-presented findings further pave the way to the development of new liquid scintillation cocktails, either introducing nanocrystal emitting centers, or nanocrystals as γ absorbers, or both. In particular, it would be important to continue the work on perovskite nanocrystals stabilization in polar environments, considering the amount of applications of LSC involving water-based samples that has been highlighted. In particular, recent publications proposed SiO_2 as an efficient material suitable for forming a protective shell around perovskite nanocrystals, thus it would be important to test such $\text{CsPbBr}_3@/\text{SiO}_2$ core/shell nanostructures as liquid scintillators, and evaluate their performances in comparison with the organic mixtures currently used.

Additionally, the results obtained via Compton-TDCR experiments can be readily extended to the more general case of composite materials involving nanocrystals in a matrix, and improve our understanding of the use of such nanostructures for scintillation purposes. In particular, so many systems of lead halide perovskite nanocrystals embedded in organic polymers have been presented in literature, but a characterization of the energy deposition mechanism in such systems is very often lacking. The here-described Compton-TDCR technique would thus be a useful addition for the study of perovskite NCs composites, whether in plastic, glass or ceramic matrices. This would be particularly useful for actual applications of perovskite NCs as gamma detectors, where thick and optically transparent materials are needed: in fact, reports of transparent and high-loading perovskite NCs/polymer nano-composite monoliths are still missing.

Consequently, the here-described approach is presented as a possible promising pathway to allow the study and thus the optimization of the coupling between the NCs and the matrix.

Following the same logic, this project has also presented different approaches developed in order to artificially modify the Stokes shift of lead halide perovskite nanocrystals assemblies in the form of thin films, by engineering energy transfers between the components.

First, a system consisting of mixtures of CsPbBr₃ nanoplatelets and nanocubes was studied, by comparing the nanocubes-associated photoluminescence of samples containing a fixed quantity of nanocubes and increasing amounts of nanoplatelets. Transfers from the latter to the nanocubes were indeed observed, both under photo- and X-ray excitation, even though some reproducibility issues would still benefit from further optimization.

A second approach involving nanoplatelets of different thickness was then presented, as these systems too were expected to give rise to energy transfers, for the same reasons of the above-mentioned nanoplatelets and nanocubes mixtures, but with the advantage of the NPLs tendency to crystallize in stacks. This approach, designed to artificially engineer the overall system's Stokes shift, led to successful results: in fact, the energy transfers from the n=2 population of NPLs to the thicker ones were detected via the study of their PLE spectra. However, other techniques such as transient absorption spectroscopy would be a good implementation to this study, as the outcome would be less hindered by the thickness of some of the tested films. This approach was found to be suitable for applications based on scintillation too, whereas further optimizations would be needed to better manipulate the order of the nanoplatelets stacks, thus achieving better reproducibility of the photo- and radioluminescence features of thick films.

A final strategy involving perovskite 2D structures was then presented, as part of a collaboration with the Nanyang Technological University of Singapore, in particular with Professors C. Dang and M. Birowosuto, and Doctor F. Maddalena. In this case, the aim was to induce the formation of sub-nanostructures inside 2D perovskite crystals, again in order to exploit energy transfers and artificially increase the overall Stokes shift. This set of experiments was successfully able to show energy transfers in such Cs-doped BA₂PbBr₄ perovskite thin films, and to identify these energy transfers as non-radiative. This approach is thus suitable for improving the system's overall Stokes shift, by decreasing the overlap between the absorption and emission centers. The next experimental step would then consist in optimizing the phenomenon, namely to be able to select and finely control the layers populations, and to further study these transfers inside the bulk 2D perovskite crystals.

In particular, it would be of great interest to test these multilayered systems in a heterostructured bulk material, as the functionalized BGO crystals filled with perovskite 2D structures studied in literature for fast-timing applications. In fact, being the observed transfers non-radiative, typically faster than the radiative ones, this strategy is expected to give good results for fast timing applications as well.

Moreover, these coupled layered systems could be a good pathway to follow also in fields not involving scintillation, for example low-loss luminescent solar concentrators: such systems require reducing the reabsorption of emitted light within the absorbing medium, while maintaining high photoluminescence quantum yield, thus the same issue that has been treated in this work. Additionally, research fields involving electronic conduction, such as energy storage devices and solar cells, could also benefit from low-loss 2D coupled systems conceived as the ones presented in this work.

Finally, it would be important to transpose the here-presented findings to lower-toxicity Pb-free systems, as of course they would be more attractive for real-life applications, if their performance is not too-compromised by the absence of lead. Compositions that it would be interesting to test as either liquid scintillators or coupled 2D scintillating systems include Sn/Ge- and Bi/Sb-based halides, as well as double perovskites as $\text{Cs}_2\text{Ag}_{0.6}\text{Na}_{0.4}\text{In}_{1-y}\text{Bi}_y\text{Cl}_6$: in fact, such compounds have already been proven to show interesting features in both radioluminescence and electronic conduction. Consequently, the implementation of such Pb-free compounds in the here-presented low energy loss systems could lead to useful insights for the development of efficient and low-toxicity scintillation detectors or opto-electronic devices.

In conclusion, this manuscript has presented various approaches for optimizing lead halide perovskite nanocrystals radioluminescence features, by engineering the Stokes shift of composite materials through efficient energy transfers. The value of this work is attributed to the variety of studied system types, either in liquid or solid environments, and involving different combinations of nanocubes or nanoplatelets, but also to the attention given at the energy deposition mechanisms involved in each of these multi-component systems. The findings described in this manuscript can be useful for the community working on scintillating nanostructures, as the energy deposition mechanisms here described can be easily extended to the more general case of composite materials involving nanocrystals in a matrix, which is a very active research field. Such efficient coupled systems can thus be a promising choice for the exploitation of lead halide perovskite nanocrystals great scintillation features, in the functionalization of composite materials involving either organic matrices or dense bulk materials: these CsPbBr_3 engineered systems are thus expected to give further exciting results in the scintillation and fast-timing research fields.

Anima mia che metti le ali
e sei un bruco possente
ti fa meno male l'oblio
che questo cerchio di velo.
E se diventi farfalla
nessuno pensa più
a ciò che è stato
quando strisciavi per terra
e non volevi le ali.

Se avess'io

Alda Merini

Acknowledgements

First, I would like to express my gratitude to my PhD supervisors, Christophe Dujardin and Benoit Mahler. Throughout these three years, you have provided guidance, resources, and expertise that have undoubtedly shaped the outcome of this project. I especially appreciate the support you offered, and your care for my well-being as I disclosed the tough time I was having, which is absolutely not granted in working environments.

I also extend my appreciation and affection to the fellow institute members who have indirectly contributed to this work through their valuable help, which truly made a significant difference. Dear iLM fellows, thank you all for your priceless friendship, I feel truly blessed to have found such nice people in my working environment. I would like to address a particular shout-out to my office mates, Mehdi and Pavlo, who truly are amazing people with a special place in my heart: guys, keep on staying hydrated and burning capitalism. Of course, my affection extends to all my fellow Luminescence team PhD students, with whom I had the blessing of sharing many fun moments, filled of deep conversations and mutual understanding. I would also like to thank iLM for deciding to build the "salle de convivialité", where I got the chance to meet so many new amazing people, and such good foosball players! You guys truly deserve all the best and I wish you good luck for the end of your PhD journeys. A special place in my heart goes to Fred, who was such an angel during my manuscript writing, and who is one of the most caring, kind and affectionate people I know: I look forward to see what adventures life will let us experience together. Mamm't.

I would also like to express my eternal gratitude to my "Jenny from Villeurbanne" Italian family in Lyon, who welcomed me as soon as I got here, alone and disoriented, and for whom I feel deep love and affection. Carolina, Clara, Francesca, Francesco, Paolo (THIS IS JUST THE ALPHABETIC ORDER, since I know my chickens), you could not be more different people, but you managed to create a wonderful family which I was blessed to feel part of. A special place in my heart goes to Kevin, who gave me so much love and support during these years and who is one of the funniest and kindest souls I got the chance to meet. Moreover, I would like to send endless love to some marvelous flatmates

I had, Emanuele and Alejandro. Guys, you freakin' slay and I am so, so proud of you amazing people. I deeply love you all so much and I wish you all the best life has to offer.

Last but not least, I am forever indebted to my family, who always showed care and support for my life decisions, even though they brought me away. A special hug is addressed to my dearest nonna Vanna, who has showed me a kind of deep and unconditional love that I think only grandparents can offer. Thank you all, so much.

My dear long-time friends from Italy, from whom I now unfortunately live far away, thank you a billion times for your unwavering support, encouragement, and understanding throughout this challenging experience. Carola, Francesca, Adele, Gaia, Marzia, Veronica, Andrea, Antonella, Sofia, the Chemistry master's program mates, the Cinghiali crew, your belief in my abilities, your patience with me never replying to texts, and the love you consistently provided were essential factors in my resilience and confidence.

I would finally thank all the mental health professionals by whom I had the privilege to be followed: the help you provided me is truly invaluable.

Truly, deeply, thank you to all these amazing people I had the blessing of meeting. I honestly would not be anywhere without you all.

References

- [1] Amrita Dey *et al.* State of the art and prospects for halide perovskite nanocrystals. *ACS Nano*, 15:10775–10981, 7 2021. ISSN 1936-0851. doi: 10.1021/acsnano.0c08903.
- [2] Quinten A. Akkerman, Gabriele Rainò, Maksym V. Kovalenko, and Liberato Manna. Genesis, challenges and opportunities for colloidal lead halide perovskite nanocrystals. *Nature Materials*, 17:394–405, 5 2018. ISSN 1476-1122. doi: 10.1038/s41563-018-0018-4.
- [3] Riley E. Brandt, Vladan Stevanović, David S. Ginley, and Tonio Buonassisi. Identifying defect-tolerant semiconductors with high minority-carrier lifetimes: beyond hybrid lead halide perovskites. *MRS Communications*, 5:265–275, 6 2015. ISSN 2159-6859. doi: 10.1557/mrc.2015.26.
- [4] He Huang, Maryna I. Bodnarchuk, Stephen V. Kershaw, Maksym V. Kovalenko, and Andrey L. Rogach. Lead halide perovskite nanocrystals in the research spotlight: Stability and defect tolerance. *ACS Energy Letters*, 2:2071–2083, 9 2017. ISSN 2380-8195. doi: 10.1021/acsenerylett.7b00547.
- [5] Jianping Deng, Jinglei Li, Zhi Yang, and Minqiang Wang. All-inorganic lead halide perovskites: a promising choice for photovoltaics and detectors. *Journal of Materials Chemistry C*, 7:12415–12440, 2019. ISSN 2050-7526. doi: 10.1039/C9TC04164H.
- [6] Constantinos C. Stoumpos and Mercouri G. Kanatzidis. The renaissance of halide perovskites and their evolution as emerging semiconductors. *Accounts of Chemical Research*, 48:2791–2802, 10 2015. ISSN 0001-4842. doi: 10.1021/acs.accounts.5b00229.
- [7] Constantinos C. Stoumpos and Mercouri G. Kanatzidis. Halide perovskites: Poor man’s high-performance semiconductors. *Advanced Materials*, 28:5778–5793, 7 2016. ISSN 09359648. doi: 10.1002/adma.201600265.

- [8] Lakshminarayana Polavarapu, Bert Nickel, Jochen Feldmann, and Alexander S. Urban. Advances in quantum-confined perovskite nanocrystals for optoelectronics. *Advanced Energy Materials*, 7:1700267, 8 2017. ISSN 16146832. doi: 10.1002/aenm.201700267.
- [9] Mark C. Weidman, Aaron J. Goodman, and William A. Tisdale. Colloidal halide perovskite nanoplatelets: An exciting new class of semiconductor nanomaterials. *Chemistry of Materials*, 29:5019–5030, 6 2017. ISSN 0897-4756. doi: 10.1021/acs.chemmater.7b01384.
- [10] Loredana Protesescu, Sergii Yakunin, Maryna I. Bodnarchuk, Franziska Krieg, Riccarda Caputo, Christopher H. Hendon, Ruo Xi Yang, Aron Walsh, and Maksym V. Kovalenko. Nanocrystals of cesium lead halide perovskites (CsPbX_3 , $x = \text{cl, br, and i}$): Novel optoelectronic materials showing bright emission with wide color gamut. *Nano Letters*, 15:3692–3696, 6 2015. ISSN 1530-6984. doi: 10.1021/nl5048779.
- [11] Javad Shamsi, Alexander S. Urban, Muhammad Imran, Luca De Trizio, and Liberato Manna. Metal halide perovskite nanocrystals: Synthesis, post-synthesis modifications, and their optical properties. *Chemical Reviews*, 119:3296–3348, 3 2019. ISSN 0009-2665. doi: 10.1021/acs.chemrev.8b00644.
- [12] Qiushui Chen, Jing Wu, Xiangyu Ou, Bolong Huang, Jawaher Almutlaq, Ayan A. Zhumeckenov, Xinwei Guan, Sanyang Han, Liangliang Liang, Zhigao Yi, Juan Li, Xiaoji Xie, Yu Wang, Ying Li, Dianyuan Fan, Daniel B. L. Teh, Angelo H. All, Omar F. Mohammed, Osman M. Bakr, Tom Wu, Marco Bettinelli, Huanghao Yang, Wei Huang, and Xiaogang Liu. All-inorganic perovskite nanocrystal scintillators. *Nature*, 561:88–93, 9 2018. ISSN 0028-0836. doi: 10.1038/s41586-018-0451-1.
- [13] Yong Churl Kim, Kwang Hee Kim, Dae-Yong Son, Dong-Nyuk Jeong, Ja-Young Seo, Yeong Suk Choi, In Taek Han, Sang Yoon Lee, and Nam-Gyu Park. Printable organometallic perovskite enables large-area, low-dose x-ray imaging. *Nature*, 550: 87–91, 10 2017. ISSN 0028-0836. doi: 10.1038/nature24032.
- [14] Haotong Wei and Jinsong Huang. Halide lead perovskites for ionizing radiation detection. *Nature Communications*, 10:1066, 3 2019. ISSN 2041-1723. doi: 10.1038/s41467-019-08981-w.
- [15] Wenjuan Zhu, Wenbo Ma, Yirong Su, Zeng Chen, Xinya Chen, Yaoguang Ma, Lizhong Bai, Wenge Xiao, Tianyu Liu, Haiming Zhu, Xiaofeng Liu, Huafeng Liu, Xu Liu, and Yang Yang. Low-dose real-time x-ray imaging with nontoxic double

- perovskite scintillators. *Light: Science & Applications*, 9:112, 6 2020. ISSN 2047-7538. doi: 10.1038/s41377-020-00353-0.
- [16] Atanu Jana, Sangeun Cho, Supriya A. Patil, Abhishek Meena, Yongcheol Jo, Vijaya Gopalan Sree, Youngsin Park, Hyungsang Kim, Hyunsik Im, and Robert A. Taylor. Perovskite: Scintillators, direct detectors, and x-ray imagers. *Materials Today*, 55:110–136, 5 2022. ISSN 13697021. doi: 10.1016/j.mattod.2022.04.009.
- [17] Shuigen Li, Xiangyu Xie, Jian Xiong, Fahui Wang, Jian Liu, and Minhua Jiang. Review: Perovskite x-ray detectors (1997–present). *Crystals*, 12:1563, 11 2022. ISSN 2073-4352. doi: 10.3390/cryst12111563.
- [18] Lu Lu, Mingzi Sun, Tong Wu, Qiuyang Lu, Baian Chen, and Bolong Huang. All-inorganic perovskite nanocrystals: next-generation scintillation materials for high-resolution x-ray imaging. *Nanoscale Advances*, 4:680–696, 2022. ISSN 2516-0230. doi: 10.1039/D1NA00815C.
- [19] Mingxi Chen, Lingjie Sun, Zhongzhu Hong, Hongyun Wang, Yan Xia, Si Liu, Xiaochen Ren, Xiaotao Zhang, Dongzhi Chi, Huanghao Yang, and Wenping Hu. Anthracene single-crystal scintillators for computer tomography scanning. *ACS Applied Materials & Interfaces*, 14:41275–41282, 9 2022. ISSN 1944-8244. doi: 10.1021/acsami.2c09732.
- [20] Jin Hyuck Heo, Dong Hee Shin, Jin Kyoung Park, Do Hun Kim, Sang Jin Lee, and Sang Hyuk Im. High-performance next-generation perovskite nanocrystal scintillator for nondestructive x-ray imaging. *Advanced Materials*, 30:1801743, 10 2018. ISSN 09359648. doi: 10.1002/adma.201801743.
- [21] Francesco Maddalena, Liliana Tjahjana, Aozhen Xie, Arramel, Shuwen Zeng, Hong Wang, Philippe Coquet, Winicjusz Drozdowski, Christophe Dujardin, Cuong Dang, and Muhammad Birowosuto. Inorganic, organic, and perovskite halides with nanotechnology for high-light yield x- and γ -ray scintillators. *Crystals*, 9:88, 2 2019. ISSN 2073-4352. doi: 10.3390/cryst9020088.
- [22] Xiuwen Xu, Wei Qian, Shuang Xiao, Jian Wang, Shizhao Zheng, and Shihe Yang. Halide perovskites: A dark horse for direct x-ray imaging. *EcoMat*, 2, 12 2020. ISSN 2567-3173. doi: 10.1002/eom2.12064.
- [23] Francesco Maddalena, Marcin E. Witkowski, Michal Makowski, Abdellah Bachiri, Benoit Mahler, Ying-Chieh Wong, Cheng Yi Eric Chua, Jia Xing Lee, Winicjusz Drozdowski, Stuart Victor Springham, Christophe Dujardin, Muhammad Danang Birowosuto, and Cuong Dang. Stable and bright commercial CsPbBr₃ quantum

- dot-resin layers for apparent x-ray imaging screen. *ACS Applied Materials & Interfaces*, 13:59450–59459, 12 2021. ISSN 1944-8244. doi: 10.1021/acsami.1c16171.
- [24] M. D. Birowosuto, D. Cortecchia, W. Drozdowski, K. Brylew, W. Lachmanski, A. Bruno, and C. Soci. X-ray scintillation in lead halide perovskite crystals. *Scientific Reports*, 6:37254, 11 2016. ISSN 2045-2322. doi: 10.1038/srep37254.
- [25] Marina Gandini, Irene Villa, Mattia Beretta, Claudio Gotti, Muhammad Imran, Francesco Carulli, Eric Fantuzzi, Mauro Sassi, Matteo Zaffalon, Chiara Brofferio, Liberato Manna, Luca Beverina, Anna Vedda, Mauro Fasoli, Luca Gironi, and Sergio Brovelli. Efficient, fast and reabsorption-free perovskite nanocrystal-based sensitized plastic scintillators. *Nature Nanotechnology*, 15:462–468, 6 2020. ISSN 1748-3387. doi: 10.1038/s41565-020-0683-8.
- [26] Yang Zhou, Jie Chen, Osman M. Bakr, and Omar F. Mohammed. Metal halide perovskites for x-ray imaging scintillators and detectors. *ACS Energy Letters*, 6: 739–768, 2 2021. ISSN 2380-8195. doi: 10.1021/acsenerylett.0c02430.
- [27] Stefaan Vandenberghe, Pawel Moskal, and Joel S. Karp. State of the art in total body pet. *EJNMMI Physics*, 7:35, 12 2020. ISSN 2197-7364. doi: 10.1186/s40658-020-00290-2.
- [28] Kateřina Děcká, Jan Král, František Hájek, Petr Průša, Vladimír Babin, Eva Mihóková, and Václav Čuba. Scintillation response enhancement in nanocrystalline lead halide perovskite thin films on scintillating wafers. *Nanomaterials*, 12: 14, 12 2021. ISSN 2079-4991. doi: 10.3390/nano12010014.
- [29] E. G. Rogers, M. D. Birowosuto, F. Maddalena, C. Dujardin, F. Pagano, N. Kratochwil, E. Auffray, P. Krause, and G. Bizarri. Two-dimensional perovskite functionalized fiber-type heterostructured scintillators. *Applied Physics Letters*, 122 (8):081901, 02 2023. ISSN 0003-6951. doi: 10.1063/5.0137890.
- [30] E. Graham, D. Gooding, J. Gruszko, C. Grant, B. Naranjo, and L. Winslow. Light yield of perovskite nanocrystal-doped liquid scintillator. *Journal of Instrumentation*, 14:P11024–P11024, 11 2019. ISSN 1748-0221. doi: 10.1088/1748-0221/14/11/P11024.
- [31] Qiang Xu, Jie Huang, Jun Liu, Juan Wang, Shuai Zhou, Xiang Wang, Jing Nie, Yong Guo, and Xiaoping Ouyang. Lead halide perovskite quantum dots based liquid scintillator for x-ray detection. *Nanotechnology*, 32:205201, 5 2021. ISSN 0957-4484. doi: 10.1088/1361-6528/abe48a.
- [32] Hao Yu, Tianheng Chen, Ziqing Han, Jiacheng Fan, and Qibing Pei. Liquid scintillators loaded with up to 40 weight percent cesium lead bromide quantum dots

- for gamma scintillation. *ACS Applied Nano Materials*, 5:14572–14581, 10 2022. ISSN 2574-0970. doi: 10.1021/acsanm.2c02930.
- [33] Sangeun Cho, Sungwoo Kim, Jongmin Kim, Yongcheol Jo, Ilhwan Ryu, Seongsu Hong, Jae-Joon Lee, SeungNam Cha, Eun Bi Nam, Sang Uck Lee, Sam Kyu Noh, Hyungsang Kim, Jungwon Kwak, and Hyunsik Im. Hybridisation of perovskite nanocrystals with organic molecules for highly efficient liquid scintillators. *Light: Science & Applications*, 9:156, 9 2020. ISSN 2047-7538. doi: 10.1038/s41377-020-00391-8.
- [34] Al. L. Efros and M. Rosen. The electronic structure of semiconductor nanocrystals. *Annual Review of Materials Science*, 30:475–521, 8 2000. ISSN 0084-6600. doi: 10.1146/annurev.matsci.30.1.475.
- [35] Emil Roduner. Size matters: why nanomaterials are different. *Chemical Society Reviews*, 35:583, 2006. ISSN 0306-0012. doi: 10.1039/b502142c.
- [36] T. Edvinsson. Optical quantum confinement and photocatalytic properties in two-, one- and zero-dimensional nanostructures. *Royal Society Open Science*, 5:180387, 9 2018. ISSN 2054-5703. doi: 10.1098/rsos.180387.
- [37] Brener R. C. Vale, Etienne Socie, Andrés Burgos-Caminal, Jefferson Bettini, Marco A. Schiavon, and Jacques-E. Moser. Exciton, biexciton, and hot exciton dynamics in CsPbBr₃ colloidal nanoplatelets. *The Journal of Physical Chemistry Letters*, 11:387–394, 1 2020. ISSN 1948-7185. doi: 10.1021/acs.jpcclett.9b03282.
- [38] Mark Fox. *Optical Properties of Solids*. Oxford University Press, 2010. ISBN 978-0199573363. doi: 10.1119/1.1691372.
- [39] Bin Cheng, Ting-You Li, Partha Maity, Pai-Chun Wei, Dennis Nordlund, Kang-Ting Ho, Der-Hsien Lien, Chun-Ho Lin, Ru-Ze Liang, Xiaohe Miao, Idris A Ajia, Jun Yin, Dimosthenis Sokaras, Ali Javey, Iman S Roqan, Omar F Mohammed, and Jr-Hau He. Extremely reduced dielectric confinement in two-dimensional hybrid perovskites with large polar organics. *Communications Physics*, 1(1):80, nov 2018. ISSN 2399-3650. doi: 10.1038/s42005-018-0082-8.
- [40] Alexander Efros and Al Efros. Interband light absorption in semiconductor spheres. *Soviet physics. Semiconductors*, 16:772–775, 07 1982.
- [41] L. E. Brus. A simple model for the ionization potential, electron affinity, and aqueous redox potentials of small semiconductor crystallites. *The Journal of Chemical Physics*, 79:5566–5571, 12 1983. ISSN 0021-9606. doi: 10.1063/1.445676.

- [42] Raghvendra S. Yadav, Priya Mishra, Rupali Mishra, Manvendra Kumar, and Avinash C. Pandey. Growth mechanism and optical property of cds nanoparticles synthesized using amino-acid histidine as chelating agent under sonochemical process. *Ultrasonics Sonochemistry*, 17(1):116–122, 2010. ISSN 1350-4177. doi: <https://doi.org/10.1016/j.ultsonch.2009.04.011>.
- [43] K. Kyhm, J.H. Kim, S.M. Kim, and Ho soon Yang. Gain dynamics and excitonic transition in cdse colloidal quantum dots. *Optical Materials*, 30(1):158–160, 2007. ISSN 0925-3467. doi: <https://doi.org/10.1016/j.optmat.2006.11.036>. Selected papers from the 4th International Symposium on Laser, Scintillator and Nonlinear Optical Matetials: ISLNOM-4.
- [44] Tijana Rajh, Olga I. Micic, and Arthur J. Nozik. Synthesis and characterization of surface-modified colloidal cadmium telluride quantum dots. *The Journal of Physical Chemistry*, 97:11999–12003, 11 1993. ISSN 0022-3654. doi: 10.1021/j100148a026.
- [45] A. Manar, A. Chergui, D. Guennani, D. Ohlmann, T. Cloitre, and R.L. Aulombard. Characteristic exciton properties of zns and znse films. *Materials Science and Engineering: B*, 43:121–125, 1 1997. ISSN 09215107. doi: 10.1016/S0921-5107(96)01845-4.
- [46] Kenichiro Tanaka, Takayuki Takahashi, Takuma Ban, Takashi Kondo, Kazuhito Uchida, and Noboru Miura. Comparative study on the excitons in lead-halide-based perovskite-type crystals $\text{CH}_3\text{NH}_3\text{PbBr}_3\text{CH}_3\text{NH}_3\text{PbI}_3$. *Solid State Communications*, 127:619–623, 9 2003. ISSN 00381098. doi: 10.1016/S0038-1098(03)00566-0.
- [47] Giovanni Mannino, Ioannis Deretzis, Emanuele Smecca, Antonino La Magna, Alessandra Alberti, Davide Ceratti, and David Cahen. Temperature-dependent optical band gap in CsPbBr_3 , MAPbBr_3 , and FAPbBr_3 single crystals. *The Journal of Physical Chemistry Letters*, 11:2490–2496, 4 2020. ISSN 1948-7185. doi: 10.1021/acs.jpcclett.0c00295.
- [48] Zhuo Yang, Alessandro Surrente, Krzysztof Galkowski, Nicolas Bruyant, Duncan K. Maude, Amir Abbas Haghighirad, Henry J. Snaith, Paulina Plochocka, and Robin J. Nicholas. Unraveling the exciton binding energy and the dielectric constant in single-crystal methylammonium lead triiodide perovskite. *The Journal of Physical Chemistry Letters*, 8:1851–1855, 4 2017. ISSN 1948-7185. doi: 10.1021/acs.jpcclett.7b00524.
- [49] Z. Yang, A. Surrente, K. Galkowski, A. Miyata, O. Portugall, R. J. Sutton, A. A. Haghighirad, H. J. Snaith, D. K. Maude, P. Plochocka, and R. J. Nicholas. Impact

- of the halide cage on the electronic properties of fully inorganic cesium lead halide perovskites. *ACS Energy Letters*, 2:1621–1627, 7 2017. ISSN 2380-8195. doi: 10.1021/acsenerylett.7b00416.
- [50] Julien Ramade, Léon Marcel Andriambariarijaona, Violette Steinmetz, Nicolas Goubet, Laurent Legrand, Thierry Barisien, Frédérick Bernardot, Christophe Testelin, Emmanuel Lhuillier, Alberto Bramati, and Maria Chamorro. Fine structure of excitons and electron–hole exchange energy in polymorphic CsPbBr₃ single nanocrystals. *Nanoscale*, 10:6393–6401, 2018. ISSN 2040-3364. doi: 10.1039/C7NR09334A.
- [51] Igor L. Medintz, H. Tetsuo Uyeda, Ellen R. Goldman, and Hedi Mattoussi. Quantum dot bioconjugates for imaging, labelling and sensing. *Nature Materials*, 4: 435–446, 6 2005. ISSN 1476-1122. doi: 10.1038/nmat1390.
- [52] Yadong Yin and A. Paul Alivisatos. Colloidal nanocrystal synthesis and the organic–inorganic interface. *Nature*, 437:664–670, 9 2005. ISSN 0028-0836. doi: 10.1038/nature04165.
- [53] Qingjiang Sun, Y. Andrew Wang, Lin Song Li, Daoyuan Wang, Ting Zhu, Jian Xu, Chunhe Yang, and Yongfang Li. Bright, multicoloured light-emitting diodes based on quantum dots. *Nature Photonics*, 1:717–722, 12 2007. ISSN 1749-4885. doi: 10.1038/nphoton.2007.226.
- [54] Yasuhiro Shirasaki, Geoffrey J. Supran, Mounqi G. Bawendi, and Vladimir Bulović. Emergence of colloidal quantum-dot light-emitting technologies. *Nature Photonics*, 7:13–23, 1 2013. ISSN 1749-4885. doi: 10.1038/nphoton.2012.328.
- [55] Michael A. Boles, Daishun Ling, Taeghwan Hyeon, and Dmitri V. Talapin. The surface science of nanocrystals. *Nature Materials*, 15:141–153, 2 2016. ISSN 1476-1122. doi: 10.1038/nmat4526.
- [56] B. O. Dabbousi, J. Rodriguez-Viejo, F. V. Mikulec, J. R. Heine, H. Mattoussi, R. Ober, K. F. Jensen, and M. G. Bawendi. (cdse)zns core/shell quantum dots: Synthesis and characterization of a size series of highly luminescent nanocrystallites. *The Journal of Physical Chemistry B*, 101:9463–9475, 11 1997. ISSN 1520-6106. doi: 10.1021/jp971091y.
- [57] Ou Chen, Jing Zhao, Vikash P. Chauhan, Jian Cui, Cliff Wong, Daniel K. Harris, He Wei, Hee-Sun Han, Dai Fukumura, Rakesh K. Jain, and Mounqi G. Bawendi. Compact high-quality cdse–cds core–shell nanocrystals with narrow emission linewidths and suppressed blinking. *Nature Materials*, 12:445–451, 5 2013. ISSN 1476-1122. doi: 10.1038/nmat3539.

- [58] Xiongbin Wang, Jiahao Yu, and Rui Chen. Optical characteristics of zns passivated cdse/cds quantum dots for high photostability and lasing. *Scientific Reports*, 8: 17323, 11 2018. ISSN 2045-2322. doi: 10.1038/s41598-018-35768-8.
- [59] Junjie Hao, Haochen Liu, Jun Miao, Rui Lu, Ziming Zhou, Bingxin Zhao, Bin Xie, Jiaji Cheng, Kai Wang, and Marie-Helene Delville. A facile route to synthesize cdse/zns thick-shell quantum dots with precisely controlled green emission properties: towards qds based led applications. *Scientific Reports*, 9:12048, 8 2019. ISSN 2045-2322. doi: 10.1038/s41598-019-48469-7.
- [60] Yashaswi Nandan and Mohan Singh Mehata. Wavefunction engineering of type-i/type-ii excitons of cdse/cds core-shell quantum dots. *Scientific Reports*, 9:2, 1 2019. ISSN 2045-2322. doi: 10.1038/s41598-018-37676-3.
- [61] Hui-Seon Kim, Chang-Ryul Lee, Jeong-Hyeok Im, Ki-Beom Lee, Thomas Moehl, Arianna Marchioro, Soo-Jin Moon, Robin Humphry-Baker, Jun-Ho Yum, Jacques E. Moser, Michael Grätzel, and Nam-Gyu Park. Lead iodide perovskite sensitized all-solid-state submicron thin film mesoscopic solar cell with efficiency exceeding 9%. *Scientific Reports*, 2:591, 8 2012. ISSN 2045-2322. doi: 10.1038/srep00591.
- [62] Wenran Wang, Meng Zhang, Zhenxiao Pan, Gill M. Biesold, Shuang Liang, Huashang Rao, Zhiqun Lin, and Xinhua Zhong. Colloidal inorganic ligand-capped nanocrystals: Fundamentals, status, and insights into advanced functional nanodevices. *Chemical Reviews*, 122:4091–4162, 2 2022. ISSN 0009-2665. doi: 10.1021/acs.chemrev.1c00478.
- [63] Mona Mittal, Soumen Sardar, and Atanu Jana. *Nanofabrication techniques for semiconductor chemical sensors*, pages 119–137. Elsevier, 2021. ISBN 978-0-12-820783-3. doi: 10.1016/B978-0-12-820783-3.00023-3.
- [64] Yeosang Yoon, Phuoc Loc Truong, Daeho Lee, and Seung Hwan Ko. Metal-oxide nanomaterials synthesis and applications in flexible and wearable sensors. *ACS Nanoscience Au*, 2:64–92, 4 2022. ISSN 2694-2496. doi: 10.1021/acsnanoscienceau.1c00029.
- [65] N. A. Isaac, I. Pikaar, and G. Biskos. Metal oxide semiconducting nanomaterials for air quality gas sensors: operating principles, performance, and synthesis techniques. *Microchimica Acta*, 189:196, 5 2022. ISSN 0026-3672. doi: 10.1007/s00604-022-05254-0.

- [66] E. Kuna, P. Pieta, R. Nowakowski, and I.S. Pieta. *Semiconductor catalysts based on surface-modified nanomaterials (SMNs) for sensors*, pages 197–222. Elsevier, 2022. ISBN 978-0-12-823386-3. doi: 10.1016/B978-0-12-823386-3.00004-0.
- [67] Hassan Shokry Hassan and Marwa Farouk Elkady. *Semiconductor Nanomaterials for Gas Sensor Applications*, pages 305–355. Springer International Publishing, 2020. ISBN 978-3-030-26672-1. doi: 10.1007/978-3-030-26672-1_10.
- [68] J. Durrani. Explainer: why have quantum dots won the 2023 nobel prize? *Royal Society of Chemistry*, 2023.
- [69] Quantum Dot Market,, 2021. URL https://www.marketsandmarkets.com/Market-Reports/quantum-dots-qd-market-694.html?gclid=EAIaIQobChMI76Ws1fGLgQMVcZGDBx2JcQTEEAAYASAAEgJD3_D_BwE.
- [70] Hamid M. Ghaithan, Zeyad A. Alahmed, Saif M. H. Qaid, Mahmoud Hezam, and Abdullah S. Aldwayyan. Density functional study of cubic, tetragonal, and orthorhombic CsPbBr₃ perovskite. *ACS Omega*, 5:7468–7480, 4 2020. ISSN 2470-1343. doi: 10.1021/acsomega.0c00197.
- [71] Denghui Ji, ShunZhen Feng, Li Wang, Shuling Wang, Mula Na, Hong Zhang, CongMin Zhang, and Xiuling Li. Regulatory tolerance and octahedral factors by using vacancy in apbi3 perovskites. *Vacuum*, 164:186–193, 6 2019. ISSN 0042207X. doi: 10.1016/j.vacuum.2019.03.018.
- [72] V. M. Goldschmidt. Die gesetze der krystallochemie. *Die Naturwissenschaften*, 14:477–485, 5 1926. ISSN 0028-1042. doi: 10.1007/BF01507527.
- [73] Wei Li, Zheming Wang, Felix Deschler, Song Gao, Richard H. Friend, and Anthony K. Cheetham. Chemically diverse and multifunctional hybrid organic–inorganic perovskites. *Nature Reviews Materials*, 2:16099, 2 2017. ISSN 2058-8437. doi: 10.1038/natrevmats.2016.99.
- [74] Christopher J. Bartel, Christopher Sutton, Bryan R. Goldsmith, Runhai Ouyang, Charles B. Musgrave, Luca M. Ghiringhelli, and Matthias Scheffler. New tolerance factor to predict the stability of perovskite oxides and halides. *Science Advances*, 5, 2 2019. ISSN 2375-2548. doi: 10.1126/sciadv.aav0693.
- [75] Yongping Fu, Haiming Zhu, Jie Chen, Matthew P. Hautzinger, X.-Y. Zhu, and Song Jin. Metal halide perovskite nanostructures for optoelectronic applications and the study of physical properties. *Nature Reviews Materials*, 4:169–188, 2 2019. ISSN 2058-8437. doi: 10.1038/s41578-019-0080-9.

- [76] Yongping Fu, Matthew P. Hautzinger, Ziyu Luo, Feifan Wang, Dongxu Pan, Michael M. Aristov, Ilia A. Guzei, Anlian Pan, Xiaoyang Zhu, and Song Jin. Incorporating large a cations into lead iodide perovskite cages: Relaxed goldschmidt tolerance factor and impact on exciton–phonon interaction. *ACS Central Science*, 5:1377–1386, 8 2019. ISSN 2374-7943. doi: 10.1021/acscentsci.9b00367.
- [77] Weijun Ke and Mercurio G. Kanatzidis. Prospects for low-toxicity lead-free perovskite solar cells. *Nature Communications*, 10:965, 2 2019. ISSN 2041-1723. doi: 10.1038/s41467-019-08918-3.
- [78] Yue Wang, Xiaoming Li, Jizhong Song, Lian Xiao, Haibo Zeng, and Handong Sun. All-inorganic colloidal perovskite quantum dots: A new class of lasing materials with favorable characteristics. *Advanced Materials*, 27:7101–7108, 11 2015. ISSN 09359648. doi: 10.1002/adma.201503573.
- [79] Samuel W. Eaton, Minliang Lai, Natalie A. Gibson, Andrew B. Wong, Letian Dou, Jie Ma, Lin-Wang Wang, Stephen R. Leone, and Peidong Yang. Lasing in robust cesium lead halide perovskite nanowires. *Proceedings of the National Academy of Sciences*, 113:1993–1998, 2 2016. ISSN 0027-8424. doi: 10.1073/pnas.1600789113.
- [80] Yue Wang, Xiaoming Li, Xin Zhao, Lian Xiao, Haibo Zeng, and Handong Sun. Nonlinear absorption and low-threshold multiphoton pumped stimulated emission from all-inorganic perovskite nanocrystals. *Nano Letters*, 16:448–453, 1 2016. ISSN 1530-6984. doi: 10.1021/acs.nanolett.5b04110.
- [81] Xiaohong Li, Weiwei Liu, Yiling Song, Hua Long, Kai Wang, Bing Wang, and Peixiang Lu. Two-photon-pumped high-quality, single-mode vertical cavity lasing based on perovskite monocrystalline films. *Nano Energy*, 68:104334, 2 2020. ISSN 22112855. doi: 10.1016/j.nanoen.2019.104334.
- [82] Jizhong Song, Jianhai Li, Xiaoming Li, Leimeng Xu, Yuhui Dong, and Haibo Zeng. Quantum dot light-emitting diodes based on inorganic perovskite cesium lead halides (CsPbX_3). *Advanced Materials*, 27:7162–7167, 11 2015. ISSN 09359648. doi: 10.1002/adma.201502567.
- [83] Xiaoming Li, Ye Wu, Shengli Zhang, Bo Cai, Yu Gu, Jizhong Song, and Haibo Zeng. CsPbX_3 quantum dots for lighting and displays: Room-temperature synthesis, photoluminescence superiorities, underlying origins and white light-emitting diodes. *Advanced Functional Materials*, 26:2435–2445, 4 2016. ISSN 1616301X. doi: 10.1002/adfm.201600109.
- [84] Guangru Li, Florencia Wisnivesky Rocca Rivarola, Nathaniel J. L. K. Davis, Sai Bai, Tom C. Jellicoe, Francisco de la Peña, Shaocong Hou, Caterina Ducati, Feng

- Gao, Richard H. Friend, Neil C. Greenham, and Zhi-Kuang Tan. Highly efficient perovskite nanocrystal light-emitting diodes enabled by a universal crosslinking method. *Advanced Materials*, 28:3528–3534, 5 2016. ISSN 09359648. doi: 10.1002/adma.201600064.
- [85] Francisco Palazon, Francesco Di Stasio, Quinten A. Akkerman, Roman Krahné, Mirko Prato, and Liberato Manna. Polymer-free films of inorganic halide perovskite nanocrystals as uv-to-white color-conversion layers in leds. *Chemistry of Materials*, 28:2902–2906, 5 2016. ISSN 0897-4756. doi: 10.1021/acs.chemmater.6b00954.
- [86] Brandon R. Sutherland and Edward H. Sargent. Perovskite photonic sources. *Nature Photonics*, 10:295–302, 5 2016. ISSN 1749-4885. doi: 10.1038/nphoton.2016.62.
- [87] Xiaoli Zhang, Bing Xu, Jinbao Zhang, Yuan Gao, Yuanjin Zheng, Kai Wang, and Xiao Wei Sun. All-inorganic perovskite nanocrystals for high-efficiency light emitting diodes: Dual-phase CsPbBr₃-CsPb₂Br₅ composites. *Advanced Functional Materials*, 26:4595–4600, 7 2016. ISSN 1616301X. doi: 10.1002/adfm.201600958.
- [88] Yuxi Tian, Aboma Merdasa, Maximilian Peter, Mohamed Abdellah, Kaibo Zheng, Carlito S. Ponseca, Tõnu Pullerits, Arkady Yartsev, Villy Sundström, and Ivan G. Scheblykin. Giant photoluminescence blinking of perovskite nanocrystals reveals single-trap control of luminescence. *Nano Letters*, 15:1603–1608, 3 2015. ISSN 1530-6984. doi: 10.1021/nl5041397.
- [89] Young-Shin Park, Shaojun Guo, Nikolay S. Makarov, and Victor I. Klimov. Room temperature single-photon emission from individual perovskite quantum dots. *ACS Nano*, 9:10386–10393, 10 2015. ISSN 1936-0851. doi: 10.1021/acsnano.5b04584.
- [90] Abhishek Swarnkar, Ramya Chulliyil, Vikash Kumar Ravi, Mir Irfanullah, Arindam Chowdhury, and Angshuman Nag. Colloidal CsPbBr₃ perovskite nanocrystals: Luminescence beyond traditional quantum dots. *Angewandte Chemie International Edition*, 54:15424–15428, 12 2015. ISSN 1433-7851. doi: 10.1002/anie.201508276.
- [91] Fengrui Hu, Huichao Zhang, Chun Sun, Chunyang Yin, Bihu Lv, Chunfeng Zhang, William W. Yu, Xiaoyong Wang, Yu Zhang, and Min Xiao. Superior optical properties of perovskite nanocrystals as single photon emitters. *ACS Nano*, 9:12410–12416, 12 2015. ISSN 1936-0851. doi: 10.1021/acsnano.5b05769.
- [92] Nikolay S. Makarov, Shaojun Guo, Oleksandr Isaienko, Wenyong Liu, István Robel, and Victor I. Klimov. Spectral and dynamical properties of single excitons,

- biexcitons, and trions in cesium–lead-halide perovskite quantum dots. *Nano Letters*, 16:2349–2362, 4 2016. ISSN 1530-6984. doi: 10.1021/acs.nanolett.5b05077.
- [93] Gabriele Rainò, Georgian Nedelcu, Loredana Protesescu, Maryna I. Bodnarchuk, Maksym V. Kovalenko, Rainer F. Mahrt, and Thilo Stöferle. Single cesium lead halide perovskite nanocrystals at low temperature: Fast single-photon emission, reduced blinking, and exciton fine structure. *ACS Nano*, 10:2485–2490, 2 2016. ISSN 1936-0851. doi: 10.1021/acsnano.5b07328.
- [94] Younghoon Kim, Emre Yassitepe, Oleksandr Voznyy, Riccardo Comin, Grant Walters, Xiwen Gong, Pongsakorn Kanjanaboos, Ana F. Nogueira, and Edward H. Sargent. Efficient luminescence from perovskite quantum dot solids. *ACS Applied Materials & Interfaces*, 7:25007–25013, 11 2015. ISSN 1944-8244. doi: 10.1021/acsami.5b09084.
- [95] Jonathan De Roo, Edwin A. Baquero, Yannick Coppel, Katrien De Keukeleere, Isabel Van Driessche, Céline Nayral, Zeger Hens, and Fabien Delpech. Insights into the ligand shell, coordination mode, and reactivity of carboxylic acid capped metal oxide nanocrystals. *ChemPlusChem*, 81:1216–1223, 11 2016. ISSN 21926506. doi: 10.1002/cplu.201600372.
- [96] Yunlong Guo, Kazutaka Shoyama, Wataru Sato, and Eiichi Nakamura. Polymer stabilization of lead(ii) perovskite cubic nanocrystals for semitransparent solar cells. *Advanced Energy Materials*, 6:1502317, 3 2016. ISSN 1614-6832. doi: 10.1002/aenm.201502317.
- [97] He Huang, Bingkun Chen, Zhenguang Wang, Tak Fu Hung, Andrei S. Sussha, Haizheng Zhong, and Andrey L. Rogach. Water resistant CsPbX₃ nanocrystals coated with polyhedral oligomeric silsesquioxane and their use as solid state luminophores in all-perovskite white light-emitting devices. *Chemical Science*, 7: 5699–5703, 2016. ISSN 2041-6520. doi: 10.1039/C6SC01758D.
- [98] Franziska Krieg, Stefan T. Ochsenein, Sergii Yakunin, Stephanie ten Brinck, Philipp Aellen, Adrian Süess, Baptiste Clerc, Dominic Guggisberg, Olga Nazarenko, Yevhen Shynkarenko, Sudhir Kumar, Chih-Jen Shih, Ivan Infante, and Maksym V. Kovalenko. Colloidal CsPbX₃ (x = cl, br, i) nanocrystals 2.0: Zwitterionic capping ligands for improved durability and stability. *ACS Energy Letters*, 3:641–646, 3 2018. ISSN 2380-8195. doi: 10.1021/acsenrgylett.8b00035.
- [99] Quinten A. Akkerman, Valerio D’Innocenzo, Sara Accornero, Alice Scarpellini, Annamaria Petrozza, Mirko Prato, and Liberato Manna. Tuning the optical properties of cesium lead halide perovskite nanocrystals by anion exchange reactions.

- Journal of the American Chemical Society*, 137:10276–10281, 8 2015. ISSN 0002-7863. doi: 10.1021/jacs.5b05602.
- [100] Georgian Nedelcu, Loredana Protesescu, Sergii Yakunin, Maryna I. Bodnarchuk, Matthias J. Grotevent, and Maksym V. Kovalenko. Fast anion-exchange in highly luminescent nanocrystals of cesium lead halide perovskites (CsPbBr_3 , $x = \text{cl, br, i}$). *Nano Letters*, 15:5635–5640, 8 2015. ISSN 1530-6984. doi: 10.1021/acs.nanolett.5b02404.
- [101] Dandan Zhang, Yiming Yang, Yehonadav Bekenstein, Yi Yu, Natalie A. Gibson, Andrew B. Wong, Samuel W. Eaton, Nikolay Kornienko, Qiao Kong, Minliang Lai, A. Paul Alivisatos, Stephen R. Leone, and Peidong Yang. Synthesis of composition tunable and highly luminescent cesium lead halide nanowires through anion-exchange reactions. *Journal of the American Chemical Society*, 138:7236–7239, 6 2016. ISSN 0002-7863. doi: 10.1021/jacs.6b03134.
- [102] Parthiban Ramasamy, Da-Hye Lim, Bumjin Kim, Seung-Ho Lee, Min-Sang Lee, and Jong-Soo Lee. All-inorganic cesium lead halide perovskite nanocrystals for photodetector applications. *Chemical Communications*, 52:2067–2070, 2016. ISSN 1359-7345. doi: 10.1039/C5CC08643D.
- [103] Francisco Palazon, Quinten A. Akkerman, Mirko Prato, and Liberato Manna. X-ray lithography on perovskite nanocrystals films: From patterning with anion-exchange reactions to enhanced stability in air and water. *ACS Nano*, 10:1224–1230, 1 2016. ISSN 1936-0851. doi: 10.1021/acsnano.5b06536.
- [104] Yehonadav Bekenstein, Brent A. Koscher, Samuel W. Eaton, Peidong Yang, and A. Paul Alivisatos. Highly luminescent colloidal nanoplates of perovskite cesium lead halide and their oriented assemblies. *Journal of the American Chemical Society*, 137:16008–16011, 12 2015. ISSN 0002-7863. doi: 10.1021/jacs.5b11199.
- [105] Dandan Zhang, Samuel W. Eaton, Yi Yu, Letian Dou, and Peidong Yang. Solution-phase synthesis of cesium lead halide perovskite nanowires. *Journal of the American Chemical Society*, 137:9230–9233, 7 2015. ISSN 0002-7863. doi: 10.1021/jacs.5b05404.
- [106] Quinten A. Akkerman, Silvia Genaro Motti, Ajay Ram Srimath Kandada, Edoardo Mosconi, Valerio D’Innocenzo, Giovanni Bertoni, Sergio Marras, Brett A. Kamino, Laura Miranda, Filippo De Angelis, Annamaria Petrozza, Mirko Prato, and Liberato Manna. Solution synthesis approach to colloidal cesium lead halide perovskite nanoplatelets with monolayer-level thickness control. *Journal of the American Chemical Society*, 138:1010–1016, 1 2016. ISSN 0002-7863. doi: 10.1021/jacs.5b12124.

- [107] Javad Shamsi, Zhiya Dang, Paolo Bianchini, Claudio Canale, Francesco Di Stasio, Rosaria Brescia, Mirko Prato, and Liberato Manna. Colloidal synthesis of quantum confined single crystal CsPbBr₃ nanosheets with lateral size control up to the micrometer range. *Journal of the American Chemical Society*, 138:7240–7243, 6 2016. ISSN 0002-7863. doi: 10.1021/jacs.6b03166.
- [108] Xianfeng Zhang, Longfei Lv, Li Ji, Guannan Guo, Limin Liu, Dandan Han, Biwei Wang, Yaqi Tu, Jianhua Hu, Dong Yang, and Angang Dong. Self-assembly of one-dimensional nanocrystal superlattice chains mediated by molecular clusters. *Journal of the American Chemical Society*, 138:3290–3293, 3 2016. ISSN 0002-7863. doi: 10.1021/jacs.6b00055.
- [109] Gabriele Rainò, Michael A. Becker, Maryna I. Bodnarchuk, Rainer F. Mahrt, Maksym V. Kovalenko, and Thilo Stöferle. Superfluorescence from lead halide perovskite quantum dot superlattices. *Nature*, 563:671–675, 11 2018. ISSN 0028-0836. doi: 10.1038/s41586-018-0683-0.
- [110] Dmitry Baranov, Stefano Toso, Muhammad Imran, and Liberato Manna. Investigation into the photoluminescence red shift in cesium lead bromide nanocrystal superlattices. *The Journal of Physical Chemistry Letters*, 10:655–660, 2 2019. ISSN 1948-7185. doi: 10.1021/acs.jpcclett.9b00178.
- [111] Yusheng Lei, Yuheng Li, Chengchangfeng Lu, Qizhang Yan, Yilei Wu, Finn Babbe, Huaxin Gong, Song Zhang, Jiayun Zhou, Ruotao Wang, Ruiqi Zhang, Yimu Chen, Hsinhan Tsai, Yue Gu, Hongjie Hu, Yu-Hwa Lo, Wanyi Nie, Taeyoon Lee, Jian Luo, Kesong Yang, Kyung-In Jang, and Sheng Xu. Perovskite superlattices with efficient carrier dynamics. *Nature*, 608:317–323, 8 2022. ISSN 0028-0836. doi: 10.1038/s41586-022-04961-1.
- [112] Miriam Koolyk, Daniel Amgar, Sigalit Aharon, and Lioz Etgar. Kinetics of cesium lead halide perovskite nanoparticle growth; focusing and de-focusing of size distribution. *Nanoscale*, 8:6403–6409, 2016. ISSN 2040-3364. doi: 10.1039/C5NR09127F.
- [113] Ioannis Lignos, Stavros Stavrakis, Georgian Nedelcu, Loredana Protesescu, Andrew J. deMello, and Maksym V. Kovalenko. Synthesis of cesium lead halide perovskite nanocrystals in a droplet-based microfluidic platform: Fast parametric space mapping. *Nano Letters*, 16:1869–1877, 3 2016. ISSN 1530-6984. doi: 10.1021/acs.nanolett.5b04981.
- [114] Margaret A. Hines and Philippe Guyot-Sionnest. Synthesis and characterization of strongly luminescing zns-capped cdse nanocrystals. *The Journal of Physical Chemistry*, 100:468–471, 1 1996. ISSN 0022-3654. doi: 10.1021/jp9530562.

- [115] Yun-Wei Cao and Uri Banin. Synthesis and characterization of inas/inp and inas/cdse core/shell nanocrystals. *Angewandte Chemie International Edition*, 38:3692–3694, 12 1999. ISSN 1433-7851. doi: 10.1002/(sici)1521-3773(19991216)38:24<3692::aid-anie3692>3.0.co;2-w.
- [116] Olga I. Micic, Calvin J. Curtis, Kim M. Jones, Julian R. Sprague, and Arthur J. Nozik. Synthesis and characterization of inp quantum dots. *The Journal of Physical Chemistry*, 98:4966–4969, 5 1994. ISSN 0022-3654. doi: 10.1021/j100070a004.
- [117] Michael M. Lee, Joël Teuscher, Tsutomu Miyasaka, Takuro N. Murakami, and Henry J. Snaith. Efficient hybrid solar cells based on meso-superstructured organometal halide perovskites. *Science*, 338:643–647, 11 2012. ISSN 0036-8075. doi: 10.1126/science.1228604.
- [118] Julian Burschka, Norman Pellet, Soo-Jin Moon, Robin Humphry-Baker, Peng Gao, Mohammad K. Nazeeruddin, and Michael Grätzel. Sequential deposition as a route to high-performance perovskite-sensitized solar cells. *Nature*, 499:316–319, 7 2013. ISSN 0028-0836. doi: 10.1038/nature12340.
- [119] Jun Hong Noh, Sang Hyuk Im, Jin Hyuck Heo, Tarak N. Mandal, and Sang Il Seok. Chemical management for colorful, efficient, and stable inorganic–organic hybrid nanostructured solar cells. *Nano Letters*, 13:1764–1769, 4 2013. ISSN 1530-6984. doi: 10.1021/nl400349b.
- [120] Research Cell Efficiency Records, Accessed August 2023. URL <https://www.nrel.gov/pv/cell-efficiency.html>.
- [121] Qingfeng Dong, Yanjun Fang, Yuchuan Shao, Padhraic Mulligan, Jie Qiu, Lei Cao, and Jinsong Huang. Electron-hole diffusion lengths \geq 175 micrometers in solution-grown $\text{CH}_3\text{NH}_3\text{PbI}_3$ single crystals. *Science*, 347:967–970, 2 2015. ISSN 0036-8075. doi: 10.1126/science.aaa5760.
- [122] Dong Shi, Valerio Adinolfi, Riccardo Comin, Mingjian Yuan, Erkki Alarousu, Andrei Buin, Yin Chen, Sjoerd Hoogland, Alexander Rothenberger, Khabiboulakh Katsiev, Yaroslav Losovyj, Xin Zhang, Peter A. Dowben, Omar F. Mohammed, Edward H. Sargent, and Osman M. Bakr. Low trap-state density and long carrier diffusion in organolead trihalide perovskite single crystals. *Science*, 347:519–522, 1 2015. ISSN 0036-8075. doi: 10.1126/science.aaa2725.
- [123] Joseph S. Manser, Jeffrey A. Christians, and Prashant V. Kamat. Intriguing optoelectronic properties of metal halide perovskites. *Chemical Reviews*, 116:12956–13008, 11 2016. ISSN 0009-2665. doi: 10.1021/acs.chemrev.6b00136.

- [124] John A. Rowlands. Material change for x-ray detectors. *Nature*, 550:47–48, 10 2017. ISSN 0028-0836. doi: 10.1038/550047a.
- [125] C. Dujardin, E. Auffray, E. Bourret-Courchesne, P. Dorenbos, P. Lecoq, M. Nikl, A. N. Vasil’ev, A. Yoshikawa, and R.-Y. Zhu. Needs, trends, and advances in inorganic scintillators. *IEEE Transactions on Nuclear Science*, 65:1977–1997, 8 2018. ISSN 0018-9499. doi: 10.1109/TNS.2018.2840160.
- [126] Ying Ding, Richeng Lin, Yali Liang, Wei Zheng, Liang Chen, Xiao Ouyang, Xiaoping Ouyang, and Feng Huang. High-efficiency down-conversion radiation fluorescence and ultrafast photoluminescence (1.2 ns) at the interface of hybrid cs 4 pbbr 6 –csi nanocrystals. *The Journal of Physical Chemistry Letters*, 12:7342–7349, 8 2021. ISSN 1948-7185. doi: 10.1021/acs.jpcllett.1c01615.
- [127] Aron Walsh, David O. Scanlon, Shiyu Chen, X. G. Gong, and Su-Huai Wei. Self-regulation mechanism for charged point defects in hybrid halide perovskites. *Angewandte Chemie International Edition*, 54:1791–1794, 2 2015. ISSN 1433-7851. doi: 10.1002/anie.201409740.
- [128] Claudio Quarti, Edoardo Mosconi, and Filippo De Angelis. Interplay of orientational order and electronic structure in methylammonium lead iodide: Implications for solar cell operation. *Chemistry of Materials*, 26:6557–6569, 11 2014. ISSN 15205002. doi: 10.1021/CM5032046.
- [129] Artem A. Bakulin, Oleg Selig, Huib J. Bakker, Yves L.A. Rezus, Christian Müller, Tobias Glaser, Robert Lovrincic, Zhenhua Sun, Zhuoying Chen, Aron Walsh, Jarvist M. Frost, and Thomas L.C. Jansen. Real-time observation of organic cation reorientation in methylammonium lead iodide perovskites. *Journal of Physical Chemistry Letters*, 6:3663–3669, 9 2015. ISSN 19487185. doi: 10.1021/ACS.JPCLETT.5B01555.
- [130] Federico Brivio, Jarvist M. Frost, Jonathan M. Skelton, Adam J. Jackson, Oliver J. Weber, Mark T. Weller, Alejandro R. Goñi, Aurélien M.A. Leguy, Piers R.F. Barnes, and Aron Walsh. Lattice dynamics and vibrational spectra of the orthorhombic, tetragonal, and cubic phases of methylammonium lead iodide. *Physical Review B - Condensed Matter and Materials Physics*, 92, 10 2015. ISSN 1550235X. doi: 10.1103/PhysRevB.92.144308.
- [131] Aurelien M. A. Leguy, Jarvist Moore Frost, Andrew P. McMahon, Victoria Garcia Sakai, W. Kockelmann, ChunHung Law, Xiaoe Li, Fabrizia Foglia, Aron Walsh, Brian C. O’Regan, Jenny Nelson, João T. Cabral, and Piers R. F. Barnes. The dynamics of methylammonium ions in hybrid organic–inorganic perovskite solar

- cells. *Nature Communications*, 6:7124, 5 2015. ISSN 2041-1723. doi: 10.1038/ncomms8124.
- [132] Tae-Youl Yang, Giuliano Gregori, Norman Pellet, Michael Grätzel, and Joachim Maier. The significance of ion conduction in a hybrid organic-inorganic lead-iodide-based perovskite photosensitizer. *Angewandte Chemie International Edition*, 54: 7905–7910, 6 2015. ISSN 14337851. doi: 10.1002/anie.201500014.
- [133] Edoardo Mosconi and Filippo De Angelis. Mobile ions in organohalide perovskites: Interplay of electronic structure and dynamics. *ACS Energy Letters*, 1:182–188, 7 2016. ISSN 2380-8195. doi: 10.1021/acsenergylett.6b00108.
- [134] Andriy Zakutayev, Christopher M. Caskey, Angela N. Fioretti, David S. Ginley, Julien Vidal, Vladan Stevanovic, Eric Tea, and Stephan Lany. Defect tolerant semiconductors for solar energy conversion. *The Journal of Physical Chemistry Letters*, 5:1117–1125, 4 2014. ISSN 1948-7185. doi: 10.1021/jz5001787.
- [135] Mohnish Pandey, Filip A. Rasmussen, Korina Kuhar, Thomas Olsen, Karsten W. Jacobsen, and Kristian S. Thygesen. Defect-tolerant monolayer transition metal dichalcogenides. *Nano Letters*, 16:2234–2239, 4 2016. ISSN 1530-6984. doi: 10.1021/acs.nanolett.5b04513.
- [136] Dmitry N. Dirin, Loredana Protesescu, David Trummer, Ilia V. Kochetygov, Sergii Yakunin, Frank Krumeich, Nicholas P. Stadie, and Maksym V. Kovalenko. Harnessing defect-tolerance at the nanoscale: Highly luminescent lead halide perovskite nanocrystals in mesoporous silica matrixes. *Nano Letters*, 16:5866–5874, 9 2016. ISSN 1530-6984. doi: 10.1021/acs.nanolett.6b02688.
- [137] W. E. Hagston, P. Harrison, and T. Stirner. Origin of the stokes shift in semiconductor quantum wells. *Advanced Materials for Optics and Electronics*, 3:95–101, 1 1994. ISSN 1057-9257. doi: 10.1002/amo.860030114.
- [138] Ronghui Zhou, Xiaomei Lu, Qin Yang, and Peng Wu. Nanocrystals for large stokes shift-based optosensing. *Chinese Chemical Letters*, 30:1843–1848, 10 2019. ISSN 10018417. doi: 10.1016/j.ccllet.2019.07.062.
- [139] Michael C. Brennan, Aaron Forde, Maksym Zhukovskiy, Andrew J. Baublis, Yurii V. Morozov, Shubin Zhang, Zhuoming Zhang, Dmitri S. Kilin, and Masaru Kuno. Universal size-dependent stokes shifts in lead halide perovskite nanocrystals. *The Journal of Physical Chemistry Letters*, 11:4937–4944, 7 2020. ISSN 1948-7185. doi: 10.1021/acs.jpcclett.0c01407.
- [140] Michael C. Brennan, John E. Herr, Triet S. Nguyen-Beck, Jessica Zinna, Sergiu Draguta, Sergei Rouvimov, John Parkhill, and Masaru Kuno. Origin of the

- size-dependent stokes shift in CsPbBr₃ perovskite nanocrystals. *Journal of the American Chemical Society*, 139:12201–12208, 9 2017. ISSN 0002-7863. doi: 10.1021/jacs.7b05683.
- [141] Michael C. Brennan, Jessica Zinna, and Masaru Kuno. Existence of a size-dependent stokes shift in CsPbBr₃ perovskite nanocrystals. *ACS Energy Letters*, 2:1487–1488, 7 2017. ISSN 2380-8195. doi: 10.1021/acsenergylett.7b00383.
- [142] Xiaoman Ma, Huaxiong Gao, Chaoying Meng, Fang Pan, and Honggang Ye. The stokes shift and exciton fine structure in strongly confined CsPbBr₃ perovskite nanoplatelets. *The Journal of Physical Chemistry Letters*, 14:6860–6866, 8 2023. ISSN 1948-7185. doi: 10.1021/acs.jpcclett.3c01641.
- [143] Pedro Ludwig Hernández-Martínez, Alexander O. Govorov, and Hilmi Volkan Demir. Generalized theory of förster-type nonradiative energy transfer in nanostructures with mixed dimensionality. *The Journal of Physical Chemistry C*, 117: 10203–10212, 5 2013. ISSN 1932-7447. doi: 10.1021/jp402242y.
- [144] Yuan Gao, Guannan Yu, Yue Wang, Cuong Dang, Tze Chien Sum, Handong Sun, and Hilmi Volkan Demir. Green stimulated emission boosted by nonradiative resonant energy transfer from blue quantum dots. *The Journal of Physical Chemistry Letters*, 7:2772–2778, 7 2016. ISSN 1948-7185. doi: 10.1021/acs.jpcclett.6b01122.
- [145] E. Cassette, S. Pedetti, B. Mahler, S. Ithurria, B. Dubertret, and G. D. Scholes. Ultrafast exciton dynamics in 2d in-plane hetero-nanostructures: delocalization and charge transfer. *Physical Chemistry Chemical Physics*, 19:8373–8379, 2017. ISSN 1463-9076. doi: 10.1039/C6CP08689F.
- [146] Jiawen Liu, Lilian Guillemeney, Benjamin Abécassis, and Laurent Coolen. Long range energy transfer in self-assembled stacks of semiconducting nanoplatelets. *Nano Letters*, 20:3465–3470, 5 2020. ISSN 1530-6984. doi: 10.1021/acs.nanolett.0c00376.
- [147] Andreas Singldinger, Moritz Gramlich, Christoph Gruber, Carola Lampe, and Alexander S. Urban. Nonradiative energy transfer between thickness-controlled halide perovskite nanoplatelets. *ACS Energy Letters*, 5:1380–1385, 5 2020. ISSN 2380-8195. doi: 10.1021/acsenergylett.0c00471.
- [148] Debarati Ghosh, Kritiman Marjit, Goutam Ghosh, Srijon Ghosh, and Amitava Patra. Charge transfer dynamics of two-dimensional ruddlesden popper perovskite in the presence of short-chain aromatic thiol ligands. *The Journal of Physical Chemistry C*, 126:14590–14597, 9 2022. ISSN 1932-7447. doi: 10.1021/acs.jpcc.2c04439.

- [149] Chen Wang, Aaron Malinoski, Jingheng Yuan, Courtney Brea, and Guoxiang Hu. A surface engineering approach for promoting dexter energy transfer from lead halide perovskite nanocrystals. *The Journal of Physical Chemistry C*, 127:1135–1144, 1 2023. ISSN 1932-7447. doi: 10.1021/acs.jpcc.2c07664.
- [150] Maksym V. Kovalenko, Loredana Protesescu, and Maryna I. Bodnarchuk. Properties and potential optoelectronic applications of lead halide perovskite nanocrystals. *Science*, 358:745–750, 11 2017. ISSN 0036-8075. doi: 10.1126/science.aam7093.
- [151] Patrick Cottingham and Richard L. Brutchey. On the crystal structure of colloidally prepared CsPbBr₃ quantum dots. *Chemical Communications*, 52:5246–5249, 2016. ISSN 1359-7345. doi: 10.1039/C6CC01088A.
- [152] Andrius Merkys, Antanas Vaitkus, Algirdas Grybauskas, Aleksandras Konovalovas, Miguel Quirós, and Saulius Gražulis. Graph isomorphism-based algorithm for cross-checking chemical and crystallographic descriptions. *Journal of Cheminformatics*, 15:25, 2 2023. ISSN 1758-2946. doi: 10.1186/s13321-023-00692-1.
- [153] Antanas Vaitkus, Andrius Merkys, and Saulius Gražulis. Validation of the Crystallography Open Database using the Crystallographic Information Framework. *Journal of Applied Crystallography*, 54(2):661–672, Apr 2021. doi: 10.1107/S1600576720016532.
- [154] Miguel Quirós, Saulius Gražulis, Saulė Girdzijauskaitė, Andrius Merkys, and Antanas Vaitkus. Using SMILES strings for the description of chemical connectivity in the Crystallography Open Database. *Journal of Cheminformatics*, 10(1), May 2018. doi: 10.1186/s13321-018-0279-6.
- [155] Andrius Merkys, Antanas Vaitkus, Justas Butkus, Mykolas Okulič-Kazarinas, Visvaldas Kairys, and Saulius Gražulis. *COD::CIF::Parser*: an error-correcting CIF parser for the Perl language. *Journal of Applied Crystallography*, 49(1), Feb 2016. doi: 10.1107/S1600576715022396.
- [156] Saulius Gražulis, Andrius Merkys, Antanas Vaitkus, and Mykolas Okulič-Kazarinas. Computing stoichiometric molecular composition from crystal structures. *Journal of Applied Crystallography*, 48(1):85–91, Feb 2015. doi: 10.1107/S1600576714025904.
- [157] Saulius Gražulis, Adriana Daškevič, Andrius Merkys, Daniel Chateigner, Luca Lutterotti, Miguel Quirós, Nadezhda R. Serebryanaya, Peter Moeck, Robert T. Downs, and Armel Le Bail. Crystallography open database (cod): an open-access

- collection of crystal structures and platform for world-wide collaboration. *Nucleic Acids Research*, 40(D1):D420–D427, 2012. doi: 10.1093/nar/gkr900.
- [158] Saulius Gražulis, Daniel Chateigner, Robert T. Downs, A. F. T. Yokochi, Miguel Quirós, Luca Lutterotti, Elena Manakova, Justas Butkus, Peter Moeck, and Armel Le Bail. Crystallography Open Database – an open-access collection of crystal structures. *Journal of Applied Crystallography*, 42(4):726–729, Aug 2009. doi: 10.1107/S0021889809016690.
- [159] R. T. Downs and M. Hall-Wallace. The american mineralogist crystal structure database. *American Mineralogist*, 88:247–250, 2003.
- [160] Koichi Momma and Fujio Izumi. Vesta3 for three-dimensional visualization of crystal, volumetric and morphology data. *Journal of Applied Crystallography*, 44: 1272–1276, 12 2011. ISSN 0021-8898. doi: 10.1107/S0021889811038970.
- [161] Jasmina A. Sichert, Yu Tong, Niklas Mutz, Mathias Vollmer, Stefan Fischer, Karolina Z. Milowska, Ramon García Cortadella, Bert Nickel, Carlos Cardenas-Daw, Jacek K. Stolarczyk, Alexander S. Urban, and Jochen Feldmann. Quantum size effect in organometal halide perovskite nanoplatelets. *Nano Letters*, 15:6521–6527, 10 2015. ISSN 1530-6984. doi: 10.1021/acs.nanolett.5b02985.
- [162] Feng Zhang, Cheng Chen, Stephen V. Kershaw, Changtao Xiao, Junbo Han, Bingsuo Zou, Xing Wu, Shuai Chang, Yuping Dong, Andrey L. Rogach, and Haizheng Zhong. Ligand-controlled formation and photoluminescence properties of $\text{ch}_3\text{nh}_3\text{pbbr}_3$ nanocubes and nanowires. *ChemNanoMat*, 3:303–310, 5 2017. ISSN 2199692X. doi: 10.1002/cnma.201700034.
- [163] Lucheng Peng, Anirban Dutta, Renguo Xie, Wensheng Yang, and Narayan Pradhan. Dot–wire–platelet–cube: Step growth and structural transformations in CsPbBr_3 perovskite nanocrystals. *ACS Energy Letters*, 3:2014–2020, 8 2018. ISSN 2380-8195. doi: 10.1021/acsenergylett.8b01037.
- [164] Yicheng Zeng, Huixue Su, Yuan Liu, Weiwei Chen, Fangze Liu, Hanfei Gao, Yuchen Wu, Liberato Manna, and Hongbo Li. Synthesis and assembly of core–shell nanorods with high quantum yield and linear polarization. *Advanced Functional Materials*, 8 2023. ISSN 1616-301X. doi: 10.1002/adfm.202306091.
- [165] Verena A. Hintermayr, Alexander F. Richter, Florian Ehrat, Markus Döblinger, Willem Vanderlinden, Jasmina A. Sichert, Yu Tong, Lakshminarayana Polavarapu,

- Jochen Feldmann, and Alexander S. Urban. Tuning the optical properties of perovskite nanoplatelets through composition and thickness by ligand-assisted exfoliation. *Advanced Materials*, 28:9478–9485, 11 2016. ISSN 0935-9648. doi: 10.1002/adma.201602897.
- [166] Fatima Haydous, James M. Gardner, and Ute B. Cappel. The impact of ligands on the synthesis and application of metal halide perovskite nanocrystals. *Journal of Materials Chemistry A*, 9:23419–23443, 2021. ISSN 2050-7488. doi: 10.1039/D1TA05242J.
- [167] Mingyang Wei, F. Pelayo García de Arquer, Grant Walters, Zhenyu Yang, Li Na Quan, Younghoon Kim, Randy Sabatini, Rafael Quintero-Bermudez, Liang Gao, James Z. Fan, Fengjia Fan, Aryeh Gold-Parker, Michael F. Toney, and Edward H. Sargent. Ultrafast narrowband exciton routing within layered perovskite nanoplatelets enables low-loss luminescent solar concentrators. *Nature Energy*, 4: 197–205, 1 2019. ISSN 2058-7546. doi: 10.1038/s41560-018-0313-y.
- [168] M.L.H. Green. A new approach to the formal classification of covalent compounds of the elements. *Journal of Organometallic Chemistry*, 500:127–148, 9 1995. ISSN 0022328X. doi: 10.1016/0022-328X(95)00508-N.
- [169] Valeriia Grigel, Laxmi Kishore Sagar, Kim De Nolf, Qiang Zhao, André Vantomme, Jonathan De Roo, Ivan Infante, and Zeger Hens. The surface chemistry of colloidal hgse nanocrystals, toward stoichiometric quantum dots by design. *Chemistry of Materials*, 30:7637–7647, 11 2018. ISSN 0897-4756. doi: 10.1021/acs.chemmater.8b02908.
- [170] J. De Roo, K. De Keukeleere, Z. Hens, and I. Van Driessche. From ligands to binding motifs and beyond; the enhanced versatility of nanocrystal surfaces. *Dalton Transactions*, 45:13277–13283, 2016. ISSN 1477-9226. doi: 10.1039/C6DT02410F.
- [171] Jonathan De Roo. The surface chemistry of colloidal nanocrystals capped by organic ligands. *Chemistry of Materials*, 35:3781–3792, 5 2023. ISSN 0897-4756. doi: 10.1021/acs.chemmater.3c00638.
- [172] Jonathan De Roo, Freya Van den Broeck, Katrien De Keukeleere, José C. Martins, Isabel Van Driessche, and Zeger Hens. Unravelling the surface chemistry of metal oxide nanocrystals, the role of acids and bases. *Journal of the American Chemical Society*, 136:9650–9657, 7 2014. ISSN 0002-7863. doi: 10.1021/ja5032979.
- [173] Sara R. Smock, Yunhua Chen, Aaron J. Rossini, and Richard L. Brutchey. The surface chemistry and structure of colloidal lead halide perovskite nanocrystals.

- Accounts of Chemical Research*, 54:707–718, 2 2021. ISSN 0001-4842. doi: 10.1021/acs.accounts.0c00741.
- [174] Yang Bai, Mengmeng Hao, Shanshan Ding, Peng Chen, and Lianzhou Wang. Surface chemistry engineering of perovskite quantum dots: Strategies, applications, and perspectives. *Advanced Materials*, 34, 1 2022. ISSN 0935-9648. doi: 10.1002/adma.202105958.
- [175] Yunhua Chen, Sara R. Smock, Anne H. Flintgruber, Frédéric A. Perras, Richard L. Brutchey, and Aaron J. Rossini. Surface termination of CsPbBr₃ perovskite quantum dots determined by solid-state nmr spectroscopy. *Journal of the American Chemical Society*, 142:6117–6127, 4 2020. ISSN 0002-7863. doi: 10.1021/jacs.9b13396.
- [176] Maryna I. Bodnarchuk, Simon C. Boehme, Stephanie ten Brinck, Caterina Bernasconi, Yevhen Shynkarenko, Franziska Krieg, Roland Widmer, Beat Aeschliemann, Detlef Günther, Maksym V. Kovalenko, and Ivan Infante. Rationalizing and controlling the surface structure and electronic passivation of cesium lead halide nanocrystals. *ACS Energy Letters*, 4:63–74, 1 2019. ISSN 2380-8195. doi: 10.1021/acsenerylett.8b01669.
- [177] Jorick Maes, Lieve Balcaen, Emile Drijvers, Qiang Zhao, Jonathan De Roo, André Vantomme, Frank Vanhaecke, Pieter Geiregat, and Zeger Hens. Light absorption coefficient of CsPbBr₃ perovskite nanocrystals. *The Journal of Physical Chemistry Letters*, 9:3093–3097, 6 2018. ISSN 1948-7185. doi: 10.1021/acs.jpcclett.8b01065.
- [178] Roberto Grisorio, Francesca Fasulo, Ana Belén Muñoz-García, Michele Pavone, Daniele Conelli, Elisabetta Fanizza, Marinella Striccoli, Ignazio Allegretta, Roberto Terzano, Nicola Margiotta, Paola Vivo, and Gian Paolo Suranna. In situ formation of zwitterionic ligands: Changing the passivation paradigms of CsPbBr₃ nanocrystals. *Nano Letters*, 22:4437–4444, 6 2022. ISSN 1530-6984. doi: 10.1021/acs.nanolett.2c00937.
- [179] Xiaopeng Zheng, Yehao Deng, Bo Chen, Haotong Wei, Xun Xiao, Yanjun Fang, Yuze Lin, Zhenhua Yu, Ye Liu, Qi Wang, and Jinsong Huang. Dual functions of crystallization control and defect passivation enabled by sulfonic zwitterions for stable and efficient perovskite solar cells. *Advanced Materials*, 30:1803428, 12 2018. ISSN 0935-9648. doi: 10.1002/adma.201803428.
- [180] Federico Montanarella, Kyle M. McCall, Kostiantyn Sakhatskyi, Sergii Yakunin, Pavel Trtik, Caterina Bernasconi, Ihor Cherniukh, David Mannes, Maryna I. Bodnarchuk, Markus Strobl, Bernhard Walfort, and Maksym V. Kovalenko. Highly

- concentrated, zwitterionic ligand-capped $\text{mn}^{2+}:\text{cspb}(\text{br} \times \text{cl}^{1-x})_3$ nanocrystals as bright scintillators for fast neutron imaging. *ACS Energy Letters*, 6:4365–4373, 12 2021. ISSN 2380-8195. doi: 10.1021/acsenerylett.1c01923.
- [181] Haobo Yuan, Zequn Zhang, Tonghui Guo, Luting Yu, Zhiqiang Deng, Rui Zhao, Jing Zhang, and Yuejin Zhu. Steric effect of amino-acids as additives for perovskite solar cells. *Journal of Alloys and Compounds*, 876:160140, 9 2021. ISSN 09258388. doi: 10.1016/j.jallcom.2021.160140.
- [182] Ajeet Kumar Sharma, Parul Bansal, Gaurav Kumar Nim, and Prasenjit Kar. Essential amino acid-enabled lead bromide perovskite nanocrystals with high stability. *Particle & Particle Systems Characterization*, 36:1900328, 12 2019. ISSN 0934-0866. doi: 10.1002/ppsc.201900328.
- [183] Sukanya Ghosh and Prasenjit Kar. Aromatic amino acid-mediated perovskite nanocrystals: Fluorescence tuning and morphological evolution. *Inorganic Chemistry*, 61:10079–10088, 7 2022. ISSN 0020-1669. doi: 10.1021/acs.inorgchem.2c01021.
- [184] Hyunki Kim, Nicholas Hight-Huf, Ji-Hwan Kang, Phoebe Bisnoff, Suvin Sundararajan, Theo Thompson, Michael Barnes, Ryan C. Hayward, and Todd Emrick. Polymer zwitterions for stabilization of CsPbBr_3 perovskite nanoparticles and nanocomposite films. *Angewandte Chemie International Edition*, 59:10802–10806, 6 2020. ISSN 1433-7851. doi: 10.1002/anie.201916492.
- [185] Christopher Cueto, Colleen Donoghue, Kimberly Bolduc, and Todd Emrick. Zwitterionic block copolymers for the synthesis and stabilization of perovskite nanocrystals. *Chemistry – A European Journal*, 28:e202200409, 5 2022. ISSN 0947-6539. doi: 10.1002/chem.202200409.
- [186] Franziska Krieg, Quy K. Ong, Max Burian, Gabriele Rainò, Denys Naumenko, Heinz Amenitsch, Adrian Süess, Matthias J. Grotevent, Frank Krumeich, Maryna I. Bodnarchuk, Ivan Shorubalko, Francesco Stellacci, and Maksym V. Kovalenko. Stable ultraconcentrated and ultradilute colloids of CsPbBr_3 ($x = \text{cl}, \text{br}$) nanocrystals using natural lecithin as a capping ligand. *Journal of the American Chemical Society*, 141:19839–19849, 12 2019. ISSN 0002-7863. doi: 10.1021/jacs.9b09969.
- [187] Jonathan Owen. The coordination chemistry of nanocrystal surfaces. *Science*, 347:615–616, 2 2015. ISSN 0036-8075. doi: 10.1126/science.1259924.
- [188] Jonathan De Roo, Yolanda Justo, Katrien De Keukeleere, Freya Van den Broeck, José C. Martins, Isabel Van Driessche, and Zeger Hens. Carboxylic-acid-passivated

- metal oxide nanocrystals: Ligand exchange characteristics of a new binding motif. *Angewandte Chemie International Edition*, 54:6488–6491, 5 2015. ISSN 14337851. doi: 10.1002/anie.201500965.
- [189] Roberto Grisorio, Doriana Debellis, Gian Paolo Suranna, Giuseppe Gigli, and Carlo Giansante. The dynamic organic/inorganic interface of colloidal pbs quantum dots. *Angewandte Chemie*, 128:6740–6745, 6 2016. ISSN 00448249. doi: 10.1002/ange.201511174.
- [190] Nicholas C. Anderson, Peter. E. Chen, Aya K. Buckley, Jonathan De Roo, and Jonathan S. Owen. Stereoelectronic effects on the binding of neutral lewis bases to cdse nanocrystals. *Journal of the American Chemical Society*, 140:7199–7205, 6 2018. ISSN 0002-7863. doi: 10.1021/jacs.8b02927.
- [191] Chenghao Bi, Zhiwei Yao, Xuejiao Sun, Xuecheng Wei, Junxi Wang, and Jianjun Tian. Perovskite quantum dots with ultralow trap density by acid etching-driven ligand exchange for high luminance and stable pure-blue light-emitting diodes. *Advanced Materials*, 33:2006722, 4 2021. ISSN 0935-9648. doi: 10.1002/adma.202006722.
- [192] Nicholas C Anderson, Mark P Hendricks, Joshua J Choi, and Jonathan S Owen. Ligand exchange and the stoichiometry of metal chalcogenide nanocrystals: spectroscopic observation of facile metal-carboxylate displacement and binding. *Journal of the American Chemical Society*, 135:18536–48, 12 2013. ISSN 1520-5126. doi: 10.1021/ja4086758.
- [193] Yang Zhou, Fudong Wang, and William E. Buhro. Large exciton energy shifts by reversible surface exchange in 2d ii–vi nanocrystals. *Journal of the American Chemical Society*, 137:15198–15208, 12 2015. ISSN 0002-7863. doi: 10.1021/jacs.5b09343.
- [194] Yang Zhou and William E. Buhro. Reversible exchange of l-type and bound-ion-pair x-type ligation on cadmium selenide quantum belts. *Journal of the American Chemical Society*, 139:12887–12890, 9 2017. ISSN 0002-7863. doi: 10.1021/jacs.7b05167.
- [195] Jari Leemans, Kim C. Dümbgen, Matthias M. Minjauw, Qiang Zhao, André Vantomme, Ivan Infante, Christophe Detavernier, and Zeger Hens. Acid–base mediated ligand exchange on near-infrared absorbing, indium-based iii–v colloidal quantum dots. *Journal of the American Chemical Society*, 143:4290–4301, 3 2021. ISSN 0002-7863. doi: 10.1021/jacs.0c12871.

- [196] Evelyn L. Rosen, Raffaella Buonsanti, Anna Llordes, April M. Sawvel, Delia J. Milliron, and Brett A. Helms. Exceptionally mild reactive stripping of native ligands from nanocrystal surfaces by using meerwein's salt. *Angewandte Chemie International Edition*, 51:684–689, 1 2012. ISSN 14337851. doi: 10.1002/anie.201105996.
- [197] Jonathan De Roo, Isabel Van Driessche, José C. Martins, and Zeger Hens. Colloidal metal oxide nanocrystal catalysis by sustained chemically driven ligand displacement. *Nature Materials*, 15:517–521, 5 2016. ISSN 1476-1122. doi: 10.1038/nmat4554.
- [198] Quinten A. Akkerman, Sungwook Park, Eros Radicchi, Francesca Nunzi, Edoardo Mosconi, Filippo De Angelis, Rosaria Brescia, Prachi Rastogi, Mirko Prato, and Liberato Manna. Nearly monodisperse insulator Cs_4PbX_3 ($x = \text{cl}, \text{br}, \text{i}$) nanocrystals, their mixed halide compositions, and their transformation into CsPbX_3 nanocrystals. *Nano Letters*, 17:1924–1930, 3 2017. ISSN 1530-6984. doi: 10.1021/acs.nanolett.6b05262.
- [199] Zeke Liu, Yehonadav Bekenstein, Xingchen Ye, Son C. Nguyen, Joseph Swabeck, Dandan Zhang, Shuit-Tong Lee, Peidong Yang, Wanli Ma, and A. Paul Alivisatos. Ligand mediated transformation of cesium lead bromide perovskite nanocrystals to lead depleted $\text{Cs}_{4-x}\text{Pb}_x\text{Br}_6$ nanocrystals. *Journal of the American Chemical Society*, 139:5309–5312, 4 2017. ISSN 0002-7863. doi: 10.1021/jacs.7b01409.
- [200] Subila K. Balakrishnan and Prashant V. Kamat. Ligand assisted transformation of cubic CsPbBr_3 nanocrystals into two-dimensional CsPb_2Br_5 nanosheets. *Chemistry of Materials*, 30:74–78, 1 2018. ISSN 0897-4756. doi: 10.1021/acs.chemmater.7b04142.
- [201] Francisco Palazon, Guilherme Almeida, Quinten A. Akkerman, Luca De Trizio, Zhiya Dang, Mirko Prato, and Liberato Manna. Changing the dimensionality of cesium lead bromide nanocrystals by reversible postsynthesis transformations with amines. *Chemistry of Materials*, 29:4167–4171, 5 2017. ISSN 0897-4756. doi: 10.1021/acs.chemmater.7b00895.
- [202] Javad Shamsi, Zhiya Dang, Palvasha Ijaz, Ahmed L. Abdelhady, Giovanni Bertoni, Iwan Moreels, and Liberato Manna. Colloidal CsX ($x = \text{cl}, \text{br}, \text{i}$) nanocrystals and their transformation to CsPbX_3 nanocrystals by cation exchange. *Chemistry of Materials*, 30:79–83, 1 2018. ISSN 0897-4756. doi: 10.1021/acs.chemmater.7b04827.

- [203] Linzhong Wu, Huicheng Hu, Yong Xu, Shu Jiang, Min Chen, Qixuan Zhong, Di Yang, Qipeng Liu, Yun Zhao, Baoquan Sun, Qiao Zhang, and Yadong Yin. From nonluminescent Cs_4PbX_6 ($x = \text{cl}, \text{br}, \text{i}$) nanocrystals to highly luminescent CsPbX_3 nanocrystals: Water-triggered transformation through a csx-stripping mechanism. *Nano Letters*, 17:5799–5804, 9 2017. ISSN 1530-6984. doi: 10.1021/acs.nanolett.7b02896.
- [204] Chris de Weerd, Junhao Lin, Leyre Gomez, Yasufumi Fujiwara, Kazutomo Suenaga, and Tom Gregorkiewicz. Hybridization of single nanocrystals of Cs_4PbBr_6 and CsPbBr_3 . *The Journal of Physical Chemistry C*, 121:19490–19496, 9 2017. ISSN 1932-7447. doi: 10.1021/acs.jpcc.7b05752.
- [205] Wei Zhai, Jing Lin, Chun Li, Shouming Hu, Yang Huang, Chao Yu, Zhikai Wen, Zhenya Liu, Yi Fang, and Chengchun Tang. Solvothermal synthesis of cesium lead halide perovskite nanowires with ultra-high aspect ratios for high-performance photodetectors. *Nanoscale*, 10:21451–21458, 2018. ISSN 2040-3364. doi: 10.1039/C8NR05683H.
- [206] Thumu Udayabhaskararao, Lothar Houben, Hagai Cohen, Matan Menahem, Iddo Pinkas, Liat Avram, Tamar Wolf, Ayelet Teitelboim, Michal Leskes, Omer Yaffe, Dan Oron, and Miri Kazes. A mechanistic study of phase transformation in perovskite nanocrystals driven by ligand passivation. *Chemistry of Materials*, 30:84–93, 1 2018. ISSN 0897-4756. doi: 10.1021/acs.chemmater.7b02425.
- [207] Sara R. Smock, Travis J. Williams, and Richard L. Brutchey. Quantifying the thermodynamics of ligand binding to CsPbBr_3 quantum dots. *Angewandte Chemie*, 130:11885–11889, 9 2018. ISSN 0044-8249. doi: 10.1002/ange.201806916.
- [208] Muhammad Imran, Palvasha Ijaz, Luca Goldoni, Daniela Maggioni, Urko Petralanda, Mirko Prato, Guilherme Almeida, Ivan Infante, and Liberato Manna. Simultaneous cationic and anionic ligand exchange for colloiddally stable CsPbBr_3 nanocrystals. *ACS Energy Letters*, 4:819–824, 4 2019. ISSN 2380-8195. doi: 10.1021/acsenergylett.9b00140.
- [209] Muhammad Imran, Binh T. Mai, Luca Goldoni, Matilde Cirignano, Houman Bahmani Jalali, Francesco Di Stasio, Teresa Pellegrino, and Liberato Manna. Switchable anion exchange in polymer-encapsulated apbx_3 nanocrystals delivers stable all-perovskite white emitters. *ACS Energy Letters*, 6:2844–2853, 8 2021. ISSN 2380-8195. doi: 10.1021/acsenergylett.1c01232.
- [210] Aizhao Pan, Bo He, Xiaoyun Fan, Zeke Liu, Jeffrey J. Urban, A. Paul Alivisatos, Ling He, and Yi Liu. Insight into the ligand-mediated synthesis of colloidal

- CsPbBr₃ perovskite nanocrystals: The role of organic acid, base, and cesium precursors. *ACS Nano*, 10:7943–7954, 8 2016. ISSN 1936-0851. doi: 10.1021/acsnano.6b03863.
- [211] Stephanie ten Brinck and Ivan Infante. Surface termination, morphology, and bright photoluminescence of cesium lead halide perovskite nanocrystals. *ACS Energy Letters*, 1:1266–1272, 12 2016. ISSN 2380-8195. doi: 10.1021/acseenergylett.6b00595.
- [212] Anirban Dutta, Sumit Kumar Dutta, Samrat Das Adhikari, and Narayan Pradhan. Tuning the size of CsPbBr₃ nanocrystals: All at one constant temperature. *ACS Energy Letters*, 3:329–334, 2 2018. ISSN 2380-8195. doi: 10.1021/acseenergylett.7b01226.
- [213] Sigalit Aharon, Małgorzata Wierzbowska, and Lioz Etgar. The effect of the alkylammonium ligand’s length on organic–inorganic perovskite nanoparticles. *ACS Energy Letters*, 3:1387–1393, 6 2018. ISSN 2380-8195. doi: 10.1021/acseenergylett.8b00554.
- [214] Feng Liu, Yaohong Zhang, Chao Ding, Syuusuke Kobayashi, Takuya Izuishi, Naoki Nakazawa, Taro Toyoda, Tsuyoshi Ohta, Shuzi Hayase, Takashi Minemoto, Kenji Yoshino, Songyuan Dai, and Qing Shen. Highly luminescent phase-stable cspbi 3 perovskite quantum dots achieving near 100 *ACS Nano*, 11:10373–10383, 10 2017. ISSN 1936-0851. doi: 10.1021/acsnano.7b05442.
- [215] Chujie Wang, Anthony S. R. Chesman, and Jacek J. Jasieniak. Stabilizing the cubic perovskite phase of cspbi 3 nanocrystals by using an alkyl phosphinic acid. *Chemical Communications*, 53:232–235, 2017. ISSN 1359-7345. doi: 10.1039/C6CC08282C.
- [216] Ju Young Woo, Youngsik Kim, Jungmin Bae, Tae Gun Kim, Jeong Won Kim, Doh C. Lee, and Sohee Jeong. Highly stable cesium lead halide perovskite nanocrystals through in situ lead halide inorganic passivation. *Chemistry of Materials*, 29:7088–7092, 9 2017. ISSN 0897-4756. doi: 10.1021/acs.chemmater.7b02669.
- [217] Yesu Tan, Yatao Zou, Linzhong Wu, Qi Huang, Di Yang, Min Chen, Muiyang Ban, Chen Wu, Tian Wu, Sai Bai, Tao Song, Qiao Zhang, and Baoquan Sun. Highly luminescent and stable perovskite nanocrystals with octylphosphonic acid as a ligand for efficient light-emitting diodes. *ACS Applied Materials & Interfaces*, 10:3784–3792, 1 2018. ISSN 1944-8244. doi: 10.1021/acsami.7b17166.

- [218] Jun Pan, Smritakshi P. Sarmah, Banavoth Murali, Ibrahim Dursun, Wei Peng, Manas R. Parida, Jiakai Liu, Lutfan Sinatra, Noktan Alyami, Chao Zhao, Erkki Alarousu, Tien Khee Ng, Boon S. Ooi, Osman M. Bakr, and Omar F. Mohammed. Air-stable surface-passivated perovskite quantum dots for ultra-robust, single- and two-photon-induced amplified spontaneous emission. *The Journal of Physical Chemistry Letters*, 6:5027–5033, 12 2015. ISSN 1948-7185. doi: 10.1021/acs.jpcclett.5b02460.
- [219] Francesco Di Stasio, Sotirios Christodoulou, Nengjie Huo, and Gerasimos Konstantatos. Near-unity photoluminescence quantum yield in CsPbBr₃ nanocrystal solid-state films via postsynthesis treatment with lead bromide. *Chemistry of Materials*, 29:7663–7667, 9 2017. ISSN 0897-4756. doi: 10.1021/acs.chemmater.7b02834.
- [220] Brent A. Koscher, Joseph K. Swabeck, Noah D. Bronstein, and A. Paul Alivisatos. Essentially trap-free CsPbBr₃ colloidal nanocrystals by postsynthetic thiocyanate surface treatment. *Journal of the American Chemical Society*, 139:6566–6569, 5 2017. ISSN 0002-7863. doi: 10.1021/jacs.7b02817.
- [221] Tasnim Ahmed, Sudipta Seth, and Anunay Samanta. Boosting the photoluminescence of CsPbBr₃ (x = cl, br, i) perovskite nanocrystals covering a wide wavelength range by postsynthetic treatment with tetrafluoroborate salts. *Chemistry of Materials*, 30:3633–3637, 6 2018. ISSN 0897-4756. doi: 10.1021/acs.chemmater.8b01235.
- [222] Shouqiang Huang, Bo Wang, Qi Zhang, Zhichun Li, Aidang Shan, and Liang Li. Postsynthesis potassium-modification method to improve stability of CsPbBr₃ perovskite nanocrystals. *Advanced Optical Materials*, 6(6):1701106, 2018. doi: <https://doi.org/10.1002/adom.201701106>.
- [223] Bernhard J. Bohn, Yu Tong, Moritz Gramlich, May Ling Lai, Markus Döblinger, Kun Wang, Robert L. Z. Hoyer, Peter Müller-Buschbaum, Samuel D. Stranks, Alexander S. Urban, Lakshminarayana Polavarapu, and Jochen Feldmann. Boosting tunable blue luminescence of halide perovskite nanoplatelets through postsynthetic surface trap repair. *Nano Letters*, 18:5231–5238, 8 2018. ISSN 1530-6984. doi: 10.1021/acs.nanolett.8b02190.
- [224] Chang Lu, Hui Li, Kathy Kolodziejski, Chaochao Dun, Wenxiao Huang, David Carroll, and Scott M. Geyer. Enhanced stabilization of inorganic cesium lead triiodide (CsPbI₃) perovskite quantum dots with tri-octylphosphine. *Nano Research*, 11:762–768, 2 2018. ISSN 1998-0124. doi: 10.1007/s12274-017-1685-1.
- [225] Jun Pan, Yuequn Shang, Jun Yin, Michele De Bastiani, Wei Peng, Ibrahim Dursun, Lutfan Sinatra, Ahmed M. El-Zohry, Mohamed N. Hedhili, Abdul-Hamid

- Emwas, Omar F. Mohammed, Zhijun Ning, and Osman M. Bakr. Bidentate ligand-passivated cspbi 3 perovskite nanocrystals for stable near-unity photoluminescence quantum yield and efficient red light-emitting diodes. *Journal of the American Chemical Society*, 140:562–565, 1 2018. ISSN 0002-7863. doi: 10.1021/jacs.7b10647.
- [226] Ye Wu, Changting Wei, Xiaoming Li, Yuelei Li, Shuangchen Qiu, Wei Shen, Bo Cai, Zhiguo Sun, Dandan Yang, Zhengtao Deng, and Haibo Zeng. In situ passivation of pbbr 6 4- octahedra toward blue luminescent CsPbBr₃ nanoplatelets with near 100 *ACS Energy Letters*, 3:2030–2037, 9 2018. ISSN 2380-8195. doi: 10.1021/acseenergylett.8b01025.
- [227] Chris Guhrenz, Albrecht Benad, C. Ziegler, Danny Haubold, Nikolai Gaponik, and Alexander Eychmüller. Solid-state anion exchange reactions for color tuning of cspb_x3 perovskite nanocrystals. *Chemistry of Materials*, 28:9033–9040, 2016. doi: 10.1021/acs.chemmater.6B03980.
- [228] Michaela Meyns, Mariano Perálvarez, Amelie Heuer-Jungemann, Wim Hertog, Maria Ibáñez, Raquel Nafria, Aziz Genç, Jordi Arbiol, Maksym V. Kovalenko, Josep Carreras, Andreu Cabot, and Antonios G. Kanaras. Polymer-enhanced stability of inorganic perovskite nanocrystals and their application in color conversion leds. *ACS Applied Materials & Interfaces*, 8:19579–19586, 8 2016. ISSN 1944-8244. doi: 10.1021/acsami.6b02529.
- [229] Shilpa N. Raja, Yehonadav Bekenstein, Matthew A. Koc, Stefan Fischer, Dandan Zhang, Liwei Lin, Robert O. Ritchie, Peidong Yang, and A. Paul Alivisatos. Encapsulation of perovskite nanocrystals into macroscale polymer matrices: Enhanced stability and polarization. *ACS Applied Materials & Interfaces*, 8:35523–35533, 12 2016. ISSN 1944-8244. doi: 10.1021/acsami.6b09443.
- [230] Qingchao Zhou, Zelong Bai, Wen-gao Lu, Yongtian Wang, Bingsuo Zou, and Haizheng Zhong. In situ fabrication of halide perovskite nanocrystal-embedded polymer composite films with enhanced photoluminescence for display backlights. *Advanced Materials*, 28(41):9163–9168, 2016. doi: <https://doi.org/10.1002/adma.201602651>.
- [231] Zhichun Li, Long Kong, Shouqiang Huang, and Liang Li. Highly luminescent and ultrastable CsPbBr₃ perovskite quantum dots incorporated into a silica/alumina monolith. *Angewandte Chemie International Edition*, 56:8134–8138, 7 2017. ISSN 14337851. doi: 10.1002/anie.201703264.
- [232] Li Na Quan, Rafael Quintero-Bermudez, Oleksandr Voznyy, Grant Walters, Ankit Jain, James Zhangming Fan, Xueli Zheng, Zhenyu Yang, and Edward H. Sargent.

- Highly emissive green perovskite nanocrystals in a solid state crystalline matrix. *Advanced Materials*, 29(21):1605945, 2017. doi: <https://doi.org/10.1002/adma.201605945>.
- [233] Leimeng Xu, Jiawei Chen, Jizhong Song, Jianhai Li, Jie Xue, Yuhui Dong, Bo Cai, Qingsong Shan, Boning Han, and Haibo Zeng. Double-protected all-inorganic perovskite nanocrystals by crystalline matrix and silica for triple-modal anti-counterfeiting codes. *ACS Applied Materials & Interfaces*, 9:26556–26564, 8 2017. ISSN 1944-8244. doi: 10.1021/acsami.7b06436.
- [234] Baodan Zhao, Sai Bai, Vincent Kim, Robin Lamboll, Ravichandran Shivanna, Florian Auras, Johannes M. Richter, Le Yang, Linjie Dai, Mejd Alsari, Xiao-Jian She, Lusheng Liang, Jiangbin Zhang, Samuele Lilliu, Peng Gao, Henry J. Snaith, Jianpu Wang, Neil C. Greenham, Richard H. Friend, and Dawei Di. High-efficiency perovskite–polymer bulk heterostructure light-emitting diodes. *Nature Photonics*, 12:783–789, 12 2018. ISSN 1749-4885. doi: 10.1038/s41566-018-0283-4.
- [235] Hongge Wu, Sheng Wang, Fan Cao, Jipeng Zhou, Qianqian Wu, Haoran Wang, Xiaomin Li, Luqiao Yin, and Xuyong Yang. Ultrastable inorganic perovskite nanocrystals coated with a thick long-chain polymer for efficient white light-emitting diodes. *Chemistry of Materials*, 31:1936–1940, 3 2019. ISSN 0897-4756. doi: 10.1021/acs.chemmater.8b04634.
- [236] Sahitya Kumar Avugadda, Andrea Castelli, Balaji Dhanabalan, Tamara Fernandez, Niccolo Silvestri, Cynthia Collantes, Dmitry Baranov, Muhammad Imran, Liberato Manna, Teresa Pellegrino, and Milena P. Arciniegas. Highly emitting perovskite nanocrystals with 2-year stability in water through an automated polymer encapsulation for bioimaging. *ACS Nano*, 16:13657–13666, 9 2022. ISSN 1936-0851. doi: 10.1021/acsnano.2c01556.
- [237] Jingjing Zhao, Liang Zhao, Yehao Deng, Xun Xiao, Zhenyi Ni, Shuang Xu, and Jinsong Huang. Perovskite-filled membranes for flexible and large-area direct-conversion x-ray detector arrays. *Nature Photonics*, 14:612–617, 10 2020. ISSN 1749-4885. doi: 10.1038/s41566-020-0678-x.
- [238] W. C. Röntgen. On a new kind of rays. *Science*, 3:227–231, 2 1896. ISSN 0036-8075. doi: 10.1126/science.3.59.227.
- [239] B D Milbrath, A J Peurrung, M Bliss, and W J Weber. Radiation detector materials: An overview. *Journal of Materials Research*, 23:2561–2581, 2008. ISSN 2044-5326. doi: 10.1557/JMR.2008.0319.
- [240] J. Daniels. The x-rays. *Science*, 3:562–563, 1986. doi: 10.1126/science.3.67.562.

- [241] K. Kamiya, K. Ozasa, S. Akiba, O. Niwa, K. Kodama, N. Takamura, E. K. Zharieva, Y. Kimura, and R. Wakeford. Long-term effects of radiation exposure on health. *The Lancet*, 386:469–478, 2015. doi: 10.1016/S0140-6736(15)61167-9.
- [242] Jolyon H Hendry, Steven L Simon, Andrzej Wojcik, Mehdi Sohrabi, Werner Burkart, Elisabeth Cardis, Dominique Laurier, Margot Tirmarche, and Isamu Hayata. Human exposure to high natural background radiation: what can it teach us about radiation risks? *Journal of Radiological Protection*, 29:A29–A42, 6 2009. ISSN 0952-4746. doi: 10.1088/0952-4746/29/2A/S03.
- [243] Alexander Vaiserman, Alexander Koliada, Oksana Zabuga, and Yehoshua Socol. Health impacts of low-dose ionizing radiation: Current scientific debates and regulatory issues. *Dose-Response*, 16:155932581879633, 7 2018. ISSN 1559-3258. doi: 10.1177/1559325818796331.
- [244] Zhongzhu Hong, Zhaowei Chen, Qiushui Chen, and Huanghao Yang. Advancing x-ray luminescence for imaging, biosensing, and theragnostics. *Accounts of Chemical Research*, 56:37–51, 1 2023. ISSN 0001-4842. doi: 10.1021/acs.accounts.2c00517.
- [245] Glenn F. Knoll. *Radiation Detection and Measurement*. John Wiley & Sons, 2010. ISBN 978-0-470-13148-0.
- [246] Michael Overdick, Christian Baumer, Klaus Jürgen Engel, Johannes Fink, Christoph Herrmann, Hans Kruger, Matthias Simon, Roger Steadman, and Gnter Zeitler. Status of direct conversion detectors for medical imaging with x-rays. *IEEE Transactions on Nuclear Science*, 56(4):1800–1809, 2009. doi: 10.1109/TNS.2009.2025041.
- [247] S.O. Kasap and J.A. Rowlands. Direct-conversion flat-panel x-ray image sensors for digital radiography. *Proceedings of the IEEE*, 90(4):591–604, 2002. doi: 10.1109/JPROC.2002.1002529.
- [248] Fei Cao, Dejian Yu, Wenbo Ma, Xiaobao Xu, Bo Cai, Yang Michael Yang, Sinan Liu, Lunhua He, Yubin Ke, Si Lan, Kwang-Leong Choy, and Haibo Zeng. Shining emitter in a stable host: Design of halide perovskite scintillators for x-ray imaging from commercial concept. *ACS Nano*, 14:5183–5193, 5 2020. ISSN 1936-0851. doi: 10.1021/acsnano.9b06114.
- [249] Lu Lu, Mingzi Sun, Qiuyang Lu, Tong Wu, and Bolong Huang. High energy x-ray radiation sensitive scintillating materials for medical imaging, cancer diagnosis and therapy. *Nano Energy*, 79:105437, 1 2021. ISSN 22112855. doi: 10.1016/j.nanoen.2020.105437.

- [250] AN Vasil'ev. Relaxation of hot electronic excitations in scintillators: account for scattering, track effects, complicated electronic structure. In *Proc. 5th Int. Conf. on Inorganic Scintillators and their Applications (SCINT99)*, pages 43–52, 2000.
- [251] P. Lecoq, A. Gektin, and M. Korzhik. *Inorganic Scintillators for Detector Systems, 2nd Edition*. Springer Cham, 2016. ISBN 978-3-319-45521-1. doi: 10.1007/978-3-319-45522-8.
- [252] Robert . Alkali halide scintillation counters. *Phys. Rev.*, 74:100–101, 1948. doi: 10.1103/PhysRev.74.100.
- [253] W. Van Sciver and R. Hofstadter. Scintillations in thallium-activated CaI_2 and CsI . *Phys. Rev.*, 84:1062–1063, Dec 1951. doi: 10.1103/PhysRev.84.1062.2.
- [254] M. J. Weber and R. R. Monchamp. Luminescence of $\text{Bi}_4\text{Ge}_3\text{O}_{12}$: Spectral and decay properties. *Journal of Applied Physics*, 44(12):5495–5499, 10 2003. ISSN 0021-8979. doi: 10.1063/1.1662183.
- [255] E. V. D. van Loef, P. Dorenbos, C. W. E. van Eijk, K. Krämer, and H. U. Güdel. High-energy-resolution scintillator: Ce^{3+} activated LaBr_3 . *Applied Physics Letters*, 79(10):1573–1575, 09 2001. ISSN 0003-6951. doi: 10.1063/1.1385342.
- [256] E V D van Loef, P Dorenbos, C W E van Eijk, K W Krämer, and H U Güdel. Scintillation and spectroscopy of the pure and Ce^{3+} -doped elpasolites: Cs_2LiYx_6 ($x = \text{Cl}, \text{Br}$). *Journal of Physics: Condensed Matter*, 14:8481–8496, 9 2002. ISSN 0953-8984. doi: 10.1088/0953-8984/14/36/307.
- [257] Carel W E van Eijk. Inorganic scintillators in medical imaging. *Physics in Medicine and Biology*, 47:R85–R106, 4 2002. ISSN 0031-9155. doi: 10.1088/0031-9155/47/8/201.
- [258] Takayuki Yanagida. Study of rare-earth-doped scintillators. *Optical Materials*, 35:1987–1992, 9 2013. ISSN 09253467. doi: 10.1016/j.optmat.2012.11.002.
- [259] Martin Nikl and Akira Yoshikawa. Recent r&d trends in inorganic single-crystal scintillator materials for radiation detection. *Advanced Optical Materials*, 3:463–481, 4 2015. ISSN 21951071. doi: 10.1002/adom.201400571.
- [260] Paul Lecoq. Development of new scintillators for medical applications. *Nuclear Instruments and Methods in Physics Research Section A: Accelerators, Spectrometers, Detectors and Associated Equipment*, 809:130–139, 2 2016. ISSN 01689002. doi: 10.1016/j.nima.2015.08.041.

- [261] C.M. Pepin, P. Berard, A.-L. Perrot, C. Pepin, D. Houde, R. Lecomte, C.L. Melcher, and H. Dautet. Properties of lyso and recent lso scintillators for phoswich pet detectors. *IEEE Transactions on Nuclear Science*, 51(3):789–795, 2004. doi: 10.1109/TNS.2004.829781.
- [262] Rihua Mao, Liyuan Zhang, and Ren-Yuan Zhu. Optical and scintillation properties of inorganic scintillators in high energy physics. *IEEE Transactions on Nuclear Science*, 55(4):2425–2431, 2008. doi: 10.1109/TNS.2008.2000776.
- [263] H. Alva-Sánchez, A. Zepeda-Barrios, V. D. Díaz-Martínez, T. Murrieta-Rodríguez, A. Martínez-Dávalos, and M. Rodríguez-Villafuerte. Understanding the intrinsic radioactivity energy spectrum from ^{176}Lu in lyso/lso scintillation crystals. *Scientific Reports*, 8:17310, 11 2018. ISSN 2045-2322. doi: 10.1038/s41598-018-35684-x.
- [264] Charles L. Melcher. Scintillation crystals for pet. *Journal of Nuclear Medicine*, 41(6):1051–1055, 2000. ISSN 0161-5505.
- [265] J. Czochralski. Ein neues verfahren zur messung der kristallisationsgeschwindigkeit der metalle. *Zeitschrift für Physikalische Chemie*, 92U:219–221, 1918. doi: 10.1515/zpch-1918-9212.
- [266] Paweł E. Tomaszewski. Jan czochralski—father of the czochralski method. *Journal of Crystal Growth*, 236:1–4, 3 2002. ISSN 00220248. doi: 10.1016/S0022-0248(01)02195-9.
- [267] P. W. Bridgman. Certain Physical Properties of Single Crystals of Tungsten, Antimony, Bismuth, Tellurium, Cadmium, Zinc, and Tin. *Proceedings of the American Academy of Arts and Sciences*, 60(6):305, 1925. ISSN 01999818. doi: 10.2307/25130058.
- [268] Donald C. Stockbarger. The Production of Large Single Crystals of Lithium Fluoride. *Review of Scientific Instruments*, 7(3):133–136, mar 1936. ISSN 0034-6748. doi: 10.1063/1.1752094.
- [269] Hans J. Scheel and Peter Capper, editors. *Crystal Growth Technology*. Wiley, jan 2008. ISBN 9783527317622. doi: 10.1002/9783527623440.
- [270] S. E. Létant and T.-F. Wang. Semiconductor quantum dot scintillation under γ -ray irradiation. *Nano Letters*, 6:2877–2880, 12 2006. ISSN 1530-6984. doi: 10.1021/nl0620942.
- [271] S. E. Létant and T.-F. Wang. Study of porous glass doped with quantum dots or laser dyes under alpha irradiation. *Applied Physics Letters*, 88(10):103110, 03 2006. ISSN 0003-6951. doi: 10.1063/1.2182072.

- [272] Zhaojun Zhang, Hanna Dierks, Nils Lamers, Chen Sun, Klára Nováková, Crispin Hetherington, Ivan G. Scheblykin, and Jesper Wallentin. Single-crystalline perovskite nanowire arrays for stable x-ray scintillators with micrometer spatial resolution. *ACS Applied Nano Materials*, 5:881–889, 1 2022. ISSN 2574-0970. doi: 10.1021/acsanm.1c03575.
- [273] Ilhwan Ryu, Jee-Yeon Ryu, Geunpyo Choe, Hyemin Kwon, Hyeji Park, Young-Seok Cho, Rose Du, and Sanggyu Yim. In vivo plain x-ray imaging of cancer using perovskite quantum dot scintillators. *Advanced Functional Materials*, 31:2102334, 8 2021. ISSN 1616-301X. doi: 10.1002/adfm.202102334.
- [274] Arie Wibowo, Md Abdul Kuddus Sheikh, Lina Jaya Diguna, Muhammad Bagas Ananda, Maradhana Agung Marsudi, Arramel Arramel, Shuwen Zeng, Liang Jie Wong, and Muhammad Danang Birowosuto. Development and challenges in perovskite scintillators for high-resolution imaging and timing applications. *Communications Materials*, 4:21, 3 2023. ISSN 2662-4443. doi: 10.1038/s43246-023-00348-5.
- [275] Andrea Erroi, Sara Mecca, Matteo L. Zaffalon, Isabel Frank, Francesco Carulli, Alessia Cemmi, Ilaria Di Sarcina, Doriana Debellis, Francesca Rossi, Francesca Cova, Kristof Pauwels, Michele Mauri, Jacopo Perego, Valerio Pinchetti, Angiolina Comotti, Francesco Meinardi, Anna Vedda, Etienne Auffray, Luca Beverina, and Sergio Brovelli. Ultrafast and radiation-hard lead halide perovskite nanocomposite scintillators. *ACS Energy Letters*, 8:3883–3894, 9 2023. ISSN 2380-8195. doi: 10.1021/acsenerylett.3c01396.
- [276] Roberto Calà, Isabel Frank, Fiammetta Pagano, Francesco Maddalena, Cuong Dang, Muhammad Danang Birowosuto, and Etienne Auffray. Sub-100-picosecond time resolution from undoped and Li-doped two-dimensional perovskite scintillators. *Applied Physics Letters*, 120(24):241901, 06 2022. ISSN 0003-6951. doi: 10.1063/5.0093606.
- [277] Weiwei Chen, Xiaosheng Tang, Peihua Wangyang, Zhiqiang Yao, Dan Zhou, Fenggui Chen, Shiqi Li, Hao Lin, Fanju Zeng, Daofu Wu, Kuan Sun, Meng Li, Yi Huang, Wei Hu, Zhigang Zang, and Juan Du. Surface-passivated cesium lead halide perovskite quantum dots: Toward efficient light-emitting diodes with an inverted sandwich structure. *Advanced Optical Materials*, 6:1800007, 7 2018. ISSN 2195-1071. doi: 10.1002/adom.201800007.
- [278] Yuhai Zhang, Ruijia Sun, Xiangyu Ou, Kaifang Fu, Qiushui Chen, Yuchong Ding, Liang-Jin Xu, Lingmei Liu, Yu Han, Anton V. Malko, Xiaogang Liu, Huanghao Yang, Osman M. Bakr, Hong Liu, and Omar F. Mohammed. Metal halide

- perovskite nanosheet for x-ray high-resolution scintillation imaging screens. *ACS Nano*, 13:2520–2525, 2 2019. ISSN 1936-0851. doi: 10.1021/acsnano.8b09484.
- [279] Aozhen Xie, Tien Hoa Nguyen, Chathuranga Hettiarachchi, Marcin E. Witkowski, Winicjusz Drozdowski, Muhammad Danang Birowosuto, Hong Wang, and Cuong Dang. Thermal quenching and dose studies of x-ray luminescence in single crystals of halide perovskites. *The Journal of Physical Chemistry C*, 122:16265–16273, 7 2018. ISSN 1932-7447. doi: 10.1021/acs.jpcc.8b03622.
- [280] Wenbo Ma, Tingming Jiang, Ze Yang, Hao Zhang, Yirong Su, Zeng Chen, Xinya Chen, Yaoguang Ma, Wenjuan Zhu, Xue Yu, Haiming Zhu, Jianbei Qiu, Xu Liu, Xuhui Xu, and Yang (Michael) Yang. Highly resolved and robust dynamic x-ray imaging using perovskite glass-ceramic scintillator with reduced light scattering. *Advanced Science*, 8(15):2003728, 2021. doi: <https://doi.org/10.1002/adv.202003728>.
- [281] Qiang Xu, Juan Wang, Wenyi Shao, Xiao Ouyang, Xiang Wang, Xinlei Zhang, Yong Guo, and Xiaoping Ouyang. A solution-processed zero-dimensional all-inorganic perovskite scintillator for high resolution gamma-ray spectroscopy detection. *Nanoscale*, 12:9727–9732, 2020. ISSN 2040-3364. doi: 10.1039/D0NR00772B.
- [282] Anne-Laure Bulin, Andrey Vasil’ev, Andrei Belsky, David Amans, Gilles Ledoux, and Christophe Dujardin. Modelling energy deposition in nanoscintillators to predict the efficiency of the x-ray-induced photodynamic effect. *Nanoscale*, 7: 5744–5751, 2015. ISSN 2040-3364. doi: 10.1039/C4NR07444K.
- [283] Lazaro A. Padilha, Wan K. Bae, Victor I. Klimov, Jeffrey M. Pietryga, and Richard D. Schaller. Response of semiconductor nanocrystals to extremely energetic excitation. *Nano Letters*, 13:925–932, 3 2013. ISSN 1530-6984. doi: 10.1021/nl400141w.
- [284] Zhou Meng. Propriétés de scintillation d’hétérostructures nanocristaux semiconductrices II-VI, 2021. Ecole Doctorale N° ED52 - Physique et Astrophysique de Lyon (PHAST). Bibliothèque Universitaire Lyon1, OCLC 1311497102.
- [285] John M. Keller. *Applied Radiation Measurements*, pages 134–162. Springer New York, 2006. ISBN 978-0-387-34123-1. doi: 10.1007/0-387-34123-4_8.
- [286] Jack D. Davidson and Philip Feigelson. Practical aspects of internal-sample liquid scintillation counting. *The International Journal of Applied Radiation and Isotopes*, 2:1–18, 4 1957. ISSN 0020708X. doi: 10.1016/0020-708X(57)90021-2.

- [287] E. Rapkin. Liquid scintillation counting 1957–1963: A review. *The International Journal of Applied Radiation and Isotopes*, 15:69–87, 2 1964. ISSN 0020708X. doi: 10.1016/0020-708X(64)90052-3.
- [288] Ryszard Broda, Philippe Cassette, and Karsten Kossert. Radionuclide metrology using liquid scintillation counting. *Metrologia*, 44:S36–S52, 8 2007. ISSN 0026-1394. doi: 10.1088/0026-1394/44/4/S06.
- [289] S. Möbius and T. L. Möbius. *Handbook of liquid scintillation spectrometry*. Eggenstein-Leopoldshafen : Karlsruhe Institute of Technology, 2012. ISBN 978-3-923704-78-1.
- [290] Philippe Cassette. Mesures de radioactivité par scintillation liquide. *Techniques d'analyse*, 6 2020. doi: 10.51257/a-v2-p2552.
- [291] B.J. Land, Z. Bagdasarian, J. Caravaca, M. Smiley, M. Yeh, and G.D. Orebi Gann. Mev-scale performance of water-based and pure liquid scintillator detectors. *Physical Review D*, 103:052004, 3 2021. ISSN 2470-0010. doi: 10.1103/PhysRevD.103.052004.
- [292] Andrew J. Parker, Michael D. Aspinall, Colin Boxall, Frank D. Cave, and Malcolm J. Joyce. Radiometric techniques for the detection and assessment of tritium in aqueous media - a review. *Progress in Nuclear Energy*, 162:104733, 8 2023. ISSN 01491970. doi: 10.1016/j.pnucene.2023.104733.
- [293] J.L. Erchinger, C.E. Aalseth, B.E. Bernacki, M. Douglas, E.S. Fuller, M.E. Keillor, S.M. Morley, C.A. Mullen, J.L. Orrell, M.E. Panisko, G.A. Warren, R.O. Williams, and M.E. Wright. Development of a low background liquid scintillation counter for a shallow underground laboratory. *Applied Radiation and Isotopes*, 105:209–218, 11 2015. ISSN 09698043. doi: 10.1016/j.apradiso.2015.08.027.
- [294] M. S. Patterson and R. C. Greene. Measurement of low energy beta-emitters in aqueous solution by liquid scintillation counting of emulsions. *Analytical Chemistry*, 37:854–857, 6 1965. ISSN 0003-2700. doi: 10.1021/ac60226a017.
- [295] Dorsey T. Mahin and Robert T. Lofberg. A simplified method of sample preparation for determination of tritium, carbon-14, or sulfur-35 in blood or tissue by liquid scintillation counting. *Analytical Biochemistry*, 16:500–509, 9 1966. ISSN 00032697. doi: 10.1016/0003-2697(66)90233-8.
- [296] J.M. Deconinck, P. van Iseghem, R. Boden, A. Daniels, P. de Regge, C. Hurtgen, D. Huys, M. Klein, and F. Verzezen. Investigation on the determination of disposal critical nuclides in waste from pwr power plants, 1993. Report EUR 14364 EN. Brussels, Commission of the European Communities, 85 pp.

- [297] Y. J. Zhu and D. Z. Yang. The use of liquid scintillation analysis in the monitoring of α emitting and transuranium nuclides in environmental samples. *Journal of Radioanalytical and Nuclear Chemistry Articles*, 194:173–175, 7 1995. ISSN 0236-5731. doi: 10.1007/BF02037624.
- [298] Tran Thi Van, Luu Tam Bat, Dang Duc Nhan, Nguyen Hao Quang, Bui Duy Cam, and Luu Viet Hung. Estimation of radionuclide concentrations and average annual committed effective dose due to ingestion for the population in the red river delta, vietnam. *Environmental Management*, 63:444–454, 4 2019. ISSN 0364-152X. doi: 10.1007/s00267-018-1007-8.
- [299] J. Caravaca, B. J. Land, M. Yeh, and G. D. Orebi Gann. Characterization of water-based liquid scintillator for cherenkov and scintillation separation. *The European Physical Journal C*, 80:867, 9 2020. ISSN 1434-6044. doi: 10.1140/epjc/s10052-020-8418-4.
- [300] P.E. Stanley and S.G. Williams. Use of the liquid scintillation spectrometer for determining adenosine triphosphate by the luciferase enzyme. *Analytical Biochemistry*, 29:381–392, 6 1969. ISSN 00032697. doi: 10.1016/0003-2697(69)90323-6.
- [301] Rodney F. Boyer. *Modern Experimental Biochemistry*. Benjamin Cummings, 3rd edition edition, 2000. ISBN 0805331115.
- [302] Chang Heon Choi, Seongmoon Jung, Kanghyuk Choi, Kwang Jae Son, Jun Sig Lee, and Sung Joon Ye. Radioactivity determination of sealed pure beta-sources by surface dose measurements and monte carlo simulations. *Nuclear Instruments and Methods in Physics Research, Section A: Accelerators, Spectrometers, Detectors and Associated Equipment*, 816:87–95, 4 2016. ISSN 01689002. doi: 10.1016/j.nima.2016.01.085.
- [303] Romain Coulon, Steven Judge, Haoran Liu, and Carine Michotte. The international reference system for pure beta-particle emitting radionuclides: an evaluation of the measurement uncertainties. *Metrologia*, 58(2):025007, mar 2021. doi: 10.1088/1681-7575/abe355.
- [304] E. Aprile *et al.* Search for light dark matter interactions enhanced by the migdal effect or bremsstrahlung in xenon1t. *Physical Review Letters*, 123:241803, 12 2019. ISSN 0031-9007. doi: 10.1103/PhysRevLett.123.241803.
- [305] A. Abusleme *et al.* Optimization of the juno liquid scintillator composition using a daya bay antineutrino detector. *Nuclear Instruments and Methods in Physics Research Section A: Accelerators, Spectrometers, Detectors and Associated Equipment*, 988:164823, 2 2021. ISSN 01689002. doi: 10.1016/j.nima.2020.164823.

- [306] I.A. Suslov, I.B. Nemchenok, Yu. A. Shitov, S.V. Kazartsev, V.V. Belov, and A.D. Bystryakov. Development of a new tellurium loaded liquid scintillator based on linear alkylbenzene. *Nuclear Instruments and Methods in Physics Research Section A: Accelerators, Spectrometers, Detectors and Associated Equipment*, 1040:167131, 10 2022. ISSN 01689002. doi: 10.1016/j.nima.2022.167131.
- [307] Y. Fukuda *et al.* Evidence for oscillation of atmospheric neutrinos. *Physical Review Letters*, 81:1562–1567, 8 1998. ISSN 0031-9007. doi: 10.1103/PhysRevLett.81.1562.
- [308] D. Castelvechi. Gigantic japanese detector seeks supernova neutrinos. *Nature, News in Focus*, 566, 2019.
- [309] Buyang Yu, Chunfeng Zhang, Lan Chen, Zhengyuan Qin, Xinyu Huang, Xiaoyong Wang, and Min Xiao. Ultrafast dynamics of photoexcited carriers in perovskite semiconductor nanocrystals. *Nanophotonics*, 10:1943–1965, 6 2021. ISSN 2192-8614. doi: 10.1515/nanoph-2020-0681.
- [310] Stefan Schoppmann. Review of novel approaches to organic liquid scintillators in neutrino physics. *Symmetry*, 15:11, 12 2022. ISSN 2073-8994. doi: 10.3390/sym15010011.
- [311] Yining He, Keke Guo, Li Yang, Li Zhang, and Ji-Min Han. Effective fluorescent turn-on detection of ionizing radiations through controllable intramolecular photoinduced electron transfer. *Journal of Photochemistry and Photobiology A: Chemistry*, 439:114635, 5 2023. ISSN 10106030. doi: 10.1016/j.jphotochem.2023.114635.
- [312] Perkin Elmer Resources, Accessed August 2023. URL https://resources.perkinelmer.com/lab-solutions/resources/docs/APP_Cocktails-for-Liquid-Scintillation-Counting-011940_01.pdf.
- [313] Yangning Zhang, Timothy D. Siegler, Cherrelle J. Thomas, Michael K. Abney, Tushti Shah, Anastacia De Gorostiza, Randalynn M. Greene, and Brian A. Korgel. A “tips and tricks” practical guide to the synthesis of metal halide perovskite nanocrystals. *Chemistry of Materials*, 32:5410–5423, 7 2020. ISSN 0897-4756. doi: 10.1021/acs.chemmater.0c01735.
- [314] Cameron F. Holder and Raymond E. Schaak. Tutorial on powder x-ray diffraction for characterizing nanoscale materials. *ACS Nano*, 13:7359–7365, 7 2019. ISSN 1936-0851. doi: 10.1021/acsnano.9b05157.
- [315] Mark C. Weidman, Michael Seitz, Samuel D. Stranks, and William A. Tisdale. Highly tunable colloidal perovskite nanoplatelets through variable cation, metal,

- and halide composition. *ACS Nano*, 10:7830–7839, 8 2016. ISSN 1936-0851. doi: 10.1021/acsnano.6b03496.
- [316] Joseph R Lakowicz. *Principles of Fluorescence Spectroscopy*, pages XXVI–954. Springer New York, NY, 2006. ISBN 978-0-387-31278-1. doi: 10.1007/978-0-387-46312-4.
- [317] Felix Fries and Sebastian Reineke. Statistical treatment of photoluminescence quantum yield measurements. *Scientific Reports*, 9:15638, 10 2019. ISSN 2045-2322. doi: 10.1038/s41598-019-51718-4.
- [318] Stefan Gundacker, Rosana Martinez Turtos, Nicolaus Kratochwil, Rosalinde Hendrika Pots, Marco Paganoni, Paul Lecoq, and Etienne Auffray. Experimental time resolution limits of modern sipms and tof-pet detectors exploring different scintillators and cherenkov emission. *Physics in Medicine & Biology*, 65:025001, 1 2020. ISSN 0031-9155. doi: 10.1088/1361-6560/ab63b4.
- [319] Michael David Abramoff, Paulo Jorge Magalhães, and Sunanda J. Ram. Image processing with imagej. *Biophotonics International*, 11:36–41, 2004. doi: 10.1201/9781420005615.
- [320] Aarya Prabhakaran, Zhiya Dang, Rohan Dhall, Fabrizio Camerin, Susana Marín-Aguilar, Balaji Dhanabalan, Andrea Castelli, Rosaria Brescia, Liberato Manna, Marjolein Dijkstra, and Milena P. Arciniegas. Real-time in situ observation of CsPbBr₃ perovskite nanoplatelets transforming into nanosheets. *ACS Nano*, 17:13648–13658, 7 2023. ISSN 1936-0851. doi: 10.1021/acsnano.3c02477.
- [321] Chuanxiao Xiao, Zhen Li, Harvey Guthrey, John Moseley, Ye Yang, Sarah Wozny, Helio Moutinho, Bobby To, Joseph J. Berry, Brian Gorman, Yanfa Yan, Kai Zhu, and Mowafak Al-Jassim. Mechanisms of electron-beam-induced damage in perovskite thin films revealed by cathodoluminescence spectroscopy. *The Journal of Physical Chemistry C*, 119:26904–26911, 12 2015. ISSN 1932-7447. doi: 10.1021/acs.jpcc.5b09698.
- [322] Zhiya Dang, Javad Shamsi, Francisco Palazon, Muhammad Imran, Quinten A. Akkerman, Sungwook Park, Giovanni Bertoni, Mirko Prato, Rosaria Brescia, and Liberato Manna. In situ transmission electron microscopy study of electron beam-induced transformations in colloidal cesium lead halide perovskite nanocrystals. *ACS Nano*, 11:2124–2132, 2 2017. ISSN 1936-0851. doi: 10.1021/acsnano.6b08324.
- [323] Daniela Caruntu, Taha Rostamzadeh, Tommaso Costanzo, Saman Saleemizadeh Parizi, and Gabriel Caruntu. Solvothermal synthesis and controlled self-assembly

- of monodisperse titanium-based perovskite colloidal nanocrystals. *Nanoscale*, 7: 12955–12969, 2015. ISSN 2040-3364. doi: 10.1039/C5NR00737B.
- [324] Chang Liu, Jing Lin, Wei Zhai, Zhikai Wen, Xin He, Mengmeng Yu, Yang Huang, Zhonglu Guo, Chao Yu, and Chengchun Tang. Solvothermal synthesis of mn-doped cspbcl₃ perovskite nanocrystals with tunable morphology and their size-dependent optical properties. *RSC Advances*, 9:39315–39322, 2019. ISSN 2046-2069. doi: 10.1039/C9RA08289A.
- [325] Duo Zhang, Mengmeng Yu, Yaobin Xu, Danyang Li, Yang Huang, Chao Yu, Chengchun Tang, and Jing Lin. Solvothermal synthesis of perovskite cspbcl₃ nanoplates and improved photoluminescence performance through postsynthetic treatment. *Optical Materials*, 127:112257, 5 2022. ISSN 09253467. doi: 10.1016/j.optmat.2022.112257.
- [326] Tarek Alammar, Ines Hamm, Viktoria Grasmik, Michael Wark, and Anja-Verena Mudring. Microwave-assisted synthesis of perovskite srsno₃ nanocrystals in ionic liquids for photocatalytic applications. *Inorganic Chemistry*, 56:6920–6932, 6 2017. ISSN 0020-1669. doi: 10.1021/acs.inorgchem.7b00279.
- [327] Heng Pan, Xiaofang Xu, Jiaming Liu, Xu Li, Hao Zhang, Anping Huang, and Zhisong Xiao. Microwave-assisted synthesis of blue-emitting cesium bismuth bromine perovskite nanocrystals without polar solvent. *Journal of Alloys and Compounds*, 886:161248, 12 2021. ISSN 09258388. doi: 10.1016/j.jallcom.2021.161248.
- [328] Mozhgan Khorasani-Motlagh, Meissam Noroozifar, and Akram Ahanin-Jan. Ultrasonic and microwave-assisted co-precipitation synthesis of pure phase lafeo₃ perovskite nanocrystals. *Journal of the Iranian Chemical Society*, 9:833–839, 10 2012. ISSN 1735-207X. doi: 10.1007/s13738-012-0100-9.
- [329] Hushui Chen, Jie Chen, Liang Zhao, Tingshun Zhu, and Zhenyu Yang. Electrochemical synthesis of colloidal lead- and bismuth-based perovskite nanocrystals. *Chemical Communications*, 57:11553–11556, 2021. ISSN 1359-7345. doi: 10.1039/D1CC04327G.
- [330] Luyao Zheng, Amin Nozariasbmarz, Yuchen Hou, Jungjin Yoon, Wenjie Li, Yu Zhang, Haodong Wu, Dong Yang, Tao Ye, Mohan Sanghadasa, Ke Wang, Bed Poudel, Shashank Priya, and Kai Wang. A universal all-solid synthesis for high throughput production of halide perovskite. *Nature Communications*, 13: 7399, 12 2022. ISSN 2041-1723. doi: 10.1038/s41467-022-35122-7.

- [331] Quinten A. Akkerman, Tan P. T. Nguyen, Simon C. Boehme, Federico Montanarella, Dmitry N. Dirin, Philipp Wechsler, Finn Beiglböck, Gabriele Rainò, Rolf Erni, Claudine Katan, Jacky Even, and Maksym V. Kovalenko. Controlling the nucleation and growth kinetics of lead halide perovskite quantum dots. *Science*, 377:1406–1412, 9 2022. ISSN 0036-8075. doi: 10.1126/science.abq3616.
- [332] Victor I. Klimov. *Nanocrystal Quantum Dots*. CRC Press, 12 2010. ISBN 9781315218632. doi: 10.1201/9781420079272.
- [333] Soon Gu Kwon and Taeghwan Hyeon. Formation mechanisms of uniform nanocrystals via hot-injection and heat-up methods. *Small*, 7:2685–2702, 10 2011. ISSN 16136810. doi: 10.1002/smll.201002022.
- [334] Binbin Luo, Ziwei Wang, Tine Curk, Garrett Watson, Chang Liu, Ahyoung Kim, Zihao Ou, Erik Luijten, and Qian Chen. Unravelling crystal growth of nanoparticles. *Nature Nanotechnology*, 18:589–595, 6 2023. ISSN 1748-3387. doi: 10.1038/s41565-023-01355-w.
- [335] J. W. Mullin. *Crystallization*. Butterworth-Heinemann, 4th edition edition, 2001. ISBN 0 7506 4833 3.
- [336] Jörg Polte. Fundamental growth principles of colloidal metal nanoparticles – a new perspective. *CrystEngComm*, 17:6809–6830, 2015. ISSN 1466-8033. doi: 10.1039/C5CE01014D.
- [337] Jörn W. P. Schmelzer, Grey Sh. Boltachev, and Vladimir G. Baidakov. Classical and generalized gibbs’ approaches and the work of critical cluster formation in nucleation theory. *The Journal of Chemical Physics*, 124, 5 2006. ISSN 0021-9606. doi: 10.1063/1.2196412.
- [338] Nguyen T. K. Thanh, N. Maclean, and S. Mahiddine. Mechanisms of nucleation and growth of nanoparticles in solution. *Chemical Reviews*, 114:7610–7630, 8 2014. ISSN 0009-2665. doi: 10.1021/cr400544s.
- [339] M. Volmer and A. Weber. Keimbildung in übersättigten gebilden. *Zeitschrift für Physikalische Chemie*, 119U:277–301, 1 1926. ISSN 2196-7156. doi: 10.1515/zpch-1926-11927.
- [340] Victor K. LaMer and Robert H. Dinegar. Theory, production and mechanism of formation of monodispersed hydrosols. *Journal of the American Chemical Society*, 72:4847–4854, 11 1950. ISSN 0002-7863. doi: 10.1021/ja01167a001.
- [341] Victor K. LaMer. Nucleation in phase transitions. *Industrial & Engineering Chemistry*, 44:1270–1277, 6 1952. ISSN 0019-7866. doi: 10.1021/ie50510a027.

- [342] Tadao Sugimoto. Underlying mechanisms in size control of uniform nanoparticles. *Journal of Colloid and Interface Science*, 309:106–118, 5 2007. ISSN 00219797. doi: 10.1016/j.jcis.2007.01.036.
- [343] W. Ostwald. Über die vermeintliche isomerie des roten und gelben quecksilberoxyds und die oberflächenspannung fester körper. *Zeitschrift für Physikalische Chemie*, 34U:495–503, 7 1900. ISSN 2196-7156. doi: 10.1515/zpch-1900-3431.
- [344] Haimei Zheng, Rachel K. Smith, Young wook Jun, Christian Kisielowski, Ulrich Dahmen, and A. Paul Alivisatos. Observation of single colloidal platinum nanocrystal growth trajectories. *Science*, 324:1309–1312, 6 2009. ISSN 0036-8075. doi: 10.1126/science.1172104.
- [345] Markus Niederberger and Helmut Cölfen. Oriented attachment and mesocrystals: Non-classical crystallization mechanisms based on nanoparticle assembly. *Phys. Chem. Chem. Phys.*, 8:3271–3287, 2006. ISSN 1463-9076. doi: 10.1039/B604589H.
- [346] Dongsheng Li, Michael H. Nielsen, Jonathan R. I. Lee, Cathrine Frandsen, Jillian F. Banfield, and James J. De Yoreo. Direction-specific interactions control crystal growth by oriented attachment. *Science*, 336(6084):1014–1018, 2012. doi: 10.1126/science.1219643.
- [347] Xiaogang Peng, Liberato Manna, Weidong Yang, Juanita Wickham, Erik Scher, Andreas Kadavanich, and A. P. Alivisatos. Shape control of cdse nanocrystals. *Nature*, 404:59–61, 3 2000. ISSN 0028-0836. doi: 10.1038/35003535.
- [348] Z. Adam Peng and Xiaogang Peng. Nearly monodisperse and shape-controlled cdse nanocrystals via alternative routes: Nucleation and growth. *Journal of the American Chemical Society*, 124:3343–3353, 4 2002. ISSN 0002-7863. doi: 10.1021/ja0173167.
- [349] C. B. Murray, D. J. Norris, and M. G. Bawendi. Synthesis and characterization of nearly monodisperse cde (e = sulfur, selenium, tellurium) semiconductor nanocrystallites. *Journal of the American Chemical Society*, 115:8706–8715, 9 1993. ISSN 0002-7863. doi: 10.1021/ja00072a025.
- [350] Kenneth J. Klabunde. *Nanoscale Materials in Chemistry*. John Wiley & Sons, Inc., 8 2001. ISBN 9780471383956. doi: 10.1002/0471220620.
- [351] Shibin Sun, Dan Yuan, Yuan Xu, Aifei Wang, and Zhengtao Deng. Ligand-mediated synthesis of shape-controlled cesium lead halide perovskite nanocrystals via reprecipitation process at room temperature. *ACS Nano*, 10:3648–3657, 3 2016. ISSN 1936-0851. doi: 10.1021/acsnano.5b08193.

- [352] He Huang, Johannes Raith, Stephen V. Kershaw, Sergii Kalytchuk, Ondrej Tomanec, Lihong Jing, Andrei S. Sussha, Radek Zboril, and Andrey L. Rogach. Growth mechanism of strongly emitting $\text{CH}_3\text{NH}_3\text{PbBr}_3$ perovskite nanocrystals with a tunable bandgap. *Nature Communications*, 8:996, 10 2017. ISSN 2041-1723. doi: 10.1038/s41467-017-00929-2.
- [353] Thumu Udayabhaskararao, Miri Kazes, Lothar Houben, Hong Lin, and Dan Oron. Nucleation, growth, and structural transformations of perovskite nanocrystals. *Chemistry of Materials*, 29:1302–1308, 2 2017. ISSN 0897-4756. doi: 10.1021/acs.chemmater.6b04841.
- [354] Muhammad Imran, Vincenzo Caligiuri, Mengjiao Wang, Luca Goldoni, Mirko Prato, Roman Krahne, Luca De Trizio, and Liberato Manna. Benzoyl halides as alternative precursors for the colloidal synthesis of lead-based halide perovskite nanocrystals. *Journal of the American Chemical Society*, 140:2656–2664, 2 2018. ISSN 0002-7863. doi: 10.1021/jacs.7b13477.
- [355] H. M. R. Hoffmann and Klaus Haase. The Synthesis of Acyl Iodides. *Synthesis*, 1981(09):715–719, 1981. ISSN 0039-7881. doi: 10.1055/s-1981-29573.
- [356] Daniel K. Harris and Mounqi G. Bawendi. Improved precursor chemistry for the synthesis of III–V quantum dots. *Journal of the American Chemical Society*, 134: 20211–20213, 12 2012. ISSN 0002-7863. doi: 10.1021/ja309863n.
- [357] Jonathan De Roo, Maria Ibáñez, Pieter Geiregat, Georgian Nedelcu, Willem Walravens, Jorick Maes, Jose C. Martins, Isabel Van Driessche, Maksym V. Kovalenko, and Zeger Hens. Highly dynamic ligand binding and light absorption coefficient of cesium lead bromide perovskite nanocrystals. *ACS Nano*, 10:2071–2081, 2 2016. ISSN 1936-0851. doi: 10.1021/acsnano.5b06295.
- [358] Aozhen Xie, Francesco Maddalena, Marcin E. Witkowski, Michal Makowski, Benoit Mahler, Winicjusz Drozdowski, Stuart Victor Springham, Philippe Coquet, Christophe Dujardin, Muhammad Danang Birowosuto, and Cuong Dang. Library of two-dimensional hybrid lead halide perovskite scintillator crystals. *Chemistry of Materials*, 32:8530–8539, 10 2020. ISSN 0897-4756. doi: 10.1021/acs.chemmater.0c02789.
- [359] A. Dyer and J. C. J. Dean. Application of the double ratio technique to emulsion systems for liquid scintillation counting of ^3H and ^{14}C labelled materials. *Journal of Radioanalytical and Nuclear Chemistry Articles*, 141:139–154, 7 1990. ISSN 0236-5731. doi: 10.1007/BF02060192.

- [360] Mingjie Liu, Lin Huang, Di Yuan, Zhiwei Li, Yunxue Teng, Juannan Zhang, Shiming Huang, and Bo Liu. Perovskite nanocrystals and dyes for high-efficiency liquid scintillator counters to detect radiation. *ACS Applied Nano Materials*, 6:370–378, 1 2023. ISSN 2574-0970. doi: 10.1021/acsanm.2c04510.
- [361] Huiwang Lian, Wenxia Zhang, Rui Zou, Simin Gu, Rongyi Kuang, Yunfei Zhu, Xinyue Zhang, Chong-Geng Ma, Jing Wang, and Yang Li. Aqueous-based inorganic colloidal halide perovskites customizing liquid scintillators. *Advanced Materials*, 9 2023. ISSN 0935-9648. doi: 10.1002/adma.202304743.
- [362] C Aberle, A Elagin, H J Frisch, M Wetstein, and L Winslow. Measuring directionality in double-beta decay and neutrino interactions with kiloton-scale scintillation detectors. *Journal of Instrumentation*, 9:P06012–P06012, 6 2014. ISSN 1748-0221. doi: 10.1088/1748-0221/9/06/P06012.
- [363] Junzhi Ye, Mahdi Malekshahi Byranvand, Clara Otero Martínez, Robert L. Z. Hoye, Michael Saliba, and Lakshminarayana Polavarapu. Defect passivation in lead-halide perovskite nanocrystals and thin films: Toward efficient leds and solar cells. *Angewandte Chemie*, 133:21804–21828, 9 2021. ISSN 0044-8249. doi: 10.1002/ange.202102360.
- [364] David P. Nenon, Kimo Pressler, Jun Kang, Brent A. Koscher, Jacob H. Olshansky, Wojciech T. Osowiecki, Matthew A. Koc, Lin-Wang Wang, and A. Paul Alivisatos. Design principles for trap-free CsPbX₃ nanocrystals: Enumerating and eliminating surface halide vacancies with softer lewis bases. *Journal of the American Chemical Society*, 140:17760–17772, 12 2018. ISSN 0002-7863. doi: 10.1021/jacs.8b11035.
- [365] V. G. Vasavi Dutt, Syed Akhil, Rahul Singh, Manoj Palabathuni, and Nimai Mishra. Year-long stability and near-unity photoluminescence quantum yield of CsPbBr₃ perovskite nanocrystals by benzoic acid post-treatment. *The Journal of Physical Chemistry C*, 126:9502–9508, 6 2022. ISSN 1932-7447. doi: 10.1021/acs.jpcc.2c01467.
- [366] Th. Förster. Zwischenmolekulare energiewanderung und fluoreszenz. *Annalen der Physik*, 437(1-2):55–75, 1948. doi: <https://doi.org/10.1002/andp.19484370105>.
- [367] D.L. Andrews. A unified theory of radiative and radiationless molecular energy transfer. *Chemical Physics*, 135(2):195–201, 1989. ISSN 0301-0104. doi: [https://doi.org/10.1016/0301-0104\(89\)87019-3](https://doi.org/10.1016/0301-0104(89)87019-3).
- [368] Garth A. Jones and David S. Bradshaw. Resonance energy transfer: From fundamental theory to recent applications. *Frontiers in Physics*, 7, 7 2019. ISSN 2296-424X. doi: 10.3389/fphy.2019.00100.

- [369] Subha Chakraborty, Katherine Harris, and Mengbing Huang. Photoluminescence properties of polystyrene-hosted fluorophore thin films. *AIP Advances*, 6(12), 12 2016. ISSN 2158-3226. doi: 10.1063/1.4972989.
- [370] Norman B. Colthup, Lawrence H. Daly, and Stephen E. Wiberley. *Introduction to Infrared and Raman Spectroscopy*. Academic Press, 3rd edition edition, 1990. ISBN 978-0-12-182554-6. doi: 10.1016/C2009-0-21628-X.
- [371] Norman B. Colthup, Lawrence H. Daly, and Stephen E. Wiberley. *Introduction to Infrared and Raman Spectroscopy*. Academic Press, 3rd edition edition, 1990. ISBN 978-0-12-182554-6. doi: 10.1016/C2009-0-21628-X.
- [372] Norman B. Colthup, Lawrence H. Daly, and Stephen E. Wiberley. *Introduction to Infrared and Raman Spectroscopy*. Academic Press, 3rd edition edition, 1990. ISBN 978-0-12-182554-6. doi: 10.1016/C2009-0-21628-X.
- [373] Benoît Sabot, Chavdar Dutsov, Philippe Cassette, and Krasimir Mitev. Performance of portable tdc systems developed at Ine-Inhb. *Nuclear Instruments and Methods in Physics Research Section A: Accelerators, Spectrometers, Detectors and Associated Equipment*, 1034:166721, 7 2022. ISSN 01689002. doi: 10.1016/j.nima.2022.166721.
- [374] R Broda. A review of the triple-to-double coincidence ratio (tdcr) method for standardizing radionuclides. *Applied Radiation and Isotopes*, 58:585–594, 5 2003. ISSN 09698043. doi: 10.1016/S0969-8043(03)00056-3.
- [375] Piotr A. Rodnyi. *Physical Processes in Inorganic Scintillators*, chapter 1: Basic Principles and Processes. CRC Press, 12 1997. ISBN 9780138743352. doi: 10.1201/9780138743352.
- [376] C. Dujardin. Matériaux scintillateurs inorganiques. *Techniques de l'Ingénieur*, 2017.
- [377] P. Cassette and Phuc Do. The compton source efficiency tracing method in liquid scintillation counting: A new standardization method using a tdc counter with a compton spectrometer. *Applied Radiation and Isotopes*, 66:1026–1032, 6 2008. ISSN 09698043. doi: 10.1016/j.apradiso.2008.02.062.
- [378] James Thomson and Simon Temple. *Sample preparation techniques for liquid scintillation analysis*, pages 803–860. Academic Press, fourth edition edition, 2020. ISBN 978-0-12-814397-1. doi: <https://doi.org/10.1016/B978-0-12-814397-1.00007-8>. Chapter 7.

- [379] R. H. Benson. Limitations of tritium measurements by liquid scintillation counting of emulsions. *Analytical Chemistry*, 38:1353–1356, 9 1966. ISSN 0003-2700. doi: 10.1021/ac60242a016.
- [380] Xiaogang Peng, Michael C. Schlamp, Andreas V. Kadavanich, and A. P. Alivisatos. Epitaxial growth of highly luminescent cdse/cds core/shell nanocrystals with photostability and electronic accessibility. *Journal of the American Chemical Society*, 119:7019–7029, 7 1997. ISSN 0002-7863. doi: 10.1021/ja970754m. doi: 10.1021/ja970754m.
- [381] Shaocong Hou, Yuzheng Guo, Yuguo Tang, and Qimin Quan. Synthesis and stabilization of colloidal perovskite nanocrystals by multidentate polymer micelles. *ACS Applied Materials & Interfaces*, 9:18417–18422, 6 2017. ISSN 1944-8244. doi: 10.1021/acsami.7b03445.
- [382] Yanjie He, Young Jun Yoon, Yeu Wei Harn, Gill V. Biesold-McGee, Shuang Liang, Chun Hao Lin, Vladimir V. Tsukruk, Naresh Thadhani, Zhitao Kang, and Zhiqun Lin. Unconventional route to dual-shelled organolead halide perovskite nanocrystals with controlled dimensions, surface chemistry, and stabilities. *Science Advances*, 5, 11 2019. ISSN 2375-2548. doi: 10.1126/sciadv.aax4424.
- [383] C.V. Mary Vijila, K. Rajeev Kumar, and M.K. Jayaraj. Stokes shift engineered, stable core-shell perovskite nanoparticle – poly(methyl methacrylate) composites with high photoluminescence quantum yield. *Optical Materials*, 94:241–248, 8 2019. ISSN 09253467. doi: 10.1016/j.optmat.2019.05.046.
- [384] Tongtong Xuan, Junjian Huang, Huan Liu, Sunqi Lou, Luyu Cao, Weijiang Gan, Ru-Shi Liu, and Jing Wang. Super-hydrophobic cesium lead halide perovskite quantum dot-polymer composites with high stability and luminescent efficiency for wide color gamut white light-emitting diodes. *Chemistry of Materials*, 31: 1042–1047, 2 2019. ISSN 0897-4756. doi: 10.1021/acs.chemmater.8b04596.
- [385] Albrecht Benad, Chris Guhrenz, Christoph Bauer, Franziska Eichler, Marcus Adam, Christoph Ziegler, Nikolai Gaponik, and Alexander Eychmüller. Cold flow as versatile approach for stable and highly luminescent quantum dot–salt composites. *ACS Applied Materials & Interfaces*, 8:21570–21575, 8 2016. ISSN 1944-8244. doi: 10.1021/acsami.6b06452.
- [386] W. Xuan, H. Shan, D. Hu, L. Zhu, T. Guan, Y. Zhao, Y. Qiang, J. Song, J. Zhang, M. Sui, X. Gu, and S. Huang. In-situ synthesis of stable zno-coated CsPbBr₃ nanocrystals for room-temperature heptanal sensors. *Materials Today Chemistry*, 26:101155, 12 2022. ISSN 24685194. doi: 10.1016/j.mtchem.2022.101155.

- [387] Li-Wei Chao, Jian-Fu Tang, Shih-Hung Lin, Yi-Ting Lee, Yi-Lun Chen, Cheng-Ho Hsieh, Lung-Chien Chen, and Zong-Liang Tseng. Facile room-temperature synthesis of highly air-stable and moisture-resistant $\text{CsPbBr}_3/\text{SiO}_2$ nanocomposites for tunable white light-emitting diodes. *Materials Science in Semiconductor Processing*, 136:106158, 12 2021. ISSN 13698001. doi: 10.1016/j.mssp.2021.106158.
- [388] Zheming Liu, Lutfan Sinatra, Marat Lutfullin, Yurii P. Ivanov, Giorgio Divitini, Luca De Trizio, and Liberato Manna. One hundred-nanometer-sized $\text{CsPbBr}_3/\text{m-SiO}_2$ composites prepared via molten-salts synthesis are optimal green phosphors for lcd display devices. *Advanced Energy Materials*, 12:2201948, 10 2022. ISSN 1614-6832. doi: 10.1002/aenm.202201948.
- [389] Jinwoo Park, Kyung Yeon Jang, Song Hee Lee, Dong-Hyeok Kim, So-Hye Cho, and Tae-Woo Lee. Stable orthorhombic CsPbBr_3 light emitters: Encapsulation-assisted in situ synthesis. *Chemistry of Materials*, 35:6266–6273, 8 2023. ISSN 0897-4756. doi: 10.1021/acs.chemmater.3c00732.
- [390] Jiangluqi Song, Tongtong Jiang, Tianyi Guo, Ling Liu, Huijie Wang, Tongyan Xia, Wenting Zhang, Xuecheng Ye, Mingya Yang, Lixin Zhu, Ruixiang Xia, and Xiaoliang Xu. Facile synthesis of water-soluble zn-doped $\text{AgIn}_5\text{S}_8/\text{ZnS}$ core/shell fluorescent nanocrystals and their biological application. *Inorganic Chemistry*, 54:1627–1633, 2 2015. ISSN 0020-1669. doi: 10.1021/ic502600u.
- [391] Vikash Kumar Ravi, Sajid Saikia, Shivam Yadav, Vaibhav V. Nawale, and Angshuman Nag. $\text{CsPbBr}_3/\text{ZnS}$ core/shell type nanocrystals for enhancing luminescence lifetime and water stability. *ACS Energy Letters*, 5:1794–1796, 6 2020. ISSN 2380-8195. doi: 10.1021/acsenerylett.0c00858.
- [392] Zhiqiang Li, Wanqing Li, Hongyu Shao, Minghao Dou, Yuye Cheng, Xiangling Wan, Xiuxian Jiang, Zhengguang Zhang, Yanyan Chen, and Shenjie Li. Water-soluble Ag-Sn-S nanocrystals partially coated with ZnS shells for photocatalytic degradation of organic dyes. *ACS Applied Nano Materials*, 6:4417–4427, 3 2023. ISSN 2574-0970. doi: 10.1021/acsanm.2c05500.
- [393] Metikoti Jagadeeswararao, Parth Vashishtha, Thomas J. N. Hooper, Anil Kanwat, Jia Wei Melvin Lim, Sujaya Kumar Vishwanath, Natalia Yantara, Taewook Park, Tze Chien Sum, Dae Sung Chung, Subodh G. Mhaisalkar, and Nripan Mathews. One-pot synthesis and structural evolution of colloidal cesium lead halide–lead sulfide heterostructure nanocrystals for optoelectronic applications. *The Journal of Physical Chemistry Letters*, 12:9569–9578, 10 2021. ISSN 1948-7185. doi: 10.1021/acs.jpcllett.1c02915.

- [394] Xiaosheng Tang, Jie Yang, Shiqi Li, Zhengzheng Liu, Zhiping Hu, Jiongyue Hao, Juan Du, Yuxin Leng, Haiyan Qin, Xing Lin, Yue Lin, Yuxi Tian, Miao Zhou, and Qihua Xiong. Single halide perovskite/semiconductor core/shell quantum dots with ultrastability and nonblinking properties. *Advanced Science*, 6:1900412, 9 2019. ISSN 2198-3844. doi: 10.1002/adv.201900412.
- [395] Anthony Kipkorir, Jeffrey DuBose, Junsang Cho, and Prashant V. Kamat. CsPbBr₃-cds heterostructure: stabilizing perovskite nanocrystals for photocatalysis. *Chemical Science*, 12:14815–14825, 2021. ISSN 2041-6520. doi: 10.1039/D1SC04305F.
- [396] Jordan W. Thomson, Kaz Nagashima, Peter M. Macdonald, and Geoffrey A. Ozin. From sulfur-amine solutions to metal sulfide nanocrystals: Peering into the oleylamine-sulfur black box. *Journal of the American Chemical Society*, 133:5036–5041, 4 2011. ISSN 0002-7863. doi: 10.1021/ja1109997.
- [397] Yuhai Zhang, Makhsud I. Saidaminov, Ibrahim Dursun, Haoze Yang, Banavoth Murali, Erkki Alarousu, Emre Yengel, Buthainah A. Alshankiti, Osman M. Bakr, and Omar F. Mohammed. Zero-dimensional cs₄pbbr₆ perovskite nanocrystals. *The Journal of Physical Chemistry Letters*, 8:961–965, 3 2017. ISSN 1948-7185. doi: 10.1021/acs.jpcl.7b00105.
- [398] Husn-Ubayda Islam, Anna Roffey, Nathan Hollingsworth, Wim Bras, Gopinathan Sankar, Nora H. De Leeuw, and Graeme Hogarth. Understanding the role of zinc dithiocarbamate complexes as single source precursors to zns nanomaterials. *Nanoscale Advances*, 2:798–807, 2020. ISSN 2516-0230. doi: 10.1039/C9NA00665F.
- [399] Maurizio Conti. Focus on time-of-flight pet: the benefits of improved time resolution. *European Journal of Nuclear Medicine and Molecular Imaging*, 38:1147–1157, 6 2011. ISSN 1619-7070. doi:10.1007/s00259-010-1711-y.
- [400] Suleman Surti and Joel S. Karp. Advances in time-of-flight pet. *Physica Medica*, 32:12–22, 1 2016. ISSN 11201797. doi: 10.1016/j.ejmp.2015.12.007.
- [401] Paul Lecoq, Christian Morel, John O Prior, Dimitris Visvikis, Stefan Gundacker, Etienne Auffray, Peter Krizán, Rosana Martinez Turtos, Dominique Thers, Edoardo Charbon, Joao Varela, Christophe de La Taille, Angelo Rivetti, Dominique Breton, Jean-François Pratte, Johan Nuyts, Suleman Surti, Stefaan Vandenberghe, Paul Marsden, Katia Parodi, Jose Maria Benloch, and Mathieu Benoit. Roadmap toward the 10 ps time-of-flight pet challenge. *Physics in Medicine & Biology*, 65, 10 2020. ISSN 1361-6560. doi: 10.1088/1361-6560/ab9500.

- [402] Yujing Liu, Wentao Yuan, Ye Shi, Xiaoqiang Chen, Yong Wang, Hongzheng Chen, and Hanying Li. Functionalizing single crystals: Incorporation of nanoparticles inside gel-grown calcite crystals. *Angewandte Chemie International Edition*, 53: 4127–4131, 4 2014. ISSN 14337851. doi: 10.1002/anie.201310712.
- [403] Yujing Liu, Huidong Zang, Ling Wang, Weifei Fu, Wentao Yuan, Jiake Wu, Xinyi Jin, Jishu Han, Changfeng Wu, Yong Wang, Huolin L. Xin, Hongzheng Chen, and Hanying Li. Nanoparticles incorporated inside single-crystals: Enhanced fluorescent properties. *Chemistry of Materials*, 28:7537–7543, 10 2016. ISSN 0897-4756. doi: 10.1021/acs.chemmater.6b03589.
- [404] Fiammetta Pagano, Nicolaus Kratochwil, Matteo Salomoni, Marco Pizzichemi, Marco Paganoni, and Etienne Auffray. Advances in heterostructured scintillators: toward a new generation of detectors for tof-pet. *Physics in Medicine & Biology*, 67:135010, 7 2022. ISSN 0031-9155. doi: 10.1088/1361-6560/ac72ee.
- [405] Philip Krause, Edith Rogers, Muhammad Danang Birowosuto, Qibing Pei, Etienne Auffray, Andrey N. Vasil'ev, and Gregory Bizarri. Design rules for time of flight positron emission tomography (tof-pet) heterostructure radiation detectors. *Heliyon*, 8:e09754, 6 2022. ISSN 24058440. doi: 10.1016/j.heliyon.2022.e09754.
- [406] Benjamin Balaban, Sage Doshay, Melissa Osborn, Yvonne Rodriguez, and Sue A. Carter. The role of fret in solar concentrator efficiency and color tunability. *Journal of Luminescence*, 146:256–262, 2 2014. ISSN 00222313. doi: 10.1016/j.jlumin.2013.09.049.
- [407] Michèle G. Greiner, Andreas Singldinger, Nina A. Henke, Carola Lampe, Ulrich Leo, Moritz Gramlich, and Alexander S. Urban. Energy transfer in stability-optimized perovskite nanocrystals. *Nano Letters*, 22:6709–6715, 8 2022. ISSN 1530-6984. doi: 10.1021/acs.nanolett.2c02108.
- [408] Alexander O. Govorov, Garnett W. Bryant, Wei Zhang, Timur Skeini, Jaebeom Lee, Nicholas A. Kotov, Joseph M Slocik, and Rajesh R. Naik. Exciton-plasmon interaction and hybrid excitons in semiconductor-metal nanoparticle assemblies. *Nano Letters*, 6:984–994, 2006.
- [409] Justine Baronnier, Julien Houel, Christophe Dujardin, Florian Kulzer, and Benoît Mahler. Doping MAPbBr₃ hybrid perovskites with cdse/cdzns quantum dots: from emissive thin films to hybrid single-photon sources. *Nanoscale*, 14:5769–5781, 2022. ISSN 2040-3364. doi: 10.1039/D1NR08473A.
- [410] Francesco Maddalena, Marcin E. Witkowski, Michal Makowski, Abdellah Bachiri, Arramel, Ting Yang, Muhammad Haris Mahyuddin, Matilde Baravaglio,

- Mohamed Boutchich, Winicjusz Drozdowski, Christophe Dujardin, Muhammad Danang Birowosuto, and Cuong Dang. Photodetection and scintillation characterizations of novel lead-bismuth double perovskite halides. *Journal of Materials Chemistry C*, 10:11266–11275, 7 2022. ISSN 2050-7526. doi: 10.1039/D2TC01646J.
- [411] Aozhen Xie, Chathuranga Hettiarachchi, Francesco Maddalena, Marcin E. Witkowski, Michał Makowski, Winicjusz Drozdowski, Arramel Arramel, Andrew T. S. Wee, Stuart Victor Springham, Phan Quoc Vuong, Hong Joo Kim, Christophe Dujardin, Philippe Coquet, Muhammad Danang Birowosuto, and Cuong Dang. Lithium-doped two-dimensional perovskite scintillator for wide-range radiation detection. *Communications Materials*, 1:37, 6 2020. ISSN 2662-4443. doi: 10.1038/s43246-020-0038-x.
- [412] Margaret Chern, Thuy T. Nguyen, Andrew H. Mahler, and Allison M. Dennis. Shell thickness effects on quantum dot brightness and energy transfer. *Nanoscale*, 9:16446–16458, 2017. ISSN 2040-3364. doi: 10.1039/C7NR04296E.